NOVA SCHOOL OF SCIENCE & TECHNOLOGY

DEPARTAMENT OF MECHANICAL AND INDUSTRIAL ENGINEERING

Multiscale optimization of non-conventional composite structures for improved mechanical response

Fábio Rúben Monteiro Conde

Master in Mechanical Engineering

DOCTORATE IN MECHANICAL ENGINEERING

NOVA University Lisbon

December, 2022

NOVA SCHOOL OF SCIENCE & TECHNOLOGY

DEPARTAMENT OF MECHANICAL AND INDUSTRIAL ENGINEERING

Multiscale optimization of non-conventional composite structures for improved mechanical response

Fábio Rúben Monteiro Conde

Master in Mechanical Engineering

Adviser: Prof. Dr. Pedro Samuel Gonçalves Coelho
Assistant Professor, FCT-UNL, NOVA University Lisbon

Co-adviser: Prof. Dr. José Arnaldo Pereira Leite Miranda Guedes
Full Professor, IST, University of Lisbon

Examination Committee:

Chair: Telmo Jorge Gomes dos Santos,
Full Professor, FCT-NOVA

Rapporteurs: Paulo Rui Alves Fernandes,
Full Professor, IST
Francisco Manuel Andrade Pires,
Full Professor, FEUP

Adviser: Pedro Samuel Gonçalves Coelho,
Assistant Professor, FCT-NOVA

Members: Hélder Carriço Rodrigues,
Full Professor, IST
Telmo Jorge Gomes dos Santos,
Full Professor, FCT-NOVA
João Mário Burguete Botelho Cardoso,
Assistant Professor, FCT-NOVA

DOCTORATE IN MECHANICAL ENGINEERING

NOVA University Lisbon
December, 2022

Multiscale optimization of non-conventional composite structures for improved mechanical response

ACKNOWLEDGMENTS

Firstly, I would like to thank Professor Dr. Pedro Coelho, my thesis adviser, from NOVA School of Science and Technology for the excellent guidance skill he has shown throughout my thesis, being always available to answer my questions. I received great advice from him, which I will certainly apply to the rest of my professional life.

I also wish to thank Professor Dr. José Guedes, my thesis co-adviser, from Instituto Superior Técnico for sharing his knowledge about homogenization, an important method that is used in this thesis. Very useful meetings were done, which I am grateful for.

Besides my advisers, during my thesis I had occasional meetings with other people that offered me support. Professor Dr. Hélder Rodrigues from Instituto Superior Técnico, is one of them. I acknowledge the interesting discussions about multi-scale optimization, and the opportunity to have participated in the optimization course given by him. Another person that always shown interest in my thesis was Professor Dr. João Cardoso. He was always available to help me, which I appreciated.

The developed methodologies presented in this thesis use some previously developed code. One of the optimizers used is the Method of Moving Asymptotes, originally developed by Professor Dr. Krister Svanberg from Royal Institute of Technology, whom I thank for kindly provided me the source code. The Spring Element Model used to predict and optimize the behaviour of fibre composites was originally developed by Dr. Rodrigo Tavares, whom I thank for providing and explaining the source code.

I attended several PhD courses abroad during my thesis, which helped me in some way to carry out my work. I want to thank Professor Dr. Ole Sigmund, the Topology Optimization course responsible from Danish Technical University in Lyngby, for the great lectures he gave that helped me to understand more clearly some concepts about Topology Optimization. Another useful course that I attended was the High-Performance Computing, given by Professor Dr. Jens Walther from Danish Technical University in Lyngby. This course helped me improve my programming skills and I am thankful for that. Finally, I want to thank Professors Dr. Jörg Schröder and Dr. Michele Marino from CISM-ECCOMAS Advanced School, for the great course that they

gave about Computational Mechanics for Novel Designs of Advanced Materials. This course was useful to deepen my knowledge about Advanced Materials.

To the Fundação para a Ciência e a Tecnologia (FCT – MCTES) I acknowledge for its financial support through the PhD scholarship SFRH/BD/136744/2018.

Finally, I would like to thank my parents (Mário Conde and Dora Conde) and my girlfriend (Irina Mitrofan) for the support they gave me throughout my thesis.

ABSTRACT

Nowadays, due to governmental requirements to control climate change, there is a great interest on the part of the automotive and aerospace industry to design structures as light as possible, without jeopardize their performance, thus increasing their efficiency. Multi-material design is a way to achieve this goal, as will be shown in this work

In this work, multi-material design is considered with the goal of improving the structure's stiffness, strength, and non-linear behaviour when it yields. Firstly, a microstructural topology optimization is carried out seeking for multi-material microstructures with increased stiffness and strength compared to equivalent single-material microstructures. Afterwards, this study is further extended to perform multi-scale topology optimization, where a concurrent optimization of material and structure is done. Ultimately, the non-linear behaviour of hybrid fibre reinforced composites is optimized in order to introduce a so-called "pseudo-ductility".

Two different optimization problems are formulated and solved here. One compliance minimization with mass constraint problem and another stress-based problem where the maximal von Mises stress is locally minimized in the unit-cell. The multi-material design is investigated here using two different approaches. On one hand, the two solids coexist being bonded together across sharp interfaces. On the other hand, a functionally graded material is obtained as an extensive smooth variation of material properties on account of varying composition's volume fractions of both solids throughout the design domain. The compliance-based optimization results show that multi-material microstructures can be stiffer compared to single-material ones for the same mass requirement. Regarding the stress-based problem, lower stress peaks are obtained in bi-material design solutions and, specially, in the case of graded material solutions.

As regards multi-scale topology optimization, the results show that a multi-material structure can be stiffer than its single-material counterpart, which is in accordance with the microstructural study performed earlier.

Hybrid composites can achieve the so-called “pseudo-ductile” behaviour mimicking the well-known elastic-plastic behaviour. To understand under what circumstances such behaviour is obtained, optimization problems are formulated and solved here. Two different types of optimization problems are considered. Firstly, one finds out the optimal properties of fibres to hybridize and get the pseudo-ductile behaviour. Once an optimal hybridization is found, another optimization problem is solved in order to understand the influence of the fibre dispersion on the composite response. The optimal results obtained show hybrid composites having a considerable pseudo-ductile behaviour.

Keywords: Multi-material, Composites, Topology, Optimization.

RESUMO

Atualmente, devido às imposições governamentais para controlar as alterações climáticas, existe um grande interesse por parte da indústria automóvel e aeroespacial para o projeto de estruturas o mais leves possíveis, sem se comprometer o seu desempenho, aumentando assim a sua eficiência. O projeto multimaterial de estruturas é um dos caminhos para se alcançar este objetivo, conforme será mostrado neste trabalho.

Neste trabalho, considera-se o projeto multimaterial de estruturas com o objetivo de se melhorar a rigidez, resistência, e comportamento não linear após cedência. Primeiro, é feita uma otimização de topologia ao nível da microestrutura procurando-se microestruturas multimateriais com maior rigidez e resistência quando comparadas com microestruturas de material único equivalentes. Depois, este estudo é explorado também no contexto de otimização topológica multi-escala, onde é realizada uma otimização concorrente do material e estrutura. Por fim, o comportamento não linear de compósitos híbridos reforçados por fibra é otimizado com vista à introdução de um efeito de "pseudo-ductilidade".

São formulados e resolvidos aqui dois problemas diferentes de otimização. Um problema de minimização de *compliance* (flexibilidade) sujeito a um constrangimento de massa e outro problema baseado na tensão, onde a tensão máxima de von Mises é localmente minimizada na célula unitária. O projeto multi-material é investigado aqui utilizando duas diferentes abordagens. Numa das abordagens, os dois sólidos coexistem na sua forma discreta originando-se interfaces com uma variação abrupta de propriedades. Na outra abordagem, obtém-se um material de gradiente funcional onde existe uma suave variação das propriedades obtida variando pontualmente a fração volúmica dos sólidos ao longo de todo o domínio de projeto. Os resultados da otimização baseada na *compliance* mostraram que microestruturas multimateriais podem ser mais rígidas quando comparadas com as de material único para o mesmo requisito de massa. Relativamente ao problema baseado na tensão, são obtidos picos de tensão mais baixos nas soluções constituídas por duas fases discretas de material e, sobretudo, nas soluções de material de gradiente funcional.

No que que diz respeito à otimização topológica multi-escala, os resultados mostraram que uma estrutura multimaterial pode ser mais rígida que uma estrutura de material único equivalente, o que está de acordo com o estudo realizado anteriormente ao nível da microestrutura.

Os compósitos híbridos conseguem alcançar um comportamento designado de "pseudo-dúctil", imitando o conhecido comportamento elasto-plástico. Para melhor se compreender sob que circunstâncias tal comportamento é obtido, são formulados e resolvidos problemas de otimização. São assim considerados dois tipos diferentes de problemas de otimização. Primeiramente, descobrem-se quais as propriedades ótimas das fibras a hibridizar, obtendo-se o comportamento pseudo-dúctil. Assim que hibridização ótima tenha sido descoberta, outro problema de otimização é resolvido de modo a perceber-se a influência da dispersão das fibras na resposta do compósito. Os resultados ótimos obtidos mostram compósitos híbridos tendo um comportamento pseudo-dúctil considerável.

Palavras chave: Multimaterial, Compósitos, Topologia, Otimização.

CONTENTS

LIST OF FIGURES

LIST OF TABLES

ACRONYMS

AM	Additive Manufacturing
API	Application Programming Interface
CONLIN	CONvex LINearization
CPU	Central Process Unit
CTE	Coefficient of Thermal Expansion
DMO	Discrete Material Optimization
DOF	Degree Of Freedom
ESP	Equi-Stress Principle
FBM	Fibre Bundle Model
FE	Finite Element
FEM	Finite Element Model
FGM	Functionally Graded Material
FGMTO	Functionally Graded Material Topology Optimization
FSD	Fully Stressed Design
GA	Genetic Algorithm
GCMMA	Globally Convergent Method of Moving Asymptotes
GLS	Global Load Sharing
GMMA	Generalized Method of Moving Asymptotes
HE	High Elongation

HPC	High-Performance Computing
HS	Hashin-Shtrikman
KKT	Karush Kuhn Tucker
LbL	Layer-by-Layer
LE	Low Elongation
LLS	Local Load Sharing
MMA	Method of Moving Asymptotes
MMTO	Multi Material Topology
MPI	Message Passing Interface
OC	Optimality Criteria
Open-MP	Open Multi Processing
PAMP	Porous Anisotropic Material with Penalization
PBC	Periodic Boundary Conditions
RVE	Representative Volume Element
SCF	Stress Concentration Factor
SCP	Sequential Convex Programming
SEM	Spring Element Model
SFP	Shape Function Parametrization
SIMP	Solid Isotropic Material with Penalization
SMP	Symmetric Multi-Processing
SMTO	Single Material Topology Optimization
TO	Topology optimization
UC	Unit-Cell
UD	UniDirectional

SYMBOLS

Chapter 2

2.1 Theory of linear elasticity

b	Body forces
C_{ijkl} or **C**	Compliance tensor
E	Elasticity (or Young's) modulus
E_{ijkl} or **E**	Stiffness tensor
G	Shear modulus
K	Bulk modulus
t	Applied load
u	Displacement field
x_i or **x**	Coordinate axes (spatial coordinates)
γ	Shear strain component
δ	Kronecker delta
δV	Infinitesimal volume
ε_{ij} or **ε**	Strain tensor
ε	Normal strain component
λ	First Lamé's constant
μ	Second Lamé's constant

ν	Poisson's ratio
σ_{ij} or $\boldsymbol{\sigma}$	Cauchy's stress tensor
σ	Normal stress component
σ_{eq}^{VM}	von Mises equivalent stress
σ_y	Yield stress
τ	Shear stress component
Ω^{body}	Body domain

2.2 Homogenization theory

d	Characteristic dimension of the smallest periodic heterogeneity
D	Characteristic dimension of the macroscopic domain
$e_{rs}^{0(kl)}$ or $\mathbf{e}^{0(kl)}$	Applied macroscopic deformation
E_{ijkl}^{H} or $\mathbf{E}^{\mathrm{H}}$	Homogenized stiffness tensor
g	General function
$\mathbf{u}^{\varepsilon}$	Asymptotic expansion of the displacement field
$\mathbf{u}^{i}$	i^{th} term of the asymptotic expansion
v_i or $\mathbf{v}$	Virtual displacement
x_i or $\mathbf{x}$	Macroscopic spatial coordinates
y_i or $\mathbf{y}$	Microscopic spatial coordinates
Y or ¥	Microscopic domain
β	An arbitrary constant
Γ_u	Displacement boundary condition
Γ_t	Applied traction boundary condition
$\sigma_{ij}^{\varepsilon}$	Local stress tensor
σ_{ij}^{0}	First approximation of the local stress tensor
σ_{ij}^{H}	Homogenized (global) stress tensor
χ_r^{kl} or $\boldsymbol{\chi}^{kl}$	Solution of the modified local problem (micro displacements)

ψ	An arbitrary Y-Periodic function
Ω^{ε}	Macroscopic domain

2.3 Structural optimization

B_e^k	Parameter used in OC method update scheme
c	Penalty constant
C	Compliance function
c_i	Sufficient large numbers in MMA
d	Search direction
$E_{ijkl}{}^{(0)}$	Base material stiffness tensor
f	Objective function
$f_0, \tilde{f}_0$	Original and approximating objective functions, respectively
$f_i, \tilde{f}_i$	Original and approximating functions of the i^{th} constraint, respectively
$\hat{f}_i$	Right-hand side of constraint i
f	Load vector
g_j	Inequality constraints vector
h_k	Equality constraints vector
H	Hessian matrix
k	Iteration step
K	Stiffness matrix
l	Applied force potential
$L_j^{(k)}$	MMA lower moving asymptote
$\mathcal{L}$	Lagrange function
m	Total number of design constraints
n	Total number of design variables
N_e	Neighbourhood of an element e
P	Penalty exponent in the SIMP law

$p_{ij}^{(k)}$, $q_{ij}^{(k)}$, $r_i^{(k)}$	MMA coefficients
R	Filter radius
s_1, s_2	Given real numbers
U	Kinematically admissible displacement fields
$U_j^{(k)}$	MMA upper moving asymptote
v_i	Volume of element *i*
V^*	Target material volume fraction
w	Weighting function
$\mathbf{x}$	Design variables vector
$\mathbf{x}^{(0)}$	Starting point in the optimization procedure
$\mathbf{x}^{(1)}$	Updated point in the optimization procedure
$\mathbf{x}_i$ or $\mathbf{x}_e$	Spatial location of element *i* or *e*
$\mathbf{y}$, z	MMA artificial variables
α	Optimal step size
$\alpha_j^{(k)}$ and $\beta_j^{(k)}$	MMA move limits
γ_0	User defined real number in MMA
Δx	Step size used to perform the finite difference
ζ	Move limit in OC method update scheme
η	Tuning parameter in OC method update scheme
λ_i	Dual variables in MMA
$\boldsymbol{\lambda}$	Adjoint variable
λ_e^- , λ_e^+	Lagrange multipliers associated with the side constraints
Λ_e	Lagrange multiplier associated with the volume constrain0074
ξ	Step function
ρ_e	Element *e* density
ρ_{min}	Lower bound of the density variable ρ_e

$\rho_j^{(k)}$	Strictly positive parameters used to ensure the convexity of the GCMMA approximation functions
$\tilde{\rho}_e$	Filtered density of element *e*
ψ	A given/general function
Ψ	Dual objective function
Ω	Design domain
Ω_{mat}	Subdomain of the design domain Ω occupied with material
Ω_{void}	Subdomain of the design domain Ω occupied with void
$\lvert\Omega_{\mathrm{e}}\rvert$	Element volume

2.4 Stress-based topology optimization

q	Exponent used in the *qp*-approach
z	Artificial design variable used in the bound formulation
ε	Small parameter used in the ε-relaxation technique
$\langle\varepsilon_{kl}^0\rangle$	Macroscopic strain tensor
σ	Stress value
$\langle\sigma_{ij}\rangle$	Macroscopic stress tensor

2.5 Multi-material topology optimization

A_e	Scaling coefficient in the Ordered SIMP interpolation
B_e	Translation coefficient in the Ordered SIMP interpolation
$E_{ijkl}{}^{(i)}$	Stiffness tensor or material properties of material phase *i*
$\mathbf{w}$ or w_m	Weight functions
ρ_{max}	Maximum allowable density variable in the Ordered SIMP interpolation
$\hat{\rho}_e^m$	Normalized density variable in the Ordered SIMP interpolation

2.6 Multiscale topology optimization

E_{ad}	Physically admissible set of stiffness tensors

ℓ	Lagrange function associated with micro problem
$\mathcal{L}$	Lagrange function associated with the macro problem
$\lvert ¥_k \rvert$	Micro FE *k* volume/area
λ	Lagrange multiplier associated with the local resource constraint
Λ	Lagrange multiplier associated with the global resource constraint
μ_k	Micro density variable
ρ_e	Macro density variable
ϕ	Functional corresponding to the maximization of the strain energy density
$\lvert \Omega_i \rvert$	Subdomain volume/area

Chapter 3

C	Compliance value
C^*	Maximum admissible compliance value
C_{ijkl}^{H} or $\mathbf{C}^{\mathrm{H}}$	Homogenized compliance tensor
$\mathbf{E}_1$	Stiffness tensor of the stiffer solid
$\mathbf{E}_2$	Stiffness tensor of the weaker solid
E_{HS}^{-}	Lower HS bound
E_{HS}^{+}	Upper HS bound
f_0	Objective function
g_i	Design constraints
m	Effective mass value
m^*	Maximum admissible mass value
n_e	Total number of elements in the FE mesh
p_1	Penalty exponent of ρ_1 intermediate values
p_2	Penalty exponent of ρ_2 intermediate values
S_n	Parallel speed-up

T_s	Execution time of the serial algorithm
T_n	Execution time of the parallel algorithm
V	Effective material volume
V^*	Maximum admissible material volume
¥	UC domain
β	Total number of "free" dual variables in MMA
ζ_1, ζ_2	Maximum admissible values for φ_1 and φ_2 parameters, respectively
$\boldsymbol{\rho}_1$, $\boldsymbol{\rho}_2$	Topological and material selection density variables, respectively
ρ_i^*	Mass density of material *i*
$\sigma_{t\|\Gamma}$	Hoop stresses along the hole free-traction boundary Γ
$\langle\boldsymbol{\sigma}\rangle$ or $\langle\sigma_{ij}\rangle$	Applied plane stress field
φ_1, φ_2	Parameters that measure the level of intermediate values present on the filtered density fields $\tilde{\boldsymbol{\rho}}_1$ and $\tilde{\boldsymbol{\rho}}_2$
ϕ_α	FE shape functions
Ω	Material domain

Chapter 4

M^*	Maximum allowable mass of the structure (global)
$\boldsymbol{\mu}_1$, $\boldsymbol{\mu}_2$	Micro design variables (topological and material selection, respectively)
$\boldsymbol{\rho}^*$	Macro design variables
ρ_1^*, ρ_2^*	Mass densities of the stiffer and weaker solids, respectively
ϕ	Macro objective function (minimization of the complementary strain energy density)
Ω	Structure domain
Ω_i	Structure design subdomains
Ω_e	Macro FE domain

Chapter 5

E^*	Longitudinal tensile modulus of a hybrid composite
E_0	Initial Young's modulus
E_{f1}, E_{f2}, E_m	Longitudinal tensile modulus of both fibres and matrix that compose the hybrid composite
L	Characteristic gauge length
L_0	Reference gauge length
m	Shape parameter (or Weibull modulus)
n^{crit}	Critical cluster size
P	Failure probability
V_{f1}, V_{f2}, V_m	Volume fraction of the respective hybrid composite component (i.e., Fibre 1, 2 or matrix)
δ	Ineffective length
ε_d	Pseudo-ductile strain
ε_{E0}	Elastic strain
ε_{max}	Strain at which the specimen loses its integrity
σ	Applied stress
σ_0	Scale parameter
Ω	Parameter that characterize the level of localization of the stress redistribution

Chapter 6

A_f^e	Fibre element cross section area
$A_m^{(1)}$, $A_m^{(2)}$	Areas on each fibre (1 or 2) of the transverse spring element representing the matrix that connects both fibres
a, b, c	RVE dimensions in x, y, z spatial directions, respectively
c_i	Normalization constants

DD	Parameter that measures the dispersion degree
E^e	Elastic modulus of the element e
f	Objective function
$\mathbf{f}_j^i$	External force vector
G	Shear modulus of the matrix
$\mathbf{K}_f^e$	Stiffness matrix of each fibre element
$\mathbf{K}_m^e$	Stiffness matrix of each matrix element
l^z	Predefined length for fibre spring elements
n_1, n_2	Number of fibres that each fibre (1 or 2) is connected to
N_f	Total number of fibre elements
N_f^b	Total number of broken fibre elements
N_m	Total number of matrix elements
R_1, R_2	Fibre (1 or 2) radius
R_{max}	Maximum fibre radius
s	Design variable responsible for assigning the fibre properties
u	Displacement vector
$V_{F_{LE}}$	Design variable responsible for assigning the LE fibres volume fraction
w_i	Weighting constants
$w_{plastic}$	Pseudo-plastic deformation energy per unit of volume
X_T^e	Fibre's strength
α	Parameter that controls the maximum allowable load drop in the response
δ	Amplitude defined as the difference between the maximum and minimum stresses in the interval between the elastic and maximum strains
δ^*	Maximum admissible value for δ
δ_x, δ_y, δ_z	User-specified parameters responsible for scaling the RVE
$\Delta\varepsilon$	Strain increment
$\langle\varepsilon\rangle$	Average failure strain

λ	Amplitude that quantifies the load drop in the response
$\langle\sigma\rangle$	Average failure stress
σ_f^e	Stress in the fibre element from the previous strain increment
σ_L	Reference stress at gauge length L

1 INTRODUCTION

This PhD thesis focuses on analysing and optimizing composite structures with microstructure composed by two or more materials. A composite structure is basically a combination of two or more different materials, giving rise to a new material with better mechanical properties than its constituents. These constituent materials can be mixed according to a predefined layout, e.g., fibres embedded in polymer matrix, or the layout can be itself a design variable in a topology optimization problem.

Structural analysis is understood as obtaining the response (e.g., displacements or stresses) of a structure when subjected to an applied external load. There are two different methods of structural analysis: (1) analytical methods and (2) numerical methods. Analytical methods are those which the response of a structure is given by a mathematical expression that yields the values of the desired unknown quantities at any location in a body (or structure) and are thus valid for an infinite number of locations in the body. Reasonable solutions can be easily obtained for simple structures, but as the complexity of the structure increases it becomes impossible to accurate simulate all the details. Therefore, for complex structures, numerical methods must be invariably employed. The numerical methods can be subdivided into two categories: (1) numerical solutions of differential equations for displacements or stresses, and (2) matrix methods based on discrete-element idealization. In the first type the equations of elasticity are solved using either finite difference techniques or direct numerical integration. In this approach the analysis is based on a mathematical approximation of differential equations. In the second type, the continuous domain occupied by the structure is replaced by a mathematical model consisted by an assembly of discrete structural elements with assumed form of displacement or stress distribution. The response of the structure is then obtained by combining each element approximate displacement or stress distributions in a manner which satisfies the force-equilibrium and displacement compatibility at

the junctions of these elements [1,2]. The well-known Finite Element Method (FEM) is a matrix method based on discrete-element idealization.

The modern development of the FEM began in the 1940s in the field of structural engineering with the work by Hrennikoff [3] in 1941 and McHenry [4] in 1943, who used a lattice of line (one-dimensional) elements (bars and beams) for the solution of stresses in continuous solids. The first treatment of two-dimensional elements was done by Turner et al. [5] in 1956 for truss elements, beam elements, and two-dimensional triangular and rectangular elements in plane stress. Extension to three-dimensional problems was done by Martin [6] in 1961. There are two general direct approaches traditionally associated with the FEM: (1) the force (or flexibility) method and (2) the displacement (or stiffness) method. In the first approach, internal forces are used as the unknowns of the problem. To obtain the governing equations, first the equilibrium equations are used. Then necessary additional equations are found by introducing compatibility equations. The result is a set of algebraic equations for determining the redundant or unknown forces. This approach was first developed by Levi [7] in 1947, and in 1953 another work of his authorship [8] suggested the use of the displacement (or stiffness) method as a promising alternative. This second approach assumes the displacements of the nodes as the unknowns of the problem. The compatibility conditions assume that elements connected at a common node, along a common edge, or on a common surface before loading remain connected at that node, edge, or surface after deformation takes place. Then the governing equations are expressed in terms of nodal displacements using the equations of equilibrium and an applicable law relating forces to displacements. Basically, these two direct approaches result in different unknowns (forces or displacements) in the analysis and different matrices associated with their formulations (flexibilities or stiffnesses). For the sake of knowledge, the displacement (or stiffness) method is more desirable because its formulation is simpler for most structural analysis problems as shown in [9]. Another general method that can be used to develop the governing equations is the variational method. The variational method includes several principles. One of these principles, is the theorem of minimum potential energy that applies to materials behaving in a linear-elastic manner. Another variational principle often used to derive the governing equations is the principle of virtual work. This principle applies more generally to materials that behave in a linear-elastic fashion, as well as those that behave in a nonlinear fashion. Summing up, the FEM involves modelling the structure using small interconnected elements called finite elements. A displacement function is associated with each finite element. Every interconnected element is linked, directly or indirectly, to every other element through common (or shared) interfaces, including nodes and/or boundary lines and/or surfaces. By using known stress/strain properties for the material making

up the structure, one can determine the behaviour of a given node in terms of the properties of every other element in the structure. The total set of equations describing the behaviour of each node results in a series of algebraic equations best ex-pressed in matrix notation. More details about FEM can be found in [10].

Structural optimization consists in finding a set of structural parameters (design variables) in order to minimize or maximize a cost (or objective) function, satisfying constraints functions (if exist). There are three main types of structural optimization problems: (1) sizing optimization, (2) shape optimization and (3) topology optimization. In the 1960s, at the beginning of modern structural optimization, structural optimization was oriented towards solving sizing optimization problems. Back then, Schmit [11] was the one who first established the mathematical model of the optimization design for elastic structures under multiple load cases and put forward the solution method based on mathematical programming. In a sizing optimization problem, the goal may be to find some type of structural thickness, i.e., the design variables can be either the cross-sectional areas of truss members, or the thickness distribution of a sheet. After a research effort mainly focused on sizing optimization, the shape optimization of structures began to be studied with more interest in the beginning of 1970s [12, 13]. In shape optimization problems, the goal is to find the form or contour of some part of the boundary of the structural domain. This boundary can be defined by a set of points, a line or a surface. These can be modelled by mathematical functions (splines or others) by defining control points. The design variables are then the coordinates of those points along the boundary. Note that the connectivity of the structure is not changed by shape optimization, i.e., new boundaries are not formed. Lastly, the most general form of structural optimization is the topology optimization. The history of topology optimization began in 1890s with Maxwell's studies [14] on the layout optimization of the truss. Thereafter, Michell [15] studied the layout optimization with stress constraints for the truss with coplanar forces applied to specified locations. However, as there was no FEM and mathematical programming at that time, this topic did not receive due attention. In 1980s, this thematic was raised with the work of Bendøe and Kikuchi [16]. Topology optimization of solid structures involves the determination of features such as the number, location and shape of holes and the connectivity of the domain. Typically, topology optimization is an optimization procedure that rationally distributes/redistributes the material over a certain domain through the gradual removal of small portions of material with low stress level that is not being used efficiently in the transmission of internal forces. In a discrete case, such as for a truss, it is achieved by taking cross-sectional areas of truss members as design variables, and then allowing these variables to take the value zero, i.e., bars are removed from the truss. If instead of a discrete structure, a continuum-type structure discretized by a finite

element mesh is considered, and considering that each finite element is assigned a density-like design variable, then topology changes can be achieved by letting these variables take the value zero, i.e., removing material. For a better understanding, imagine a two-dimensional sheet. In this case, the density design variables can be seen as the thickness of the sheet, and if the thickness (or density) goes to zero it means absence of material. This approach is the so-called density-based topology optimization [17]. An alternative approach for density-based topology optimization is the well-known level set method, where the structural boundary is represented by a level set model that is embedded in a scalar function of a higher dimension [18]. Other examples of topology optimization methods are methods based on the topological derivative [19], phase-field method [20] and bubble method [21]. In addition to the three main aforementioned categories, another category of structural optimization should also be mentioned, which is the material optimization. In this case, the geometry and dimensions of the structure are not changed. The aim is to find the optimum material. More details about structural optimization can be found in [22] and [23].

The analysis and optimization of composite structures can be done in three different scales: macroscale, mesoscale and microscale [24]. The macroscale models simulate the structure, where it is considered homogeneous and continuous, and the material's behaviour follows an anisotropic constitutive law [25]. These models require less computational effort than models in the other scales, allowing the analysis of complex and large structures. However, the absence of important microstructure information about the interaction between the constituents and the contribution of each one to the failure of the structure, make these models very limited. The mesoscale models simulate the composite's layers, where the laminate is considered homogeneous and orthotropic or transversely isotropic. Using these models, reasonable predictions of the composite's behaviour can be obtained. However, there is a lack of relevant information about the microstructure, which can lead to less realistic results [26]. The microscale models are used to simulate the microstructure of the material and its properties, e.g., the fibres and matrix. These models are based on a Representative Volume Element (RVE) or Unit Cell (UC) which is a sample that is structurally entirely typical of the whole mixture on average and contains a sufficient number of inclusions for the apparent overall moduli to be effectively independent of the surface values of traction and displacement, so long as these values are macroscopically uniform [27]. In other words, a RVE or UC is the smallest volume capable of represent a whole heterogenous material. These models present a more realistic approximation of the properties of the composite materials, thus leading to more satisfactory results. However, this comes with a high computational cost and complexity, making these models more challenging to implement.

Composite materials are heterogenous and usually, comprise of a matrix which could be metal, polymeric (like plastics) or ceramic, and a re-enforcement or inclusion, which could be particles or fibres of steel, aluminium, silicon etc. The simplest case of a composite material is a cellular body, comprising solids and voids. If composites with sufficiently regular heterogeneities are considered, a periodic structure for the composite can be assumed. It should be emphasized that in comparison with the dimensions of the body, the size of these non-homogeneities should be very small. Owing to this, these types of material are sometimes called composites with periodic microstructures, which can be described through a RVE or UC. If the periodic microstructure has a large number of heterogeneities, numerical modelling of its detail becomes impracticable. A natural way to overcome this difficulty is to replace the composite with a kind of equivalent material model. This procedure is usually called homogenization. The mathematical theory of homogenization has been developed since the 1970s and it is used to find the effective properties of the equivalent homogenized material [28-30]. From a mathematical point of view, the theory of homogenization is a limit theory which uses the asymptotic expansion and the assumption of periodicity to substitute the differential equations with rapidly oscillating coefficients, with differential equations whose coefficients are constant or slowly varying in such a way that the solutions are close to the initial equations [31]. This method makes it possible to predict both the overall (macroscale) and local (microscale) properties of processes in composites. For more details about homogenization theory, see chapter 2.2. More details about homogenization can be found in [32].

The design of the structure (macroscale) and material (microscale) can be done separately or not. If the design of the structure is done concurrently with the material design, one is facing a multi-scale problem. In a multi-scale problem, efficient distribution of the material in the domain of the structure is seek simultaneously with the design of the most efficient material in each point of that domain. Various multiscale computational techniques in the modern era can be classified into the following two categories: (a) multiple scale expansion methods, and (b) superposition-based methods. These two methods differ on how information is transferred between different scales. In the first type of methods, the information (typically material properties) between scales is passed from the smallest to the largest length scales through homogenization (the so-called *bottom-up transfer*) [1, 33-37]. Lastly, the second type of methods implement the concept of *substructuring* and concurrently consider different models (with different scales) in different regions [38-43].

1.1 Motivation and objectives of the dissertation

Nowadays, conventional materials like steel and aluminum have been increasingly replaced by non-conventional materials like composite materials in various applications, e.g., aerospace, automotive and aeronautic industries. In fact, lightweight construction industries are the most prominent in the use of non-conventional materials. Parts such as fuselage and wings can make extensive use of composites. There are innumerous reasons to choose non-conventional materials over conventional ones. For instance, composite materials typically offer better strength-to-weight ratio and has less sensitivity to fatigue and corrosion.

The present thesis explores multi-material design to improve even further the mechanical behaviour of composites. Typical composite materials are only composed by two distinct material phases. One typically may have the combination of one solid material and void (cellular materials) or the combination of a polymeric matrix where fibres are embedded (fibre-reinforced composite materials). The multi-material setting of composite materials in the context of this thesis implies three or more distinct material phases, e.g., two or more solid materials plus void, or fibres of two or more materials embedded in a matrix (hybrid fibre-reinforced composite materials). In this dissertation, one explores the multi-material design of composite materials to improve their stiffness, strength and plastic deformation behaviour. In engineering practice, it is quite common to open holes in structures for various reasons, e.g., weight reduction or porosity requirements for fluid flow. In fact, for some cases, multi-material design allows to obtain better trade-offs between design criteria involving weight, stiffness, and strength, when compared to the single-material counterparts. When designing and optimizing single-material structures, the weight and stiffness go hand-to-hand, i.e., an increased stiffness is sometimes only possible by increasing the weight of the structure. In this thesis, one explores the possibility of increasing the stiffness of a structure through multi-material design, while maintaining its weight. Another important design criterion is the structure's strength. If a structure presents highly stressed regions when subject to some load, these regions will be the first to fail during service. Therefore, it is important to reduce these highly stressed regions as much as possible, ideally having an even distribution of stresses. Again, multi-material design can be explored to smooth the stress distribution field, thus reducing the maximum equivalent stress value in the structure. The maximum equivalent stress of a structure should be less than the yield stress of the material that composes it, ensuring that the structure only deforms elastically. If the yield stress is exceeded in some point of the structure, then two different scenarios can occur: (1) the material deforms plastically (ductile materials) or (2) it fails catastrophically (brittle materials). Fibre-reinforced composite materials are characterized by

having a brittle failure. A ductile failure is preferred over a brittle and catastrophic one that occurs without warning. Therefore, fibre hybridization is a technique that mix fibres of different materials in a matrix with the purpose of introducing a pseudo-ductile behaviour in fibre-reinforced composite materials.

The objectives of this work are to design and optimize materials with improved mechanical behaviour, both in linear elastic and non-linear regimes. In the elastic regime, one tries to improve the stiffness or weight and the strength of composite materials. If the limit elastic stress of the material is exceeded, then one tries to introduce a pseudo-ductile behaviour, allowing a reduction on the high safety factors typically applied to design fibre-reinforced composite materials. These objectives meet environmental and sustainability challenges by the rational use of resources and energy.

1.2 Structure of the dissertation

This dissertation is structured in three parts, all naturally linked through the common theme that is multi-material design. In the first part, the multi-material design combined with topology optimization is applied to improve the structural performance, namely the stiffness and strength, when the material does not yield (linear elastic regime). This is done either in the microstructure level (Chapter 3) or in a multiscale framework (Chapter 4). For a better understanding of the work done in this part, some important concepts are presented in Chapter 2. In the second part, the multi-material design is applied to fibre reinforced composites with the goal of improving the material behaviour after the yielding point (non-linear plastic regime). The optimal combination of fibres in a hybrid composite is discovered by solving an optimization problem. One also studies the influence of the fibre dispersion in the composite's response with the aid of a layout optimization problem (Chapter 6). In Chapter 5 are introduced some important concepts required for better understanding this part of the work. Lastly, the third part of this dissertation has the final remarks of this work and possible future works.

PART ONE

Topology Optimization in Linear Elastic Regime

2 STATE OF THE ART: LINEAR ELASTIC REGIME

This chapter covers the fundamentals for a better understanding of this first part of the dissertation. Firstly, a brief review on the theory of linear elasticity is done. Then, the homogenization theory used to compute the homogenized properties and stresses in periodic microstructures is introduced. Afterwards, an extensive chapter on structural optimization covers the key concepts to perform topology optimization. After that, a state of the art about multi-material topology optimization is done. Lastly, a brief introduction to multi-scale topology optimization is done.

2.1 Theory of linear elasticity

Elasticity is a property that almost all structural materials have. When an elastic body is subjected to external forces, it deforms, and equilibrium is attained. In the theory of linear elasticity, it is assumed that the bodies undergoing the action of external forces are perfectly elastic, i.e., the body returns to its undeformed state with the removal of the applied external forces, if a certain limit (yield strength) is not surpassed. If the internal stresses caused by the applied external forces exceed the yield point, the material deforms plastically and therefore the body is no longer able to completely resume its initial form. This chapter is mainly based on [44-47].

Let the deformable body shown in Fig. 2.1 be in equilibrium. The body is subjected to a distributed load over the exterior (**t**), properly called surface force, and loads distributed within the interior (**b**) known as body forces. An example of the latter is the effect of gravity which produces

the self-weight of the body. Focusing on an element with an infinitesimal volume δV within the body, one can represent all the stress components acting on it. These stress components can be organized in the well-known Cauchy's stress tensor σ_{ij}, defined bellow in Eq. 2.1 for a three-dimensional problem.

$$\sigma_{ij} = \begin{bmatrix} \sigma_{11} & \tau_{12} & \tau_{13} \\ \tau_{21} & \sigma_{22} & \tau_{23} \\ \tau_{31} & \tau_{32} & \sigma_{33} \end{bmatrix} \tag{2.1}$$

where σ are the normal stresses and τ are the shear stresses.

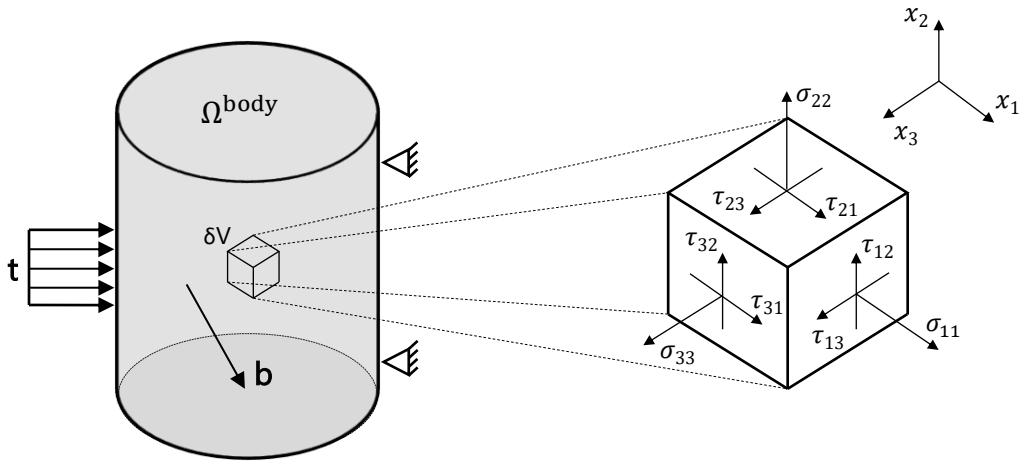

Fig. 2.1: Deformable body subjected to external loads and respective stress components acting on a differential volume element δV.

The equations governing the distribution of stresses are known as the equilibrium equations, represented below in its differential form:

$$\frac{\partial \sigma_{ij}}{\partial x_i} + b_j = 0 \tag{2.2}$$

where b_j correspond to body forces components, e.g., effect of gravity. Additionally, the stress tensor must be symmetric, i.e., it is fully defined with six components. These equations must be satisfied at all points throughout the volume of the body, Ω^{body}. Obviously, the stress components may vary over the volume and at the boundary they must be such as to be in equilibrium with the external forces, so that external forces may be regarded as a continuation of the internal stress distribution. These conditions of equilibrium at the boundary are named as boundary conditions. There are essentially two types of boundary conditions: (1) force boundary condition (Neumann condition); (2) displacement boundary condition (Dirichlet condition). Briefly, a force boundary condition ensures that the internal forces are equal to the applied external forces and a displacement boundary condition ensures that a displacement in a certain point of the body is obtained.

In the example shown in Fig. 2.1, there are one force boundary condition and two displacement boundary condition, corresponding to the applied load and supports respectively. These are given by the following equations:

$$\sigma_{ij} n_i = t_j \tag{2.3}$$

$$\mathbf{u} = 0 \tag{2.4}$$

where n_i are cosines of the outwards unit normal vector on the boundary.

The problem of the theory of elasticity usually is to determine the stress state in a body submitted to external forces. It is necessary to solve the differential equations of equilibrium, and the solution must be such as to satisfy the boundary conditions. However, these equations are not sufficient for the determination of all the six independent stress components present in Cauchy's tensor (see Eq. 2.1). The problem is a statically indeterminate one, and in order to obtain the solution, the elastic deformation of the body must also be considered.

In the deformation of an elastic body, it is assumed that there are enough constraints to prevent rigid body motion, so that no displacements of particles of the body are possible without deforming it. Also, only small deformations are considered. The small displacements of particles of a deformed body are usually resolved into components u_1, u_2 and u_3 parallel to the coordinate axes x_1, x_2 and x_3, respectively. Now, it shall be introduced the definition of strain. Basically, strain is a geometrical measure of deformation representing the relative displacement between particles in a material body. The Cauchy's strain tensor is obtained through displacements using the *strain–displacement* or *kinematic* equations, given by:

$$\varepsilon_{ij} = \frac{1}{2}\left(\frac{\partial u_i}{\partial x_j} + \frac{\partial u_j}{\partial x_i}\right) = \begin{bmatrix} \varepsilon_{11} & \varepsilon_{12} & \varepsilon_{13} \\ \varepsilon_{21} & \varepsilon_{22} & \varepsilon_{23} \\ \varepsilon_{31} & \varepsilon_{32} & \varepsilon_{33} \end{bmatrix} = \begin{bmatrix} \varepsilon_{11} & \gamma_{12}/2 & \gamma_{13}/2 \\ \gamma_{21}/2 & \varepsilon_{22} & \gamma_{23}/2 \\ \gamma_{31}/2 & \gamma_{32}/2 & \varepsilon_{33} \end{bmatrix} \tag{2.5}$$

where ε is the normal strain and γ is the shear strain.

The strain components ε_{ij} are expressed by displacement functions u_i, hence they cannot be taken arbitrarily, and there exists a certain relation between the strain components, ensuring that these components will integrate into a unique displacement field. The relation between strain components are the *compatibility equations*, which are given by:

$$\frac{\partial \varepsilon_{ij}}{\partial x_k \partial x_l} + \frac{\partial \varepsilon_{kl}}{\partial x_i \partial x_j} = \frac{\partial \varepsilon_{ik}}{\partial x_j \partial x_l} + \frac{\partial \varepsilon_{jl}}{\partial x_i \partial x_k} \tag{2.6}$$

representing $3^4 = 81$ equations, where only six of which are distinct. Even though we have the compatibility equations, the formulation is still incomplete in that there is no connection between

the equilibrium equations (see Eq. 2.2), three equations in six unknowns σ_{ij}, and the kinematic equations (see Eq. 2.6), six equations in nine unknowns ε_{ij} and u_i. Next, it is sought the connection between the equilibrium and the kinematic equations in the laws of physics governing material behavior. This coupling is accomplished by considering the mechanical properties of the materials for which the theory of elasticity is to be applied and is expressed by *constitutive* or *material* laws.

The most elementary description of material behavior is the well-known *Hooke's law* stated by Robert Hooke in the late 17th century. The generalized Hooke's law is written in the form of a fourth-order tensor:

$$\sigma_{ij} = E_{ijkl}\varepsilon_{kl} \tag{2.7}$$

in which the 81 coefficients (3D problem) of the stiffness tensor E_{ijkl} are called the elastic constants. The Hooke's law can be written in its inverse form as:

$$\varepsilon_{ij} = C_{ijkl}\sigma_{kl} \tag{2.8}$$

where C_{ijkl} is the compliance tensor computed as the inverse of the stiffness tensor and, using the Kronecker delta **δ** operator, the equation below must be verified:

$$E_{ijkl}C_{ijkl} = \frac{1}{2}\left(\delta_{ik}\delta_{jl} + \delta_{il}\delta_{jk}\right) \tag{2.9}$$

Since both stress and strain tensors are symmetric and that, usually, the material can be considered hyper elastic, the stiffness tensor has the following symmetries:

$$E_{ijkl} = E_{jikl} = E_{ijlk} = E_{klij} \tag{2.10}$$

Therefore, the number of independent equations in Eq. (2.7) for 3D problems reduces from nine to six and the independent elastic constants from 81 to 21 (half of the off-diagonal plus diagonal constants looking at the Hooke's law written in the matrix form, see Eq. 2.11):

$$\begin{bmatrix}\sigma_{11}\\ \sigma_{22}\\ \sigma_{33}\\ \tau_{12}\\ \tau_{23}\\ \tau_{31}\end{bmatrix} = \begin{bmatrix} E_{1111} & E_{1122} & E_{1133} & E_{1112} & E_{1123} & E_{1131} \\ & E_{2222} & E_{2233} & E_{2212} & E_{2223} & E_{2231} \\ & & E_{3333} & E_{3312} & E_{3323} & E_{3331} \\ & & & E_{1212} & E_{1223} & E_{1231} \\ & \text{sym} & & & E_{2323} & E_{2331} \\ & & & & & E_{3131} \end{bmatrix} \begin{bmatrix}\varepsilon_{11}\\ \varepsilon_{22}\\ \varepsilon_{33}\\ 2\varepsilon_{12}\\ 2\varepsilon_{23}\\ 2\varepsilon_{31}\end{bmatrix} \tag{2.11}$$

The preceding characterization is the most general, where such material is termed *anisotropic*. Most engineering materials possess properties of symmetry toward one or more planes or axes, which allow the number of independent constants to be further reduced. The first reduction is for

one plane of symmetry, allowing the reduction of 8 elastic constants, meaning that only 13 elastic constants are independent. Such material is called *monoclinic*. Some materials show a higher level of symmetry characterized by three mutually orthogonal planes of symmetry. This type of material is called an *orthotropic* material, and it has 9 independent elastic constants. Next, a material presenting symmetry about an axis that is normal to a plane of isotropy is called *transversely isotropic*. This type of materials has 5 independent constants. Finally, an isotropic material is characterized by an identical response in all directions, leading to the following stress-strain relationship:

$$\sigma_{ij} = \overbrace{\lambda\delta_{ij}\delta_{kl} + \mu\left(\delta_{ik}\delta_{jl} + \delta_{il}\delta_{jk}\right)}^{E_{ijkl}}\varepsilon_{kl} = \lambda\delta_{ij}\varepsilon_{kk} + \mu\left(\varepsilon_{ij} + \varepsilon_{ji}\right) \tag{2.12}$$

or, in matrix form:

$$\begin{bmatrix}\sigma_{11}\\ \sigma_{22}\\ \sigma_{33}\\ \tau_{12}\\ \tau_{23}\\ \tau_{31}\end{bmatrix} = \begin{bmatrix}\lambda+2\mu & \lambda & \lambda & 0 & 0 & 0\\ & \lambda+2\mu & \lambda & 0 & 0 & 0\\ & & \lambda+2\mu & 0 & 0 & 0\\ & & & 2\mu & 0 & 0\\ & \text{sym} & & & 2\mu & 0\\ & & & & & 2\mu\end{bmatrix}\begin{bmatrix}\varepsilon_{11}\\ \varepsilon_{22}\\ \varepsilon_{33}\\ \varepsilon_{12}\\ \varepsilon_{23}\\ \varepsilon_{31}\end{bmatrix} \tag{2.13}$$

From Eq. (2.13) it is possible to see that only two independent constants are needed to fully define the stiffness tensor of an isotropic material. These two constants are called Lamé's constants, since they were correctly established first by Gabriel Lamé in the middle of the 19th century. Although the Lamé's constants are perfectly suitable from a mathematical standpoint, it is common to use engineering material constants that are related to measurements from elementary mechanical tests.

Solving Eq. (2.12) or (2.13) for a uniaxial stress σ_{11} constant and all other $\sigma_{ij} = 0$, gives the basic form of Hooke's law:

$$\sigma_{11} = \frac{\mu(2\mu + 3\lambda)}{\mu + \lambda}\varepsilon_{11} = E\varepsilon_{11} \tag{2.14}$$

where E is the Young's modulus. From the same uniaxial stress state, the fractional contraction may be computed as:

$$-\frac{\varepsilon_{22}}{\varepsilon_{11}} = -\frac{\varepsilon_{33}}{\varepsilon_{11}} = \frac{\lambda}{2(\mu + \lambda)} = \nu \tag{2.15}$$

where ν is the Poisson's ratio.

A third engineering constant is obtained from the state of pure shear in two dimensions, given by $\sigma_{12} = \sigma_{21} =$ constant, all other $\sigma_{12} = 0$. From Eq. (2.12) or (2.13),

$$\sigma_{12} = 2\mu\varepsilon_{12} = 2G\varepsilon_{12} \tag{2.16}$$

where G is the shear modulus.

Although the engineering constants *E*, ν, and *G* are convenient, only two of these constants are independent since G = μ and both E and ν are defined in terms of λ and μ. The relationships between the Lamé and engineering constants are collected as:

$$\lambda = \frac{\nu E}{(1+\nu)(1-2\nu)} \tag{2.17}$$

$$\mu = \frac{E}{2(1+\nu)} \tag{2.18}$$

$$E = \frac{\mu(2\mu+3\lambda)}{\mu+\lambda} \tag{2.19}$$

$$\nu = \frac{\lambda}{2(\mu+\lambda)} \tag{2.20}$$

Another relationship between the constants is defined as the Bulk Modulus, which defines how resistant the material is under compression (hydrostatic pressure):

$$K = \frac{E}{3(1-2\nu)} \tag{2.21}$$

Many physical problems are reducible from three- to two-dimensions, making the generalized Hooke's law simplified, which facilitates their eventual solution. If there is no traction on one plane passing through the body, this state is known as *plane stress* since all nonzero stresses are confined to planes parallel to the traction-free plane. This happens for bodies with one dimension much smaller than the other two, such as a thin sheet. Another possibility is a body in which one dimension is much greater than the other two, making the strain in one direction be negligible comparing with the other two directions, e.g., a long pipe. This state is known as *plane strain*.

For an isotropic material in plane stress, assuming that the z-axis is stress-free, i.e., $\sigma_{13} = \sigma_{23} = \sigma_{33} = 0$, the generalized Hooke's law containing only the relevant components of stress and strain, becomes:

$$\begin{bmatrix}\sigma_{11}\\ \sigma_{22}\\ \sigma_{12}\end{bmatrix} = \frac{E}{1-\nu^2}\begin{bmatrix}1 & \nu & 0\\ \nu & 1 & 0\\ 0 & 0 & 1-\nu\end{bmatrix}\begin{bmatrix}\varepsilon_{11}\\ \varepsilon_{22}\\ \varepsilon_{12}\end{bmatrix} \tag{2.22}$$

For an isotropic material in plane strain, assuming that the z-axis is strain-free, i.e., $\varepsilon_{13} = \varepsilon_{23} = \varepsilon_{33} = 0$, the generalized Hooke's law containing only the relevant components of stress and strain, becomes:

$$\begin{bmatrix}\sigma_{11}\\ \sigma_{22}\\ \sigma_{12}\end{bmatrix} = \begin{bmatrix}\lambda+2\mu & \lambda & 0\\ \lambda & \lambda+2\mu & 0\\ 0 & 0 & 2\mu\end{bmatrix}\begin{bmatrix}\varepsilon_{11}\\ \varepsilon_{22}\\ \varepsilon_{12}\end{bmatrix} \tag{2.23}$$

So far, the equations that govern the elasticity problem were presented. It is also of great importance knowing when the material will fail or sustain permanent damage such as cracks or plastic deformations. For this, there are *failure criterions*. The Von-Mises' criterion is among the most used criteria in engineering, mainly in metal constructions. The Von Mises' yield criterion is expressed by the following inequality:

$$\sigma_{eq}^{VM} = \sqrt{\frac{1}{2}[(\sigma_{11}-\sigma_{22})^2 + (\sigma_{22}-\sigma_{33})^2 + (\sigma_{33}-\sigma_{11})^2] + 3({\tau_{12}}^2 + {\tau_{23}}^2 + {\tau_{13}}^2)} \leq \sigma_y \tag{2.24}$$

where the first equality defines the equivalent stress, σ_{eq}^{VM}. The Von Mises' criterion states that the yield condition is reached under the combined loading, when the equivalent stress, σ_{eq}^{VM}, reaches the yield stress measured in the standard test of uniaxial stress state applied, σ_y.

2.2 Homogenization theory

If a structure is built from periodic materials (e.g., cellular or composite materials), it is often too cumbersome or even computationally prohibitive the modelling of every geometrical detail of the periodic medium under consideration. When there is a low number of heterogeneities, the solution may be obtained analytically or, numerically, using the finite element method. However, when the number of heterogeneities is really large, the aforementioned methods are not attractive, leading us to the application of homogenization techniques. The general idea of homogenization theory is to replace the heterogeneous medium by a homogeneous equivalent one. The homogenized or equivalent properties reflect the structure behavior on account of its material microstructure but without looking at the details of all the material points of the body. Rather, the focus is on the behavior of the UC only.

In the first part of the dissertation, the homogenization theory for periodic media based on asymptotic expansions at two scales is applied. This theory assumes basically three hypotheses

that must be verified. In the first hypothesis, the homogenization theory assumes that the distribution of heterogeneity is periodic throughout the macroscopic domain. This does not imply that the microstructure is the same all over the macroscopic domain. In fact, smooth transitions of topology in the UC are acceptable as long as periodicity is still verified locally. In other words, asymptotic homogenization is only applicable to periodic, or quasi-periodic materials. Another hypothesis of the homogenization theory is that the stress or strain macroscopic fields are seen as uniform or as averages of local/microscopic distributions. Therefore, this technique in not valid in situations where those macroscopic fields have significant variations, e.g., cracks, which display high stress concentration factors. Finally, there must exist scale separation, i.e., the UC representing the heterogeneity must have a characteristic dimension d, much smaller than the characteristic dimension of the macroscopic domain, D. The ratio between these dimensions defines the parameter ε, i.e.:

$$\varepsilon = \frac{d}{D} \tag{2.25}$$

In the homogenization theory it is assumed that $\varepsilon << 1$, and the homogenized properties are actually computed for the limit $\varepsilon \to 0$. In practice, such condition is not possible since both characteristic dimensions are finite values in real materials. However, if the condition $d << D$ is assured, then the results obtain by the homogenization method are guaranteed to be sufficiently accurate.

Consider the elasticity problem illustrated in Fig. 2.2, characterized by a body of periodic heterogeneous medium, e.g., composite material, subjected to some load and boundary conditions. For instance, assume that the body is made of two different material phases (solid material and void) whose mixture is represented by an UC that is very small, of order ε (where ε is a very small positive number defined above, see Eq. 2.25), compared with the dimensions of the structural body. The variable **x** defines the position vector for the macroscopic length scale, while the variable **y** defines the position vector for the microscale. These two variables are related as follows:

$$\mathbf{y} = \frac{\mathbf{x}}{\varepsilon} \tag{2.26}$$

This means that the microscopic domain Y defined by an UC can be seen from the macroscopic domain Ω^{ε} when magnified by a factor of $1/\varepsilon$. In general, the characteristic functions (e.g., strains or stresses) of these highly heterogeneous media, rapidly vary within a very small neighborhood of a point **x**. This fact inspires the consideration of two different scales of dependencies for all quantities: one on the macroscopic or global level **x**, which indicates slow variations, and the

other on the microscopic or local level **y**, which describes rapid oscillations. Consequently, assuming a general function g, we can say that $g = g(\mathbf{x}, \mathbf{x}/\varepsilon) = g(\mathbf{x}, \mathbf{y})$.

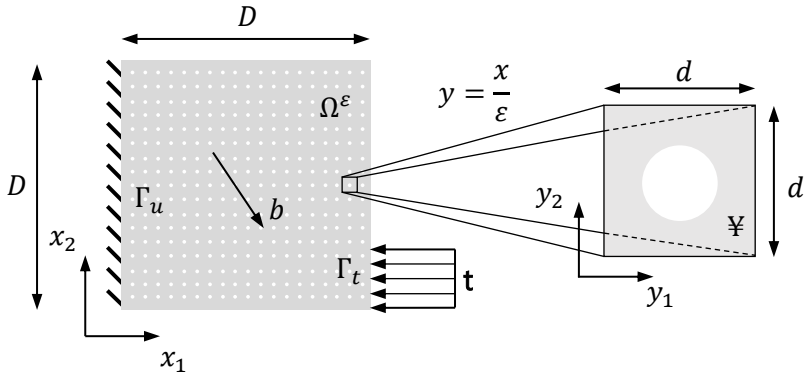

Fig. 2.2: Body with size *D* composed of a periodic heterogeneous medium represented through an UC with size *d*.

The objective here is to investigate the mechanical behavior (e.g., displacements $\mathbf{u}^\varepsilon$) in a volume of a regular enough domain Ω^ε in a periodic heterogeneous medium through the homogenization method. The homogenization process here involves solving elasticity problems in the periodic UC (local problem, where the equilibrium equations and constitutive laws are known) and then contemplating its effect on the macroscopic scale (global problem). In the asymptotic homogenization it is assumed that functions determining the behavior of the composite can be expanded as an asymptotic expansion. For instance, the expansion for the displacement field can be written as:

$$\mathbf{u}^\varepsilon(\mathbf{x}) = \mathbf{u}^0(\mathbf{x}, \mathbf{y}) + \varepsilon \mathbf{u}^1(\mathbf{x}, \mathbf{y}) + \varepsilon^2 \mathbf{u}^2(\mathbf{x}, \mathbf{y}) + \cdots = \sum_{i=0}^{\infty} \varepsilon^i \mathbf{u}^i(\mathbf{x}, \mathbf{y}) \tag{2.27}$$

Considering the symmetries present in the stiffness tensor (see Eq. 2.10) and assuming that the strain energy density is always positive, the tensor must be positive definite:

$$\exists_{\beta>0} : E^\varepsilon_{ijkl} \varepsilon_{ij} \varepsilon_{km} = \beta \varepsilon_{ij} \varepsilon_{ij}, \forall \varepsilon_{ij} = \varepsilon_{ji} \tag{2.28}$$

The equations of equilibrium and boundary conditions of the elasticity problem presented in Eq. (2.2)-(2.4) can be rewritten for the current problem as follows:

$$\frac{\partial}{\partial x_i}\left(E^\varepsilon_{ijkl} \frac{\partial u^\varepsilon_k}{\partial x_l}\right) + b_j = 0 \text{ in } \Omega^\varepsilon \tag{2.29}$$

$$E^\varepsilon_{ijkl} \frac{\partial u^\varepsilon_k}{\partial x_l} n_i = t_j \text{ in } \Gamma_t \tag{2.30}$$

$$\mathbf{u}^{\varepsilon} = 0 \text{ in } \Gamma_u \tag{2.31}$$

Since ε is a very small number, it is impossible to directly obtain an analytical or numerical solution of $\mathbf{u}^{\varepsilon}$. Alternatively, one can seek a solution in the form present in Eq. (2.27). The elasticity problem can be equivalently expressed in the weak form (*principle of virtual work*) thus serving as the basis for a finite element formulation:

$$\int_{\Omega^{\varepsilon}} E_{ijkl}^{\varepsilon} \frac{\partial u_k^{\varepsilon}}{\partial x_l} \frac{\partial v_i}{\partial x_j} \mathrm{d}\Omega = \int_{\Omega^{\varepsilon}} b_i^{\varepsilon} v_i \, \mathrm{d}\Omega + \int_{\Gamma_t} t_i v_i \, \mathrm{d}\Gamma, \qquad \forall \, \mathbf{v} \in V_{\Omega^{\varepsilon}} \tag{2.32}$$

where **v** is the virtual displacement. Basically, the weak form is defined to be a weighted-integral statement of a differential equation in which the differentiation is transferred from the dependent variable **u** to the weight function **v,** such that all boundary conditions of the problem are also included in the integral statement. This form is not only equivalent to Eq. (2.29) but it also contains the boundary conditions of the problem Eq. (2.30)-(2.31). Just for the sake of knowledge, notice that the Eq. (2.32) and the following developments on homogenization theory can also be obtained through the *minimum total potential energy principle*. The purpose of the homogenization process is to find an equilibrium problem equivalent to Eq. (2.32) that is only described using macroscopic quantities.

Introducing Eq. (2.27) until term ε^2 in Eq. (2.32) the following is obtained after some mathematical manipulation:

$$\begin{aligned} &\int_{\Omega^{\varepsilon}} E_{ijkl}^{\varepsilon} \left\{ \frac{1}{\varepsilon^2} \frac{\partial u_k^0}{\partial y_l} \frac{\partial v_i}{\partial y_j} + \frac{1}{\varepsilon} \left[\left(\frac{\partial u_k^0}{\partial x_l} + \frac{\partial u_k^1}{\partial y_l} \right) \frac{\partial v_i}{\partial y_j} + \frac{\partial u_k^0}{\partial y_l} \frac{\partial v_i}{\partial x_j} \right] \right. \\ &\quad \left. + \left[\left(\frac{\partial u_k^0}{\partial x_l} + \frac{\partial u_k^1}{\partial y_l} \right) \frac{\partial v_i}{\partial x_j} + \left(\frac{\partial u_k^1}{\partial x_l} + \frac{\partial u_k^2}{\partial y_l} \right) \frac{\partial v_i}{\partial y_j} \right] + \cdots \right\} \mathrm{d}\Omega \\ &\quad = \int_{\Omega^{\varepsilon}} b_i^{\varepsilon} v_i \, \mathrm{d}\Omega + \int_{\Gamma_t} t_i v_i \, \mathrm{d}\Gamma, \qquad \forall \, \mathbf{v} \in V_{\Omega^{\varepsilon}} \end{aligned} \tag{2.33}$$

To obtain the equation above it should be reminded that the spatial derivative with respect to **x** of any function $\psi(\mathbf{x}, \mathbf{y})$ depending on two length scales is given by:

$$\left(\frac{\partial \psi(\mathbf{x}, \mathbf{y})}{\partial x_i} \right)_{\mathbf{y} = \frac{\mathbf{x}}{\varepsilon}} = \left(\frac{\partial \psi}{\partial x_i} + \frac{\partial \psi}{\partial y_i} \frac{1}{\varepsilon} \right)_{\mathbf{y} = \frac{\mathbf{x}}{\varepsilon}} \tag{2.34}$$

For a *Y*-periodic function $\psi(\mathbf{x}, \mathbf{y})$ and considering it is smooth enough, when $\varepsilon \to 0^+$ the following is proven (see [48]):

$$\lim_{\varepsilon \to 0} \int_{\Omega^{\varepsilon}} \psi(\mathbf{x}, \mathbf{y}) \, \mathrm{d}\Omega = \int_{\Omega} \frac{1}{|Y|} \int_{¥} \psi(\mathbf{y}) \, \mathrm{d}Y \mathrm{d}\Omega \tag{2.35}$$

The equation shown above has a physical interpretation. Assuming small values of ε, the value of the limit calculated at a **y** coordinate for any macroscopic point **x** is the same as considering the integral of the average value of the function ψ in a small enough neighborhood of **y**. In other words, this means that instead of considering the function ψ in each microscopic point to characterize the macroscopic behavior, one can simply compute the volumetric average of such function in the UC domain, ¥. The volumetric average of ψ is expressed as follows:

$$\langle \psi \rangle = \frac{1}{|Y|} \int_{¥} \psi(\mathbf{y}) \, \mathrm{d}Y \tag{2.36}$$

Equating the terms with the same power of ε in Eq. (2.33) and considering Eq. (2.35) the following is obtained:

$$\int_{\Omega} \frac{1}{|Y|} \int_{¥} E_{ijkl} \frac{\partial u_k^0}{\partial y_l} \frac{\partial v_i}{\partial y_j} \, \mathrm{d}Y \, \mathrm{d}\Omega = 0, \quad \forall \, \mathbf{v} \in V_{\Omega^\varepsilon} \tag{2.37}$$

$$\int_{\Omega} \frac{1}{|Y|} \int_{¥} E_{ijkl} \left[\left(\frac{\partial u_k^0}{\partial x_l} + \frac{\partial u_k^1}{\partial y_l} \right) \frac{\partial v_i}{\partial y_j} + \frac{\partial u_k^0}{\partial y_l} \frac{\partial v_i}{\partial x_j} \right] \mathrm{d}Y \, \mathrm{d}\Omega = 0, \quad \forall \, \mathbf{v} \in V_{\Omega^\varepsilon} \tag{2.38}$$

$$\begin{aligned} \int_{\Omega} \frac{1}{|Y|} \int_{¥} E_{ijkl} \left[\left(\frac{\partial u_k^0}{\partial x_l} + \frac{\partial u_k^1}{\partial y_l} \right) \frac{\partial v_i}{\partial x_j} + \left(\frac{\partial u_k^1}{\partial x_l} + \frac{\partial u_k^2}{\partial y_l} \right) \frac{\partial v_i}{\partial y_j} \right] \mathrm{d}Y \, \mathrm{d}\Omega \\ = \int_{\Omega} \frac{1}{|Y|} \int_{¥} b_i v_i \, \mathrm{d}Y \, \mathrm{d}\Omega + \int_{\Gamma_t} t_i v_i \, \mathrm{d}\Gamma, \quad \forall \, \mathbf{v} \in V_{\Omega^\varepsilon} \end{aligned} \tag{2.39}$$

Note that the stiffness tensor has now a local nature, characterizing the base material of the microstructure, i.e., depends only on the variable **y** in the domain *Y*.

Taking a more detailed look at Eq. (2.37), the following problem within the microstructure (local problem) is obtained:

$$\frac{1}{|Y|} \int_{¥} E_{ijkl} \frac{\partial u_k^0}{\partial y_l} \frac{\partial v_i}{\partial y_j} \, \mathrm{d}Y \; = 0, \quad \forall \, \mathbf{v} \in V_{¥} \tag{2.40}$$

The solution of this problem exists, and it is independent of **y** (see [48]). Based on this, it can be said that the first term of the expansion for the displacement field (Eq. 2.27) depends only on the macroscale **x**, i.e.:

$$\mathbf{u}^0(\mathbf{x}, \mathbf{y}) = \mathbf{u}^0(\mathbf{x}) \tag{2.41}$$

Using this result in Eq. (2.38), the following local problem arises:

$$\int_{¥} E_{ijkl} \frac{\partial u_k^1}{\partial y_l} \frac{\partial v_i}{\partial y_j} \, \mathrm{d}Y = -\frac{\partial u_k^0(\mathbf{x})}{\partial x_l} \int_{¥} E_{ijkl} \frac{\partial v_i}{\partial y_j} \, \mathrm{d}Y, \quad \forall \, \mathbf{v} \in V_{¥} \tag{2.42}$$

Due to the linearity of the problem in Eq. (2.42), the solution $\mathbf{u}^1$ can be written as:

$$u_i^1(\mathbf{x}, \mathbf{y}) = -\frac{\partial u_k^0(\mathbf{x})}{\partial x_l} \chi_i^{kl} + \hat{u}_i^1(\mathbf{x}) \tag{2.43}$$

where $\hat{u}_i^1$ are arbitrary additive constants in $\mathbf{y}$ and χ_i^{kl} is the solution of the modified local problem:

$$\int_{¥} E_{ijrs} \frac{\partial \chi_r^{kl}}{\partial y_s} \frac{\partial v_i}{\partial y_j} \, \mathrm{d}Y = \int_{¥} E_{ijkl} \frac{\partial v_i}{\partial y_j} \, \mathrm{d}Y, \quad \forall \, \mathbf{v} \in V_{¥} \tag{2.44}$$

Note that Eq. (2.44) can be seen as a system of linear equations and the right-hand side can be rewritten as follows:

$$\int_{¥} E_{ijrs} \frac{\partial \chi_r^{kl}}{\partial y_s} \frac{\partial v_i}{\partial y_j} \, \mathrm{d}Y = \int_{¥} E_{ijrs} \, e_{rs}^{0(kl)} \frac{\partial v_i}{\partial y_j} \, \mathrm{d}Y, \quad \forall \, \mathbf{v} \in V_{¥} \tag{2.45}$$

where $\boldsymbol{\chi}^{kl}$ vectors can be interpreted as characteristic deformations when unit states of macroscopic deformation are applied, $\mathbf{e}^{0(kl)}$. Assuming plane stress or plane strain cases, three "load cases" must be solved, i.e., corresponding to $\mathbf{e}^{0(11)}$, $\mathbf{e}^{0(22)}$ and $\mathbf{e}^{0(12)}$, in order to get the $\boldsymbol{\chi}^{11}$, $\boldsymbol{\chi}^{22}$ and $\boldsymbol{\chi}^{12}$, respectively.

Next choosing the arbitrary field $\mathbf{v}$ in Eq. (2.39) as a function only of the macroscopic variable $\mathbf{x}$, i.e., $\mathbf{v} = \mathbf{v}(\mathbf{x})$, the following equation is obtained:

$$\begin{aligned} \int_{\Omega} \left[\frac{1}{|Y|} \int_{¥} E_{ijkl} \left(\frac{\partial u_k^0}{\partial x_l} + \frac{\partial u_k^1}{\partial y_l} \right) \mathrm{d}Y \right] \frac{\partial v_i}{\partial x_j} \mathrm{d}\Omega \\ = \int_{\Omega} \frac{1}{|Y|} \int_{¥} b_i v_i \, \mathrm{d}Y \, \mathrm{d}\Omega + \int_{\Gamma_t} t_i v_i \, \mathrm{d}\Gamma, \quad \forall \, \mathbf{v} \in V_{\Omega} \end{aligned} \tag{2.46}$$

Substituting Eq. (2.43) into Eq. (2.46), a macroscopic (global) equilibrium problem can be stated as:

$$\int_{\Omega} E_{ijkl}^H \frac{\partial u_k^0(\mathbf{x})}{\partial x_l} \frac{\partial v_i(\mathbf{x})}{\partial x_j} \mathrm{d}\Omega = \int_{\Omega} \langle b_i \rangle \, v_i(\mathbf{x}) \, \mathrm{d}\Omega + \int_{\Gamma_t} t_i v_i(\mathbf{x}) \, \mathrm{d}\Gamma, \quad \forall \, \mathbf{v} \in V_{\Omega} \tag{2.47}$$

where $\langle b_i \rangle$ are the average body forces and E_{ijkl}^H is equal to:

$$E_{ijkl}^H = \frac{1}{|Y|} \int_{¥} E_{ijkl} - E_{ijrs} \frac{\partial \chi_r^{kl}}{\partial y_s} \, dY = \frac{1}{|Y|} \int_{¥} E_{ijrs} \left(\delta_{rk} \delta_{sl} - \frac{\partial \chi_r^{kl}}{\partial y_s} \right) dY \tag{2.48}$$

which are the equivalent or homogenized material properties and δ_{ij} is the Kronecker delta. The homogenized tensor has some symmetries, also obeying the properties present in Eq. (2.10). The homogenized stiffness tensor equation (Eq. 2.48) can be rewritten in a symmetrical form given by:

$$E^H_{ijkl} = \frac{1}{|Y|}\int_{¥} E_{pqrs}\left(\delta_{rk}\delta_{sl} - \frac{\partial \chi^{kl}_r}{\partial y_s}\right)\left(\delta_{pi}\delta_{qj} - \frac{\partial \chi^{ij}_p}{\partial y_q}\right) dY \tag{2.49}$$

Once the solution $\mathbf{u}^0$ has been found by solving the equivalent macroscopic equilibrium problem (Eq. 2.47), $\mathbf{u}^1$ can be completely characterized by Eq. (2.43). The displacement field $\mathbf{u}^\varepsilon$ up to the first term is no longer unknown, and if higher terms on the asymptotic expansion (Eq. 2.27) are required, they can be obtained by investigating the local and global problems that arise from the different power of ε in Eq. (2.33). It is important to point out that when $\varepsilon \to 0^+$, the solution $\mathbf{u}^\varepsilon$ converges in weak sense (energy) to the solution $\mathbf{u}^0$ (see [48]). The displacement field $\mathbf{u}^\varepsilon$ involving details of the microstructure is given by:

$$u^\varepsilon_i(\mathbf{x}) \approx u^0_i(\mathbf{x}) + \varepsilon u^1_i(\mathbf{x},\mathbf{y}) = u^0_i(\mathbf{x}) + \varepsilon\left(-\frac{\partial u^0_k(\mathbf{x})}{\partial x_l}\chi^{kl}_i(\mathbf{y}) + \hat{u}^1_i(\mathbf{x})\right) \tag{2.50}$$

After the homogenization problem is solved, Eq. (2.50) can be used to compute the stresses in each point of the domain (local stresses), which are given by:

$$\sigma^\varepsilon_{ij} = E_{ijkl}\frac{\partial u^\varepsilon_k}{\partial x_l} \tag{2.51}$$

substituting Eq. (2.50) in Eq. (2.51) gives the first approximation of the stress as:

$$\sigma^0_{ij} = E_{ijkl}\left(\frac{\partial u^0_k}{\partial x_l} + \frac{\partial u^1_k}{\partial y_l}\right) \tag{2.52}$$

and then introducing Eq. (2.43) into Eq. (2.52) gives:

$$\sigma^0_{ij}(\mathbf{x},\mathbf{y}) = E_{ijrs}\left(\delta_{rk}\delta_{sl} - \frac{\partial \chi^{kl}_r}{\partial y_s}\right)\frac{\partial u^0_k}{\partial x_l} \tag{2.53}$$

The relation between the homogenized stress (global or averaged) σ^{H}_{ij} and σ^0_{ij} can readily be seen by applying the "average" operator (Eq. 2.36), i.e.

$$\sigma^H_{ij}(\mathbf{x},\mathbf{y}) = \frac{1}{|Y|}\int_{¥}\sigma^0_{ij}\,\mathrm{d}Y = E^H_{ijkl}\frac{\partial u^0_k}{\partial x_l} \tag{2.54}$$

To conclude, the homogenization method was characterized by derivations of equations. It is important to emphasize that all these derivations were performed assuming that all functions and functionals involved were smooth enough. Basically, the homogenization method was characterized by the solution of three distinct problems: two in the microscopic level (Eq. 2.42 and 2.44), and the other in the macroscopic level (Eq. 2.49). The principle of virtual work was used to derive such problems in order to formulate the homogenization method using the FEM. The FEM formulation of the homogenization method will not be covered here. More details about the homogenization method can be found in [37].

2.3 Structural optimization

Structural optimization consists in formulating the design problem of structural components as an optimization problem in order to take advantage of mathematical programming tools. The formulation of the optimization problem must be mathematically rigorous and mirror the problem that is intended to be solved in practice, using design variables, objective function (in some cases, more than one objective function is required) and constraints. The design variables can be seen as parameters that can be modified to improve the design. The objective function is a cost function or a performance index to be minimized or maximized aiming a better design. And finally, the design constraints h_k and g_j. The standard optimization problem formulation is as follows:

$$\min_{\mathbf{x}} \quad f(\mathbf{x}) \tag{2.55a}$$

$$\text{s.t.} \quad h_k(\mathbf{x}) = 0; \qquad k = 1, \dots, p \tag{2.55b}$$

$$g_j(\mathbf{x}) \leq 0; \qquad j = 1, \dots, m \tag{2.55c}$$

$$\underline{x_i} \leq x_i \leq \overline{x}_i; \quad i = 1, \dots, n \tag{2.55d}$$

where $\mathbf{x}$ are the design variables, $f(\mathbf{x})$ is the objective function, h_k are the equality constraints and g_j are the inequality constraints. Once the optimization problem is properly formulated, it can be solved using an optimization algorithm.

There are essentially two categories of optimization algorithms: (1) gradient-based optimization algorithms (see Chapter 2.3.2) and (2) gradient-free optimization algorithms (e.g., Genetic Algorithm, see Chapter 6). The first category needs gradient information of the objective function as well as the constraints, therefore it is necessary to guarantee the differentiability of these functions at all points of the design domain. Regarding the gradient-free optimization algorithms, these do not require gradient information since they rely on probabilistic and/or heuristic

techniques to progress in the optimization process. An advantage of these algorithms is the ability to escape from local minima, but it is not guaranteed (and there is no way to prove) that the final solution is a global minimum in multimodal problems. The main disadvantage of these algorithms is typically their computational time cost.

As introduced in Chapter 1, there are three main types of structural optimization problems. In this work, the focus will be on Topology Optimization (TO) which has been the most active research area in structural and multidisciplinary optimization in the past decades [7].

2.3.1 Topology Optimization

Topology optimization was already introduced in Chapter 1 but now is more detailed. Consider a domain Ω that represents a fixed area or volume. The classical topology optimization problem involves to distribute/redistribute a material phase over the domain Ω, in such way that at the end there is a clear distinction between the regions occupied with material Ω_{mat} and void Ω_{void}, see Fig. 2.3. In order to obtain the optimal distribution of material in the domain Ω it is necessary to determine to which subdomain, Ω_{mat} or Ω_{void}, each of the points $\mathbf{x}$ of that domain belongs. The most basic approach for that is defining discrete design variables with the aid of the following step function:

$$\xi(\mathbf{x}) = \begin{cases} 1, & \mathbf{x} \in \Omega_{\text{mat}} \\ 0, & \mathbf{x} \in \Omega_{\text{void}} \end{cases} \tag{2.56}$$

The stiffness tensor E_{ijkl} may vary from point to point according to the following relationship:

$$E_{ijkl}(\xi(\mathbf{x})) = \xi(\mathbf{x}) {E_{ijkl}}^{(0)} \tag{2.57}$$

where ${E_{ijkl}}^{(0)}$ is the stiffness tensor of the given base material that is intended to be distributed over Ω.

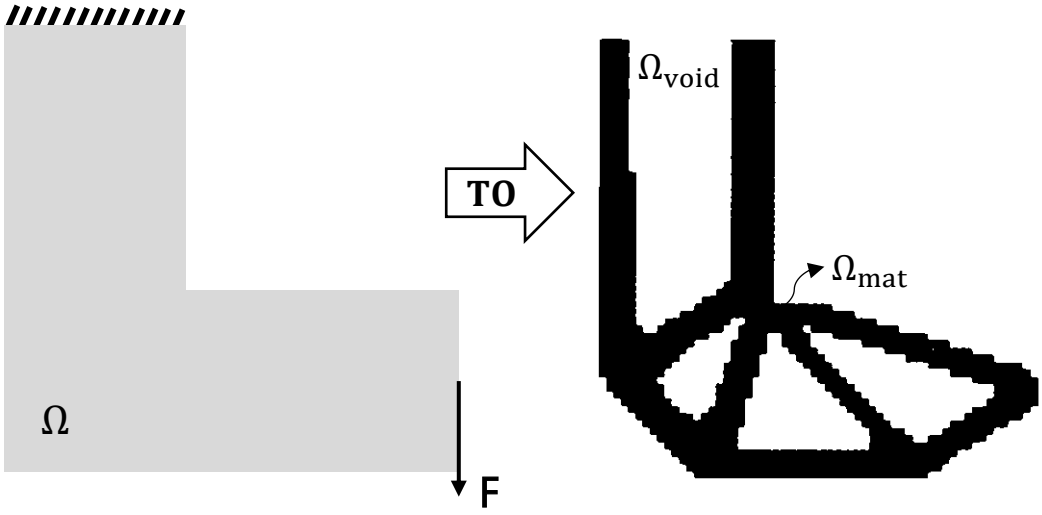

Fig. 2.3: TO applied to a L-bracket example. Adapted from [17].

Topology optimization problems are efficiently solved using gradient-based optimization algorithms (see Chapter 2.3.2) and therefore, the design variables must be continuous. In 1989, Bendsøe [50] proposed the SIMP (*Solid Isotropic Material with Penalization*), also known as a *power-law approach*, where the stiffness tensor or material properties of each element e of the domain are interpolated according to:

$$E_{ijkl}(\rho_e) = \rho_e^p {E_{ijkl}}^{(0)}, \qquad p \geq 1 \ \wedge \ \rho_e \in]0,1] \tag{2.58}$$

where ρ_e is the so-called element "density" and p is the penalty exponent. In a classical topology optimization problem, one seeks designs consisting almost entirely of regions of material or void. The penalty exponent p ensures that intermediate density variables are penalized when $p > 1$ (typically $p = 3$ or 4 is chosen). This is a standard procedure for stiffness/compliance-based optimization problems. The penalization effect to render "black-white" or "1-0" designs has to do with the fact that intermediate densities become unfavourable in the sense that the stiffness obtained is small compared to the cost (volume) of the material, see Fig. 2.4.

To better understand how this penalization works, consider the standard minimum compliance (or maximum global stiffness) formulation:

$$\min_{\rho_e} \ \ l(\mathbf{u}) = \int_\Omega b_i u_i \, \mathrm{d}\Omega + \int_{\Gamma^t} t_i u_i \, \mathrm{d}\Gamma \tag{2.59a}$$

$$\text{s.t.} \quad \int_\Omega E_{ijkl}(\rho_e)\, \varepsilon_{ij}(\mathbf{u}) \varepsilon_{kl}(\mathbf{v}) \mathrm{d}\Omega = l(\mathbf{v}), \qquad e = 1, \dots, n \tag{2.59b}$$

$$\int_\Omega \rho_e \, \mathrm{d}\Omega - V^* \leq 0, \qquad e = 1, \dots, n \tag{2.59c}$$

$$0 < \rho_{\min} \leq \rho_e \leq 1; \qquad e = 1, \dots, n \tag{2.59d}$$

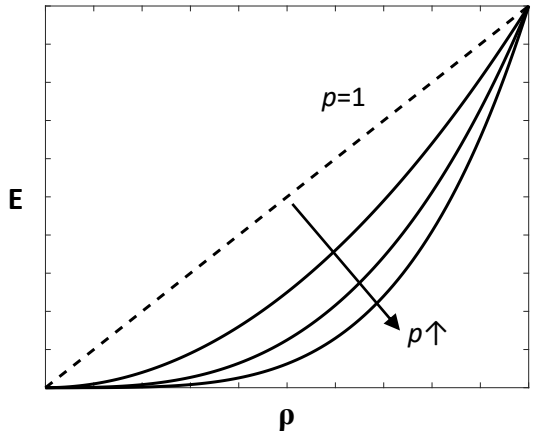

Fig. 2.4: Graphical representation of the SIMP law for increasing penalization *p* exponent.

where the objective function $l(u)$ is the applied force potential that is intended to be minimized when subjected to a volume constraint, with V^* as the target volume. The equilibrium equation (Eq. 2.59b) is written in its weak form, where ε_{ij} are the linearized strains, which depend on the displacement fields **u** (solution of the equilibrium equations) and **v** (virtual). Both **u** and **v** belong to the set of kinematically admissible displacement fields *U*, i.e., $\mathbf{u}, \mathbf{v} \in U$. To avoid singularities, $\rho_{\min}$ is defined as a small number. The volume of material is computed through the integral $\int_\Omega \rho_e \, \mathrm{d}\Omega$. Rather than having the equilibrium condition as a constraint, one could alternatively express it as part of the objective function using the principle of minimum potential energy:

$$\max_{\rho_e} \min_{\mathbf{u} \in U} \left\{ \frac{1}{2} \int_\Omega E_{ijkl}(\rho_e)\, \varepsilon_{ij}(\mathbf{u}) \varepsilon_{kl}(\mathbf{u}) \mathrm{d}\Omega - l(\mathbf{u}) \right\} \tag{2.60a}$$

$$\text{s.t.} \quad \int_\Omega \rho_e \, \mathrm{d}\Omega - V^* \leq 0, \qquad e = 1, \dots, n \tag{2.60b}$$

$$0 < \rho_{\min} \leq \rho_e \leq 1; \qquad e = 1, \dots, n \tag{2.60c}$$

In practice, the equilibrium conditions are verified when running a FEM software, therefore assuming now that **u** is the unique solution of the equilibrium, i.e., a minimizer of the total potential energy, Eq. (2.60a) can be rewritten as:

$$\max_{\rho_e} \; -\frac{1}{2} l(\mathbf{u}) = -\frac{1}{2} \int_\Omega E_{ijkl}(\rho_e)\, \varepsilon_{ij}(\mathbf{u}) \varepsilon_{kl}(\mathbf{u}) \mathrm{d}\Omega \tag{2.61}$$

Alternatively, the objective function in Eq. (2.61) could be written resorting to the complementary energy $-\frac{1}{2}\int_\Omega C_{ijkl}(\rho_e)\, \sigma_{ij}(\mathbf{u})\; \sigma_{kl}(\mathbf{u}) \mathrm{d}\Omega$, where C_{ijkl} is the compliance tensor and σ_{ij} are the stresses. Furthermore, the maximization of a negative quantity as objective is equivalent to the minimization of its positive value.

It is well known that density-based TO is prone to checkerboard and mesh-dependency problems. Checkerboards are regions of alternating solid and void elements ordered in a checkerboard like fashion. Mesh-dependence concerns the effect that qualitatively different optimal solutions are reached for different mesh-sizes or discretizations. To overcome these issues, filtering techniques promoting a regularization of the density field can be conveniently applied. These techniques will be further explored in Chapter 2.3.4.

2.3.2 Gradient-based Optimization Algorithms

Gradient-based optimization algorithms are suitable to solve TO problems. These algorithms start by the starting design point, $\mathbf{x}^{(0)}$, definition. Then, if it does not satisfy a given convergence criterion, it is necessary to calculate a search direction **d** using gradient information of the objective function and constraints, ensuring that **d** is a descent direction in terms of the objective function value, while satisfying the constraints. An optimal step α in the search direction **d** should also be found. A new point $\mathbf{x}^{(1)} = \mathbf{x}^{(0)} + \alpha\mathbf{d}$ with better performance than $\mathbf{x}^{(0)}$ is found in design domain. Next, the same procedure is applied to the point $\mathbf{x}^{(1)}$ and so on, until a solution meets the convergence criteria.

One of the simplest gradient-based optimization algorithms to perform small-size TO is the Optimality Criteria (OC). This algorithm is based on the necessary conditions of optimality. For TO problems of high size, i.e., with high number of design variables and constraints, the Method of Moving Asymptotes (MMA) is preferred. These two algorithms will be summarized next.

2.3.2.1 Optimality Criteria (OC) Method

Implementing the OC to solve problem (2.60), involves deriving the necessary conditions of optimality. The Lagrange function, based on objective function (2.61), can be written as:

$$\mathcal{L} = -\frac{1}{2}\int_{\Omega} E_{ijkl}\,\varepsilon_{ij}\varepsilon_{kl}\mathrm{d}\Omega - \Lambda_e\left(\int_{\Omega}\rho_e\,\mathrm{d}\Omega - V^*\right) - \int_{\Omega}\lambda_e^{+}(\rho_e - 1)\,\mathrm{d}\Omega - \int_{\Omega}\lambda_e^{-}(\rho_{\min} - \rho_e)\,\mathrm{d}\Omega \tag{2.62}$$

where Λ_e is the Lagrange multiplier associated with the volume constraint (Eq. 2.60b), and λ_e^{+} and λ_e^{-} are the Lagrange multiplier associated with the side constraints (Eq. 2.60c). To obtain the necessary conditions of optimality, one must evaluate the stationarity of the Lagrange function w.r.t. the design variables ρ_e:

$$\frac{\partial \mathcal{L}}{\partial \rho_e} = 0 \rightarrow \frac{1}{2}\frac{\partial E^e_{ijkl}}{\partial \rho_e}\varepsilon_{ij}\varepsilon_{kl}|\Omega_e| = \Lambda_e|\Omega_e| + \lambda_e^+|\Omega_e| - \lambda_e^-|\Omega_e| \tag{2.63}$$

where $|\Omega_e|$ is the element volume and the derivatives of the compliance function $C = \frac{1}{2}\int_\Omega E_{ijkl}\,\varepsilon_{ij}\varepsilon_{kl}\mathrm{d}\Omega$ are obtained using the adjoint method, which simply gives $\frac{\partial C}{\partial \rho_e}$ $\frac{1}{2}\frac{\partial E^e_{ijkl}}{\partial \rho_e}\varepsilon_{ij}\varepsilon_{kl}|\Omega_e|$ (solution of the self-adjoint problem, see [17]). For intermediate values of the design values, i.e., $\rho_{\min} < \rho_e < 1$, the conditions can be written as:

$$\frac{\partial E^e_{ijkl}}{\partial \rho_e}\varepsilon_{ij}\varepsilon_{kl} = 2\Lambda_e \tag{2.64}$$

The OC method simply consists in implementing the following update scheme based on the optimality conditions:

$$\rho_e^{k+1} = \begin{cases} \max[(1-\zeta)\rho_e^k, \rho_{\min}] & \text{if } \rho_e^k\left(B_e^k\right)^\eta \le \max[(1-\zeta)\rho_e^k, \rho_{\min}] \\ \min[(1+\zeta)\rho_e^k, 1] & \text{if } \min[(1+\zeta)\rho_e^k, 1] \le \rho_e^k\left(B_e^k\right)^\eta \\ \rho_e^k\left(B_e^k\right)^\eta & \text{otherwise} \end{cases} \tag{2.65}$$

where k denotes the iteration step, ζ is a move limit, η is a tuning parameter and B_e^k is given by the expression:

$$B_e^k = \frac{\frac{\partial E^e_{ijkl}}{\partial \rho_e^k}\varepsilon_{ij}\varepsilon_{kl}}{2\Lambda_e^k} \tag{2.66}$$

with the update scheme for the Lagrange multiplier Λ_e^k given by:

$$\Lambda_e^{k+1} = \max\left[0, \Lambda_e^k + c\left(\int_\Omega \rho_e^k\,\mathrm{d}\Omega - V^*\right)\right] \tag{2.67}$$

where c is a penalty constant. The expression for the update scheme of the Lagrange multiplier Λ_e^k can be easily obtained by alternatively defining the augmented Lagrangian as in [51] and then compute its stationarity w.r.t. the Lagrange multiplier Λ_e. Simply put, the update scheme in Eq. (2.65) promotes the decrease of the element density, ρ_e, in case $\left(B_e^k\right)^\eta \le (1-\zeta)$ or the increase of ρ_e in case $\left(B_e^k\right)^\eta \ge (1+\zeta)$.

2.3.2.2 Method of Moving Asymptotes (MMA)

MMA is a Sequential Convex Programming (SCP) method, firstly introduced by Krister Svanberg [52] in 1987, to solve non-linear constrained optimization problems. Generally, a SCP

method combines the concepts of approximation and dual solution, which will be summarized next.

In most of the structural optimization problems, especially in topology optimization, obtaining a solution directly can be prohibitive, due to the computational cost of the structural and sensitivity analysis of the problem. An interesting way to circumvent this problem is using the approximation concepts approach, which replaces the primary optimization problem by a sequence of explicit approximate subproblems. MMA does exactly that, with the original objective function f_0 and constraints f_i replaced by approximating convex functions ($\tilde{f}_0$ and $\widetilde{f}_i$, respectively) mainly based on gradient information at the current iteration point, and also (implicitly) on information from previous iteration points. In MMA, each subproblem for a given iteration *k* is formulated in the following way:

$$\min_{\mathbf{x}} \quad \widetilde{f}_0^{(k)}(\mathbf{x}) + z + \sum_{i=1}^{m} c_i y_i \tag{2.68a}$$

$$\text{s.t.} \quad \widetilde{f}_i^{(k)}(\mathbf{x}) - y_i \leq \hat{f}_i; \qquad i = 1, \dots, m \tag{2.68b}$$

$$\alpha_j^{(k)} \leq x_j \leq \beta_j^{(k)}; \qquad j = 1, \dots, n \tag{2.68c}$$

$$y_i \geq 0; \qquad i = 1, \dots, m \tag{2.68d}$$

$$z \geq 0 \tag{2.68e}$$

where $\mathbf{x} = (x_1, \dots, x_n)$ are the design variables, and both $\mathbf{y} = (y_1, \dots, y_n)$ and z are the so-called artificial variables. Artificial variables are meant to never get unfeasible solutions from the optimization problem, and it is also ensured that the solution is as close as possible to being feasible by choosing an appropriate "cost" for these variables. Constants c_i are sufficient large numbers so that the variables y_i become expensive, $\hat{f}_i$ is the right-hand side of constraint i, n and m are the total number of design variables and constraints, respectively. Both the objective function f_0 and the constraints f_i are continuously differentiable, real-valued functions. The parameters $\alpha_j^{(k)}$ and $\beta_j^{(k)}$ are usually referred as *move limits*. To avoid the possibility of any unexpected "division by zero" while solving the subproblem, the following rule must be applied when choosing the move limits:

$$L_j^{(k)} < \alpha_j^{(k)} < x_j^{(k)} < \beta_j^{(k)} < U_j^{(k)} \tag{2.69}$$

For example, $\alpha_j^{(k)}$ and $\beta_j^{(k)}$ can be chosen as:

$$\alpha_j^{(k)} = \max\left\{x_j^{min}, 0.9L_j^{(k)} + 0.1x_j^{(k)}\right\} \tag{2.70}$$

$$\beta_j^{(k)} = \min\left\{x_j^{max}, 0.9U_j^{(k)} + 0.1x_j^{(k)}\right\} \tag{2.71}$$

with x_j^{min} and x_j^{max} being the original design variables bounds which satisfy $x_j^{min} < x_j^{max}$.

The parameters $L_j^{(k)}$ and $U_j^{(k)}$ are the *moving asymptotes*. The default rules for updating the asymptotes are as follows. In the first two iterations, i.e., for $k = 1$ and $k = 2$, the asymptotes are given by:

$$L_j^{(k)} = x_j^{(k)} - \gamma_0\left(x_j^{max} - x_j^{min}\right) \tag{2.72}$$

$$U_j^{(k)} = x_j^{(k)} + \gamma_0\left(x_j^{max} - x_j^{min}\right) \tag{2.73}$$

where γ_0 is a given real number less than unity, e.g., $\gamma_0 = 0.5$. In latter iterations, i.e., for $k \geq 3$, the asymptotes are given by:

$$L_j^{(k)} = x_j^{(k)} - \gamma_j^{(k)}\left(x_j^{(k-1)} - L_j^{(k-1)}\right) \tag{2.74}$$

$$U_j^{(k)} = x_j^{(k)} + \gamma_j^{(k)}\left(U_j^{(k-1)} - x_j^{(k-1)}\right) \tag{2.75}$$

where $\gamma_j^{(k)}$ is computed as follows:

$$\gamma_j^{(k)} = \begin{cases} s_1 \text{ if } \left(x_j^{(k)} - x_j^{(k-1)}\right)\left(x_j^{(k-1)} - x_j^{(k-2)}\right) < 0 \\ s_2 \text{ if } \left(x_j^{(k)} - x_j^{(k-1)}\right)\left(x_j^{(k-1)} - x_j^{(k-2)}\right) > 0 \\ 1 \text{ if } \left(x_j^{(k)} - x_j^{(k-1)}\right)\left(x_j^{(k-1)} - x_j^{(k-2)}\right) = 0 \end{cases} \tag{2.76}$$

s_1 and s_2 are given real numbers, e.g., $s_1 = 0.7$ and $s_2 = 1.2$, that obey the following rule. If the optimization process tends to oscillate, i.e., the signs of $\left(x_j^{(k)} - x_j^{(k-1)}\right)$ and $\left(x_j^{(k-1)} - x_j^{(k-2)}\right)$ are opposite, then it needs to be stabilized. This stabilization may be accomplished by moving the asymptotes closer to the current iteration point, i.e., choosing $s_1 < 1$. On the other hand, if the optimization process is monotone and slow, i.e., the signs of $\left(x_j^{(k)} - x_j^{(k-1)}\right)$ and $\left(x_j^{(k-1)} - x_j^{(k-2)}\right)$ are equal, it needs to be "relaxed". This may be accomplished by moving the asymptotes away from the current iteration point, i.e., choosing $s_2 > 1$.

The approximating functions $\tilde{f}_i^{(k)}$, for each $i = 0,1,\ldots,m$, used in the subproblem are defined by:

$$\tilde{f}_i^{(k)}(x) = \sum_{j=1}^{n}\left(\frac{p_{ij}^{(k)}}{U_j^{(k)} - x_j} + \frac{q_{ij}^{(k)}}{x_j - L_j^{(k)}}\right) + r_i^{(k)} \tag{2.77}$$

where

$$p_{ij}^{(k)} = \begin{cases} \left(U_j^{(k)} - x_j^{(k)}\right)^2 \dfrac{\partial f_i}{\partial x_j}, & \text{if} \quad \dfrac{\partial f_i}{\partial x_j} > 0 \\ 0, & \text{if} \quad \dfrac{\partial f_i}{\partial x_j} \leq 0 \end{cases} \tag{2.78}$$

$$q_{ij}^{(k)} = \begin{cases} 0, & \text{if} \quad \dfrac{\partial f_i}{\partial x_j} \geq 0 \\ -\left(x_j^{(k)} - L_j^{(k)}\right)^2 \dfrac{\partial f_i}{\partial x_j}, & \text{if} \quad \dfrac{\partial f_i}{\partial x_j} < 0 \end{cases} \tag{2.79}$$

$$r_i^{(k)} = f_i\left(\mathbf{x}^{(k)}\right) - \sum_{j=1}^{n} \left(\frac{p_{ij}^{(k)}}{U_j^{(k)} - x_j^{(k)}} + \frac{q_{ij}^{(k)}}{x_j^{(k)} - L_j^{(k)}} \right) \tag{2.80}$$

An arbitrary function f_i is represented in the Fig. 2.5, as well as its convex approximating function $\widetilde{f}_i$ between the lower L_j and upper U_j asymptotes in a point x_j^0. This figure helps understanding some of the concepts mentioned above.

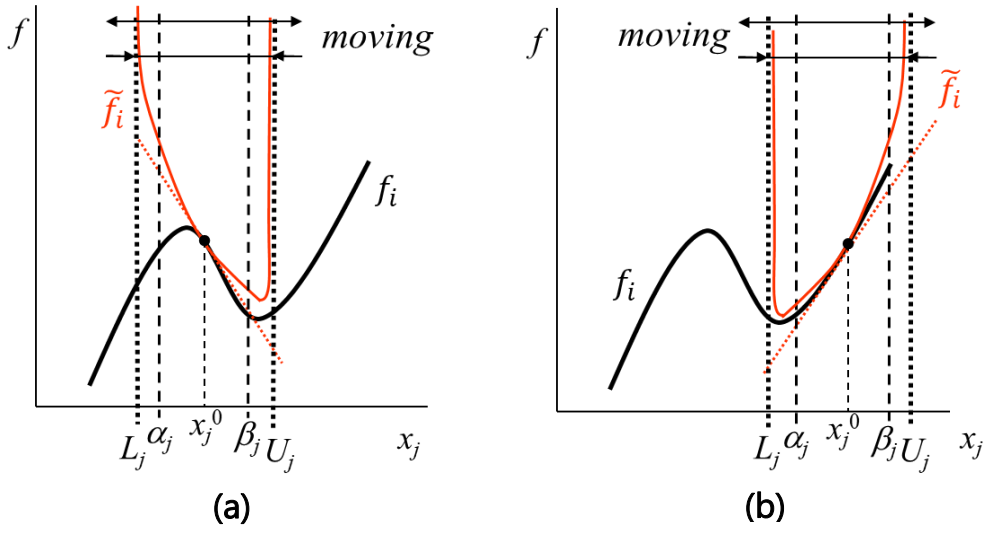

Fig. 2.5: Convex approximation function $\widetilde{f}_i$ of an arbitrary function f_i assuming (a) $\frac{\partial f_i}{\partial x_j^0} < 0$ and (b) $\frac{\partial f_i}{\partial x_j^0} > 0$.

In 1995, Svanberg [53] proposed an MMA extension, so-called Globally Convergent Method of Moving Asymptotes (GCMMA), which uses simultaneously both asymptotes to create a non-homogeneous approximating function $\widetilde{f}_i$. This can be done while using the same formula of the

approximating function shown above (Eq. 2.89), but with different coefficients $p_{ij}^{(k)}$ and $q_{ij}^{(k)}$ which are now non-zero in general. The coefficients are chosen as follows:

$$p_{ij}^{(k)} = \begin{cases} \left(U_j^{(k)} - x_j^{(k)}\right)^2 \left(\frac{\partial f_i}{\partial x_j} + \frac{\rho_j^{(k)}}{2}\left(U_j^{(k)} - L_j^{(k)}\right)\right), & \text{if} \quad \frac{\partial f_i}{\partial x_j} > 0 \\ \left(U_j^{(k)} - x_j^{(k)}\right)^2 \left(\frac{\rho_j^{(k)}}{2}\left(U_j^{(k)} - L_j^{(k)}\right)\right), & \text{if} \quad \frac{\partial f_i}{\partial x_j} \leq 0 \end{cases} \tag{2.81}$$

$$q_{ij}^{(k)} = \begin{cases} \left(x_j^{(k)} - L_j^{(k)}\right)^2 \left(\frac{\rho_j^{(k)}}{2}\left(U_j^{(k)} - L_j^{(k)}\right)\right), & \text{if} \quad \frac{\partial f_i}{\partial x_j} \geq 0 \\ -\left(x_j^{(k)} - L_j^{(k)}\right)^2 \left(\frac{\partial f_i}{\partial x_j} + \frac{\rho_j^{(k)}}{2}\left(U_j^{(k)} - L_j^{(k)}\right)\right), & \text{if} \quad \frac{\partial f_i}{\partial x_j} < 0 \end{cases} \tag{2.82}$$

where $\rho_j^{(k)}$ are strictly positive parameters (to ensure the convexity of the approximation) which are updated together with the asymptotes. These parameters allow the approximating function to be non-monotonous by using both asymptotes at the same time. In 2002, Svanberg [54] proposed an improved version of GCMMA that converges faster.

In 1996, Zhang et al. [55] proposed a new version of MMA called Generalized Method of Moving Asymptotes (GMMA). The main difference between this version and the original MMA version of Svanberg is that in GMMA, each design variable x_j in each function $\widetilde{f_i}$ is associated with its proper moving asymptote L_{ij} or U_{ij} to improve the approximation quality. For example, moving asymptotes can be largely relaxed for linear inequality constraints and tightened for non-linear ones.

The success of the approximation strategy adopted by MMA comes from the fact that the subproblems generated can be solved efficiently. One of the most efficient strategies to solve the subproblems is the dual method proposed initially by Fleury [56]. Dual methods are suitable to structural problems because the dimensionality of the dual solution space is generally much lower than the primal design space. With efficient algorithms, dual solvers can solve sub-problems within a reasonable computational time. Next, some basic concepts about dual solution algorithms will be explored.

Firstly, one shall define the Lagrange function associated to the subproblem defined in Eq. (2.68):

$$\mathcal{L}(x_j,\lambda_i)=\sum_{j=1}^{n}\left(\frac{p_{0j}+\sum_{i=1}^{m}(\lambda_i p_{ij})}{U_j-x_j}+\frac{q_{0j}+\sum_{i=1}^{m}(\lambda_i q_{ij})}{x_j-L_j}\right)+\sum_{i=1}^{m}\left(c_i y_i-\lambda_i(y_i+b_i)\right)+z+r_0 \tag{2.83}$$

where $\lambda_i \geq 0$ is the vector of Lagrange multipliers or "dual variables" and $b_i=\hat{f}_i-r_i$. Note that the Lagrange transformation replaces the constraints by a linear term in the Lagrange function. This can be interpreted as adding to the objective function a linear cost, with marginal price λ_i, which has to be paid whenever a constraint is violated. The dual objective function Ψ can now be defined as follows:

$$\Psi(\boldsymbol{\lambda})=\min_{\mathbf{x}}\left\{\mathcal{L}(\mathbf{x},\boldsymbol{\lambda})|\ \alpha_j\leq x_j\leq\beta_j\right\} \tag{2.84}$$

To find out the solution x_j that minimizes the Lagrangian, one must derive the necessary conditions for optimality (KKT conditions), computing the following derivative:

$$\frac{\partial\mathcal{L}(x_j,\lambda_i)}{\partial x_j}=\frac{p_{0j}+\sum_{i=1}^{m}(\lambda_i p_{ij})}{(U_j-x_j)^2}-\frac{q_{0j}+\sum_{i=1}^{m}(\lambda_i q_{ij})}{(x_j-L_j)^2} \tag{2.85}$$

It is proven in [52] that the unique solution $x_j(\lambda_i)$ of (2.84), corresponding to the relation between primal (x_j) and dual (λ_i) variables, is obtained doing $\partial\mathcal{L}_j(x_j,\lambda_i)/\partial x_j=0$, which gives the following explicit expression for $x_j(\lambda_i)$:

$$x_j(\lambda_i)=\frac{(p_{0j}+\sum_{i=1}^{m}(\lambda_i p_{ij}))^{\frac{1}{2}}L_j+(q_{0j}+\sum_{i=1}^{m}(\lambda_i q_{ij}))^{\frac{1}{2}}U_j}{(p_{0j}+\sum_{i=1}^{m}(\lambda_i p_{ij}))^{\frac{1}{2}}+(q_{0j}+\sum_{i=1}^{m}(\lambda_i q_{ij}))^{\frac{1}{2}}} \tag{2.86}$$

In GMMA there is no such explicit expression or closed form due to non-linearity of the Lagrange function derivative (Eq. 2.88), see [55]. In this case, where each approximate function has its own pair of asymptotes, the Lagrange function associated to the subproblem takes the following form:

$$\mathcal{L}(x_j,\lambda_i)=\sum_{j=1}^{n}\left(\frac{p_{0j}}{U_{0j}-x_j}+\frac{q_{0j}}{x_j-L_{0j}}+\frac{\sum_{i=1}^{m}(\lambda_i p_{ij})}{U_{ij}-x_j}+\frac{\sum_{i=1}^{m}(\lambda_i q_{ij})}{x_j-L_{ij}}\right)+\sum_{i=1}^{m}\left(c_i y_i-\lambda_i(y_i+b_i)\right)+z+r_0 \tag{2.87}$$

and the optimality condition of the separable Lagrangian function takes the form:

$$\frac{\partial \mathcal{L}(x_j, \lambda_i)}{\partial x_j} = \frac{p_{0j}}{\left(U_{0j} - x_j\right)^2} - \frac{q_{0j}}{\left(x_j - L_{0j}\right)^2} + \frac{\sum_{i=1}^{m}\left(\lambda_i p_{ij}\right)}{\left(U_{ij} - x_j\right)^2} - \frac{\sum_{i=1}^{m}\left(\lambda_i q_{ij}\right)}{\left(x_j - L_{ij}\right)^2} = 0 \tag{2.88}$$

Since an explicit relation between primal and dual variables is impossible to obtain in this case, the Newton-Raphson method can be adopted to obtain the values of the primal variables given the values of the dual ones. The developments below applied to MMA could also be easily adapted to GMMA just considering that each function has its own pair of asymptotes, i.e., L_{ij} and U_{ij}.

Once primal and dual variables are related (explicitly or implicitly), the dual objective function can be written as $\Psi(\boldsymbol{\lambda}) = \mathcal{L}\left(x_j(\boldsymbol{\lambda}), \boldsymbol{\lambda}\right)$. The derivatives of $\Psi(\boldsymbol{\lambda})$, w.r.t. the dual variables $\boldsymbol{\lambda}$, are given by:

$$\frac{\partial \Psi(\boldsymbol{\lambda})}{\partial \boldsymbol{\lambda}} = \sum_{j=1}^{n}\left(\frac{p_{ij}}{U_j - x_j(\boldsymbol{\lambda})} + \frac{q_{ij}}{x_j(\boldsymbol{\lambda}) - L_j}\right) - y_i - b_i \tag{2.89}$$

Finally, the dual problem corresponding to MMA sub-problem (2.68) can be stated as:

$$\max_{\boldsymbol{\lambda}} \quad \Psi(\boldsymbol{\lambda}) \quad \text{s.t.} \quad \boldsymbol{\lambda} \geq 0 \tag{2.90}$$

The dual problem can be solved by any gradient method. In MMA, it is solved by the steepest ascent method, in the first two iterations, followed by the Newton's method. Regardless of the method used, once the search direction is found, a line search is carried out to find the next point. This iterative process ends when a specified convergence tolerance is met. Once the dual problem has been solved, the optimal solution of the "primal" sub-problem Eq. (2.68) is obtained through Eq. (2.86), for the obtained optimal dual solution $\boldsymbol{\lambda}^*$. The dual problem has the following properties: (1) if the primal problem is a minimization problem, the dual problem is a maximization problem; (2) the dual problem possesses a solution if the primal problem does; and (3) a solution of the dual problem also provides a solution to the primal problem.

As specified above, the Newton's method is used to solve the dual problem. The method implies setting and solving repeatedly the following system of equations:

$$\mathbf{H}(\boldsymbol{\lambda})\mathbf{d} = \frac{\partial \Psi(\boldsymbol{\lambda})}{\partial \lambda_i} \tag{2.91}$$

where $\mathbf{H}(\boldsymbol{\lambda})$ is the Hessian matrix of the dual objective function and $\mathbf{d}$ is the search direction. Using results from Lagrangian duality (see [57]), the Hessian can be computed as:

$$\mathbf{H}(\boldsymbol{\lambda}) = -\frac{\partial}{\partial x_j}\left(\frac{\partial \Psi(\boldsymbol{\lambda})}{\partial \boldsymbol{\lambda}}\right)\left[\frac{\partial^2 \mathcal{L}}{\partial {x_j}^2}\right]^{-1}\left(\frac{\partial}{\partial x_j}\left(\frac{\partial \Psi(\boldsymbol{\lambda})}{\partial \boldsymbol{\lambda}}\right)\right)^{\mathsf{T}} \tag{2.92}$$

where

$$\frac{\partial}{\partial x_j}\left(\frac{\partial \Psi(\boldsymbol{\lambda})}{\partial \boldsymbol{\lambda}}\right) = \frac{p_{ij}}{\left(U_j - x_j\right)^2} - \frac{q_{ij}}{\left(x_j - L_j\right)^2} \tag{2.93}$$

and

$$\frac{\partial^2 \mathcal{L}}{\partial {x_j}^2} = \frac{2\left(p_{0j} + \sum_{i=1}^{m}\left(\lambda_i p_{ij}\right)\right)}{\left(U_j - x_j\right)^3} + \frac{2\left(q_{0j} + \sum_{i=1}^{m}\left(\lambda_i q_{ij}\right)\right)}{\left(x_j - L_j\right)^3} \tag{2.94}$$

In this work, one uses the MMA version implemented by Professor Krister Svanberg himself in Fortran code. This code has several subroutines that implement the equations presented throughout this chapter. Fig. 2.6 tries to help the reader to link the mathematical equations with their computational implementation.

To conclude, there are basically two key features that subproblems must satisfy: (1) **convexity** to ensure that there is a unique solution, and that the solution of the dual problem is the solution of the original problem; and (2) **separability** which is essential to obtain the relations between the primal design variables and the Lagrange multipliers that are easy to compute.

2.3.3 Sensitivity analysis

Sensitivity analysis is required whenever a gradient-based optimization algorithm is used. It consists of studying the variation of a given function with respect to a design variable or a set of design variables. The sensitivity calculation is then equivalent to the mathematical problem of obtaining the derivatives of a given function. When dealing with complex functions, the direct differentiation may be impractical. Instead, the gradients can be computed using a numerical or analytical method.

The most widely used numerical method is the Finite Difference Method. This method is easy to implement, however it is computationally expensive.

Regarding analytical methods, the two most used are the direct method and the adjoint method. These have the advantage of being more accurate and less computationally expensive comparing to the Finite Difference Method, but they are more difficult to implement. The three aforementioned methods will be detailed next.

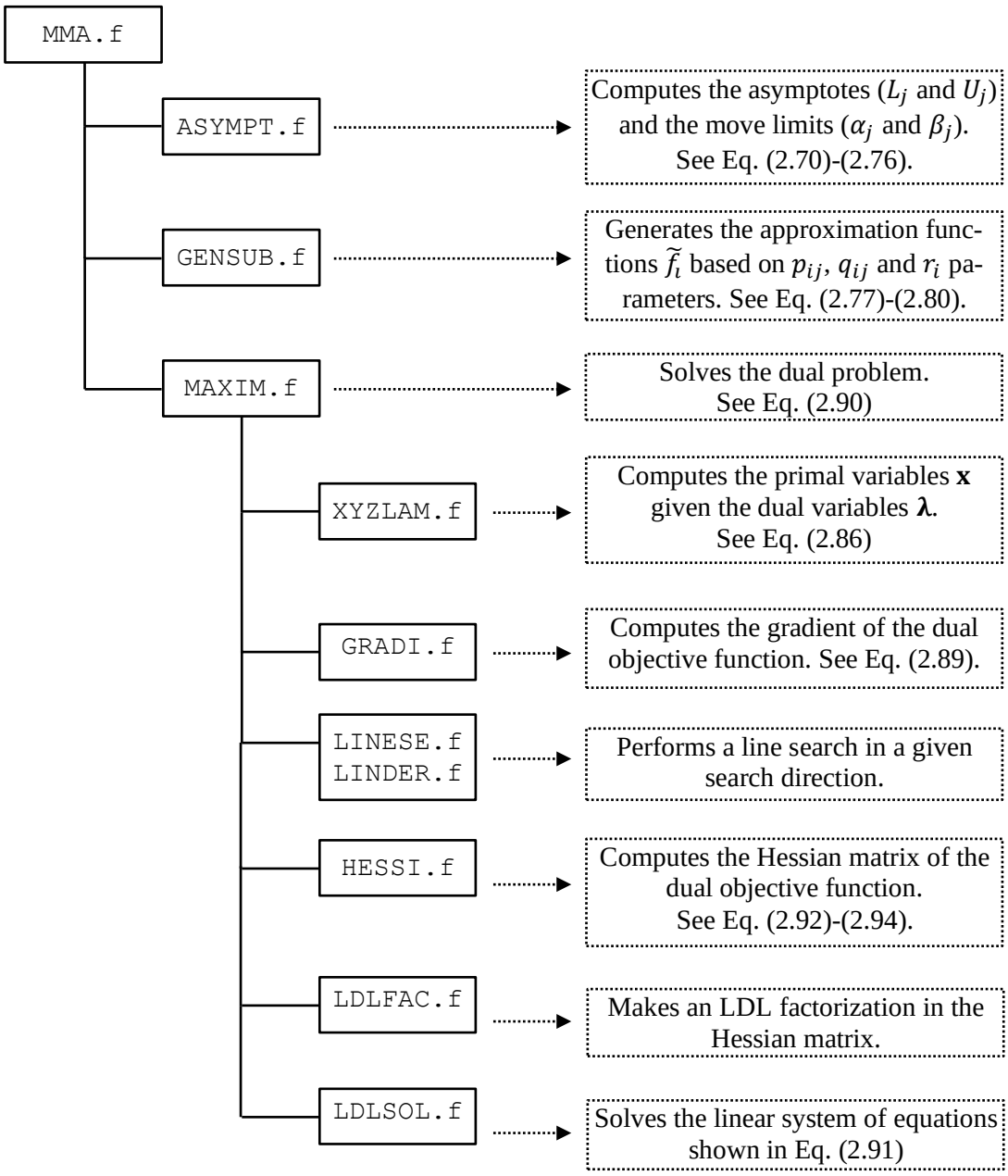

Fig. 2.6: Schematic representation of the MMA Fortran computational implementation.

2.3.3.1 Finite Difference Method

Given a function $\psi(x)$ of a design variable x, the finite difference approximation $\Delta\psi/\Delta x$ to the derivative $\mathrm{d}\psi/\mathrm{d}x$ is obtained by slightly perturb the design variable Δx (called *step size*) and compute the ratio between the perturbation obtained in the function $\Delta\psi$ and the design variable perturbation. The finite difference can be computed in three different ways: (1) *forward-*

difference approximation; (2) *backward*-difference approximation; and (3) *central*-difference approximation.

The *forward*-difference approximation is given by:

$$\frac{\mathrm{d}\psi}{\mathrm{d}x} \approx \frac{\Delta\psi}{\Delta x} = \frac{\psi(x+\Delta x)-\psi(x)}{\Delta x} \tag{2.95}$$

The *backward*-difference approximation is given by:

$$\frac{\mathrm{d}\psi}{\mathrm{d}x} \approx \frac{\Delta\psi}{\Delta x} = \frac{\psi(x)-\psi(x-\Delta x)}{\Delta x} \tag{2.96}$$

The *central*-difference approximation is given by:

$$\frac{\mathrm{d}\psi}{\mathrm{d}x} \approx \frac{\Delta\psi}{\Delta x} = \frac{\psi\left(x+\frac{1}{2}\Delta x\right)-\psi\left(x-\frac{1}{2}\Delta x\right)}{\Delta x} \tag{2.97}$$

It is also possible to employ higher-order finite-difference approximations, but they are rarely used in structural optimization applications due to the high computational cost associated. If one needs to find the derivatives of structural response with respect to *n* design variables, the *forward* or *backward*-difference approximation requires *n* additional analyses, the *central*-difference approximation 2*n* additional analyses, and higher order approximations are even more expensive [58].

2.3.3.2 Analytical methods

When applying the FEM, the static equilibrium equations are stated in terms of the nodal displacement vector $\mathbf{u}$ in the well-known form $\mathbf{Ku} = \mathbf{f}$, where $\mathbf{K}$ and $\mathbf{f}$ are the stiffness matrix and load vector, respectively. The equilibrium equations of the local homogenization problem in Eq. (2.44) when solved by FEM takes a similar form considering the micro-displacements vector $\boldsymbol{\chi}$ for a single load case, i.e., $\mathbf{K}\boldsymbol{\chi} = \mathbf{f}$. The developments shown below consider the local homogenization problem, but they follow a standard procedure that could be applied to the static equilibrium problem in like manner (just replace $\boldsymbol{\chi}$ by $\mathbf{u}$).

Consider now a general function $\psi(x, \boldsymbol{\chi}(x))$ that depends explicitly and implicitly (through the solution $\boldsymbol{\chi}$ of the equilibrium equations) on the design variable x. The sensitivity of a functional ψ w.r.t. x cannot be calculated directly, thus requiring the chain rule to be applied. Therefore, the total derivative can be calculated through:

$$\frac{\mathrm{d}\psi}{\mathrm{d}x} = \underbrace{\frac{\partial\psi}{\partial x}}_{\substack{\text{Explicit}\\ \text{part}}} + \underbrace{\frac{\partial\psi}{\partial\boldsymbol{\chi}}\frac{\mathrm{d}\boldsymbol{\chi}}{\mathrm{d}x}}_{\substack{\text{Implicit}\\ \text{part}}} \tag{2.98}$$

The explicit part of the derivative is straightforward to obtain. Therefore, henceforth one discusses only how to obtain the implicit part of the derivative.

Differentiating both sides of the equilibrium conditions w.r.t. x, i.e.:

$$\frac{\mathrm{d}(\mathbf{K}\boldsymbol{\chi})}{\mathrm{d}x} = \frac{\mathrm{d}(\mathbf{f})}{\mathrm{d}x} \Leftrightarrow \frac{\mathrm{d}\mathbf{K}}{\mathrm{d}x}\boldsymbol{\chi} + \mathbf{K}\frac{\mathrm{d}\boldsymbol{\chi}}{\mathrm{d}x} = \frac{\mathrm{d}\mathbf{f}}{\mathrm{d}x} \tag{2.99}$$

Doing some mathematical manipulation on Eq. (2.99), one gets the derivative of $\boldsymbol{\chi}$ w.r.t x:

$$\frac{\mathrm{d}\boldsymbol{\chi}}{\mathrm{d}x} = \mathbf{K}^{-1}\left[\frac{\mathrm{d}\mathbf{f}}{\mathrm{d}x} - \frac{\mathrm{d}\mathbf{K}}{\mathrm{d}x}\boldsymbol{\chi}\right] = \mathbf{K}^{-1}\left[\frac{\partial\mathbf{f}}{\partial x} - \frac{\partial\mathbf{K}}{\partial x}\boldsymbol{\chi}\right] \tag{2.100}$$

Note that the total derivatives of $\mathbf{f}$ and $\mathbf{K}$ w.r.t. x coincide with the respective partial derivatives. Substituting Eq. (2.100) in Eq. (2.98), the following is obtained:

$$\frac{\mathrm{d}\psi}{\mathrm{d}x} = \frac{\partial\psi}{\partial x} + \underbrace{\frac{\partial\psi}{\partial\boldsymbol{\chi}}\mathbf{K}^{-1}}_{\boldsymbol{\lambda}^{\mathrm{T}}}\left[\frac{\partial\mathbf{f}}{\partial x} - \frac{\partial\mathbf{K}}{\partial x}\boldsymbol{\chi}\right] \tag{2.101}$$

The direct computation of $\mathbf{K}^{-1}$ is impractical. Two different methods are proposed to circumvent this drawback: **direct differentiation method** and **adjoint variable method**. The direct differentiation method consists of numerically solve Eq. (2.99) for $\mathrm{d}\boldsymbol{\chi}/\mathrm{d}x$ and insert the result in Eq. (2.98). On the other hand, the adjoint variable method simplifies Eq. (2.101) introducing the so-called *adjoint variable* $\boldsymbol{\lambda}$ defined as:

$$\boldsymbol{\lambda} \equiv \left[\frac{\partial\psi}{\partial\boldsymbol{\chi}}\mathbf{K}^{-1}\right]^{\mathrm{T}} = \mathbf{K}^{-1}\left(\frac{\partial\psi}{\partial\boldsymbol{\chi}}\right)^{\mathrm{T}} \tag{2.102}$$

Multiplying both sides of Eq. (2.102) by $\mathbf{K}$, the following adjoint equation is obtained:

$$\mathbf{K}\boldsymbol{\lambda} = \left(\frac{\partial\psi}{\partial\boldsymbol{\chi}}\right)^{\mathrm{T}} \tag{2.103}$$

The solution of $\boldsymbol{\lambda}$ is obtained solving Eq. (2.103) and then it can be inserted in Eq. (2.101).

These two analytical methods differ in computational effort depending on the relative number of constraints and design variables in the optimization problem to be solved. In structural optimization, it is common to have multiple design constraints and variables. The direct differentiation method requires the solution of Eq. (2.99) once for each design variable. On the other hand, the adjoint variable method requires the solution of Eq. (2.103) once for each design constraint.

Therefore, the direct method is more efficient than the adjoint method when the number of design variables is smaller than the number of constraints. However, when the number of design constraints is smaller than the number of variables, the adjoint method is preferable.

2.3.4 Filtering techniques in TO

As already mentioned in Chapter 2.3.1, filtering techniques aim to regularize the density field in TO problems, avoiding problems such as checkerboards and mesh-dependency of results. The two most popular filtering methods are: (1) the **density filtering** and (2) the **sensitivity filtering** [59]. The **density filtering** consists in redefining the density in each element based on the weighted average of the densities of neighbouring elements. This is done before calling the finite element solver, and afterwards the sensitivities are modified in a consistent way. On the other hand, the **sensitivity filtering** consists in heuristically modify the sensitivities, after solving the finite element problem in standard way, based on the weighted averages of the neighbour sensitivities. Both methods use the concept of neighbourhood. The neighbourhood of an element N_e is defined by the elements that have centres included in the range of a filter radius R defined from the centre of element e, i.e.:

$$N_e = \{i \mid \|\mathbf{x}_i - \mathbf{x}_e\| \leq R\} \tag{2.104}$$

where $\mathbf{x}_i$ is the spatial (centre) location of element i.

2.3.4.1 Density filtering

Density filters work by modifying the density fields according to the specified neighbourhood of an element. Therefore, the modified element density $\tilde{\rho}_e$ is a function of the neighbouring density variables, i.e., $\tilde{\rho}_e(\rho_i \in N_e)$. It is important to note that all the properties related with the FEM analysis (e.g., material properties, volume or stresses) must be based upon the filtered density.

In 2001, Bruns and Tortorelli [60] introduced the density filtering that was latter mathematically proven as a viable approach by [61]. The filtered density is computed as:

$$\tilde{\rho}_e = \frac{\sum_{i \in N_e} w(\mathbf{x}_i) v_i \rho_i}{\sum_{i \in N_e} w(\mathbf{x}_i) v_i} \tag{2.105}$$

where v_i is the volume of element i and $w(\mathbf{x}_i)$ is the weighting function given by the linearly decaying (cone-shape) function:

$$w(\mathbf{x}_i) = R - \|\mathbf{x}_i - \mathbf{x}_e\| \tag{2.106}$$

Recall that the functions used to formulate the TO problem depend on the filtered density but these ones in turn depend on the non-filtered densities. These last ones are defined as the problem design variables, i.e., the ones being updated by the optimizer used. Therefore, sensitivities of the objective and constraint functions w.r.t. non-filtered densities are required. The sensitivity of a given function, say ψ, w.r.t. a design variable ρ_e, depends on the respective filtered density $\tilde{\rho}_i$ by applying the chain rule:

$$\frac{\mathrm{d}\psi}{\mathrm{d}\rho_e} = \sum_{i \in N_e} \frac{\partial \psi}{\partial \tilde{\rho}_i} \frac{\mathrm{d}\tilde{\rho}_i}{\mathrm{d}\rho_e} = \sum_{i \in N_e} \frac{\partial \psi}{\partial \tilde{\rho}_i} \left[\frac{w(\mathbf{x}_i) v_i}{\sum_{j \in N_i} w(\mathbf{x}_j) v_j} \right] \tag{2.107}$$

2.3.4.2 Sensitivity filtering

In 1997, Sigmund [62] introduced the sensitivity filtering as a technique to base the design updates on the filtered sensitivities instead of the real sensitivities. The filtered sensitivities can be computed based on the non-filtered sensitivities as:

$$\frac{\widetilde{\mathrm{d}\psi}}{\mathrm{d}\rho_e} = \frac{\sum_{i \in N_e} w(\mathbf{x}_i) v_i \frac{\mathrm{d}\psi}{\mathrm{d}\rho_i}}{\rho_e \sum_{i \in N_e} w(\mathbf{x}_i)} \tag{2.108}$$

where $w(\mathbf{x}_i)$ is the weighting function given by Eq. (2.106). Just to clarify, these filtered sensitivities are intended to be the "input" of the optimizer along with the non-filtered densities which are the problem design variables.

2.4 Stress-based topology optimization

Topology optimization problems with stress-based criteria are especially interesting to engineering practice because they guarantee very efficient designs and directly address aspects of material failure. The stresses on a structure can be controlled using stress constraints, i.e., one simply adds constraints to the problem formulation saying that the stresses in the structure must be less than the stress limit, or directly minimizing the maximum stress in the structure. The former is the most used approach to control stresses (see e.g., [63] and [64]), due to its less complicated calculus. The latter aims to get most effective design in terms of stresses, but a min-max problem raises differentiability issues. One way to circumvent these issues is using the so-called "bound formulation" as suggested by [65]. This approach replaces the objective function $\max(\sigma)$ by an artificial design variable $z \in]0, +\infty]$ to be minimized, and consequently adds constraint(s)

in the form of $\sigma < z$. In this formulation, z can be seen as an unknown stress limit that it is intended to be the smallest possible value. Table 2.1 tries to summarize the ideas above presented, where f is a given objective function (e.g., compliance). Note that additional constraints would be required to properly solve a stress-based problem.

Table 2.1: Different stress-based problems formulation.

Stress constrained formulation	Bound formulation	Min-max formulation
$\min f$ s.t. $\sigma \leq \sigma^*$	$\min z$ s.t. $\sigma \leq z$	$\min \max \sigma$

Dealing with stresses is quite challenging, mainly due to: (1) local nature of the stress constraint(s); (2) highly non-linear stress behavior w.r.t. design changes; and (3) design singularity phenomenon [63]. There are many works tackling these issues on the macrostructure (e.g., [66] and [67]), but not so many on the microstructure (e.g., [68]) due to higher complexity. Even more complex to work on is multi-scale topology optimization controlling stresses, which is even quite scarce in the published literature (see e.g., [69]).

In the framework of finite element discretization, to ensure that the stress in each element is less than an admissible limit, the stresses must be controlled pointwisely or locally, i.e., there must be a stress constraint per element in the mesh. This implies that the number of constraints to consider in the optimization problem greatly increases which is dictated by the FE discretization level. To circumvent this problem, many authors have used aggregation techniques to lump the local stress constraints into a single aggregation function. In 1996, Yang and Cheng [70] control the stress level on three different structures by minimizing a linear combination of the compliance and a p-norm of the macroscopic stresses. Thereafter, Duysinx and Sigmund [71] in 1998 proposed to use a single constraint aggregating the local stress constraints taking the singularity problem into account, which in [70] was not considered. This approach has been used by many authors after these two publications, see e.g. [72]. Some authors consider a regional stress control, i.e., the local stress constraints are sorted and aggregated in clusters or groups (see e.g. [73]). Using this latter approach, it is possible to play between the local and global approaches, depending on the number of clusters, where the opposite cases are a number of clusters equal to the number of design variables or to just one, respectively. Despite the less computational effort associated to these strategies, it is not possible to control the peak stress values effectively or accurately.

Typically, the stress field is highly non-linear with design sensitivities strongly dependent on design geometrical details. Boundaries exhibiting strong curvatures (holes) or re-entrant corners

possess high stress concentration factors, thus having high stress gradient values. Therefore, it is expected that errors related to the FE discretization occur. In case stresses are not being computed accurately, reliable optimal designs cannot be expected. To address this issue, a mesh convergence analysis is mandatory.

The singularity phenomenon was first observed in 1968 by Sved and Ginos [74] and, years later, by Kirsch [75]. This phenomenon occurs since optimal points are singular, i.e., they are located in degenerate feasible domain subspaces, which are of a lower dimension than the design space, and thus unreachable by gradient-based optimization algorithms [63]. Degenerate feasible domain subspaces are associated with the fact that there is a finite (non-zero) stress value in the "absence" of material. Stress-constraints relaxation techniques can overcome the singularity phenomenon, such as: (1) ***ε*-relaxation** and (2) ***qp*-approach**.

In 1997, Cheng and Guo [76] presented ***ε*-relaxation** technique to overcome the singularity phenomenon. It consists of introducing a very small parameter ε in the constraints to slightly tolerate a stress constraint violation, i.e., considering a stress constraint in the form $g \leq 0$, this technique modifies it to $g \leq \varepsilon$. This technique modifies the design space, smoothing the constraints, in such way that the optimal value obtained by solving the relaxed problem differs from the one obtained in the original (non-relaxed) problem. Thus, a continuation approach is usually applied to the parameter ε, such that one meets at the end of design iterations the optimal values of the design variables and objective function associated with the original problem. Note that as $\varepsilon \rightarrow 0$, the relaxed problem tends to the original problem.

In 1998, Duysinx and Bendsøe [77] proposed a stress criterion for layered composites (including the optimal rank-2 material, which consist of a layering at two length scales, see the reference for more details) and power-law materials (which use SIMP law to interpolate material properties, see Eq. 2.58). In order to establish a stress criterion for power-law materials at intermediate densities, it is necessary to propose a relationship between stresses, and the stress limit of the given material and the density parameter. This relationship must satisfy the following requirements: (1) the local stresses are a function of the inverse of the density parameter and (2) the local stresses must remain finite and non-zero at zero density. One approach that satisfies all these requirements is to consider that the local stress tensor σ_{ij} is given by:

$$\sigma_{ij} = \frac{\langle \sigma_{ij} \rangle}{\rho^q} = \frac{\rho^p}{\rho^q} E_{ijkl} \langle \varepsilon_{kl}^0 \rangle \tag{2.109}$$

where the exponent q is a number (greater than 1) that must be equal to p (p is the SIMP penalty exponent) to satisfy requirement (2), $\langle \sigma_{ij} \rangle$ is the macroscopic stress tensor and $\langle \varepsilon_{kl}^0 \rangle$ is the

macroscopic strain tensor. Therefore, the stress constraint for the SIMP model using a von Mises criterion for the local stresses can be expressed as:

$$\frac{\langle\sigma\rangle_{\mathrm{eq}}}{\rho^{q}} \leq \sigma_{\mathrm{Y}} \tag{2.110}$$

where $\langle\sigma\rangle_{\mathrm{eq}}$ is the von Mises equivalent stress and σ_{Y} is the stress limit. In [77] the stress constraints were imposed locally, and the singularity phenomenon was overcome using the ε-relaxation technique.

As an alternative to ε-relaxation, Bruggi proposed in 2008 [78] the *qp*-approach to overcome the singularity problem. In [77] it was said that the penalty exponents (p and q) must be equal to assure a physical consistency to the final optimal design all over the density range. However, with such condition one incurs in the singularity phenomenon. In [78] it was shown that the choice $q < p$ gives no discontinuity of local stress at zero density. This choice thus eliminates the arising of the singularity phenomenon, although a single optimization performed with $q < p$ implements a stress constraint that is not physically consistent all over the density range, and the proposed power relaxation must be regarded as a pure mathematical manipulation to solve the problem. The relaxed problem converges to the original problem as $q \to p$. Typically, a continuation approach on q is adopted, where the value of q gradually approaches p. In a nutshell, the *qp*-approach consists in formulate the stress constraint as stated in Eq. (2.110) choosing a value for $q < p$. This method may be likened to an adaptive ε-relaxation, where the magnitude of the stress constraints relaxation depends on the q range.

2.5 Multi-Material Topology Optimization

Performing TO of a structure considering two or more different non-void material phases is called Multi-Material Topology Optimization (MMTO). Considering multiple material phases when designing a structure may lead to better performance than considering just one material phase plus void. Several authors considered MMTO to improve the stiffness of a structure when subjected to volume and/or mass constraints, see e.g. [79-81]. Strength-oriented MMTO considering stress control, by adding constraints or directly minimizing the maximum stress in a structure, has been investigated to a much less extend, see e.g., [82-84]. In recent years, MMTO has increasingly interest due to the advancements of additive manufacturing technologies, see e.g. [85,86]. There are quite a few interpolation schemes to perform MMTO and some of the most relevant used are summarized next.

2.5.1 Multi-material interpolation schemes for topology optimization

Multi-material interpolation schemes are mathematical expressions that allow to obtain the distribution of material in a structure based on two or more base materials. For density-based TO there are essentially two different types of material interpolation schemes: (1) SIMP method extensions and (2) Discrete Material Optimization (DMO). These material interpolation schemes should allow intermediate material choices (i.e., intermediate densities) in the optimization process. However, if a discrete material design is aimed, one should penalize intermediate solutions in such way that at the end a clear distinction between the material phases is obtained. Within the scope of other methodologies for performing topology optimization, such as the Level-set method or Phase-field method, there are also techniques capable of dealing with multiple materials that are not covered here. For the Level-set method, one suggests see [87], where the so-called *"color" level sets* methodology is applied. Regarding the Phase-field method, the following references are suggested [88] and [89], where a MMTO minimizing the compliance is performed.

2.5.1.1 SIMP method extensions

In density-based TO, the SIMP method shown in Eq. (2.58) is the most popular and easiest approach to interpolate between one solid material and void. In 1997, Sigmund and Torquato [90] were the first to extend the classic SIMP method to consider more than one solid material phase. A natural extension to this model able to consider two solid material phases without adding extra design variables is simply given by:

$$E_{ijkl}(\rho_e) = \rho_e^p {E_{ijkl}}^{(1)} + \left(1-\rho_e^p\right){E_{ijkl}}^{(2)}, \qquad p \geq 1 \ \wedge \ \rho_e \in \,]0,1] \tag{2.111}$$

where p is the penalty exponent, ρ_e is the element e artificial density, and ${E_{ijkl}}^{(i)}$ is the stiffness tensor or material properties of material phase i. Note that if void is considered as second material phase, i.e., ${E_{ijkl}}^{(2)} = 0$, Eq. (2.111) becomes the classic SIMP interpolation (Eq. 2.58).

For three-phase materials, Eq. (2.111) can be extended in the following way:

$$\begin{aligned} E_{ijkl}\left(\rho_{e,1},\rho_{e,2}\right) = \rho_{e,1}^{p_1}\left(\rho_{e,2}^{p_2}{E_{ijkl}}^{(1)} + \left(1-\rho_{e,2}^{p_2}\right){E_{ijkl}}^{(2)}\right) \\ + \left(1-\rho_{e,1}^{p_1}\right){E_{ijkl}}^{(3)}, \qquad p \geq 1 \ \wedge \ \rho_{e,1},\rho_{e,2} \in \,]0,1] \end{aligned} \tag{2.112}$$

where two design variables per element are now required, $\rho_{e,1}$ and $\rho_{e,2}$, each of which may have its own penalty exponent, p_1 and p_2. This equation is represented in Fig. 2.7a and it can be written in its discrete form as:

$$E_{ijkl}(\rho_{e,1},\rho_{e,2}) = \begin{cases} {E_{ijkl}}^{(1)} & \text{if } \rho_{e,1}=1 \wedge \rho_{e,2}=1 \\ {E_{ijkl}}^{(2)} & \text{if } \rho_{e,1}=1 \wedge \rho_{e,2}=0, \ \forall\ \rho_{e,1},\rho_{e,2} \in \{0;1\} \\ {E_{ijkl}}^{(3)} & \text{if } \rho_{e,1}=0 \wedge \rho_{e,2}=0 \end{cases} \tag{2.113}$$

In the case void is considered as material phase, i.e., ${E_{ijkl}}^{(3)} = 0$, one can rewritten Eq. (2.113) as:

$$\begin{aligned} E_{ijkl}(\rho_{e,1},\rho_{e,2}) &= \rho_{e,1}^{p_1}\left(\rho_{e,2}^{p_2}{E_{ijkl}}^{(1)} + \left(1-\rho_{e,2}^{p_2}\right){E_{ijkl}}^{(2)}\right), \\ & p \geq 1 \ \wedge\ \rho_{e,1},\rho_{e,2} \in \,]0,1] \end{aligned} \tag{2.114}$$

where the design variable $\rho_{e,1}$ can be seen as a topology variable, since it controls the presence or absence of material. The design variable $\rho_{e,2}$ can then be seen as the material selection variable.

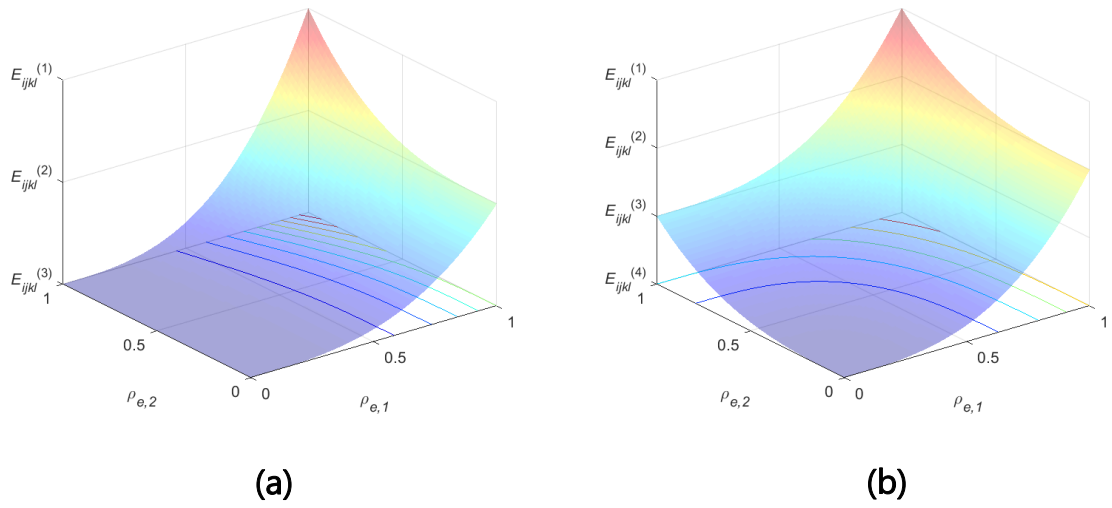

Fig. 2.7: Extended SIMP interpolation schemes plots considering two design variables per element for (a) three-phase materials and (b) four-phase materials.

The three-phase materials interpolation scheme can be further extended to accommodate four material phases without increasing the number of design variables per element:

$$\begin{aligned} E_{ijkl}(\rho_{e,1},\rho_{e,2}) &= \rho_{e,1}^{p_1}\left(\rho_{e,2}^{p_2}{E_{ijkl}}^{(1)} + \left(1-\rho_{e,2}^{p_2}\right){E_{ijkl}}^{(2)}\right) \\ &+ \left(1-\rho_{e,1}^{p_1}\right)\left(\rho_{e,2}^{p_2}{E_{ijkl}}^{(3)} + \left(1-\rho_{e,2}^{p_2}\right){E_{ijkl}}^{(4)}\right), \\ & p \geq 1 \ \wedge\ \rho_{e,1},\rho_{e,2} \in \,]0,1] \end{aligned} \tag{2.115}$$

This equation is represented in Fig. 2.7b and it can be written in its discrete form as:

$$E_{ijkl}(\rho_{e,1},\rho_{e,2}) = \begin{cases} {E_{ijkl}}^{(1)} & \text{if } \rho_{e,1}=1 \wedge \rho_{e,2}=1 \\ {E_{ijkl}}^{(2)} & \text{if } \rho_{e,1}=1 \wedge \rho_{e,2}=0 \\ {E_{ijkl}}^{(3)} & \text{if } \rho_{e,1}=0 \wedge \rho_{e,2}=1 \\ {E_{ijkl}}^{(4)} & \text{if } \rho_{e,1}=0 \wedge \rho_{e,2}=0 \end{cases}, \quad \forall\ \rho_{e,1},\rho_{e,2} \in \{0;1\} \tag{2.116}$$

These four-phase materials interpolation scheme is equivalent to the Shape Function Parametrization (SFP) which is explained in the light of the FEM theory where the shape functions of a quadrilateral first order finite element are used to interpolate material phases (see [91]).

The three-phase materials law shown in Eq. (2.112) can be generalized for *n* material phases as shown in the literature [92]:

$$E_{ijkl}(\rho_{e,1},\rho_{e,2},\dots,\rho_{e,n}) = \sum_{m=1}^{n}\left[\underbrace{\left(1-\left(\rho_{e,m}^{p}-\rho_{e,m}^{p}\delta_{m,n}\right)\right)\left(\prod_{q=1}^{m-1}\left(\rho_{e,q}\right)^{p}\right)}_{w_m}{E_{ijkl}}^{(n-m+1)}\right] \tag{2.117}$$

where w_m can be seen as the weight that the properties of a given material phase *m* has on the final design and $\delta_{m,n}$ is a Kronecker delta, i.e.:

$$\delta_{m,n} = \begin{cases} 1, & m=n \\ 0, & m\neq n \end{cases} \tag{2.118}$$

With such generalization, one requires $(n-1)$ design variables per finite element to interpolate material properties between n materials. The four-phase materials scheme in Eq. (2.115) can be similarly generalized (see [93]) reducing the required design variables per finite element to $\log_2 n$.

In fact, the number of design variables per finite element is an important issue when performing TO since it is directly related with the computational time. Taking this into account, Zuo and Saitou [94] proposed the so-called Ordered SIMP interpolation. This interpolation scheme allows to interpolate among n materials using only one design variable. The material properties are sorted in the ascending order of the normalized density variable, $\hat{\rho}_e^m$:

$$\rho_e^m = \frac{\hat{\rho}_e^m}{\rho_{max}} \quad , \quad m=(1,\dots,n) \tag{2.119}$$

where ρ_{max} is the maximum of the all candidate densities. Using the normalized density in Eq. (2.119), the classical single-material SIMP in Eq. (2.58) is extended to construct the ordered interpolation of the elastic modulus of multiple materials, as shown in Fig. 2.8. Introducing the scaling coefficient A_E and translation coefficient B_E, the extended power function is formulated as:

$$E_{ijkl}(\rho_e) = A_E \rho_e^p + B_E \quad , \quad 0 < \rho_e \leq 1 \tag{2.120}$$

where A_E and B_E for $\rho_e \in \rho_m, \rho_{m+1}$ are given as:

$$A_E = \frac{E_m - E_{m+1}}{\rho_m^p - \rho_{m+1}^p} \tag{2.121}$$

$$B_E = E_m - A_E \rho_m^p \tag{2.122}$$

and E_m and E_{m+1} are the elastic modulus or material properties of ordered material i and $i+1$, respectively. The Ordered SIMP interpolation shown in Eq. (2.120) is continuous, but the first order derivatives w.r.t. ρ_e are discontinuous at the interpolation points. It is well-known that discontinuity of derivatives leads to numerical instabilities in the optimization processes if a gradient-based optimizer is used. Zuo and Saitou [94] acknowledge this issue, but they argue that it is an extremely rare event that design variables hit exactly an interpolation point.

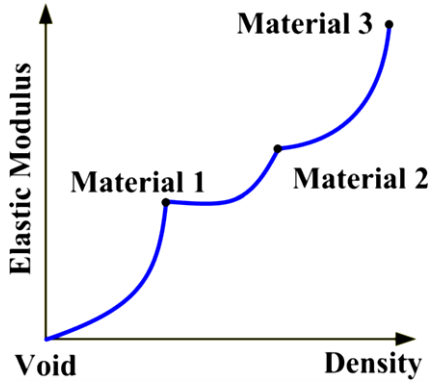

Fig. 2.8: Ordered SIMP interpolation scheme plot. Retrieved from [94].

2.5.1.2 Discrete Material Optimization (DMO)

In 2005, Stegmann and Lund [92] proposed a different approach to interpolate material properties among any distinct number of materials, called Discrete Material Optimization (DMO). Although this methodology is density-based, it differs from SIMP in the way the weight functions of each material phase are assigned. In DMO, the weight functions are uniform, i.e., they are identical, differing only in the design variables that make the selection of each material phase. This method requires n design variables per finite element to interpolate between n different solid materials. The resulting material properties in each finite element (E_{ijkl}) is given by the weighted sum of the different material properties that one wants to interpolate:

$$E_{ijkl} = \sum_{m=1}^{n} w_{e,m} E_{ijkl}^{(m)} = w_{e,1} E_{ijkl}^{(1)} + w_{e,2} E_{ijkl}^{(2)} + \cdots + w_{e,m} E_{ijkl}^{(n)} \tag{2.123}$$

where $w_{e,m} \in]0;1]$ are the weight functions of each material properties, $E_{ijkl}^{(m)}$.

Since 2005, several DMO schemes were proposed, differing only in the weight functions used [92,95]. Here, only DMO 1 is presented, which is the simplest version of DMO and consists of having only one design variable per weight function, i.e.:

$$E_{ijkl} = \sum_{m=1}^{n} \rho_{e,m}^{p} E_{ijkl}^{(m)} = \rho_{e,1}^{p} E_{ijkl}^{(1)} + \rho_{e,2}^{p} E_{ijkl}^{(2)} + \cdots + \rho_{e,m} E_{ijkl}^{(n)} \tag{2.124}$$

where $\rho_{e,m} \in]0;1]$ is the density design variable of element e associated with the properties of the base material m. In Fig. 2.9 is represented the interpolation surface for three material phases (two solid materials plus void), which is given by:

$$E_{ijkl} = \rho_{e,1}^{p} E_{ijkl}^{(1)} + \rho_{e,2}^{p} E_{ijkl}^{(2)} \tag{2.125}$$

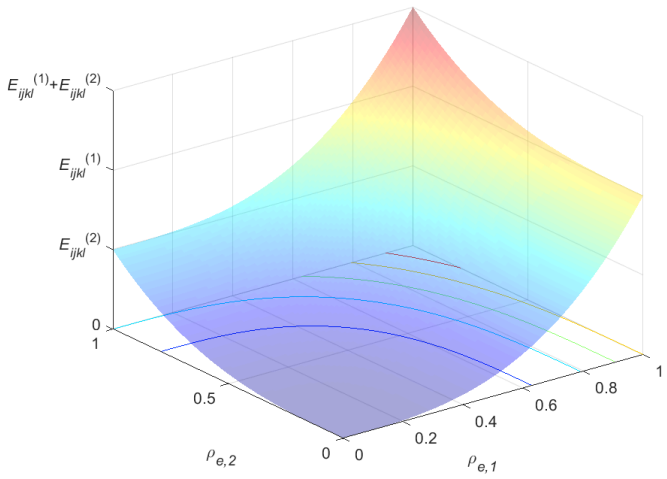

Fig. 2.9: DMO1 interpolation scheme plot considering two solid materials plus void.

Taking a closer look to Eq. (2.125) or Fig. 2.9, it is possible to see that the resulting material properties for $(\rho_{e,1}^{p}, \rho_{e,2}^{p}) = (1,1)$ is $E_{ijkl} = E_{ijkl}^{(1)} + E_{ijkl}^{(2)}$, i.e., the resulting material is the sum of the two materials to interpolate. This cannot happen in multi-material optimization. Later, in 2011, the works [96,97] proposed a linear constraint that prevents the sum of the weight functions (or element densities) from exceeding 1. Besides this, in [97] an additional constraint to prevent intermediate density values is also proposed. Without these later constraints, it would be impossible to obtain a realistic multi-material solution, with clear distinction between material phases.

To conclude, DMO has the advantage of not increasing the complexity of the interpolation law, when the number of material phases increases. However, the number of design variables and constraints highly increases, as it is typically necessary to have several design variables and one extra constraint per finite element to correctly interpolate material properties.

2.5.2 Functionally Graded Material (FGM)

Functionally Graded Materials (FGMs) were introduced in 1980s by a group of materials scientists as a new class of advanced composite materials whose equivalent properties vary gradually along one (or more) direction(s) to obtain modified response to external loadings [98]. The versatility (or freedom) of FGM designs makes them a perfect candidate for topology optimization problems. Topology optimization readily accommodate multi-material design, using interpolation schemes, as seen in the previously chapter. FGMs can be seen as a particular solution of a multi-material topology optimization problem, where the mixture of materials is allowed. In fact, FGMs have been recently explored in the framework of topology optimization.

Perhaps, the first attempt to apply topology optimization to FGM designs was by Xia and Wang in 2008 [99]. They utilized a volume fraction model of material composition and averaged the Hashin-Shtrikman bounds [100] to compute the effective elastic modulus in each finite element, where their objective function was the sum of the mean compliance. In this work, as in others since then (see e.g. [101-103]), the FGM is seen as an extensive smooth variation of material properties on account of varying composition's volume fractions throughout the design domain, while allowing simultaneous lay-out optimization (i.e., where to put holes). In such works, the mixture of two distinct materials prevails extensively over their discrete distribution.

In the literature, one can find ways to obtain the FGM effect slightly different from what was just described above. In [104] the FGM effect is created varying the microstructure with location, where it is observed a continuous transition in space from denser microstructures to highly porous microstructures related to a functional gradation. Another type of FGM aims to achieve smoothly varying interface regions (transition zones) between discrete materials in composites, which is appropriately obtained with the level-set approach in topology optimization, see [105,106].

FGM structures are very appealing for lightweight construction. The classical compliance minimization problem is the most addressed in the literature (see the above-mentioned contributions). However, in many applications it is of central importance to control stress concentrations inside composite structural components. Regions of large stresses (e.g., sharp material interfaces) are most likely the first to exhibit failure during service. Despite this, stress-based optimization, and specially in the context of FGM designs, is poorly covered in the literature (see e.g., [107-

109]). In 2021, Coelho et al. [68] considered the design of FGM-like microstructures using strength criteria and setting $p = 1$ in the classic SIMP interpolation law (see Eq. 2.58). Therefore, intermediate densities were not penalized in the classical way. Instead, to ensure the correctness of material volume calculations, a Heaviside-like function was implemented for volume evaluation. This methodology guarantees that intermediate values of density count to volume as one (i.e., presence of solid material). In each point the isotropic elastic tensor E_{ijkl} is obtained by linearly interpolating between void and base material, depending on the local density value. This is the so-called free-material optimization (see [81]), where the densities can be seen as the thickness of a 2D sheet. Simply put, the material gradation model here is obtained by varying the microstructure's thickness. In reality, this work does not explore the full concept of FGM because the mixture of two homogeneous solids is overlooked.

Actually, to perform TO aiming FGM designs obtained by mixing two homogeneous solid materials, it would be required a multi-material interpolation scheme. More recently, Conde et al. [82] performed MMTO seeking discrete multi-material and FGM microstructures that were optimal in terms of stress distribution. To correctly model FGM microstructures, the authors considered the multi-material SIMP interpolation scheme in Eq. (2.114) with specific values for p_1 and p_2, as it will be explained in Chapter 3.

2.6 Multiscale Topology Optimization

Multi-scale structures are defined using different length scales. The most common case of a multi-scale structure has two length scales, macroscale and microscale, where each point in the macroscale structure effectively represents a periodic repetition of a local microstructure, see Fig. 2.10. Multi-scale structures can be found in nature, e.g., bone and bamboo, and they hold the promise of achieving superior performance while being intrinsically lightweight, robust and multi-functional. Actually, a necessary condition to achieve ultimate stiffness is having a composite material consisted of several length scales [110], so-called rank-N laminates, which are capable of achieving the theoretical upper bounds for maximum strain energy density [111-114].

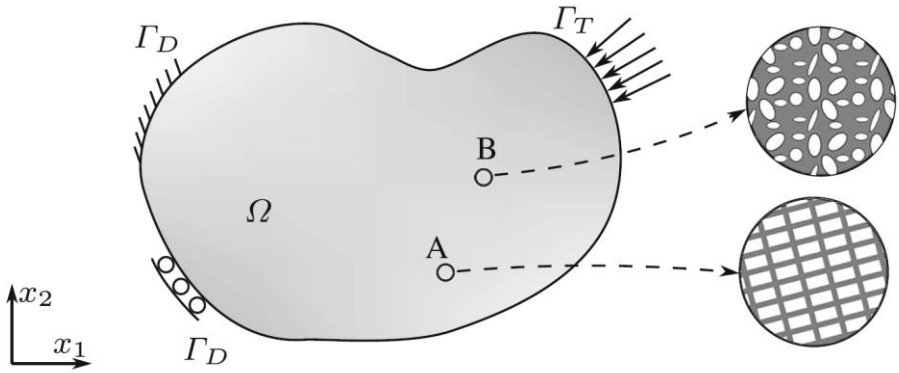

Fig. 2.10: Illustration of a multi-scale structure. Retrieved from [115].

Over the past years, there has been a growing interest in optimal design of multi-scale structures due to the rapid developments in Addictive Manufacturing (AM). AM provides an effective means to fabricate complex mono-scale structures, as well as delicate multi-scale structures, i.e., exhibiting fine geometrical details. Combining AM with TO gives a powerful tool to design these multi-scale structures, that promise superior performance in a general case. Fig. 2.11 illustrates some examples of multi-scale structures designed by TO.

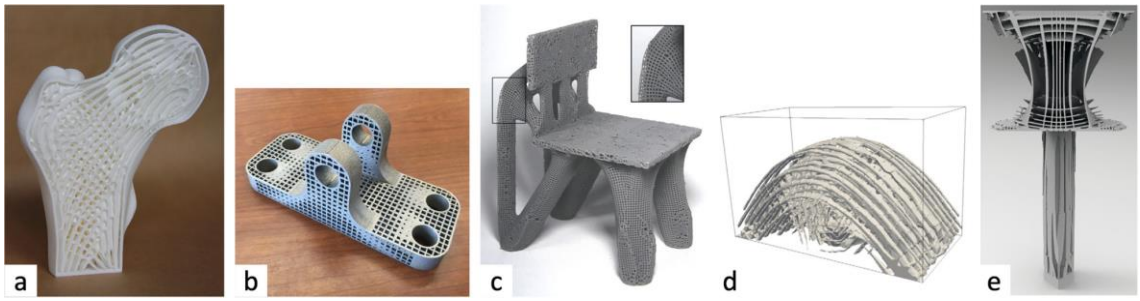

Fig. 2.11: Some examples of 3D multi-scale structures designed by topology optimization. Retrieved from [115].

The term multi-scale has been used extensively in the literature to describe structures and modelling techniques, as well as design approaches. Many design approaches make use of multi-scale modelling, i.e., they assume separation of length scales. However, mono-scale modelling can also be used to design multi-scale structures. The former design approaches are typically referred to as multi-scale approaches. Approaches that do not make this assumption, i.e., mono-scale approaches, optimize distribution of a homogeneous material. When the design domain is discretized by a finite-sized mesh, such mono-scale approaches typically result in mono-scale structures. However, as the discretization of the design domain increases, it can directly be used to achieve multi-scale structures, since theoretical stiffness optimal structures span multiple scales. By employing careful continuation techniques and sufficiently fine meshes, and in the absence of regularization for mesh independence such as control of minimum length, perimeter,

or slope, multi-scale structures should appear naturally. However, the appearance of fine scale structures may also be stimulated by controlling the layout locally. In these approaches, analysis and optimization of structures are performed in the full resolution of the domain (full-scale approaches). For local control approaches, two strategies can be distinguished: (1) pattern repetition and (2) local volume constraints. In the former strategy, the design domain is partitioned into a number of subdomains that are further refined. The layout in each subdomain is enforced to be the same as that in the others, leading to periodic patterns in the full domain. In a variation, the subdomains are grouped, and an identical layout is enforced in subdomains per group, resulting in, for instance, periodic patterns along one axis with gradation along another. The pattern repetition strategy can be applied in full-scale approaches [116] as well as multi-scale approaches. The second strategy to stimulate fine scale structures is to apply local volume constraints [117]. The idea is to impose an upper bound on the fraction of solid elements in the neighbourhood of every point in the full design domain. Fig. 2.12 compares compliance-minimized structures optimized using a conventional mono-scale formulation under a total volume constraint (left), with pattern repetition (middle) and with local volume constraints (right). By analysing the figure, the following conclusions can be drawn: (1) porous structures from local volume constraints exhibit continuous variations in orientation, while periodic patterns have a constant orientation. In this sense, local volume constraints are less restrictive than pattern repetition in constraining the optimization problem; and (2) both pattern repetition and local volume constraints restrict the solution space, and the structure is expected to be less optimal than obtained from a formulation on the same resolution without these constraints. [115]

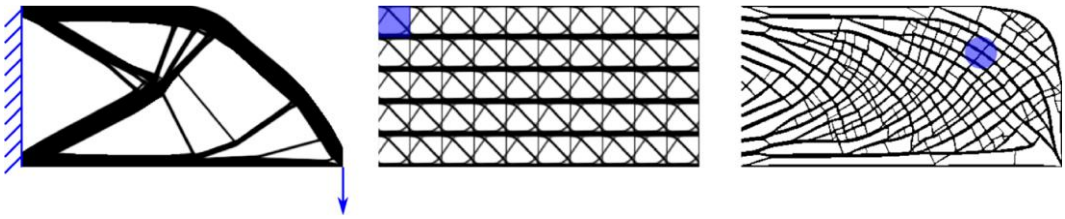

Fig. 2.12: Full-scale optimized structures using the same amount of material.
Retrieved from [115].

As aforementioned, multi-scale structures can also be obtained through multi-scale modelling, existing different approaches to do so. It is now important to accurately define the multi-scale optimization problem. One can rewrite the compliance minimization problem for mono-scale structures in Eq. (2.60) to accommodate the hierarchical optimization of multi-scale structures considering spatially varying microstructures [118]:

$$\max_{\rho_e} \min_{u_j \in U} \left\{ \frac{1}{2} \int_\Omega \max_{E_{mnpq} \in E_{ad}} E_{mnpq}(\rho_e)\, \varepsilon_{mn}(u_j) \varepsilon_{pq}(u_j) \mathrm{d}\Omega - l(u_j) \right\} \tag{2.126a}$$

$$\text{s.t.} \quad \int_\Omega \rho_e \, \mathrm{d}\Omega - V^* \leq 0, \qquad e = 1, \dots, n \tag{2.126b}$$

$$0 < \rho_{\min} \leq \rho_e \leq 1; \qquad e = 1, \dots, n \tag{2.126c}$$

where ρ_e is now the macroscale design variable describing the porosity of the varying microstructures, which is subject to an upper bound on the available material V^*. E_{ijkl} describes the effective stiffness tensor of the microstructures, which must be in the physically admissible set of stiffness tensors E_{ad}. Note that usually, the homogenization method is used to obtain the homogenized stiffness tensor of the microstructures, i.e., $E_{ijkl} \equiv E^H_{ijkl}$.

In [115] the authors classify the different multi-scale topology optimization approaches by (1) the restrictions that are applied to the admissible set of properties E_{ad} that can be achieved by the parameterized microstructure, and (2) the restrictions that are applied to the (macro) density distribution ρ_e.

Regarding the restrictions applied to E_{ad}, one can categorize approaches based on the following restrictions, starting with the least restricted category:

I. Optimal set of elasticity tensors: E_{ad} is represented by a geometry parameterization that allows the local problem to be solved to optimality. This is for elasticity and conduction problems the set of rank-N laminates [119].

II. Unrestricted unit-cell design: E_{ad} contains the set of unit cells that can be obtained using inverse homogenization (i.e., design of the microstructure with desired properties, see [120]), without restrictions on the material distribution, shape, connectivity, or orientation of the unit cell. This means that if a fine enough discretization is used, the microstructures should converge to what is theoretically possible.

III. Restricted unit-cell design: E_{ad} contains the set of unit cells that can be obtained using inverse homogenization with restrictions on material distribution, unit-cell shape, connectivity, or orientation. For example, this can be a square unit cell or a design with predefined solid elements, both resulting in severely restricted design freedom.

IV. Parameterized unit cell with multiple parameters: E_{ad} contains a set of pre-computed parameterized unit cells such that the microstructure is parameterized using more than one parameter. For example, this can be the rectangular hole microstructure by [16], see Fig. 2.13. Due to the rotational freedom, the rectangular hole cell actually performs almost as well as rank-2 microstructures [81], if properly de-homogenized (process of

constructing connected and physically realizable designs from homogenization-based optimization, see [121]).

V. Parameterized unit cell based on density: E_{ad} contains a single constitutive tensor E_{ijkl} or E^H_{ijkl} for a given microstructure density ρ_e. This is the most restrictive case since it does not involve a local optimization problem. Isotropic microstructures satisfying the Hashin-Shtrikman bounds [100] fall in this category since the isotropic elasticity tensor depends only on the density. Likewise, the SIMP approach with a penalty parameter p (see Eq. 2.58) that satisfies the Hashin-Shtrikman bounds [81] falls into this category.

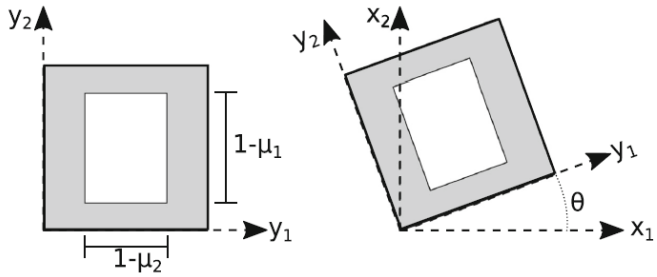

Fig. 2.13: Layout of the unit cell with a rectangular hole, in local (y1, y2), and global (x1, x2) coordinate systems. Retrieved from [115].

As regards the restrictions applied to ρ_e, the different multi-scale topology optimization approaches can be categorized into three different categories:

A. Unrestricted density: There are no restrictions on the density, i.e., $\rho_e \in [0,1]$.

B. Restricted density: Only a few values of ρ_e are allowed. For example, this applies to the SIMP method (possibly combined with a projection method [122] to reduce elements with intermediate densities), and also the Porous Anisotropic Material with Penalization (PAMP) approach (see [123]) falls into this category. This also applies to interface bounded approaches [124-126] with a fixed infill density and a solid outer shell.

C. Fixed density: The density field ρ_e is fixed, i.e., there is no outer optimization problem. This is, for example, a uniform density field or a density distribution based on some prior optimization problem.

Finally, one can identify 5×3 different categories of multiscale topology optimization problems, which are summarized on Table 2.2. It is also provided a fundamental paper for each category.

Table 2.2: Categories of multi-scale topology optimization problems and representative papers according to [115].

	A: Unrestricted density	B: Restricted density	C: Fixed density
I: Optimal set of elasticity tensors	Rank-2 [50]	[128]	[129]
II: Unrestricted unit-cell design	[127]	-	-
III: Restricted unit-cell design	[118]	[123]	[130]
IV: Parametrized unit-cell with multiple parameters	[16]	[125]	[131]
V: Parametrized unit-cell based on density	SIMP [50]	[122]	Finite element analysis

This work aims to perform multi-scale topology optimization using restricted unit-cell design with unrestricted density values, falling into Category III.A of Table 2.2. Hierarchical optimization of structure and material dates back to [118] which was later extended to 3D [132], both using SIMP. The formulation involves one problem at the global (or macro) scale and many problems at the local (or micro) scale. The global problem determines the macroscopic spatial distribution of homogenized material, and local problems determine microscopic spatial distribution of solid and void phases by optimizing for homogenized properties. In each iteration of a hierarchical solution process, following a solved global problem, the local problems become independent from each other. On the positive side, the independent problems can be solved in parallel by sending sets of local problems to different processors [133], gaining a recognized computational speed-up. On the other hand, the independent nature of the local problems creates a critical challenge regarding the compatibility of microstructures across the shared boundary. Note that the problem of concern is related to structural properties beyond the disconnected geometry, and thus one chooses to use compatibility in lieu of connectivity. The compatibility problem arises since disconnections between adjacent microstructures are not captured in the global analysis using homogenized properties (separation of scales). In the literature, there are some approaches for improving connectivity (e.g., [134,135]), where the connectivity is often visually assessed, but a mechanical assessment is unfortunately missing. A compatibility improvement can be obtained by using extended domains that overlap in local optimizations, see [136]. To completely circumvent the compatibility issue, the optimization problem must be reformulated to design structures consisting of repetitive microstructures, at the cost of reduced structural performance (see [130]). When the structural analysis is performed on the full resolution, a poor connectivity is reflected

by a suboptimal objective. Thus, full-scale approaches naturally ensure good connectivity between microstructures or subdomains, at the price of intensive full-scale analyses. Therefore, results from relevant full-scale approaches may serve as a reference for multi-scale approaches. Compatibility is an important topic that has yet to be fully explored. In this work, the compatibility of microstructures is disregarded. This important issue will be addressed in the near future.

In this work, multi-scale topology optimization of multi-material structures aiming improved stiffness is performed in Chapter 4.

2.6.1 Hierarchical problem formulation

Assume a structure in equilibrium defined in the macro domain Ω composed by a periodic heterogeneous material. The material behaviour can then be modelled by means of the homogenization theory through an UC representing the micro domain ¥, i.e., the smallest periodic heterogeneity. Multiscale TO consists then in concurrently optimize the topology of the structure Ω, as well as its microstructure ¥. Therefore, two different but coupled optimization problems must be formulated and solved. One can discretize the macro domain Ω into several subdomains Ω_i that are aimed to be optimized in the microscopic level, see Fig. 2.14. Note that this domain discretization must not be confused with the FEM discretization where the finite elements domain Ω_e may or may not coincide with the subdomains Ω_i, i.e., $\Omega_e \equiv \Omega_i$ or $\Omega_e \subset \Omega_i$.

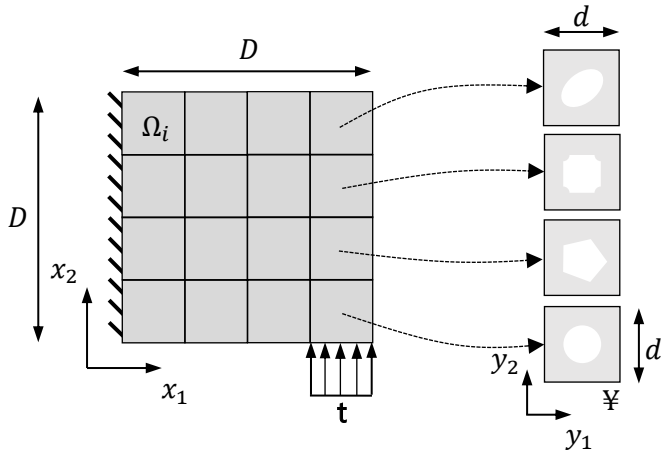

Fig. 2.14: Multiscale material model with the macro domain Ω divided into subdomains Ω_i. Each subdomain has defined a microstructure in the micro domain ¥.

The multi-scale optimization problem in Eq. (2.126) can be rewritten to highlight the hierarchical structure of the problem:

$$\max_{\rho_e} \quad \min_{u_j \in U} \quad \left\{ \frac{1}{2} \int_{\Omega} \phi(\rho_e, u_j)\, \mathrm{d}\Omega - l(u_j) \right\} \tag{2.127a}$$

$$\text{s.t.} \quad \int_{\Omega} \rho_e \, \mathrm{d}\Omega - V^* \leq 0 \tag{2.127b}$$

$$0 < \rho_{\min} \leq \rho_e \leq 1 \tag{2.127c}$$

where the functional $\phi(\rho_e, u_j)$ is given by:

$$\phi(\rho_e, u_j) = \max_{E_{mnpq} \in E_{ad}} \frac{\int_{\Omega_i} E^H_{mnpq} \varepsilon_{mn}(u_j) \varepsilon_{pq}(u_j)\, \mathrm{d}\Omega_i}{|\Omega_i|} \tag{2.128}$$

Thus problem (2.127) is the outer problem that determines the macroscopic spatial distribution of material, while (2.128) is the inner problem that determines the effective properties of the optimal microstructure within the class of allowable set of properties.

Assuming that **u** is the unique solution of the equilibrium equations (minimizer of the total potential energy) found by the FEM (analogously to what was done in the Section 2.3.1, see Eq. 2.61) and, in order to control the lay-out of the microstructures by means of topology design methods (i.e., SIMP method), the hierarchical problem comprised by the problems (2.127) and (2.128) can be rewritten in its final form:

$$\max_{\rho_e} \quad -\frac{1}{2} \int_{\Omega} \phi(\rho_e, u_j)\, \mathrm{d}\Omega \tag{2.129a}$$

$$\text{s.t.} \quad \int_{\Omega} \rho_e \, \mathrm{d}\Omega - V^* \leq 0 \tag{2.129b}$$

$$0 < \rho_{\min} \leq \rho_e \leq 1 \tag{2.129c}$$

where the functional $\phi(\rho_e, u_j)$ is given by:

$$\phi(\rho_e, u_j) = \max_{\mu_k} \frac{\int_{\Omega_i} E^H_{mnpq}(\mu_k) \varepsilon_{mn}(u_j) \varepsilon_{pq}(u_j)\, \mathrm{d}\Omega_i}{|\Omega_i|} \tag{2.130a}$$

$$\text{s.t.} \quad \int_{¥} \mu_k \, \mathrm{d}¥ - \rho_e = 0 \tag{2.130b}$$

$$0 < \mu_{\min} \leq \mu_k \leq 1 \tag{2.130c}$$

The set of equations (2.129) states the TO problem of the macrostructure, while the set of equations (2.130) states the TO problem of the microstructure, where $|\Omega_i|$ is the subdomain volume or area. The macrostructural TO problem is equivalent to the minimum compliance problem, while the microstructural TO problem corresponds to the maximization of the strain energy density. Note that these problems are coupled through the so-called macro densities ρ_e (design variables of the macro problem) as seen in Eq. (2.130b). The macro densities establish the porosity

distribution in the macro domain Ω, taking into account that the maximum allowable material volume V^* cannot be exceeded (see Eq. 2.129b). Therefore, in each point of the macrostructure is associated a material with periodic microstructure defined in the domain ¥ and volume fraction equal to ρ_i (see Eq. 2.130b). The so-called micro densities μ_k define the microstructure topology.

2.6.2 Optimality conditions

To obtain the necessary conditions for the optimal design of the multiscale problem, the Lagrange functions for both macro and micro problems must be defined. The Lagrange function associated with the macro problem (Eq. 2.129) at points where $\boldsymbol{\rho}$ takes intermediate values (i.e., bound or side constraints are inactive) is stated as:

$$\mathcal{L} = -\frac{1}{2}\int_{\Omega} \phi(\boldsymbol{\rho}, \mathbf{u})\, \mathrm{d}\Omega - \Lambda\left(\int_{\Omega} \boldsymbol{\rho}\, \mathrm{d}\Omega - V^*\right) \tag{2.131}$$

where $\Lambda \geq 0$ is the Lagrange multiplier associated with the global resource (inequality) constraint. The stationarity of the Lagrange function $\mathcal{L}$ defined above w.r.t the design variable $\boldsymbol{\rho}$ is given by:

$$\frac{\partial \mathcal{L}}{\partial \boldsymbol{\rho}} = 0 \Leftrightarrow \frac{1}{2}\frac{\partial \phi}{\partial \boldsymbol{\rho}}|\Omega_i| = \Lambda|\Omega_i| \Leftrightarrow \frac{\partial \phi}{\partial \boldsymbol{\rho}} = 2\Lambda \tag{2.132}$$

Remember that the derivatives of the compliance function $C = \frac{1}{2}\int_{\Omega} \phi\, \mathrm{d}\Omega$ are obtained using the adjoint method, where $\partial C/\partial \boldsymbol{\rho} < 0$ (see Chapter 2.3.2). The condition (2.132) imposes that the derivative of the weighted sum of the strain energy densities w.r.t. $\boldsymbol{\rho}$ is constant at all points of the macrostructure. This shall be verified at the optimal solution $\boldsymbol{\rho}^*$.

Regarding the Lagrange function associated with the micro problem (Eq. 2.130) at points where μ_k takes intermediate values, it is defined as:

$$\ell = E^H_{mnpq}\frac{\int_{\Omega_i} \varepsilon_{mn}\varepsilon_{pq}\, \mathrm{d}\Omega_i}{|\Omega_i|} - \lambda\left(\int_{¥} \mu_k\, \mathrm{d}¥ - \rho_e\right) \tag{2.133}$$

where λ is the Lagrange multiplier associated with the local resource constraint (porous material relative density). The stationarity of the Lagrange function ℓ defined above w.r.t the design variable μ_k is given by:

$$\frac{\partial \ell}{\partial \mu_k} = 0 \Leftrightarrow \frac{\partial E^H_{mnpq}}{\partial \mu_k}\frac{\int_{\Omega_i} \varepsilon_{mn}\varepsilon_{pq}\, \mathrm{d}\Omega_i}{|\Omega_i|} = \lambda|¥_k| \tag{2.134}$$

Note that the macro strains $\boldsymbol{\varepsilon}$ do not depend on the micro density field because these are fixed from the macro problem when solving the micro problem.

Since $\phi(\boldsymbol{\rho}, \mathbf{u})$ is the objective function value of the micro problem at the optimum, using the sensitivity theorem it is easy established that (see e.g. [137]):

$$\frac{\partial \phi}{\partial \boldsymbol{\rho}} = \lambda \tag{2.135}$$

and substituting this result into Eq. (2.132) one obtains the following relation, between the macro and micro Lagrange multipliers, that should be satisfied at the optimum:

$$\lambda = 2\Lambda \tag{2.136}$$

3

MULTI-MATERIAL MICROSTRUCTURAL TOPOLOGY OPTIMIZATION

The present chapter addresses multi-material topology optimization of a periodic composite material UC, with properties predicted by homogenization, using strength and/or stiffness design criteria, under bulk and mixed loading cases. Depending on the material interpolation law settings, two design solutions are investigated. On one hand, two solids coexist being bonded together across sharp interfaces, so-called Multi-Material Topology Optimization (MMTO). On the other hand, a FGM is obtained as an extensive smooth variation of material properties on account of varying composition's volume fractions of both solids throughout the design domain, so-called Functionally Graded Material Topology Optimization (FGMTO).

The classical TO problem of minimizing the compliance is revisited here for the multi-material case considering mass and/or material volume constraints. Such approach aims to obtain an increase on stiffness compared to the optimal single-material designs, while maintaining the same mass and/or volume requirements. In many applications, it is of central importance to control stress concentrations inside composite structural components. Regions highly stressed are most likely to fail first during service. So, another performance criterion explored here is the material mechanical strength, where the maximal von Mises stress is intended to be minimized in the UC full domain. This tends to favour Fully Stressed Designs (FSD), meaning that, ideally, every material point of the structure is equally stressed.

The well-known single-material Vigdergauz microstructures [138,139], obtained for plane stress conditions with macroscopic applied stresses of same sign and magnitude (bulk-type load), are equally optimal for both stiffness and strength considering Single-Material Topology

Optimization (SMTO). The Vigdergauz solutions satisfy the Equi-Stress Principle (ESP, see [140]) which means that the hoop stresses σ_t, along the hole free-traction boundary Γ, are constant and with magnitude $\sigma_{t|\Gamma} = \mathrm{tr}\langle\boldsymbol{\sigma}\rangle/V$, where $\boldsymbol{\sigma}$ is the average applied stress tensor and V is the material volume fraction. Therefore, the ESP identifies the optimal hole shape that minimizes both compliance and stress concentration. Although the single-material Vigdergauz microstructures under bulk load, are equally optimal for both stiffness and strength, a stress concentration factor arises at the hole‑free traction boundary. This can be reduced on account of introducing a softer homogeneous layer (ring) around the hole [68,141]. This can be done through bi-material TO. However, the resulting sharp interfaces between the two homogeneous solid phases lead to interfacial mismatch-induced stresses jeopardizing resistance to delamination or fatigue. An improved design solution involves a continuous gradation of material properties in the vicinity of the interface region (transition zone) between discrete materials. This localized FGM design solution can be extended to the full-design domain to completely explore its stress mitigation potential. The fabrication of such advanced composite (FGM) constitutes another challenging work yet to be met by the research community [142].

The contents of this chapter are based upon a peer-reviewed paper already published in journal, see [82]. This chapter is structured as follows. Firstly, the material model used is described in Section 3.1. Afterwards, Section 3.2 focuses on the methodology used to perform MMTO and FGMTO based upon original problem formulations, sensitivity analysis and parallel computing techniques. The results obtained are presented in Section 3.3. Finally, the main conclusions of this part of the work are presented in the Section 3.4.

3.1 Material model

The material model used here considers the in-plane repetition of a UC composed of three different material phases (two solids and void), defined in the square domain ¥ with feature size *d*, representing the smallest periodic heterogeneity of the material domain **Ω** of size *D*, see Fig. 3.1. A plane stress field $\langle\sigma_{ij}\rangle$ is remotely applied to **Ω**. Separation of scales is assumed, i.e., *d* is much smaller than *D*. Periodic displacement-based boundary conditions are applied to ¥.

The behavior of the periodic material is extracted from the UC analysis through asymptotic homogenization [37], as detailed in Section 2.2. The FEM is applied to numerically solve the continuous homogenization equations, i.e.: (1) the equilibrium problem defined in Eq. (2.44) in order to obtain the micro displacements **χ**; (2) the homogenized stiffness tensor $\mathbf{E}^{\mathrm{H}}$ defined in Eq.

(2.49); and (3) the local stress tensor components $\boldsymbol{\sigma}$ defined in Eq. (2.53). The domain ¥ is discretized by a square-grid FE mesh, as illustrated in Fig. 3.1, having the element e area $|\mathrm{Y}_e|$. The von Mises stress σ_e^{VM}, in each Y_e, considers the volume average of the values computed at each Gauss point of the FE, i.e.,

$$\sigma_e^{VM} = \frac{\displaystyle\int_{\mathrm{Y}_e} \sqrt{\frac{1}{2}[(\sigma_{11}^e - \sigma_{22}^e)^2 + (\sigma_{11}^e)^2 + (\sigma_{22}^e)^2] + 3(\sigma_{12}^e)^2}\, \mathrm{dY_e}}{|\mathrm{Y}_e|} \tag{3.1}$$

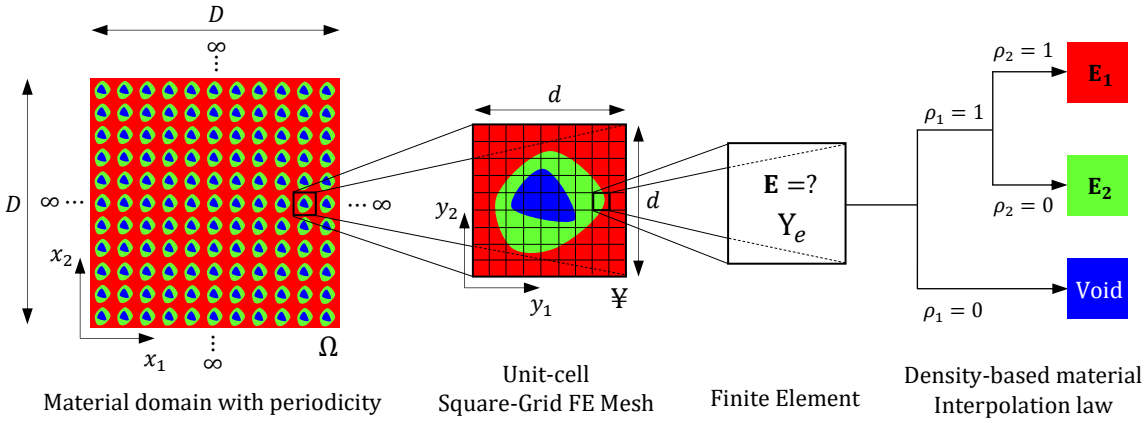

Fig. 3.1: Material model considering a porous composite with periodic multi-material microstructure. Retrieved from [82].

The micro-displacements $\boldsymbol{\chi}$ and the homogenized stiffness tensor $\mathbf{E}^{\mathrm{H}}$ are obtained through the FE implementation named `PREMAT`, and then the postprocessor named `POSTMAT` is used to obtain the micro-stresses $\boldsymbol{\sigma}$ and the von Mises stresses σ_e^{VM}, see [37].

To perform MMTO or FGMTO with up to three phases based on density design variables, a material interpolation scheme is required to interpolate among void (blue), stiffer solid $\mathbf{E}_1$ (red) and weaker solid $\mathbf{E}_2$ (green), as illustrated in Fig. 3.1. Both SIMP (see Section 2.5.1.1) and DMO (see Section 2.5.1.2) interpolation schemes are suitable for this purpose. However, the SIMP is chosen here as its application is straightforward to either MMTO or FGMTO problems. As explained below, SIMP adequately models the rule of mixtures in FGMTO. Therefore, the SIMP-based multi-material interpolation scheme in Eq. (2.114) is used here.

In the case that the objective is to obtain designs presenting two distinct solid phases plus void (typical MMTO), the design variables ρ_1 and ρ_2 should touch their bounds at the end of the design iterations. In this case, depending on the combination of extreme values of ρ_1 and ρ_2, a unique phase is selected, see Fig. 3.1. In this setting, the design variable ρ_1 works as a topological variable

as it identifies presence or absence of solid phase, and the design variable ρ_2 is responsible for material selection.

In case that the objective is to obtain FGM microstructures, p_1 and p_2 in Eq. (2.114) must be carefully chosen to accommodate desired penalization effects and consistency with the physics of solid mixtures. In this setting, intermediate values of the design variable ρ_1 are unfavorable such that void and solid regions can be identified. Additionally, intermediate values of ρ_2, which sets the proportion of each solid phase ($\mathbf{E}_1$ and $\mathbf{E}_2$) in the resulting solid mixture, must be consistent with the bounds provided for the effective elastic moduli of multiphase materials, e.g., the Hashin-Shtrikman (HS) bounds [100]. These are upper and lower bounds for the elastic moduli of composite materials depending on the volume fractions of each constituent materials, and it is assumed that these materials are mixed uniformly with no microstructure. Assuming the 2D case and that both materials are isotropic, as well as their mixture, with the same Poisson's ratio, equal to 1/3, the HS bounds can be expressed as (see also [81,99]):

$$E_{HS}^{-} = \frac{(2+\rho)E_1 + (1-\rho)E_2}{2(1-\rho)E_1 + (1+2\rho)E_2} E_2 \tag{3.2}$$

$$E_{HS}^{+} = \frac{\rho E_1 + (3-\rho)E_2}{(3-2\rho)E_1 + 2\rho E_2} E_1 \tag{3.3}$$

where E_{HS}^{-} and E_{HS}^{+} are respectively the lower and upper HS bounds. The volume fraction of the stiffest constituent material E_1 (Young's Modulus) is given by $\rho \in [0,1]$, while the volume fraction of the softest constituent material E_2 is given by $1-\rho$. The HS bounds are plotted in Fig. 3.2 to check how the interpolation law (Eq. 2.114), function of ρ_2 only (one sets $\rho_1 = 1$), compares with HS bounds. In Fig. 3.2, different values of exponent p_2 are tested to investigate curve fitting.

From Fig. 3.2 is seen that, mixing two different isotropic solids, the resulting elastic properties do not linearly correlate with the volume fraction of each constituent. Therefore, to adequately capture FGM properties, the interpolation scheme predictions must be within the HS bounds for the entire volume fraction range. It is clearly observed that p_2 value must be comprised between 1 and 2. A value of 1.6 seems to render a good enough approximation in the scope of a Power-law based interpolation scheme. In fact, the match is not perfect as seen for some volume fractions. For low and high ρ values the bounds are slightly violated. The proposed value, $p_2 = 1.6$, is kind of a trade-off that avoids violating too much the bounds either for lower or higher ρ values. For an improved fitting, one might use another scheme, e.g., the average of the two HS bounds [99]. In terms of physics that strategy is sound, but it introduces much more mathematical

complexity especially when it comes to sensitivity analysis. As a Power-law mimics just that, without much loss of accuracy, and it is mathematically much simpler, one proceeds with Eq. (2.114) in this work.

To sum up, the material model used here is a twofold one. As explained, it models either a composite material comprised by two discrete solids (conventional composite) or a mixture of two solids (advanced composite, FGM), plus void. Furthermore, the model assumes: linear elasticity; perfectly bonded solid phases; ductile solids such that failure can be predicted by the von Mises stress criterion.

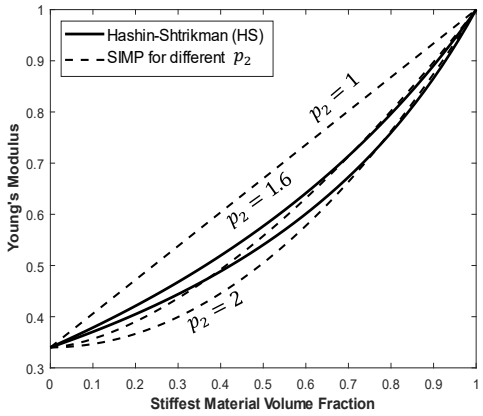

Fig. 3.2: Plot comparing the HS bounds with the SIMP interpolation scheme interpolating two isotropic solids using different values of exponent p_2. Retrieved from [82].

3.2 Topology optimization framework

To perform TO, an algorithm was developed in Fortran language, see Fig. 3.3, as explained next. This algorithm starts by generating an initial design for the periodic microstructure based on the two density design variables, $\boldsymbol{\rho}_{0,1}$ and $\boldsymbol{\rho}_{0,2}$. It is well known that optimal solutions obtained by gradient-based optimizers might not be the global optimum, and highly depend on the starting point. So, it is important to test out different initial designs, see Fig. 3.4. The initial designs should be comprised by intermediate densities with non-uniform distribution across the domain ¥ such that gradient of the elastic properties exists in order to have micro-displacements $\boldsymbol{\chi}$ different from zero. Density-based TO requires the use of filtering techniques, as explained previously in Subchapter 2.3.4. Both the density and sensitivity filter are suitable to solve compliance-based TO problems. However, when dealing with stress-based TO problems, the density filtering is the most appropriate, see Eq. (2.105). Filtered densities $\tilde{\boldsymbol{\rho}}_1$ and $\tilde{\boldsymbol{\rho}}_2$ are the input for the homogenization

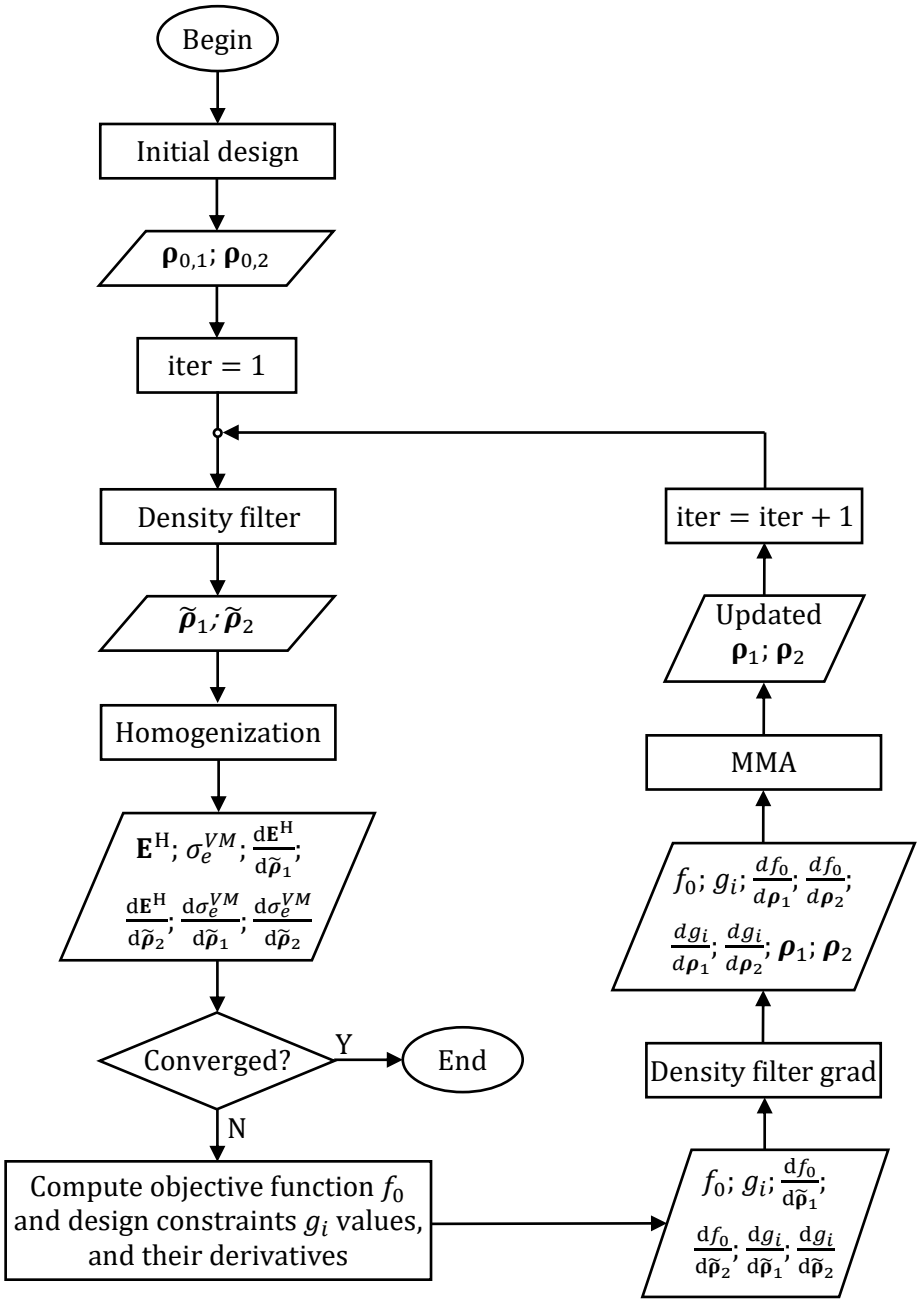

Fig. 3.3: Flowchart of the developed algorithm to perform multi-material TO.

procedure. All the physical quantities computed through homogenization are based on these filtered densities, including their derivatives. After the homogenization is completed, a convergence criterion (e.g., number of iterations) is evaluated. If this convergence criterion is verified, the algorithm stops. Otherwise, it continues iterating. The objective function f_0 and design constraints g_i values, and their derivatives are then computed. Depending on the optimization problem to be solved these functions may differ, see Subchapter 3.2.1. The optimizer (MMA) updates the design variables, i.e., the non-filtered densities. So, sensitivities w.r.t. the non-filtered density design

variables must be computed using the chain rule in Eq. (2.107). This process is called “Density filter grad” in the flowchart. This algorithm keeps running until the convergence criterion is met.

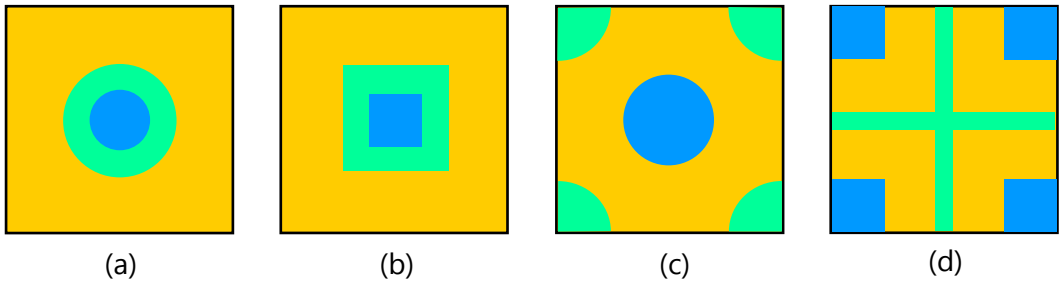

Fig. 3.4: Examples of initial designs: (a) centred circles; (b) centred squares; (c) centred circle plus corners; and (d) cross plus square corners. The colours illustrate intermediate values of density variables, representing a mixture of material phases.

3.2.1 Optimization problems formulation

Two different TO problems are formulated. Firstly, the compliance-based problem (Section 3.2.1.1) is presented in the context of MMTO to be compared to SMTO. The stress-based problem (Section 3.2.1.2) is presented in the context of both MMTO and FGMTO to be compared to SMTO as well.

3.2.1.1 Compliance-based MMTO

Compliance C is minimized subject to (s.t.) mass and/or material volume constraints. In the context of SMTO the mass and volume fraction constraints are equivalent. However, in MMTO, different materials have different mass density ρ^*. Therefore, the compliance-based MMTO problem, with two solids plus void, is formulated as follows:

$$\min_{\boldsymbol{\rho_1},\boldsymbol{\rho_2}} \quad C(\widetilde{\boldsymbol{\rho}}_1,\widetilde{\boldsymbol{\rho}}_2) = \frac{1}{2}\langle\boldsymbol{\sigma}\rangle\mathbf{C}^{\mathbf{H}}\langle\boldsymbol{\sigma}\rangle|\mathrm{Y}| \tag{3.4a}$$

$$\text{s.t.} \quad \frac{m}{m^*} = \frac{\sum_{e=1}^{n^e}[\widetilde{\rho}_{1,e}(\widetilde{\rho}_{2,e}\rho_1^* + (1-\widetilde{\rho}_{2,e})\rho_2^*)|\mathrm{Y_e}|]}{m^*} \leq 1 \tag{3.4b}$$

$$\frac{V}{V^*} = \frac{\sum_{e=1}^{n^e}[\widetilde{\rho}_{1,e}|\mathrm{Y_e}|]}{V^*} \leq 1 \tag{3.4c}$$

where the design variables $\boldsymbol{\rho}_1, \boldsymbol{\rho}_2 \in [\rho_{min}, 1]$; $\langle\boldsymbol{\sigma}\rangle$ is the macroscopic average applied stress tensor; $\mathbf{C}^{\mathbf{H}}$ is the homogenized compliance tensor computed as the inverse of the homogenized stiffness tensor $\mathbf{E}^{\mathrm{H}}$, see Eq. (2.9); $|\mathrm{Y}|$ is the UC area (considered here unitary); m is the effective mass,

which interpolates, at each FE, mass densities ρ^* and void resembling the material properties interpolation (Eq. 2.114) but now considering $p_1 = p_2 = 1$; m^* is an upper bound on m; V is the material volume fraction with an upper bound V^*; and n^e is the total number of elements present in the FE mesh. When solving the MMTO problem (3.4), one seeks the stiffest design for a given mass and/or volume requirement.

3.2.1.2 Stress-based MMTO and FGMTO

In this optimization problem formulation, the minimization of the maximum von Mises stress σ_e^{VM} is sought. However, a min-max problem raises non-differentiability issues. To overcome these issues, the so-called "bound formulation" is used here [65,68]. This means replacing the original min-max stress problem by the problem of minimizing a variable z subject to stress constraints bounded by z, i.e., $\sigma_e^{VM} < z$. The bound z is an additional design variable that replaces the non-differentiable original functional, $\max \sigma_e^{VM}$, and $z \in]0,+\infty[$.

The proposed stress-based MMTO, with two solids plus void, is formulated as:

$$\min_{\boldsymbol{\rho_1},\boldsymbol{\rho_2},z} \quad z \tag{3.5a}$$

$$\text{s.t.} \quad \frac{\sigma_e^{VM}}{z} \leq 1 \quad , \quad e = 1, \dots, n^e \tag{3.5b}$$

$$\frac{C}{C^*} \leq 1 \tag{3.5c}$$

$$\frac{V}{V^*} \leq 1 \tag{3.5d}$$

$$\frac{m}{m^*} \leq 1 \tag{3.5e}$$

$$\frac{\varphi_1 - \zeta_1}{\zeta_1} = \frac{\sum_{e=1}^{n^e}[(1-\tilde{\rho}_{1,e})(\tilde{\rho}_{1,e}-\rho_{min})]-\zeta_1}{\zeta_1} \leq 1 \tag{3.5f}$$

$$\frac{\varphi_2 - \zeta_2}{\zeta_2} = \frac{\sum_{e=1}^{n^e}[(1-\tilde{\rho}_{2,e})(\tilde{\rho}_{2,e}-\rho_{min})]-\zeta_2}{\zeta_2} \leq 1 \tag{3.5g}$$

where the design variables $\boldsymbol{\rho}_1, \boldsymbol{\rho}_2 \in [\rho_{min}, 1]$; C^* is a compliance upper bound; V^* and m^* are limits on volume fraction V and effective mass m, respectively, as defined in Eq. (3.4); φ_1 and φ_2 measure the level of intermediate values (gray) present on filtered density fields $\tilde{\boldsymbol{\rho}}_1$ and $\tilde{\boldsymbol{\rho}}_2$, and $\zeta_1 \in]0, +\infty]$ and $\zeta_2 \in]0, +\infty]$ are their respective upper bounds, to be kept small. The constraints in formulations (3.4) and (3.5) are written in the format to be read by MMA (Fortran version).

The bound C^* in Eq. (3.5c) is used to ensure that the resulting design is stiff enough, i.e., connectivity of the solid phase exists, and the trivial solutions of uniform intermediate density or

structure absence are avoided [143,144]. In the context of MMTO, one expects that the optimal design obtained through Eq. (3.5) presents discrete material phases. To that purpose, the presence of intermediate densities (gray) is penalized through the exponents p_1 and p_2 in Eq. (2.114). However, this may not suffice in strength-oriented design. That is why constraints (3.5f) and (3.5g) are added here. Bear in mind that, the averaging imposed by the density filter (Eq. 2.105), necessarily opens an exception regarding the presence of gray. Gray always appears at the border of each two neighboring phases. In fact, such border looks like a bit blurred as shown later in the results (Section 3.3). Hence, careful choice of parameters ζ_1 and ζ_2 is demanded which, comprehensively, can be problem dependent. To illustrate, for high material volume fractions, ζ_1 and ζ_2 are possibly lower comparing to low material volume fractions. The reason why is that higher material volume fractions may exhibit interfaces between phases with less perimeter and thus less gray appears. Results in Section 3.3 show this trend. Adjusting such parameters may thus require running the optimization problem more than once to get insight. In general, it is good to start not having such ζ bounds too tight. Then they must become gradually smaller by means of a continuation approach such that at the end of the design iterations their values are small enough to evidence shaper interfaces which facilitates design interpretation.

Regarding the stress constraints present in (3.5b), the bound z is both the design variable and the objective to be minimized. Here, there is no interpolation among different material yielding stresses depending on the materials present in the pool for selection. Such formulation goes beyond the scope of the developed work here, but it might be interesting to explore it in the future as it also benefits engineering practice. In the present framework, one seeks instead the optimal spatial distribution of two solids amidst void to reduce the peak stress. No particular stress relaxation, i.e., *qp*-approach [78] or *epson*-relaxation [77], is required when solving the problem using the bound formulation [68]. To sum up, the stress-based MMTO aims here to find multi-material designs, with multiple discrete solid phases, which are optimal in terms of strength, for compliance, volume fraction and/or mass requirements.

The stress-based FGMTO problem formulation is very similar to the MMTO case. FGM designs are achieved here by interpolating the two solids according to Fig. 3.2, as previously explained in Section 3.1. The intermediate density values of $\widetilde{\boldsymbol{\rho}}_2$ have physical meaning now, as they represent different proportions of each solid present in the mixture. Therefore, the constraint (3.5g) is not used. However, the intermediate values of $\widetilde{\boldsymbol{\rho}}_1$ remain penalized, such that solid-void regions can be obtained, i.e., constraint (3.5f) must be kept.

3.2.2 Sensitivity analysis of the optimization problems

Remember that the derivatives of the objective function and constraints w.r.t. non-filtered densities $\boldsymbol{\rho}$ are computed applying the chain rule (Eq. 2.107), which depend on the respective filtered density $\tilde{\boldsymbol{\rho}}$. The required derivatives w.r.t. $\tilde{\boldsymbol{\rho}}$ to solve the problems formulated in Section 3.2.1 are show below. Keep in mind that index $j \in \{1,2\}$ defines the corresponding density field (i.e., $\tilde{\boldsymbol{\rho}}_{\mathbf{1}}$ or $\tilde{\boldsymbol{\rho}}_{\mathbf{2}}$), indexes $i, e \in \{1, \dots, n^e\}$ correspond to the FE index, and index $l \in \{1,2\}$ defines the respective functions ζ_1 and ζ_2. The compliance derivative is,

$$\frac{\mathrm{d}C}{\mathrm{d}\tilde{\boldsymbol{\rho}}} = -\frac{1}{2}\langle\boldsymbol{\sigma}\rangle\mathbf{C}^{\mathrm{H}}\frac{\partial\mathbf{E}^{\mathrm{H}}}{\partial\tilde{\boldsymbol{\rho}}}\mathbf{C}^{\mathrm{H}}\langle\boldsymbol{\sigma}\rangle|\mathrm{Y}| \tag{3.6}$$

The volume derivative is,

$$\frac{\mathrm{d}V}{\mathrm{d}\tilde{\rho}_{j,i}} = \begin{cases} |\mathrm{Y}_i| & \text{if } j = 1 \\ 0 & \text{if } j = 2 \end{cases} \tag{3.7}$$

The mass derivative is,

$$\frac{\mathrm{d}m}{\mathrm{d}\tilde{\rho}_{j,i}} = \begin{cases} \left(\tilde{\rho}_{2,i}\rho_1^* + \left(1-\tilde{\rho}_{2,i}\right)\rho_2^*\right)|\mathrm{Y}_i| & \text{if } j = 1 \\ \tilde{\rho}_{1,i}(\rho_1^* - \rho_2^*)|\mathrm{Y}_i| & \text{if } j = 2 \end{cases} \tag{3.8}$$

The penalization function φ derivative is,

$$\frac{\mathrm{d}\varphi_l}{\mathrm{d}\tilde{\rho}_{j,i}} = \begin{cases} -2\tilde{\rho}_{j,i} + \rho_{min} + 1 & \text{if } j = l \\ 0 & \text{if } j \neq l \end{cases} \tag{3.9}$$

The von Mises stress derivative is,

$$\frac{\mathrm{d}\sigma_e^{VM}}{\mathrm{d}\tilde{\rho}_{j,i}} = \frac{\partial\sigma_e^{VM}}{\partial\tilde{\rho}_{j,i}} + \frac{\partial\sigma_e^{VM}}{\partial\chi_k^{mn}}\frac{\mathrm{d}\chi_k^{mn}}{\mathrm{d}\tilde{\rho}_{j,i}} \tag{3.10}$$

In Eq. (3.6), the derivative of the homogenized stiffness tensor w.r.t. density field $\tilde{\rho}_{j,i}$, can be easily evaluated solving a self-adjoint problem as explained in [17], which gives the following result:

$$\frac{\partial E_{nlkm}^{\mathrm{H}}}{\partial\tilde{\rho}_{j,i}} = \frac{1}{|\mathrm{Y}|}\int_{\mathrm{Y}_i}\frac{\partial E_{pqrs}}{\partial\tilde{\rho}_{j,i}}\left(\delta_{pk}\delta_{qm} - \frac{\partial\chi_p^{km}}{\partial y_q}\right)\left(\delta_{rn}\delta_{sl} - \frac{\partial\chi_r^{nl}}{\partial y_s}\right)\mathrm{dY} \tag{3.11}$$

where the derivatives of E_{pqrs} are simply obtained deriving the SIMP multi-material interpolation scheme (see Eq. 2.114), i.e.:

$$\frac{\partial E_{pqrs}}{\partial \tilde{\rho}_{j,i}} = \begin{cases} p_1 \tilde{\rho}_{1,i}^{(p_1-1)} \left(\tilde{\rho}_{2,i}^{p_2} {E_{pqrs}}^{(1)} + (1 - \tilde{\rho}_{2,i}^{p_2}) {E_{pqrs}}^{(2)} \right) & \text{if } j = 1 \\ \tilde{\rho}_{1,i}^{p_1} p_2 \tilde{\rho}_{2,i}^{(p_2-1)} \left({E_{pqrs}}^{(1)} - {E_{pqrs}}^{(2)} \right) & \text{if } j = 2 \end{cases} \tag{3.12}$$

The total derivatives of the von Mises stresses in Eq. (3.10) depend explicitly and implicitly (through the solution $\boldsymbol{\chi}$ of the homogenization equations) on the design variable $\tilde{\rho}_{j,i}$. To compute these derivatives, the adjoint method is used, review Section 2.3.3.2.

The total derivatives of χ_k^{rs} w.r.t. $\tilde{\rho}_{j,i}$ in Eq. (3.10) are obtained differentiating both sides the equilibrium equations of the local homogenization problem Eq. (2.44) in its FE or discrete form $\mathbf{K}\boldsymbol{\chi} = \mathbf{F}$. Therefore, Eq. (3.10) can be rewritten in the following way:

$$\frac{\mathrm{d}\sigma_{\mathrm{e}}^{\mathrm{VM}}}{\mathrm{d}\widetilde{\boldsymbol{\rho}}} = \frac{\partial \sigma_{\mathrm{e}}^{\mathrm{VM}}}{\partial \widetilde{\boldsymbol{\rho}}} + \boldsymbol{\lambda}^{\mathsf{T}} \left[\frac{\partial \mathbf{F}}{\partial \widetilde{\boldsymbol{\rho}}} - \frac{\partial \mathbf{K}}{\partial \widetilde{\boldsymbol{\rho}}} \boldsymbol{\chi} \right] \tag{3.13}$$

where $\boldsymbol{\lambda}$ is solution of the following adjoint problem:

$$\mathbf{K}\boldsymbol{\lambda} = \left(\frac{\partial \sigma_e^{VM}}{\partial \boldsymbol{\chi}} \right)^{\mathsf{T}} \tag{3.14}$$

The challenge now is to analytically derive the Von-Mises stress function σ_e^{VM} (see Eq. 3.1) w.r.t. the micro-displacements $\boldsymbol{\chi}$. This is given by:

$$\frac{\partial \sigma_e^{VM}}{\partial \boldsymbol{\chi}} = \frac{\displaystyle\int_{Y_e} \frac{(\sigma_{11} - \sigma_{22}) \left(\frac{\partial \sigma_{11}}{\partial \boldsymbol{\chi}} - \frac{\partial \sigma_{22}}{\partial \boldsymbol{\chi}} \right) + \frac{\partial \sigma_{11}}{\partial \boldsymbol{\chi}} \sigma_{11} + \frac{\partial \sigma_{22}}{\partial \boldsymbol{\chi}} \sigma_{22} + 6 \frac{\partial \sigma_{12}}{\partial \boldsymbol{\chi}} \sigma_{12}}{2 \sqrt{\frac{(\sigma_{11} - \sigma_{22})^2}{2} + \frac{{\sigma_{11}}^2}{2} + \frac{{\sigma_{22}}^2}{2} + 3{\sigma_{12}}^2}} \, \mathrm{d}Y_e}{|Y_e|} \tag{3.15}$$

where the local stress tensor components σ_{ij} for a given applied averaged macroscopic stress state $\langle \sigma_{kl} \rangle$ are given by:

$$\sigma_{ij} = E_{ijrs} \left(\delta_{rk} \delta_{sl} - \frac{\partial \chi_r^{kl}}{\partial y_s} \right) C_{klpq}^{\mathrm{H}} \langle \sigma_{pq} \rangle \tag{3.16}$$

where $C_{klpq}^{\mathrm{H}} \langle \sigma_{pq} \rangle$ is the applied average macro strain tensor $\langle \varepsilon_{kl} \rangle$. The local stress components derivatives w.r.t. $\boldsymbol{\chi}$ are computed in the following way:

$$\frac{\partial \sigma_{ij}}{\partial \chi_{r\alpha}^{kl}} = -E_{ijrs} \frac{\partial \phi_\alpha}{\partial y_s} C_{klpq}^{\mathrm{H}} \langle \sigma_{pq} \rangle \tag{3.17}$$

where ϕ_α are shape functions. Remember that in FEM, the nodal displacements are multiplied by shape functions to estimate displacements at any point in the element's domain, i.e., $\chi_r^{kl} = \chi_{r\alpha}^{kl} \phi_\alpha$.

With the developments shown above, it is possible to calculate the implicit part of the Von-Misses stress derivative in Eq. (3.10), remaining only the calculation of the explicit part of the derivative. The Von-Misses stress derivatives w.r.t. $\widetilde{\boldsymbol{\rho}}$ are given as follows:

$$\frac{\partial \sigma_e^{VM}}{\partial \widetilde{\boldsymbol{\rho}}} = \frac{\displaystyle\int_{Y_e} \frac{(\sigma_{11}-\sigma_{22})\left(\frac{\partial \sigma_{11}}{\partial \widetilde{\boldsymbol{\rho}}}-\frac{\partial \sigma_{22}}{\partial \widetilde{\boldsymbol{\rho}}}\right)+\frac{\partial \sigma_{11}}{\partial \widetilde{\boldsymbol{\rho}}}\sigma_{11}+\frac{\partial \sigma_{22}}{\partial \widetilde{\boldsymbol{\rho}}}\sigma_{22}+6\frac{\partial \sigma_{12}}{\partial \widetilde{\boldsymbol{\rho}}}\sigma_{12}}{2\sqrt{\frac{(\sigma_{11}-\sigma_{22})^2}{2}+\frac{{\sigma_{11}}^2}{2}+\frac{{\sigma_{22}}^2}{2}+3{\sigma_{12}}^2}}\,\mathrm{d}Y_e}{|Y_e|} \tag{3.18}$$

where the derivatives w.r.t. $\tilde{\rho}_{j,i}$ of the local stress components of an element e are computed as follows:

$$\begin{aligned}\frac{\partial \sigma_{mn}^e}{\partial \tilde{\rho}_{j,i}} = {} & \frac{\partial E_{mnrs}(\tilde{\rho}_{j,e})}{\partial \tilde{\rho}_{j,i}}\left(\delta_{rk}\delta_{sl}-\frac{\partial \chi_r^{kl}}{\partial y_s}\right)C_{klpq}^{\mathrm{H}}\langle\sigma_{pq}\rangle\delta_{ie} \\ & + E_{mnrs}(\tilde{\rho}_{j,e})\left(\delta_{rk}\delta_{sl}-\frac{\partial \chi_r^{kl}}{\partial y_s}\right)\frac{\partial C_{klpq}^{\mathrm{H}}(\tilde{\rho}_{j,e})}{\partial \tilde{\rho}_{j,i}}\langle\sigma_{pq}\rangle\end{aligned} \tag{3.19}$$

The Kronecker delta δ_{ie} means that the first term of Eq. (3.19) is always zero apart from $i = e$. The homogenized compliance tensor derivatives are given as:

$$\frac{\partial C_{klpq}^{\mathrm{H}}}{\partial \tilde{\rho}_{j,i}} = -C_{kltu}^{\mathrm{H}}\frac{\partial E_{tuhv}^{\mathrm{H}}}{\partial \tilde{\rho}_{j,i}}C_{hvpq}^{\mathrm{H}} \tag{3.20}$$

where the homogenized stiffness tensor derivatives are shown in Eq. (3.11).

3.2.3 Parallel computing

To speed up computations, the developers of computing systems started to think on using several of their existing computing machines in a joint manner. Nowadays, parallel computers are very common. Most of the computers available in the market have a processor (CPU) with several cores that allows the user to perform parallel computing. However, the generation of codes able to use the parallel capabilities of the hardware is not an easy task. Back in April 1958, Stanley Gill [145] started discussing parallel programming and the need for branching and waiting.

There are mainly two different families of parallel machines that can be identified: (1) shared-memory architectures and (2) distributed-memory architectures. The shared-memory machines are built up on a set of processors which have access to a common memory. Usually, the name of SMP machines is used for computers based on this architecture, where SMP stands for Symmetric

Multi-Processing. In contrast, in distributed-memory machines each processor has its own private memory and information is interchanged between the processors through messages. The name of clusters is commonly used for this type of computing devices. Each one of these two families has its advantages and disadvantages, and the actual parallel programming standards try to exploit these advantages by focusing only on one of these architectures.

For shared-memory machines, Open Multi-Processing (OpenMP) is the most suitable approach for parallel programming. OpenMP is an Application Programming Interface (API), and consists of a set of compiler directives, library routines, and environment variables that can be used to specify shared-memory parallelism. In the past, limited support for coarse-grain parallelism has led developers to think that shared-memory parallel programming was inherently limited to fine-grain parallelism. Nowadays, OpenMP addresses the inability of previous shared-memory directive sets to deal with coarse-grain parallelism. Coarse-grain parallelism means that the parallelism in the program is achieved through a decomposition of the target domain into a set of subdomains that is distributed over the different processors of the machine. Fine-grain parallelism means that the parallelism in the program is achieved by distributing the work of the do-loops over the different processors, so that each processor computes part of the iterations or loops [146].

On the contrary, the Message Passing Interface (MPI) [147] is the most suitable approach for parallel programming in distributed-memory machines. MPI is a communication protocol for parallel programming, where data is transferred from one processor/node to another processor/node through “send” and “receive” calls. Both point-to-point and collective communications are supported. MPI and OpenMP can run on a computer cluster simultaneously, such that OpenMP is used for parallelism within a (multi-core) node while MPI is used for parallelism between nodes.

The hardware used in this work is a Workstation HP Z8 G4 (shared-memory machine), 2 CPUs Intel Xeon 6242R 3.1GHz 2933MHz 20C, 256GB RAM. This workstation allows us to use up to 40 physical CPU cores (plus 40 logical cores with hyperthreading). Furthermore, one uses Intel® software for programming, OneAPI Base and HPC Toolkits.

In this part of the work, parallel computing is used to speed up the two main bottlenecks in running the algorithm developed, which are the sensitivity analysis and the optimizer (MMA). To study the impact of parallel computing on the algorithm run, one has to choose a test case. Therefore, the stress-based FGMTO problem for $V^* = 0.90$ is chosen here for that purpose. Nonetheless, the conclusions drawn from this study also apply for all the stress-based problems solved later in Subchapter 3.3. In Fig. 3.5, one shows the percentage of time spent in different program routines in several iterations. It is clearly seen that in the first design iterations sensitivity analysis is alone the bottleneck. After some iterations, the MMA becomes the main bottleneck.

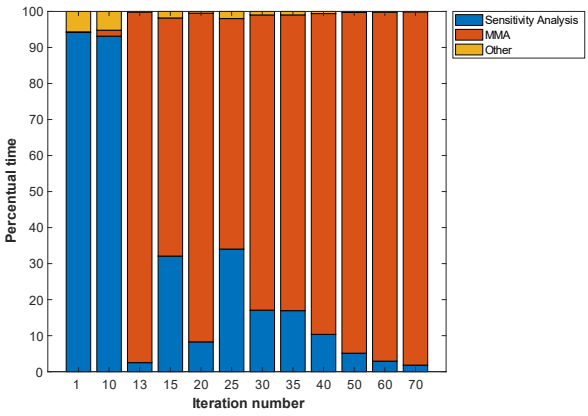

Fig. 3.5: Bottlenecks identification throughout the optimization process for the stress-based FGMTO problem with $V^* = 0.90$. Retrieved from [82].

Regarding the sensitivity analysis, it is usually a time-consuming task. Here, the total number of stress constraints equals the total number of finite elements considered. This means stresses are treated as they are, local, but that also means many problem constraints. Furthermore, each function requires derivatives w.r.t. all density variables. Comparing to SMTO, the number of these variables doubles in the MMTO and FGMTO cases considered here, as two density fields are needed. The derivatives computation involves nested loops. Basically, two main loops. An outer loop through all constraints and an inner loop through all density variables. Notice that the sensitivity evaluation of each stress constraint is independent of another. To speed up the computational time spent here, the code is parallelized resorting to OpenMP directives for Fortran. The parallel implementation considered here splits the outer loop into several parts, each one handled by a different processor.

As regards the optimizer (MMA), due to the large number of stress constraints in the stress-based MMTO and FGMTO problems, an important bottleneck appears in MMA when it fully runs in serial. That may discourage its use. Therefore, an MMA parallel framework is proposed here, with important speedups when many constraints are treated. In [148], the MPI is used to propose a MMA parallel framework dealing well with huge number of design variables. Recall that one considers in this work two design variables per FE, but more variables could be considered in case more phases would be interpolated. As previously discussed, MPI is undoubtedly suitable for distributed-memory computer architectures. In the case of shared-memory architectures, OpenMP is the most suitable protocol for code parallelization since, unlike MPI, no communications through “send” and “receive” calls among processors are required [149]. This is the main reason to propose here an alternative parallel version of MMA to be used in shared-memory architectures and when thousands of constraints are treated. In next paragraph, a detailed

description of the parallelization work done in the original Svanberg's MMA [52] is shown. Please recall some important concepts about MMA explained back in Section 2.3.2.2.

Finding the solution of the dual problem described in Eq. (2.90) requires computing Eq. (2.84) and Eq. (2.85) several times. Therefore, parallel computing can be conveniently applied to these parts of MMA code. Equations (2.84) and (2.85) are programmed in MMA Fortran subroutines `XYZLAM` and `GRADI`, respectively. Each one involves nested loops, being the outer loop parallelized here. In Eq. (2.84) it corresponds to $j = 1, \dots, n$ (number of primal variables) and in Eq. (2.85) corresponds to $i = 1, \dots, m$ (number of dual variables).

An even more important part to be parallelized is the Newton's method itself, as it iterates a lot. The method implies setting and solving repeatedly the system of equations in Eq. (2.91), which can be expensive. The Hessian matrix (Eq. 2.92) construction is carried out in MMA Fortran subroutine `HESSI`, and it can be expensive as it involves nested loops in each iteration of Newton's method. The outer loop corresponds to the index $j = 1, \dots, n$ and the inner loop corresponds to the index $i = 1, \dots, m$. The Hessian dimension is equal to the number β of "free" dual variables, i.e., dual variables λ_i that correspond to $y_i > 0$ in MMA subproblem. Comprehensively, this dimension can change during the iterative process of solving the dual problem. This is an active set constraints strategy which is helpful in case a relatively small number of constraints are active. However, in MMTO and FGMTO one expects a high number of active ones. Hence, for the construction of Hessian matrices with dimension $\beta \geq 100$, parallel computing is used here. It is important to notice that this parallelization is only possible due to the OpenMP directive `!$OMP ATOMIC` that prevents several processors from overwriting/updating the same memory location simultaneously. Finally, to solve the system of equations one takes advantage of LAPACK routines available in Intel® oneAPI Math Kernel Library (oneMKL). These are efficient routines that support parallel computing. Here one uses the driver routine `DPPSV` that solves the system of linear equations, $\mathbf{Ax} = \mathbf{B}$, where $\mathbf{A}$ is a symmetric positive definite packed matrix using Cholesky decomposition. The parallel version of this routine here is only used for system of equations with dimensions $\beta \geq 1000$.

Table 3.1 summarizes the required modifications in the original MMA Fortran source files (and respective subroutines): maxim.f (`HESSI` and `SUBSPA`) and maxsu.f (`XYZLAM`, `GRADI` and `LINDER`). See that the date indicated in Table 3.1 for these sources correspond to the MMA version modified. Before compiling the modified code, enable the compiler to use the OpenMP directives as well as the Intel Math Kernel Library (check the actual Fortran project properties).

Table 3.1: Modifications for MMA parallelization to be inserted at the indicated lines of the original MMA code. Retrieved from [82].

Source	Lines	Modifications	Lines	Modifications
maxim.f (*Oct. 1999*)	95	*add* USE OMP_LIB	265	*add* USE OMP_LIB

	176	*add* NYDIM *as an argument*	302	*add the code below*
				MAXPROC = OMP_get_max_threads()
				IBETA=100
				IF (NYDIM.LE.IBETA) THEN
				NPROC=1
				ELSE
				NPROC=MAXPROC !User specified
				ENDIF
				IF (NPROC.LE.2) THEN

	211	*delete* CALL LDLFAC		
	220	*delete* CALL LDLSOL		

	221	*add the code below*
		MAXPROC = OMP_get_max_threads()
		IBETA=1000
		IF (NYDIM.LE.IBETA) THEN
		NPROC=1
		ELSE
		NPROC=MAXPROC !User specified
		ENDIF
		CALL mkl_set_num_threads(NPROC)
		CALL DPPSV('Lower', NYDIM, 1, HESSF, UU, NYDIM, INFO)
			345	*add the code below*
				ELSE
				!$OMP PARALLEL DO PRIVATE (PJ, QJ, MJ1, PIJ, QIJ, SRPJ, SRQJ, XJ,UJXJ, XJLJ, UJXJ2, XJLJ2, RR, KK, PKJ, QKJ, TTK, IK, TTI), NUM_THREADS(NPROC)
				Repeat lines 303-339 updating statement labels
				!$OMP ATOMIC
				Repeat lines 340-344 updating statement labels
				!$OMP END PARALLEL DO
				ENDIF

	222-224	*delete the lines below* DO 80 I=1,M UU(I)=DSRCH(I) 80 CONTINUE		
	255	*add* NYDIM *as an argument*		
maxsu.f (*Oct. 1999*)	19	*add the code below* NPROC=8 !User-specified !$OMP PARALLEL DO PRIVATE (PJ, QJ, MJ1, PIJ, QIJ, SRPJ, SRQJ, XJ), NUM_THREADS(NPROC)	94	*add the code below* !$OMP END PARALLEL DO
	40	*add the code below* !$OMP END PARALLEL DO	133	*add the code below* NPROC=8 !User-specified !$OMP PARALLEL DO PRIVATE (MJ1, UJXJ, XJLJ, PIJ, QIJ), NUM_THREADS (NPROC)
	82	*add the code below* NPROC=8 !User-specified !$OMP PARALLEL DO PRIVATE (MJ1, UJXJ, XJLJ, PIJ, QIJ), NUM_THREADS (NPROC)	134-	*Replace the original code by:* DO 30 I=1,M IF(IYFREE(I).EQ.0) GOTO 30 DO 40 J=1,N MJ1=M*(J-1) UJXJ=XUPP(J)-X(J) XJLJ=X(J)-XLOW(J) PIJ=P(MJ1+I) QIJ=Q(MJ1+I) UU(I)=UU(I)+PIJ/UJXJ+QIJ/XJLJ 40 CONTINUE 30 CONTINUE
	83-93	*Replace the original code by:* DO 20 I=1,M DO 30 J=1,N MJ1=M*(J-1) UJXJ=XUPP(J)-X(J) XJLJ=X(J)-XLOW(J) PIJ=P(MJ1+I) QIJ=Q(MJ1+I) GRADF(I) = GRADF(I) + PIJ / UJXJ + QIJ / XJLJ 30 CONTINUE 20 CONTINUE	145	*add the code below* !$OMP END PARALLEL DO

Speedup curves for the sensitivity analysis and the Hessian matrix construction (`HESSI` subroutine in MMA) are plotted in Fig. 3.6. Remind that the speedup S_n is defined by:

$$S_n = \frac{T_s}{T_n} \tag{3.21}$$

where T_s is the execution time of the serial algorithm and T_n is the execution time of the parallel algorithm with n cores. The Hessian matrix dimension β considered here to generate the `HESSI` speedup curve shown is fixed, $\beta = 2316$. This curve initially exhibits a plateau since parallelization is skipped for `NPROC`$\leq$2, see Table 8. The reason is that the needed command for parallelization `!$OMP ATOMIC` has a time cost such that only when the number of processors is above 2 it becomes worthy.

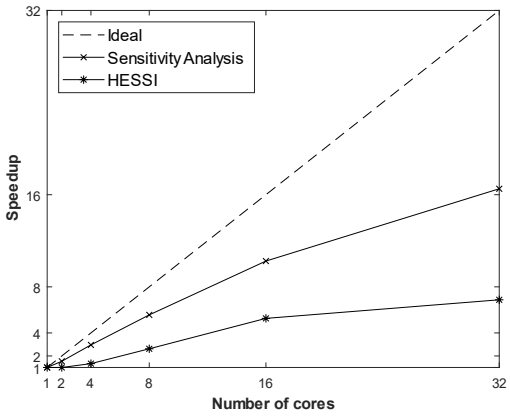

Fig. 3.6: Speed up curves of the sensitivity analysis and Hessian matrix construction for the stress-based FGMTO problem with $V^* = 0.90$. Retrieved from [82].

As previously mentioned, one also parallelizes the MMA subroutines, `GRADI` and `LINDER`, to reduce the computational time even further since these subroutines are called quite often. From experience running the examples of this work, the number of processors used in these subroutines that gives a meaningful speedup is up to 8, the user-specified number indicated in Table 3.1.

The factorization of the Hessian matrix and the solution of the system of equations is now efficiently carried out at once by the oneMKL driver routine, `DPPSV`, instead of the original `LDLFAC` and `LDLSOL` subroutines. For instance, one notices that the original computational time spent in these computations is reduced at least by 99%. The subroutine `DPPSV` is suitable to solve large-scale system of equations and it also supports parallel computing.

In the present framework, the parallelization of the Hessian matrix construction and the replacement of the `LDLFAC` and `LDLSOL` subroutines by the `DPPSV` subroutine are indeed the two main factors which greatly impact on the MMA speedup.

Ultimately, a runtime comparison between serial and parallel codes for the entire design optimization history is shown in Fig. 3.7. The proposed parallel code can reduce 82% of the total optimization runtime compared to the serial run.

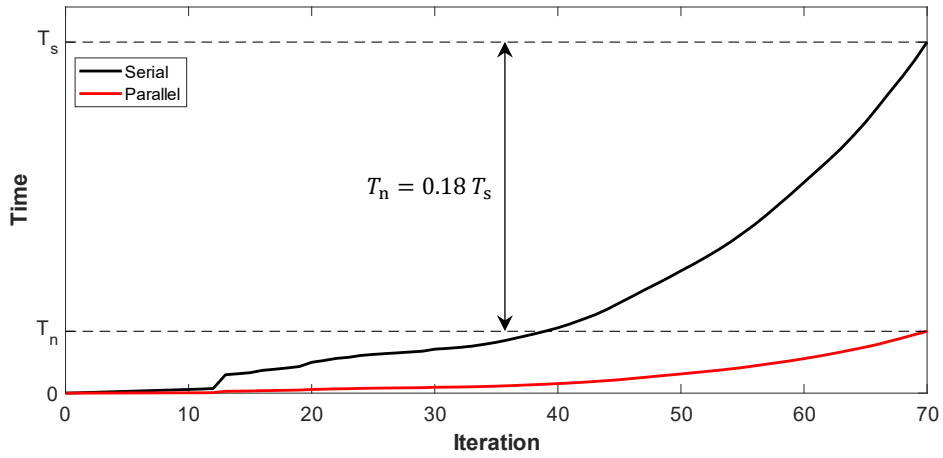

Fig. 3.7: Graph comparing serial and parallel runtimes (cumulative) for the stress-based FGMTO problem with $V^* = 0.90$. Retrieved from [82].

3.3 Results: Microstructural Topology Optimization

This Section presents the obtained results solving the MMTO and FGMTO problems formulated in Section 3.2.1 for three different prescribed macroscopic (average) stress tensors, one bulk-type load (Eq. 3.22) and two mixed loading cases (Eqs. 3.23 and 3.24). The solid material phases (stiff and weak) selected for the examples that follow are presented in Table 3.2. To simplify, the values of ratios E/E_{Steel} and $\rho^*/\rho^*_{\text{Steel}}$ (in bold) are here used as problem data for E [GPa] and ρ^* [kg/m^3], respectively, instead of the absolute values indicated. Interestingly, this normalization also highlights that Young's Modulus ratios and mass densities ratios between engineering alloys are similar, see [150]. A Poisson ratio of 0.3 is assumed for both solids.

$$\langle \boldsymbol{\sigma}_1 \rangle = \begin{bmatrix} -1 & 0 \\ 0 & -1 \end{bmatrix} \quad \text{[MPa]} \tag{3.22}$$

$$\langle \boldsymbol{\sigma}_2 \rangle = \begin{bmatrix} -1 & -0.1 \\ -0.1 & -0.5 \end{bmatrix} \text{[MPa]} \tag{3.23}$$

$$\langle \boldsymbol{\sigma}_3 \rangle = \begin{bmatrix} -1 & 0.1 \\ 0.1 & 0.5 \end{bmatrix} \quad \text{[MPa]} \tag{3.24}$$

Table 3.2: Material properties of Steel (stiff solid) and Aluminium (weak solid). Property ratios highlighted in bold.

Materials	E[GPa]	E/E_{Steel}	ρ^*[Kg/m^3]	$\rho^*/\rho^*_{\text{Steel}}$
Steel	200	**1**	7900	**1**
Aluminium	68	**0.34**	2700	**0.34**

Due to symmetry, only a quarter of the UC needs to be considered in the bulk case which is an advantage in terms of reducing the number of design variables and stress constraints. In contrast, the mixed loading cases require the full UC meshing and thus the computational cost increases considerably because of the same number of stress constraints and finite elements. Typically, in SMTO, an active-set strategy reduces this cost [68,151]. However, in MMTO, stresses tend to be more evenly distributed, especially in the FGMTO case, which means that much more constraints become active. For example, the FGMTO results, as shown later, for the bulk case (with V^* = 0.9) and the last mixed loading case (with V^* = 0.8) have 2315 (out of 2500) and 3552 (out of 4096) active stress constraints, respectively. Hence, the active-set strategy savings can be questioned. Notice also that one needs an enlarged design space (two design variables per finite element) to interpolate between two solid phases plus void. Therefore, one conveniently resorts to parallel computing to reduce the computational cost (see Section 3).

The mesh discretization must balance well between accuracy and runtime. In [63], a 2D mesh convergence analysis in SMTO problems concludes that square-grid meshes between 64x64 and 128x128 are reasonable choices. Therefore, the results here are obtained on the top of 100×100 meshes for the bulk load case and 64×64 meshes for the mixed loading cases. The initial designs either exhibit a centered square or circle of low density surrounded by a higher density region, see Fig. 3.4a) and b).

This Section is outlined as follows. Firstly, one addresses the bulk-type load in Section 3.3.1 performing a compliance-based MMTO (Section 3.3.1.1), a stress-based MMTO (Section 3.3.1.2) and a stress-based FGMTO (Section 3.3.1.3). SMTO results are revisited for comparison purposes. Finally, the two mixed loading cases are addressed in Section 3.3.2 performing a compliance and stress-based SMTO (Section 3.3.2.1), a stress-based MMTO (Section 3.3.2.2) and a stress-based FGMTO (Section 3.3.2.3).

3.3.1 Bulk-type load

Due to symmetry, results can be presented in quarters of the UC domain as shown in Fig. 3.8. The final topology is characterized by the **E** distribution, remember the colour map in Fig. 3.1. In

multi-material designs the individual density fields are plotted next to each other for comprehension. Notice that the density field $\boldsymbol{\rho}_2$ is only meaningful in FEs where $\boldsymbol{\rho}_1 = 1$.

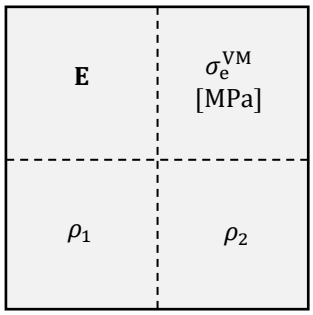

Fig. 3.8: Template chosen to present the multi-material results for the bulk-type load. Retrieved from [82].

3.3.1.1 Compliance-based MMTO

In this section, results of problem (3.4) are shown considering different upper bounds on mass and volume fraction, m^* and V^*, respectively. A continuation approach is applied to p_1 and p_2 in SIMP-based multi-material interpolation law (see Eq. 2.114), i.e., $p_1 = p_2 = 2 \rightarrow 4$ during the first 20 design iterations for all m^* considered, exception made to the $m^* = 0.9$ where such gradual increment takes 40 iterations.

The compliance-based MMTO problem with only a volume constraint always privileges selection of the stiffest materials available, which is trivial and thus skipped here. Here, one imposes a global mass constraint with $m^* \in \{0.6; 0.7; 0.8; 0.9\}$. Fig. 3.9 (top) shows the SMTO results for these mass thresholds when only steel is used. In this case Eqs. (3.4b) and (3.4c) coincide, as $\tilde{\rho}_2 = \rho^* = 1$. The optimal layout change from a square-type into a circle, across different volume fractions, is consistent with the Vigdergauz results [111,112]. These results can be compared to the MMTO results shown in Fig. 3.9 (bottom), obtained for the same mass, i.e., only constraint (3.4b) exists as the total volume fraction is free. The multi-material case mixes the stiff and weak solids to the point of eliminating the original void. This results in a non-porous composite where the stiffer phase embraces the weaker phase. Table 3.3 presents all the compliance values, the steel volume fraction V_{Steel} in MMTO designs, and the percentage δ that shows how less compliant the multi-material design is comparing to SMTO. So, material combinations can outperform here hole openings. In fact, for compliance and mass (or weight) performances, regardless which one is constrained, the other one, as an objective, can be further reduced in the multi-material setting.

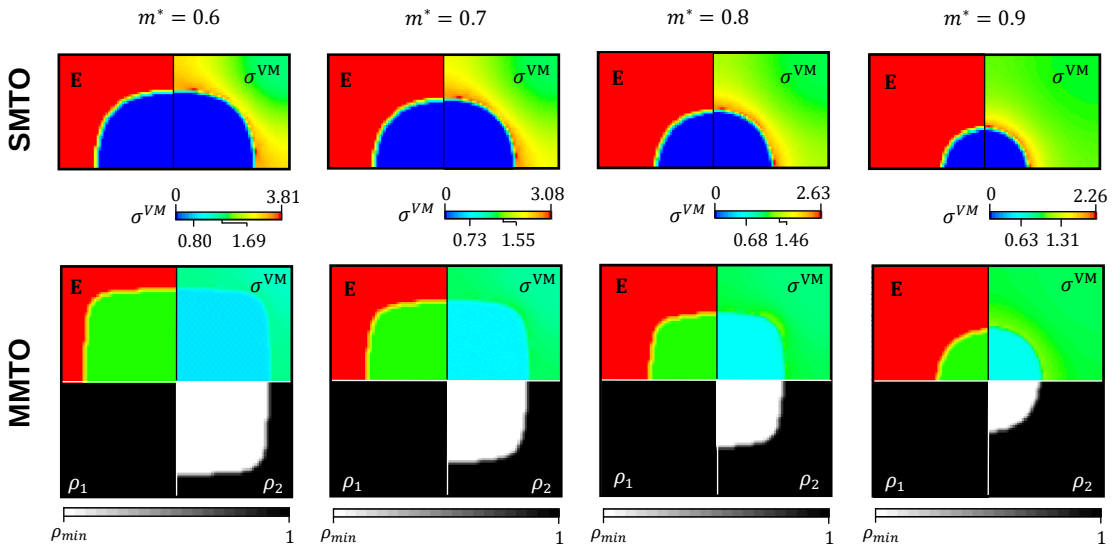

Fig. 3.9: SMTO (top) and MMTO (bottom) results for compliance minimization with different mass thresholds. The lowest and highest stress values in SMTO and MMTO designs are indicated in the colour scale between pictures. Retrieved from [82].

Table 3.3: Compliance values [J] for the SMTO and MMTO results shown in Fig. 3.9.

		m^*			
		0.6	0.7	0.8	0.9
SMTO	C	2133	1619	1239	944
MMTO	V_{Steel}	0.39	0.55	0.70	0.85
	C	1379	1171	995	839
δ [%]		**- 35,3**	**- 27.7**	**- 19.7**	**- 11.1**

Comparing the top and bottom stress plots in Fig. 3.9, see the stress scale in between, one can conclude that MMTO not only lowers compliance but also the von Mises stress (at least in 40%). However, the stress-based formulation is best adequate to find equi-stress holes (ESP) comparing to the compliance-based, as compliance is a quite flat function and rather insensitive to local stress changes [63,68]. This explains some lack of equi-stressness (unevenly distribution of stresses) seen in the stress plot of Fig. 3.9 (top), compare to Fig. 3.11 (top), being the peak stress there higher than the theoretical value (minimum) obtained through $\sigma_{t|\Gamma} = \text{tr}\langle\boldsymbol{\sigma}\rangle/V$.

In practice, certain engineering applications may require a porous composite material. In that case it is of interest solving problem (3.4) with mixed constraints. However, mass and volume upper bounds must be carefully chosen such that room is still found in MMTO to improve the compliance of SMTO. This means that if the SMTO design has mass m^{opt} (e.g., 0.6), which

coincides with volume V^{opt} (e.g., 0.6), the MMTO problem with $m^* = m^{opt}$ must have at least $V^* > V^{opt}$ (e.g., 0.9). For these example values ($m^* = 0.6$ and $V^* = 0.9$), the MMTO compliance is 1558, which is above the prior MMTO result of 1379 but still below the SMTO compliance result of 2133. Fig. 3.10 shows the corresponding layout. It is the stiffer solid that embraces the hole and also notice that the peak stress is still below the SMTO case.

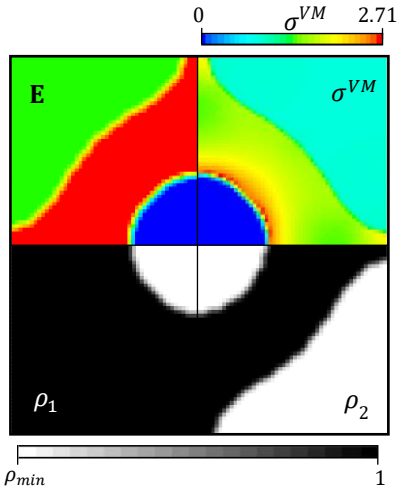

Fig. 3.10: Result for compliance-based MMTO with mass (m^* = 0.60) and volume (V^* = 0.90) constraints. Optimal compliance is 1558J and peak stress is 2.71MPa. Retrieved from [82].

3.3.1.2 Stress-based MMTO

Solving problem (3.5) with mass and compliance constraints, choosing as upper bounds the previous values in Section 3.3.1.1, one obtains the same plots of Fig. 3.9 (bottom) where stress improvements can already be recognized. Therefore, one now optimizes for different volume fraction limits, i.e., $V^* \in \{0.60; 0.70; 0.80; 0.90\}$. This way the original hole area in Fig. 3.9 (top) is not compromised. For each V^*, further stress reduction is possible in MMTO on account of introducing a more compliant second material phase. This means that the original compliance value, from SMTO, is now increased. To that purpose, the constraint (3.5c) is considered with a compliance limit C^* that is 25% higher, compare compliance values in Table 3.4. Although compliance increases, its upper limit still ensures that the optimized solid part of the design domain is connected (the design is stiff enough). Even so, constraint (3.5c) may not suffice to capture well-defined discrete phases, i.e., two solids plus void. Undoubtedly, the exponents p_1 and p_2 in the multi-material SIMP law (Eq. 2.114) play an important penalization role. In MMTO here, these exponents are constant and equal to 4 during the optimization history. However, it can still be difficult to get rid of intermediate densities. In fact, "gray" is in favour of lowering stresses. In order to eliminate such "gray", one penalizes the intermediate values of $\boldsymbol{\rho}_1$ and $\boldsymbol{\rho}_2$ through

constraints (3.5f) and (3.5g), respectively. In these equations, ζ_1 and ζ_2 must be tuned and Table 3.5 presents their final values.

Table 3.4: Compliance [J], mass and stress [MPa] results for the SMTO and MMTO problems. Comparative study.

		V^*			
		0.60	0.70	0.80	0.90
SMTO	C	2133	1619	1239	944
	m	$\equiv V^*$			
	$\sigma_{\max}^{\mathrm{VM}}$	3.40	2.83	2.40	2.04
MMTO	C	2632	2024	1520	1141
	m^*	0.534	0.634	0.734	0.834
	$\sigma_{\max}^{\mathrm{VM}}$	3.08	2.41	2.01	1.48
δ (%)	C	**+ 23.4**	**+ 25**	**+ 22.7**	**+ 20.9**
	m	**- 11**	**- 9.4**	**- 8.3**	**- 7.3**
	$\sigma_{\max}^{\mathrm{VM}}$	**- 9.41**	**- 14.8**	**- 16.3**	**- 27.4**

Table 3.5: Parameters ζ_1 and ζ_2 for each V^* considered in stress-based MMTO.

	V^*			
	0.60	0.70	0.80	0.90
ζ_1	50	57	50	26
ζ_2	105	83	85	53

Interestingly, since $\rho_1^* = 1$, constraints (3.5d) and (3.5e) would coincide in case only solid $\mathbf{E}_1$ exists, i.e., V^* in (3.5d) would be also the total mass of Steel (St). In the MMTO case, the strategy pursued here is selecting a mass threshold m^* in (3.5e) such that $m^* < V^*$, which then enforces the presence of a certain amount of solid $\mathbf{E}_2$, Aluminum (Al). Considering the relationships $V^* = V_{St}^* + V_{Al}^*$, $m^* = \rho_{\mathrm{St}}^* V_{St}^* + \rho_{\mathrm{Al}}^* V_{Al}^*$ and the following data $\rho_{\mathrm{St}}^* = 1$, $\rho_{Al}^* = 0.34$, V_{Al}^*=0.1, after some algebra, one obtains $m^* = V^* - 0.066$ which justifies the m^* values presented in Table 3.4. Therefore, constraint (3.5e) can be interpreted as equivalent to the Aluminium volume fraction constraint with a minimum threshold of 10%, i.e., $V_{Al} \geq 0.1$. The rationale of using the mass constraint,

instead of two volume fraction constraints, is to better highlight the fact that the obtained stress reduction comes also along with mass savings on account of more compliant designs, compared to SMTO, as highlighted in bold at the bottom of Table 3.4.

Ideally in multi-material optimization, numerical issues apart, the algorithm should be able to distribute softer solid $\mathbf{E}_2$ in the UC domain to reduce stresses without having its amount prescribed. This statement is supported in [68] where multi-material shape optimization is carried out. However, in the density-based MMTO case, allowing an extra solid phase, $\mathbf{E}_2$, implies increasing ζ_2 such that more "gray" can be accommodated. Bear in mind that including more phases in design means also more interface perimeter, i.e., it really means more "gray" presence because of density filtering. Therefore, one realizes that unless a minimal amount of phase $\mathbf{E}_2$ be enforced, the algorithm simply finds a blurry transition between void and solid $\mathbf{E}_1$ resembling a FGM, as much as threshold ζ_2 allows. The FGM is really effective in stress mitigation as addressed in the next Section. However, in this Section, one aims discrete phases characterization, MMTO. Therefore, for the sake of a well-defined solid $\mathbf{E}_2$ presence, one proceeds adding the mass constraint as just justified above.

To avoid convergence issues some strategies are followed. A continuation approach that gradually decreases C^*, ζ_1 and ζ_2 values during the first design iterations is applied. The design variable *z* update is prevented from jumping too much by changing the ALBEFA parameter in MMA, i.e., ALBEFA $= 0.995 \rightarrow 0.5$ during the first design iterations.

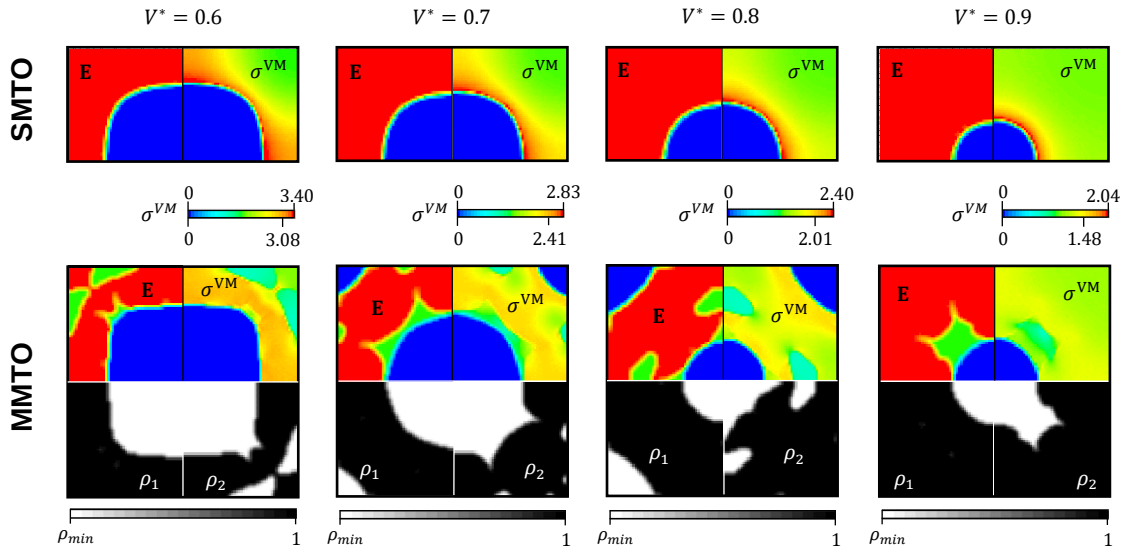

Fig. 3.11: Stress-based SMTO and MMTO results for different material volume fractions. Retrieved from [82].

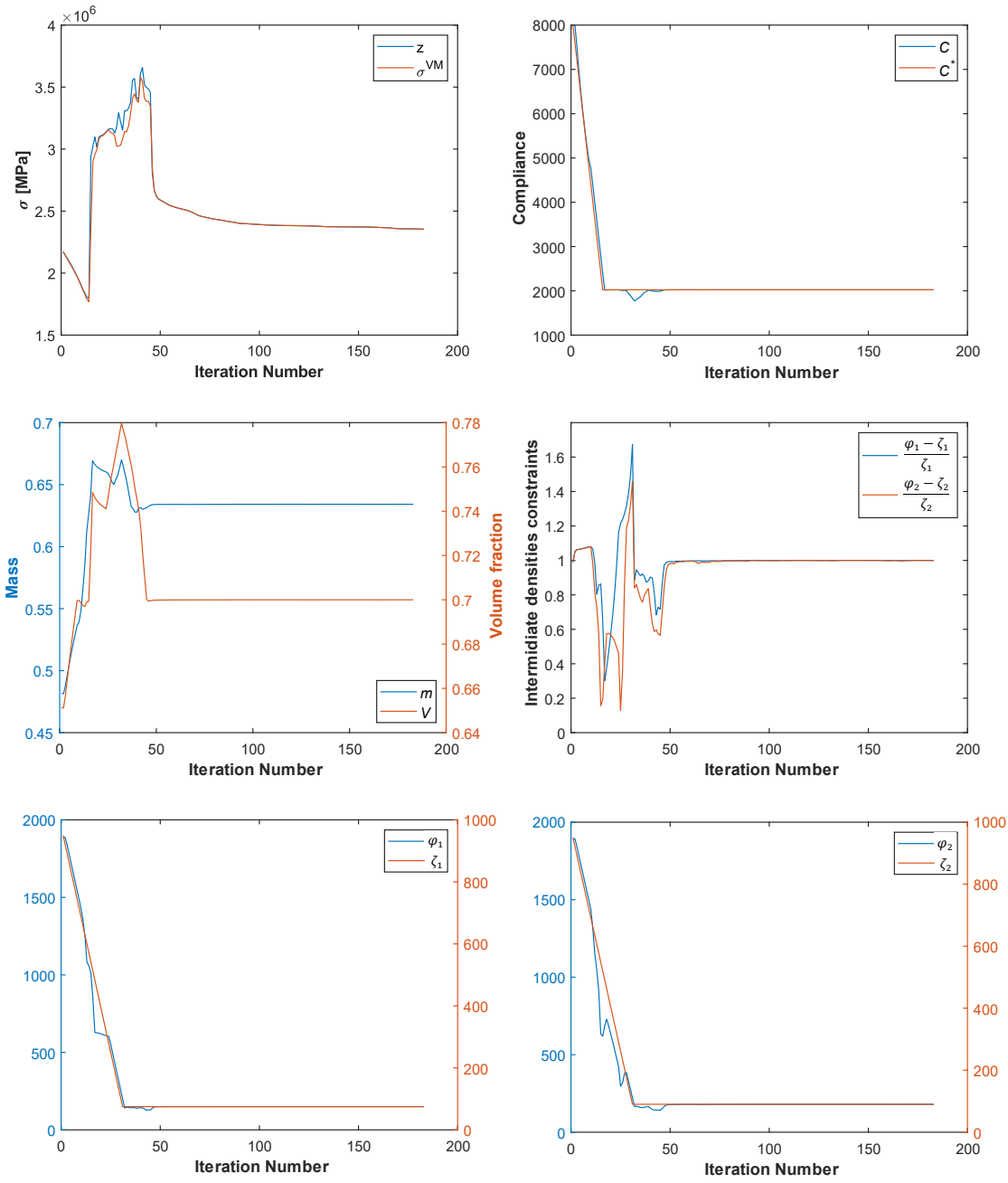

Fig. 3.12: Optimization history of the stress-based MMTO problem for $V^* = 0.70$. Retrieved from [82].

Fig. 3.11 presents the results for MMTO and compares them to the SMTO results. The stress-based SMTO results better capture the ESP, compare to Fig. 3.9 (top). The compliance and the maximum stress values between SMTO and MMTO can be compared in Table 3.4. The percentage δ summarizes how more compliant and lighter MMTO designs are, and how less stressed they are when compared to SMTO ones. Therefore, MMTO designs can be stronger and lighter than SMTO ones although more compliant for the same material volume fraction. Furthermore,

higher material volume fractions have more potential in stress reduction. Finally, one representative case ($V^* = 0.7$) is selected as an example of the optimization history of the objective and constraint functions as well as the continuation approaches used for compliance and ζ values along design iterations, see Fig. 3.12.

3.3.1.3 Stress-based FGMTO

Problem (3.5) here is simplified since constraints (3.5e) and (3.5g) are discarded. As in Section 3.3.1.2 one considers $V^* \in \{0.60; 0.70; 0.80; 0.90\}$ but now the compliance originally obtained in SMTO is worsened till 40%. Remind that the penalization exponents in the multi-material SIMP law (Eq. 2.114) are now constant and equal to $p_1 = 4$ and $p_2 = 1.6$ (as explained in Section 3.1) throughout the optimization history. Intermediate values of $\boldsymbol{\rho}_1$ are penalized through (3.5f) with $\zeta_1 \in \{80; 70; 60; 50\}$ for the respective V^* values. Fig. 3.13 shows the FGMTO results and Table 3.6 summarizes the respective compliances and peak stresses. The percentage δ summarizes how less stressed FGMTO designs are compared to SMTO and MMTO designs. Relevant stress mitigation is attained on account of approaching a fully stressed design, see the stress maps in Fig. 3.13. Every FGMTO result here, in terms of compliance, touches bound C^*. In fact, to reduce stresses, the more compliant the better. Ultimately, the trivial optimal solution would be structure absence.

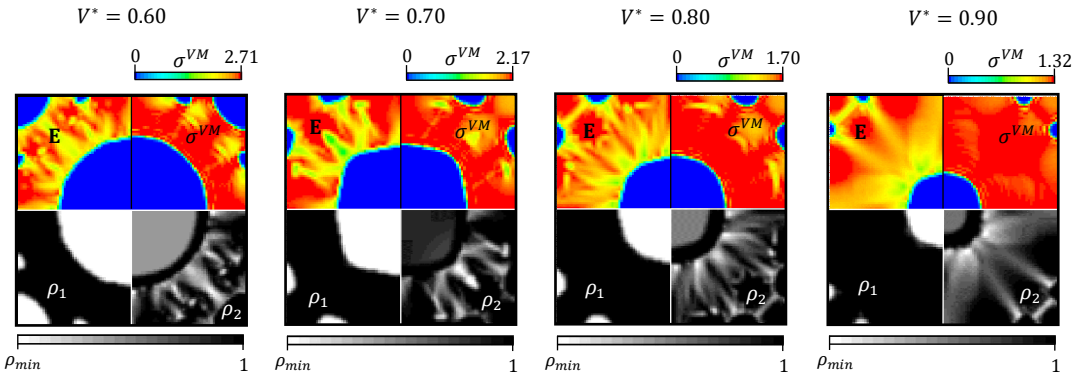

Fig. 3.13: Optimal designs obtained for the stress-based FGMTO problem considering different material volume fractions. Retrieved from [82].

Table 3.6: Compliance [J] and stress [MPa] results for the stress-based FGMTO problem considering different material volume fractions.

		V^*			
		0.60	0.70	0.80	0.90
FGMTO	C	2986	2267	1735	1323
	$\sigma_{\max}^{\mathrm{VM}}$	2.71	2.17	1.70	1.32
δ (%)	SMTO	**- 23.8**	**- 26.4**	**- 32.0**	**- 36.8**
	MMTO	**- 12.0**	**- 10.0**	**- 15.4**	**- 10.8**

3.3.2 Mixed loading cases

Consider now the mixed loading cases in (3.23) and (3.24). For demonstration purposes, the SMTO problems are here solved for a specified volume fraction, $V^* = 0.80$.

3.3.2.1 Compliance and stress-based SMTO

The SMTO results serve as reference in the subsequent Sections for comparative purposes. In fact, benchmarks for the single-material UC subjected to the generalized average stress case are not so common in the literature, unlike the bulk and shear-type load cases. Firstly, one minimizes compliance subjected to constraint on mass (or volume, equivalently). The optimal compliance value found is then defined as the upper bound on compliance to minimize the maximal von Mises stress. The same design is found with both compliance and stress-based formulations, i.e., the stiffest and strongest designs coincide here. Fig. 3.14 shows the optimal layouts, a kind of an inclined ellipse is obtained when different normal stresses of same sign dominate (3.23) and a kind of perforated plate exhibiting distorted rectangular holes is obtained when such remote applied stresses have opposite signs (3.24), shear dominated load. The respective stress plots are provided.

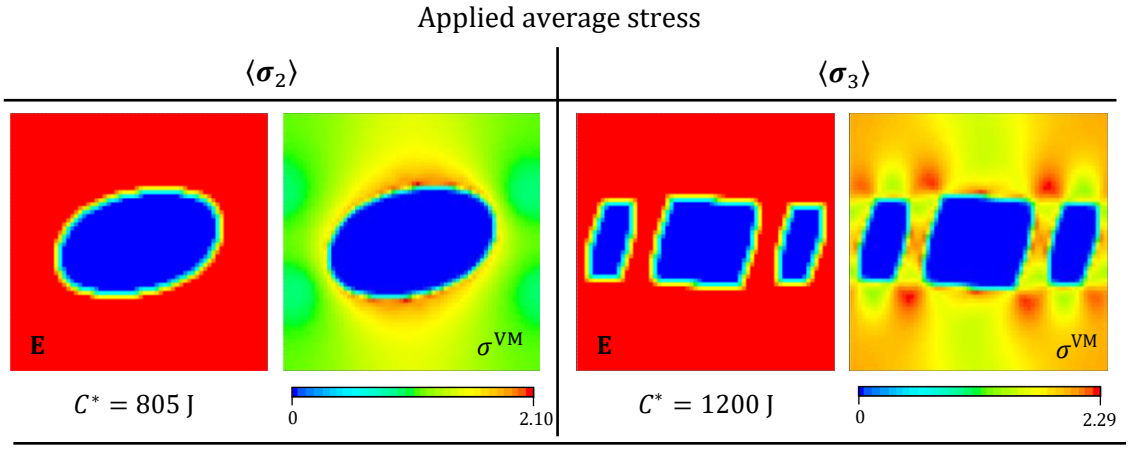

Fig. 3.14: SMTO results for both compliance and stress [MPa] minimization considering two average stress fields and $V^* = 0.80$. Retrieved from [82].

3.3.2.2 Stress-based MMTO

The approach here is similar to Section 3.3.1.2. One selects the case $V^* = 0.80$ with $m^* = 0.734$, which enforces presence of solid $\mathbf{E}_2$ (at least 10%), and compliance is worsened in approximately 25% comparing to the SMTO counterpart. The values of ζ_1 and ζ_2 for both load cases are presented in Table 3.7. Fig. 3.15 shows the layouts obtained which resemble those in Fig. 3.14 apart from the emerging small areas of solid $\mathbf{E}_2$. We realize that the softer phase around the hole now can lower the initial peak stress located at the hole border, on account of increasing the stresses located in inner subregions such that new stress peaks appear of lower magnitude. Table 3.7 also compares the compliance and peak stress between the SMTO and MMTO designs. The percentage δ shows a relevant peak stress decrease for the load $\langle \boldsymbol{\sigma}_2 \rangle$, 21.9%, but not that much for $\langle \boldsymbol{\sigma}_3 \rangle$, only 6.6%. This is consistent with the prior observations in [68], i.e., the multi-material potential for stress reduction is seen more on the side of bulk-type loads rather than shear dominated loads.

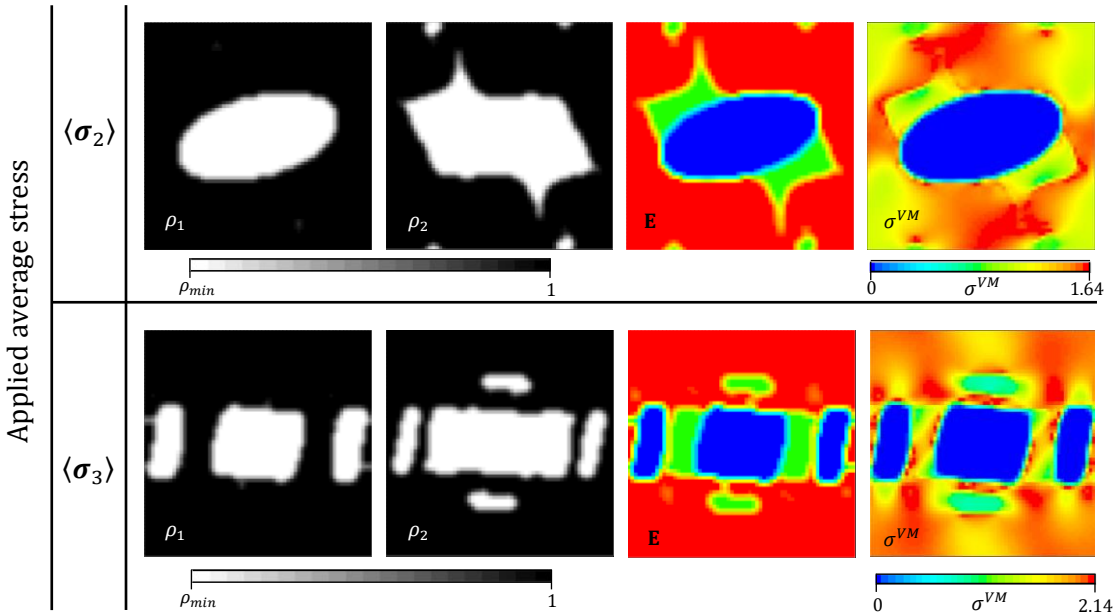

Fig. 3.15: Stress-based MMTO results considering two average stress fields, $V^* = 0.80$ and $m^* = 0.734$. Retrieved from [82].

Table 3.7: Results of compliance and peak stress for stress-based MMTO compared to SMTO. Values of parameters ζ_1 and ζ_2 used in MMTO.

		Applied average stress	
		$\langle\sigma_2\rangle$	$\langle\sigma_3\rangle$
SMTO	C	805	1200
	$\sigma_{\max}^{VM}$	2.10	2.29
MMTO	C	990	1521
	$\sigma_{\max}^{VM}$	1.64	2.14
	ζ_1	23	41
	ζ_2	40	54
δ_σ (%)		**- 21.9**	**- 6.6**

3.3.2.3 Stress-based FGMTO

The approach here is similar to Section 3.3.1.3, the compliance is worsened in approximately 40% comparing to the SMTO counterpart. Fig. 3.16 shows the layouts obtained which now differ

more from Figs. 3.14 and 3.15, as more design freedom is allowed. Table 3.8 summarizes the compliance and peak stress obtained with FGMTO in both load cases, and values of ζ_1 are also provided. The percentage δ shows a relevant peak stress decrease for load $\langle \boldsymbol{\sigma}_2 \rangle$ when compared to the SMTO case. Stress improvements are much lower, and similar for both loads, when results are compared to MMTO. Yet, FGM overall results clearly show, in both load types, an interesting stress mitigation effect as one approaches a fully stressed design (see the stress plots in Fig. 3.16), though a less remarkable stress decrease is again seen in shear dominated loads.

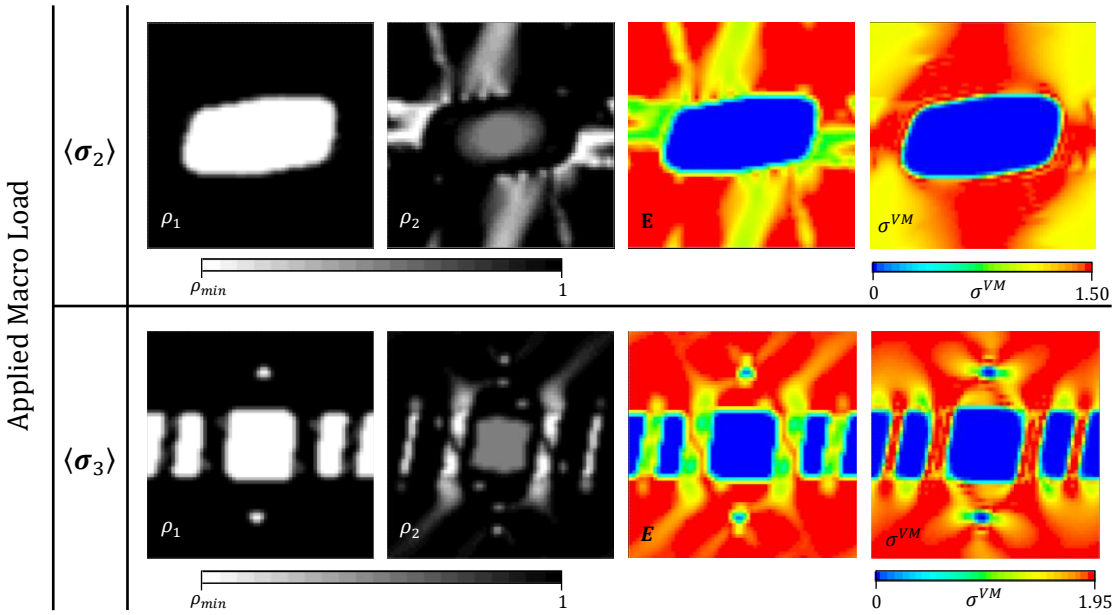

Fig. 3.16: Stress-based FGMTO results considering two average stress fields, $V^* = 0.80$. Retrieved from [82].

Table 3.8: Results of compliance and peak stress values for stress-based FGMTO compared to SMTO and MMTO. The values of parameter ζ_1 used in FGMTO.

		Applied Macro Load	
		$\langle \sigma_2 \rangle$	$\langle \sigma_3 \rangle$
FGMTO	C	1127	1704
	$\sigma_{\max}^{\mathrm{VM}}$	1.50	1.95
	ζ_1	25	54
δ_σ (%)	SMTO	**- 28.6**	**- 14.9**
	MMTO	**- 8.5**	**- 8.9**

3.4 Conclusions: Microstructural Topology Optimization

Topology optimization with stress constraints is currently a quite active research topic as it brings to the conceptual design stage an important design criterion in engineering practice that is the admissible stress. The anticipation of stress influence at earlier design stages helps attaining more efficient feasible designs at the end stage of product development. Acknowledging that, this part of the work is a contribution to the state-of-the-art in strength-oriented microstructural TO. The minimization of maximal von Mises stress, not well covered in the literature, is explored and extended to the multi-material setting (MMTO) to find the benefits in stress mitigation considering different types of loads, which is the main contribution here.

Two different MMTO formulations are addressed, compliance and stress-based. Firstly, the compliance-based MMTO problem is solved for a bulk-type load to find a stiffer design comparing to SMTO for the same mass requirement. Solving such problem, one shows that multi-material designs can outperform single material ones regarding stiffness, and it also impacts favourably on stress distributions. That is observed in connection with an increase in the total material volume fraction. Therefore, in applications where porosity is not mandatory, material combinations can outperform hole openings. Secondly, the stress-based problem is explored in two different ways. On one hand, one optimizes the distribution of three discrete phases, two solids plus void, which results in a conventional composite material. On the other hand, one optimizes the variation (gradation) of material properties across the UC continuous domain on account of two solids mixture amidst void, which results in an advanced composite known as FGM. The stress-based MMTO for the bulk load, renders stronger and lighter designs than SMTO while keeping the same total material volume fraction and letting the compliance be worsened. This happens on account of allowing the selection of an extra more compliant solid phase. Eventually, for no upper limit on compliance, the best for stress minimization would mean either uniform distribution of density (likely an intermediate value to comply with the volume requirement), in case no void (or hole) is enforced, or structure absence, in case porosity is enforced on design. These trivial solutions are thus skipped here as one always limit compliance enough. Also notice that under the same mass and compliance requirements, the stress-based MMTO just replicate the compliance-based MMTO optimal designs. Furthermore, fully stressed designs are here well approximated through FGMTO, which results in quite low stress levels. The corresponding designs reveal ideal solid mixtures in the continuum setting for a specific total material volume fraction. The

compliance upper bound used in FGMTO is further increased, comparing to MMTO, such that enough freedom is given to the gradation of properties resulting in greater stress mitigation benefits.

The study is also extended here to other average stress fields to gain insight on how multi-material plays an important role in stress mitigation as one moves farther away from the well-studied bulk-type load. Two fields are considered, one more bulk dominated and another more shear dominated. The multi-material design advantage in lowering stresses is recognized in both cases but, as one moves toward loads where shear dominates, lesser benefits can be found. This observation gives valuable insight on the multiscale problem where material and structure are concurrently optimized. In that more complex framework, a variety of stress fields exist, spanning loads from bulk to shear type, which, as envisaged here, will impact differently in material combinations for stress mitigation. Since multiscale TO is nowadays quite a hot research topic [115], it is an interesting research avenue bringing stress control into such problem (see e.g., [69,152]), where in Chapter 4 an exploratory work is made to reach this end, thus advancing previous works [1,118,132]. The connectivity issue of microstructures in the multiscale problem would be also an interesting aspect to consider (see e.g., [153]).

Finally, another relevant contribution of the present work is the parallelization of two important bottlenecks, i.e., the sensitivity analysis and the MMA optimizer. As regards the first one, important speedups are attained as shown in Fig. 3.6. As regards MMA, an existing MPI-based parallel framework from [148] is quite relevant to attain important speedups when dealing with huge number of design variables. However, the greatest concern in this part of the work is having MMA dealing well with thousands of constraints. That is why the original MMA Fortran code [52] was revisited here, where the focus is on the dual problem parallelization resorting to intel® oneAPI Math Kernel Library as well as explicit OpenMP instructions. This is detailed in Section 3.2.3 hoping that the optimization community can easily take advantage of a few extra lines of code in original MMA to speedup computations when, in general, many problem constraints need to be considered.

The density-based MMTO methodology proposed here has its own pros and cons. Whereas it offers a well-known design freedom to efficiently capture disruptive optimal layouts, it lacks on rendering well-defined solid boundary contours. Density filtering blurs discrete phase transitions (interfaces are “gray”) which raises some issues that are in the present work properly handled to accommodate discrete phase selection. However, it would be interesting to see other TO methods being applied to the same problem (e.g., the Level-set method [18]), which possibly could better handle this kind of multi-phase modelling issues.

4

MULTI-SCALE OPTIMIZATION OF MULTI-MATERIAL STRUCTURES

Multi-scale Topology Optimization (TO) of multi-material structures is covered in this chapter. This part of the work is structured as follows. The multi-scale material model is detailed in Section 4.1. The hierarchical optimization problem formulated back in Section 2.6.1 (see Eqs. 2.129 and 2.130) is revisited here and reformulated to solve the minimum compliance problem considering a mass constraint (instead of volume) and multi-material setting. This is done in Section 4.2. Actually, the hierarchical optimization problem can be solved using different algorithmic strategies [1]. In Section 4.3, a brief discussion about the two different algorithmic strategies is presented. A comparison between these two strategies is also carried out by solving the compliance minimization hierarchical problem in a single material setting, see Section 4.5.1. This also serves to validate the hierarchical model developed. The details about the computational implementation of the hierarchical algorithm are given in Section 4.4. The obtained results are shown in Section 4.5 and the main conclusions of this part of the work are in Section 4.6.

4.1 Hierarchical material model

The material model used here is two dimensional and comprises two scales: the structure domain Ω (macro or global scale) and the material domain ¥ (micro or local scale) from which the structure is manufactured. At the microscale it is assumed a cellular/composite material with local periodicity. Since there exists separation of length scales, i.e., the periodic microstructure has a

characteristic dimension much smaller than the characteristic dimension of the structure, the homogenization method can be conveniently applied (see Section 2.2). By applying the homogenization method, it is possible to treat a heterogeneous medium as an equivalent homogeneous one, i.e., with equivalent or homogenized mechanical properties. At the macroscale level, the goal is to find an optimal structure layout, defined by the macro design variable $\boldsymbol{\rho}^*$. Whereas at the microscale level the aim is to find the optimal design for the representative unit cell defined by the micro design variables $\boldsymbol{\mu}_1$ and $\boldsymbol{\mu}_2$. Details about the formulation of the hierarchical optimization are given next in Section 4.2.

The macrostructure considered here is the classical example of a cantilever beam, where on one side all degrees of freedom (DOFs) are constrained and on the opposite side the load is applied in a distributed fashion, see Fig. 4.1. The FEM is used to solve the macrostructural equilibrium problem. The FEM used in this work is the version in Fortran proposed by Kikuchi (FEM2D, [154]), but could be alternatively used any FEM software (e.g., ANSYS). Based on a structure design domain discretized using a conforming finite element mesh, the natural way to perform the hierarchical optimization is to associate each finite element with a cellular material design, thus aiming at a (global) pointwise or element-by-element definition of optimal material. This design model parametrization leads to a very high number of local problems required for the material microstructure characterization across the whole structural domain, demanding parallel computing to speedup computations. Alternatively, the structure domain Ω can be divided into a number of larger design subdomains Ω_i where the material microstructure remains uniform, i.e., the design variables are constant within each Ω_i level. Although more constrained, this parameterization helps to maintain the material continuity in the structure, reduces the number of design variables and the spatial variation of properties and thus facilitates manufacturing [155]. These two different design model parametrizations are carried out in this part of the work. On one hand, each subdomain Ω_i coincide with the FE domain Ω_e, i.e., $\Omega_e \equiv \Omega_i$. On the other hand, each subdomain consists of symmetric layers distributed in the x_2 direction, containing several finite elements, i.e., $\Omega_e \subset \Omega_i$. In the present work, the layers coincide with a row of finite elements, but they do not necessarily have to coincide.

To each design subdomain corresponds a periodic medium with microstructure, whose material properties are homogenized [37], defined by a single unit cell. The microstructure is assumed to be composed of three different materials phases (void and two different base materials). Therefore, the microstructure design is done using the multi-material interpolation SIMP law presented in Section 2.5.1.1 in Eq. (2.114).

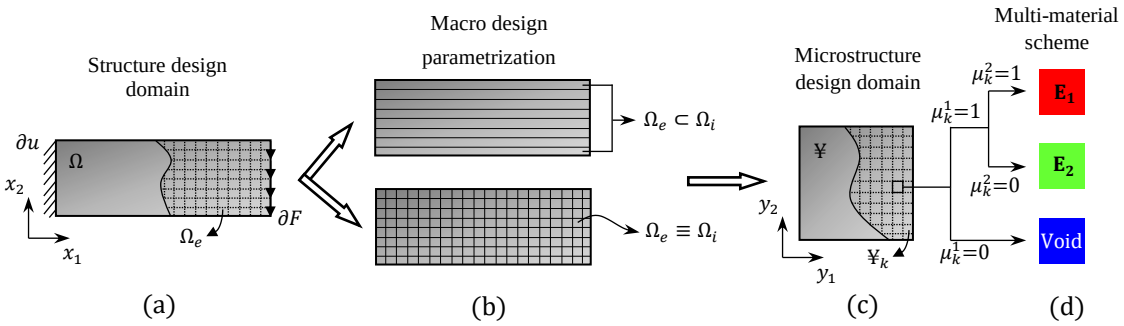

Fig. 4.1: Hierarchical material model description: (a) structure design domain Ω discretised into 8-node quadrilateral finite elements Ω_e; (b) two different macro design parametrizations; (c) microstructure design domain ¥ discretised into 4-node quadrilateral finite elements ¥$_k$; and (d) multi-material interpolation scheme.

4.2 Hierarchical optimization problem

With the goal of improving the stiffness (compliance minimization) of structures composed of periodic multi-material microstructures, one proposes the following hierarchical problem formulation:

$$\min_{\boldsymbol{\rho}^*} \frac{1}{2}\int_\Omega \phi(\boldsymbol{\rho}^*, \mathbf{u})\,\mathrm{d}\Omega \tag{4.1a}$$

$$\text{s.t.} \quad \int_\Omega \boldsymbol{\rho}^*\,\mathrm{d}\Omega - M^* \leq 0 \tag{4.1b}$$

$$0 < {\rho^*}_{\min} \leq \boldsymbol{\rho}^* \leq {\rho^*}_{\max} \leq \rho_1^* \tag{4.1c}$$

with $\phi(\boldsymbol{\rho}^*, \mathbf{u})$ given by:

$$\phi(\boldsymbol{\rho}^*, \mathbf{u}) = \min_{\boldsymbol{\mu}_1, \boldsymbol{\mu}_2} \frac{\int_{\Omega_i} C^H_{mnpq}(\boldsymbol{\mu}_1, \boldsymbol{\mu}_2)\sigma_{mn}(\mathbf{u})\sigma_{pq}(\mathbf{u})\,\mathrm{d}\Omega_i}{|\Omega_i|} \tag{4.2a}$$

$$\text{s.t.} \quad \int_¥ \boldsymbol{\mu}_1(\boldsymbol{\mu}_2\rho_1^* + (1-\boldsymbol{\mu}_2)\rho_2^*)\,\mathrm{d}¥ - \boldsymbol{\rho}^*|¥| \leq 0 \tag{4.2b}$$

$$\frac{\int_¥ \boldsymbol{\mu}_1(1-\boldsymbol{\mu}_2)\,\mathrm{d}¥}{|¥|} - V_2^* \leq 0 \tag{4.2c}$$

$$0 < \mu_{\min} \leq \boldsymbol{\mu}_1 \leq 1 \tag{4.2d}$$

$$0 < \mu_{\min} \leq \boldsymbol{\mu}_2 \leq 1 \tag{4.2e}$$

The set of equations (4.1) states the TO problem of the macrostructure, while the set of equations (4.2) states the TO problem of the microstructure. The macro design variable $\boldsymbol{\rho}^*$ is a vector containing the mass densities (i.e., mass per unit of volume) of all subdomains Ω_i, and must not

be confused with the dimensionless density variable typically used in TO. To correctly model and optimize multi-material microstructures composed of three material phases, two micro design variables $\boldsymbol{\mu}_1$ and $\boldsymbol{\mu}_2$ are now required. The micro design variables are the standard density variables used in TO.

The macro problem aims the global compliance minimization of the structure (Eq. 4.1a) while subject to a global mass constraint (Eq. 4.1b) with M^* as the mass limit of the structure. This mass limit value can be easily obtained by defining a limit on the global mass density ${\rho^*}_{\text{lim}} \in \left[{\rho^*}_{\text{min}}; {\rho^*}_{\text{max}}\right]$ and multiplying it by the structure volume $|\Omega|$. The micro problem aims the local minimization of the complementary strain energy density of the material domain Ω_i (Eq. 4.2a) while subject to a local mass constraint (Eq. 4.2b), where ρ_1^* and ρ_2^* are the mass densities of the stiffer and weaker solids, respectively. The local mass constraint is originally an equality constraint, but for reasons of computational implementation it is considered here as an inequality constraint. However, since the objective is the compliance minimization, the constraint is active or nearly active during the optimization procedure. This local mass constraint is responsible for relating the macro and micro design variables enabling the hierarchical optimization.

To avoid singularities $\boldsymbol{\mu}_1$ and $\boldsymbol{\mu}_2 \in [\mu_{\text{min}}; 1]$ with $\mu_{\text{min}} = 0.001$. Note that if all micro densities $\boldsymbol{\mu_1}$ and $\boldsymbol{\mu_2}$ touch their bounds, the Lagrangian multiplier λ (provided by MMA) related to the local mass constraint is undefined. Consequently, the derivative of the functional ϕ (macro objective function, see Table 4.1) is also undefined. Either the density filter (see Section 2.3.4.1) or the sensitivity filter (see Section 2.3.4.2) can be used to help overcome this setback since these techniques ensure some "gray" (i.e., $\boldsymbol{\mu_1}$ and $\boldsymbol{\mu_2}$ intermediate values) on the local solutions, while also avoid problems such as checkerboards and mesh-dependency of results. Even so, in the global problem, the variable $\boldsymbol{\rho}^*$ could take the lower or upper bounds, i.e., ${\rho^*}_{\text{min}}$ or ${\rho^*}_{\text{max}}$. If ${\rho^*}_{\text{min}} = \mu_{\text{min}}\, \rho_1^*$ or ${\rho^*}_{\text{max}} = \rho_1^*$, the values of all $\boldsymbol{\mu_1}$ and $\boldsymbol{\mu_2}$ would be enforced by Eq. (4.2b) such that $\boldsymbol{\mu_1} = \mu_{\text{min}} \cap \boldsymbol{\mu_2} = 1$ or $\boldsymbol{\mu_1} = 1 \cap \boldsymbol{\mu_2} = 1$, respectively. To prevent this from happening, one considers bounds for $\boldsymbol{\rho}^*$ slightly modified, i.e., ${\rho^*}_{\text{min}} = \mu_{\text{min}}\, \rho_1^* + \zeta$ and ${\rho^*}_{\text{max}} = \rho_1^* - \zeta$, where ζ is a small positive number (e.g., $\zeta = 0.009$). This strategy is sound for single material design [1]. However, for multi-material design another scenario might happen where all values of $\boldsymbol{\mu_1}$ and $\boldsymbol{\mu_2}$ are forced to their bounds. This is the case of a microstructure composed only by the weaker solid, i.e., $\boldsymbol{\mu_1} = 1 \cap \boldsymbol{\mu_2} = \mu_{\text{min}}$. A clever way to prevent this scenario from happening is to constrain (Eq. 4.2c) the volume fraction of the weaker solid such that it can never be unity, i.e., $V_2^* = 0.99$. This method requires then one additional local constraint for each material phase added. If more than three material phases were considered, it will be more efficient to consider a single porosity constraint instead of multiple material volume fraction constraints.

These strategies used to prevent the design variables $\boldsymbol{\mu}_1$ and $\boldsymbol{\mu}_2$ from touching their bounds provide a way to obtain defined values for the Lagrangian multiplier λ. However, such strategies make it impossible to obtain microstructures fully composed of only one material phase without any "gray", see results in Section 4.5 (e.g., Fig. 4.15). Consequently, a disrupted stress field is obtained for those cases.

4.2.1 Optimality conditions

In Section 2.6.2, the optimality conditions were already derived for the hierarchical optimization problem of single material structures subject to a material volume constraint. The same procedure is once again applied to obtain the optimality conditions of the hierarchical optimization problem (4.1) and (4.2) of multi-material structures subject to a mass constraint.

The Lagrange function associated with the macro problem (4.1) at points where $\boldsymbol{\rho}^*$ takes intermediate values (i.e., bound constraints are inactive) is stated as:

$$\mathcal{L} = \frac{1}{2}\int_{\Omega} \phi(\boldsymbol{\rho}^*, \mathbf{u})\, \mathrm{d}\Omega + \Lambda\left(\int_{\Omega} \boldsymbol{\rho}^*\, \mathrm{d}\Omega - M^*\right) \tag{4.3}$$

where $\Lambda \geq 0$ is the Lagrange multiplier associated with the global mass (inequality) constraint. The stationary of the Lagrange function $\mathcal{L}$ defined above w.r.t the design variable $\boldsymbol{\rho}^*$ is given by:

$$\frac{\partial \mathcal{L}}{\partial \boldsymbol{\rho}^*} = 0 \Leftrightarrow \frac{1}{2}\frac{\partial \phi}{\partial \boldsymbol{\rho}^*}|\Omega_i| = -\Lambda|\Omega_i| \Leftrightarrow \lambda = 2\Lambda \tag{4.4}$$

The sensitivity theorem (see e.g. [137]) is applied in the above equation to obtain the relation between the macro and micro Lagrange multipliers, i.e., $\frac{\partial \phi}{\partial \boldsymbol{\rho}^*} = -\lambda$. Note that this relation is identical to the one obtained back in Section 2.6.2 (see Eq. 2.136).

Now consider inactive the constraints on the volume fraction of the weaker solid (Eq. 4.2c) and design variables bounds (Eqs. 4.2d and 4.2e), the Lagrange function of the micro problem (4.2) can be written as:

$$\begin{aligned} \ell = C^H_{mnpq}\frac{\int_{\Omega_i}\sigma_{mn}\sigma_{pq}\,\mathrm{d}\Omega_i}{|\Omega_i|} \\ + \lambda\left(\int_{¥}\mu_{k,1}\left(\mu_{k,2}\rho_1^* + \left(1-\mu_{k,2}\right)\rho_2^*\right)\mathrm{d}¥ - \rho_e^*|¥|\right) \end{aligned} \tag{4.5}$$

where λ is the Lagrange multiplier of the local mass constraint. The stationary of the Lagrange function ℓ defined above w.r.t both design variables $\mu_{k,1}$ and $\mu_{k,2}$ is given by:

$$\frac{\partial \ell}{\partial \mu_{k,1}} = 0 \Leftrightarrow \frac{C^H_{mnpq}}{\partial \mu_{k,1}} \frac{\int_{\Omega_i} \sigma_{mn}\sigma_{pq}\, \mathrm{d}\Omega_i}{|\Omega_i|} = -\lambda\left(\mu_{k,2}\rho_1^* + \left(1-\mu_{k,2}\right)\rho_2^*\right)|¥_k| \tag{4.6}$$

$$\frac{\partial \ell}{\partial \mu_{k,2}} = 0 \Leftrightarrow \frac{C^H_{mnpq}}{\partial \mu_{k,2}} \frac{\int_{\Omega_i} \sigma_{mn}\sigma_{pq}\, \mathrm{d}\Omega_i}{|\Omega_i|} = -\lambda\left(\mu_{k,1}\rho_1^* - \mu_{k,1}\rho_2^*\right)|¥_k| \tag{4.7}$$

Note that the macro stresses **σ** do not depend on the micro density fields because these are fixed from the macro problem when solving the micro problem.

4.2.2 Sensitivity analysis

Sensitivity analysis must be performed whenever a gradient-based optimizer is used and consists in computing the derivatives of the objective and constraint functions of a given optimization problem. The hierarchical optimization problem has two coupled optimization problems (macro and micro), and therefore the sensitivity analysis must be performed for both problems. Table 4.1 shows all the functions and their corresponding derivatives required to solve the hierarchical optimization problem.

4.3 Hierarchical algorithmic strategies

This section presents different algorithmic strategies [1] to solve the hierarchical optimization problem. In Section 4.5.1.1, these algorithmic strategies are tested and compared solving the single material version of the hierarchical problem, i.e., only one design variable per FE (**μ**) and global mass constraint (Eq. 4.1b) are considered. The algorithmic strategies can be divided into two main categories:

- **Type I Strategies:** assume the micro design variables as independent ones while the macro design variables are implicitly computed through the micro design variables once these are known.
- **Type II Strategies:** assume both design variables, the macro and micro, as independent design variables, each at its respective scale.

Table 4.1: Objective and constraint functions of the hierarchical problem with the corresponding derivatives.

	Macro problem (4.1)	**Micro Problem (4.2)**
Objective Function	$F = \frac{1}{2}\int_{\Omega} \phi \, \mathrm{d}\Omega$	$f = \frac{\int_{\Omega_i} C^H_{mnpq}\sigma_{mn}\sigma_{pq} \, \mathrm{d}\Omega_i}{\lvert\Omega_i\rvert}$
	$\frac{\mathrm{d}F}{\mathrm{d}\rho_i^*} = -\frac{1}{2}\lambda\lvert\Omega_i\rvert$	$\frac{\mathrm{d}f}{\mathrm{d}\mu_{k,1}} = \frac{C^H_{mnpq}}{\partial\mu_{k,1}}\frac{\int_{\Omega_i}\sigma_{mn}\sigma_{pq}\,\mathrm{d}\Omega_i}{\lvert\Omega_i\rvert}$
		$\frac{\mathrm{d}f}{\mathrm{d}\mu_{k,2}} = \frac{C^H_{mnpq}}{\partial\mu_{k,2}}\frac{\int_{\Omega_i}\sigma_{mn}\sigma_{pq}\,\mathrm{d}\Omega_i}{\lvert\Omega_i\rvert}$
Constraint functions	$G = \int_{\Omega}\rho_i^* \, \mathrm{d}\Omega - M^*$	$g_1 = \int_{¥}\mu_{k,1}\left(\mu_{k,2}\rho_1^* + \left(1-\mu_{k,2}\right)\rho_2^*\right)\mathrm{d}¥ - \rho_i^*\lvert¥\rvert$
	$\frac{\mathrm{d}G}{\mathrm{d}\rho_i^*} = \lvert\Omega_i\rvert$	$g_2 = \frac{\int_{¥}\mu_{k,1}\left(1-\mu_{k,2}\right)\mathrm{d}¥}{\lvert¥\rvert} - V_2^*$
		$\frac{\mathrm{d}g_1}{\mathrm{d}\mu_{k,1}} = \left(\mu_{k,2}\rho_1^* + \left(1-\mu_{k,2}\right)\rho_2^*\right)\lvert¥_k\rvert$
		$\frac{\mathrm{d}g_1}{\mathrm{d}\mu_{k,2}} = \left(\mu_{k,1}\rho_1^* - \mu_{k,1}\rho_2^*\right)\lvert¥_k\rvert$
		$\frac{\mathrm{d}g_2}{\mathrm{d}\mu_{k,1}} = \frac{\left(1-\mu_{k,2}\right)\lvert¥_k\rvert}{\lvert¥\rvert}$
		$\frac{\mathrm{d}g_2}{\mathrm{d}\mu_{k,2}} = \frac{-\mu_{k,1}\lvert¥_k\rvert}{\lvert¥\rvert}$

4.3.1 Type I strategy

The *Type I Strategy* is the simplest way to solve the hierarchical problem. In fact, this algorithmic strategy allows to treat the hierarchical problem in a simplified way, where the minimization of the global strain energy is done through the micro design variables. The macro design variables $\boldsymbol{\rho}^*$ are thus obtained by the following relation (single material case):

$$\boldsymbol{\rho}^* = \frac{\int_{¥}(\boldsymbol{\mu}\rho_1^* + (1-\boldsymbol{\mu})\rho_2^*)\,\mathrm{d}¥}{\lvert¥\rvert} \tag{4.2b}$$

Two different optimizers are used here to solve the hierarchical problem using this strategy: (1) Optimality Criteria (OC) Method and (2) Method of Moving Asymptotes (MMA). These optimizers were described back in Section 2.3.2. Depending on the optimizer used, the methodology to solve the hierarchical problem is different.

The OC method typically use a fix-point type update scheme to update the design variables based on the optimality conditions, see Eq. (2.65). The flowchart presented in Fig. 4.2 describes the algorithm developed in Fortran that solves the hierarchical problem using the OC method. The algorithm starts by generating an initial design equal in each macro subdomain i, i.e., the initial micro design variables $\boldsymbol{\mu}_0$ that define the microstructure are equal in all macro subdomains. This leads to equal macro design variables $\boldsymbol{\rho}_0^*$ in all macro subdomains defined through Eq. (4.2b). Since the microstructure is equal in all macro subdomains, the homogenization subroutine only needs to be called once. The homogenization subroutine provides the initial homogenized stiffness or compliance ($\mathbf{E}_0^{\mathrm{H}}$ or $\mathbf{C}_0^{\mathrm{H}}$) tensor and its corresponding derivatives w.r.t. the micro design variables. The algorithm has two main loops. An outer loop that runs the global problem and an inner loop that runs through the various local problems. The global problem starts by performing a FE analysis to solve the global equilibrium problem. Then, the global objective function (strain energy) F and the Lagrange multiplier Λ are computed. The outer loop runs while the convergence criterion is not met. Regarding the inner loop, there are as much local problems to solve as the number of macro design subdomains N_i. Each local problem runs the OC method giving updated values for the micro design variables ${}^{i}\boldsymbol{\mu}$ corresponding to the macro subdomain i, which naturally leads to a new ρ_i^* value. Afterwards, the homogenization subroutine computes the new homogenized material properties of the microstructure that composes the macro subdomain i, and the new derivatives.

An alternative optimizer to the OC method to solve the hierarchical problem is the MMA. In this case, one has a single optimization problem with $N_k \times N_i$ design variables $\boldsymbol{\mu}$, where N_k is the total number of micro elements and N_i is the total number of macro subdomains. Unlike OC method, MMA optimizes all design variables at once. The flowchart presented in Fig. 4.3 describes the algorithm developed in Fortran that solves the hierarchical problem using the MMA.

This algorithm starts by defining the initial design variables ($\boldsymbol{\mu}_0$ and $\boldsymbol{\rho}_0^*$) and the initial homogenized stiffness or compliance ($\mathbf{E}_0^{\mathrm{H}}$ or $\mathbf{C}_0^{\mathrm{H}}$) tensor along with its derivatives, likewise the algorithm described previously that used OC method. Again, this algorithm has two main loops. The outer loop runs the macro FE model and MMA. In each outer loop iteration, an inner loop that goes through all the local problems to find out the new homogenized material properties tensor and corresponding derivatives is performed.

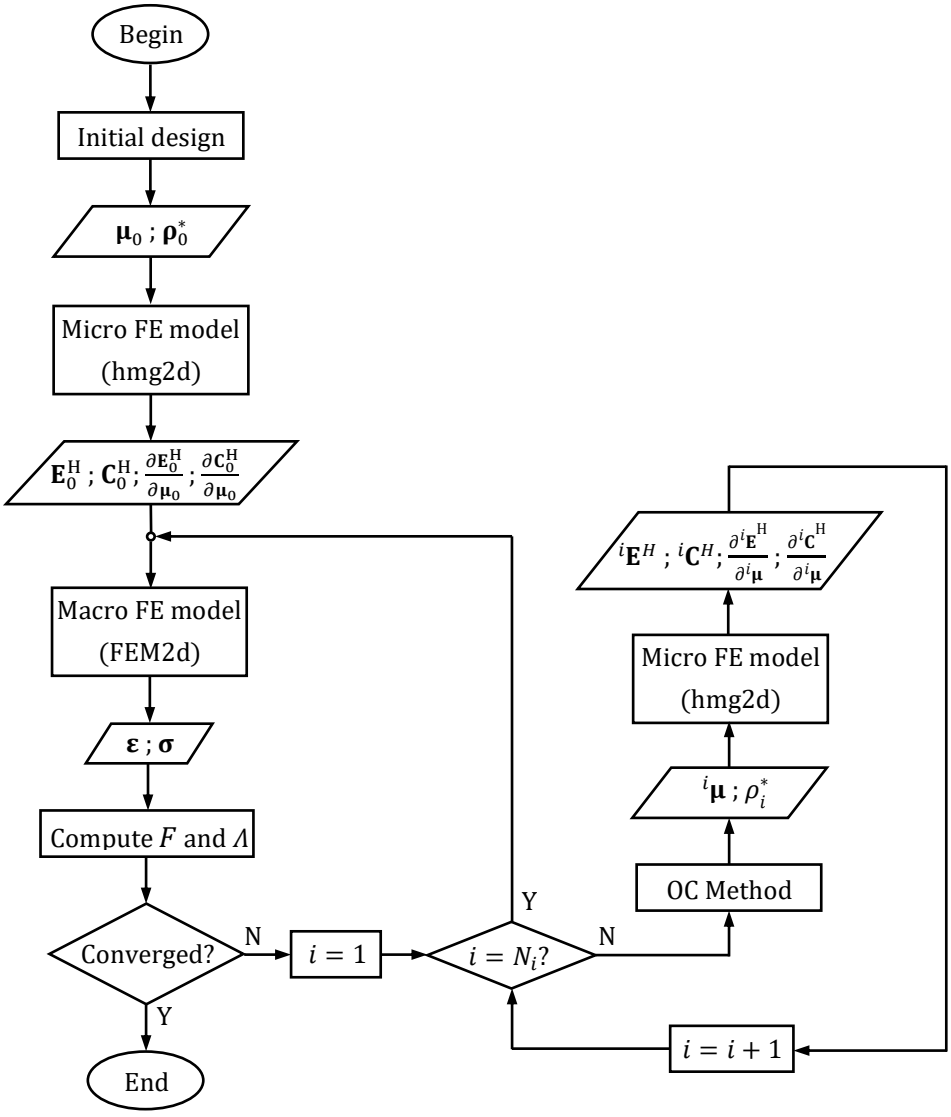

Fig. 4.2: Flowchart of the algorithm developed in Fortran to perform the hierarchical optimization considering a Type I Strategy using OC method.

To conclude, this strategy allows a simple algorithmic implementation to solve the hierarchical TO problem either using OC method or MMA. The OC method is easy to implement, however it proves to be only efficient handling just one constraint (material volume fraction or mass) in single-material compliance minimization problems. Also, this method requires tuning some parameters, which is a monotonous and time-consuming task. A more versatile and efficient method to solve optimization problems is MMA. However, using such algorithmic strategy, MMA faces one high-dimensional optimization problem since all micro design variables are being optimized at the same time. To speed-up the optimization procedure, a parallel version of MMA could be used [82,148]. A far more interesting (and complex) approach to solve the hierarchical problem is to consider the so-called *Type II Strategy*, which will be described next.

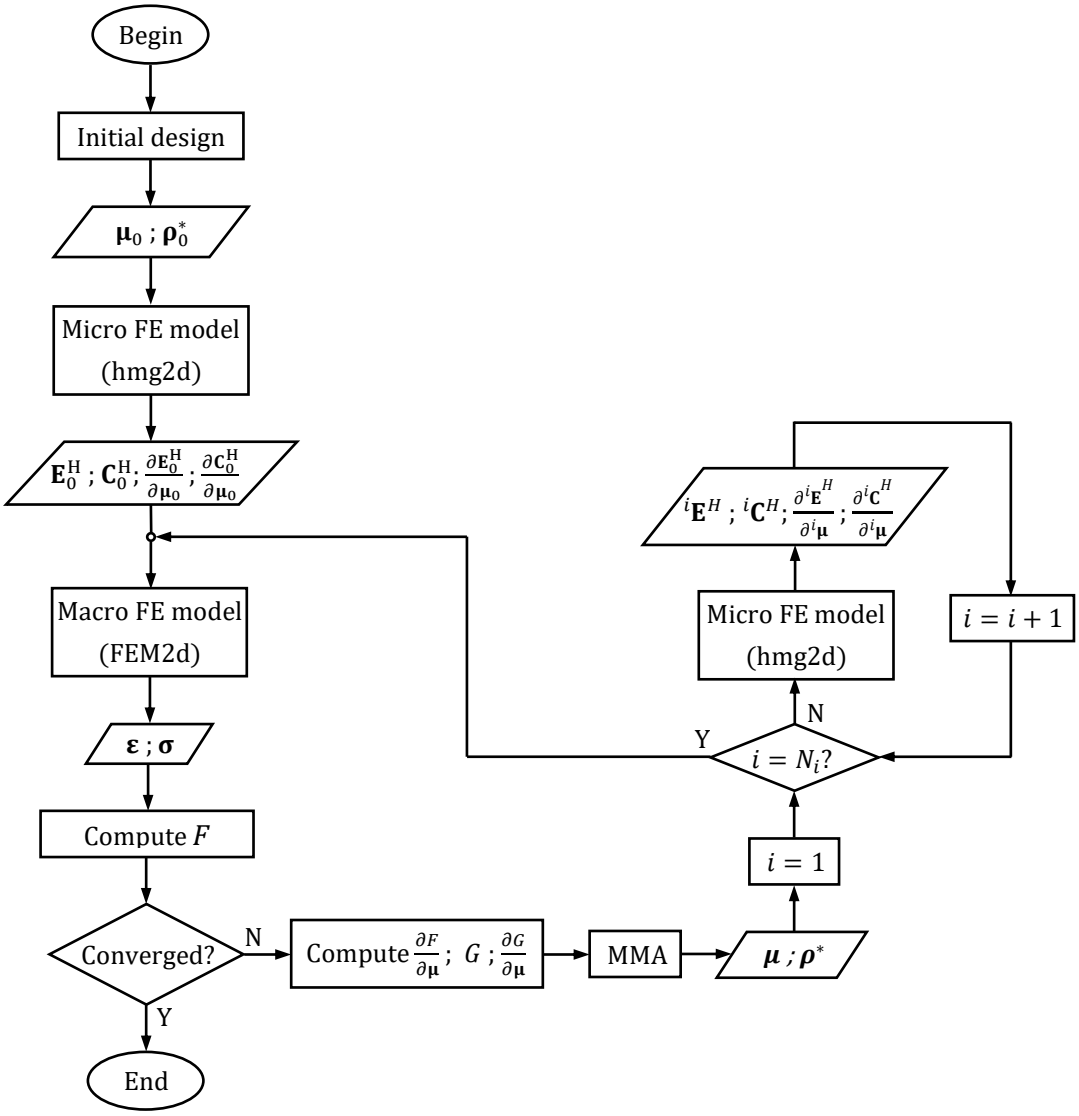

Fig. 4.3: Flowchart of the algorithm developed in Fortran to perform the hierarchical optimization considering a Type I Strategy using MMA.

4.3.2 Type II strategy

The *Type II Strategy* naturally fits the original hierarchical problem formulation, where the two optimization problems at different scales are solved in a coupled fashion using two separate optimizers. One can think in several combinations of optimizers to solve the global and local optimization problems. Here, MMA is used to solve both. This obviously improves the quality of the final solution, not being so prone to getting stuck in local minima. However, such strategy greatly increases the complexity of the optimization problem. In fact, there are a few key factors to consider for this strategy to work smoothly, which will be discussed later in Section 4.4.

In Fig. 4.4 is shown the flowchart of the algorithm developed in Fortran to solve the hierarchical TO problem using a Type II Strategy with MMA as the optimizer to solve both the global and local problems. In a similar manner to the algorithms presented previously, this algorithm starts with an initialization to define the initial design variables ($\boldsymbol{\mu}_0$ and $\boldsymbol{\rho}_0^*$) and the initial homogenized stiffness or compliance ($\mathbf{E}_0^{\mathrm{H}}$ or $\mathbf{C}_0^{\mathrm{H}}$) tensor along with its derivatives. Two main loops can be identified in the flowchart. The outer loop optimizes the macrostructure ($\boldsymbol{\rho}^*$), while the inner loop optimizes the microstructure ($\boldsymbol{\mu}$). Only one MMA iteration is performed in the inner loop to avoid premature convergence. To speedup computations the inner loop can be conveniently parallelized, to solve and optimize different local problems in different CPU cores [133].

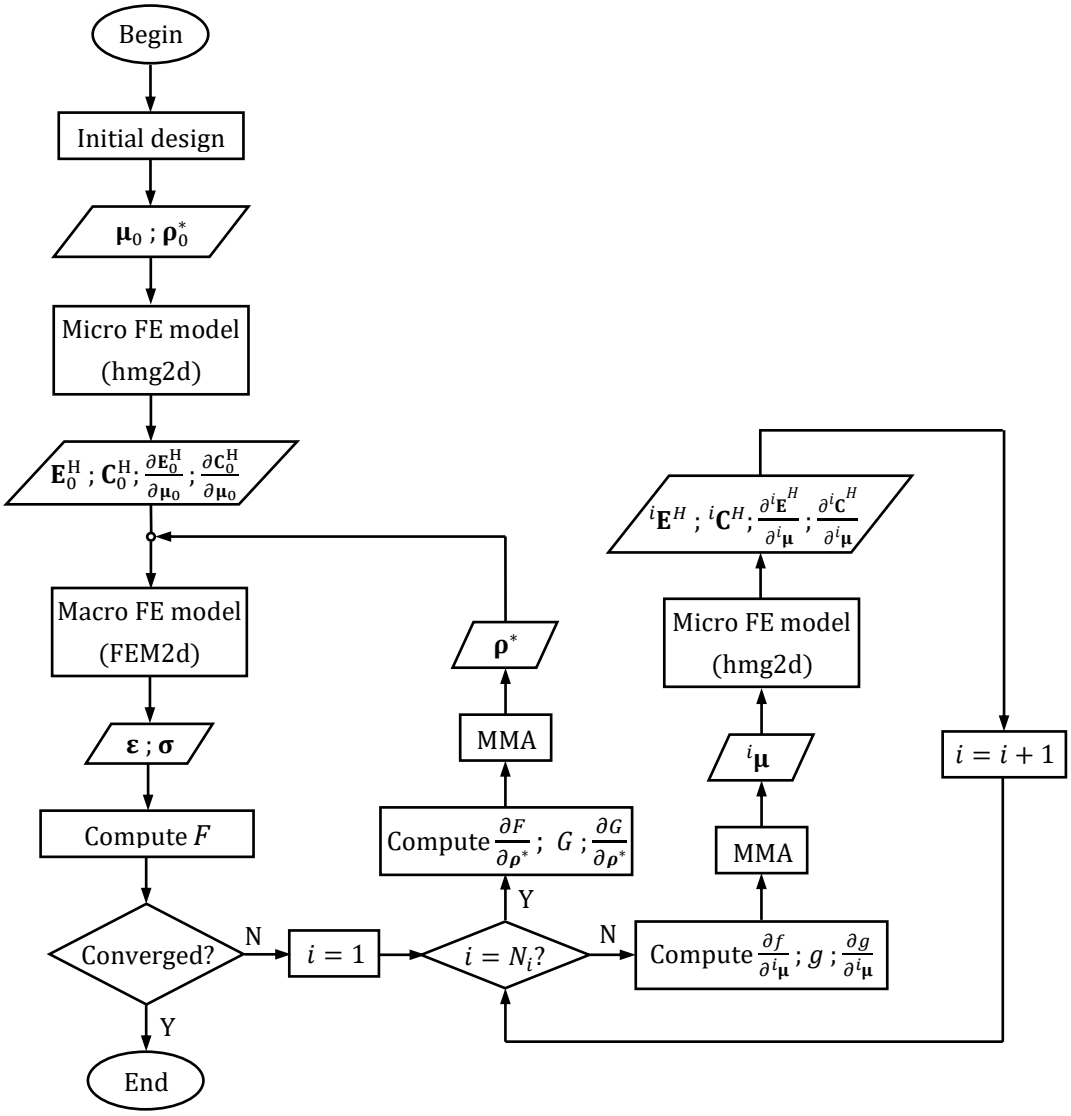

Fig. 4.4: Flowchart of the algorithm developed in Fortran to perform the hierarchical optimization considering a Type II Strategy using MMA.

To sum up, this algorithmic strategy is the most promising one due to its ability to efficiently solve the hierarchical TO problem in its multi-material version considering several constraints. Despite its undeniable efficiency, this strategy requires some care to obtain a stable convergence and, therewith, a good optimal solution. Some important key factors and advices to apply when solving hierarchical TO problems using this algorithmic strategy are given in next section.

4.4 Methodology

The focus of this section is to provide an efficient methodology to solve the hierarchical TO problem. As mentioned before, the type II strategy requires some care when implementing and solving it. Some key factors to improve the algorithm efficiency are provided next.

Firstly, it is advisable to use a variant of MMA called GMMA (see Section 2.3.2.2). Using GMMA, different functions might have different asymptotes, improving the quality of the approximating functions. To solve the hierarchical problem stated in (4.1) and (4.2), it is advisable to have a convex approximation of the compliance function based on moving asymptotes and a linear approximation of the constraints based on fixed and distant asymptotes. Note that the constraints are linear functions w.r.t. each design variable (i.e., bilinear functions), meaning that the approximation is exact. Actually, this methodology sounds very similar to what CONLIN (another variant of MMA) does. However, the approximation of the compliance function on CONLIN is not based on moving asymptotes. Instead, the lower and upper asymptotes are fixed to zero and infinity, respectively. This gives a crude approximation of the compliance function.

In fact, the asymptotes play an important role in the optimization process. Both global and local optimization problems use GMMA as the optimizer. However, the asymptotes are not built in the same manner in both problems. In the global problem, the update scheme for the asymptotes used to approximate the global strain energy follow the original methodology described in Section 2.3.2.2. In each local problem, only one GMMA iteration is performed, which means that the asymptotes are only computed based on Eqs. (2.72) and (2.73). To improve algorithm's convergence, a continuation approach on the parameter that controls distance between the lower and upper asymptotes γ_0 (`GHINIT` in Fortran GMMA) is suggested. This ensures that as the algorithm converges to the optimum, the approximation of the complementary strain energy density function becomes more conservative and, consequently, more accurate.

Another important issue is the move limits (see Eqs. 2.70 and 2.71) that control the variation of the design variables. To obtain stable convergence, it is important to tighten the variation

bounds of the global design variables, and relax the variation bounds of the local design variables. This means that the move limits should be closed to each other when solving the global problem, and distant when solving the local problems. The parameter that controls the distance between the move limits is the so-called `ALBEFA` in Fortran GMMA. A high `ALBEFA` value means tight move limits and vice-versa.

A continuation approach applied to the penalization exponents in the material interpolation scheme has been proved to be an efficient method to improve the quality of the optimal solution. Also, a filtering technique (sensitivity or density filter) is required to solve the local problems. The global problem does not require a filtering technique.

Parallel computing can be conveniently applied when solving large-scale problems. For instance, solving the hierarchical problem using an Element-by-Element parametrization on the macro design implies solving as many local problems as the total number of macro elements. Even for coarse mesh discretizations, thousands of local problems need to be solved. Since the local problems are independent from each other, these can be tackled in different processors. Both MPI and OpenMP are suitable to parallelize the code in Fortran language. The hardware used in this work is a Workstation HP Z8 G4 (shared-memory machine), and therefore OpenMP is used to parallelize the code.

4.5 Results: Multiscale Topology Optimization

This section presents the obtained results for the multiscale topology optimizations solved. The hierarchical TO problem is solved for single material (Section 4.5.1) and multi-material (Section 4.5.2). Both versions are solved assuming two different micro design parametrizations: (1) Element-by-Element and (2) Layer-by-Layer. An Element-by-Element parametrization assumes that to each macro FE exists a set of micro design variables that define the microstructure. This approximates a pointwise optimal material definition, thus leading to very efficient designs but of problematic manufacturability. To improve manufacturability, the Layer-by-Layer parametrization can be used. This parametrization assumes a uniform micro design within each subdomain Ω_i characterized by two symmetric layers (see Fig. 4.1). Now, instead of having a set of micro design variables per FE, one has a set of micro design variables per subdomain, thus significantly reducing the total number of micro design variables.

The different algorithmic strategies presented in Section 4.3 are tested out within the frame of single material hierarchical TO using a Layer-by-Layer design parametrization. This study helps

to understand the most effective strategy to subsequently solve high-dimensional (Element-by-Element parametrization) and more complex problems (multi-material).

As in the previous Chapter, Steel and Aluminum are used here as solid material phases, where the ratios of their properties (E/E_{Steel} and $\rho^*/\rho^*_{\text{Steel}}$) are used instead of their absolute values, see Table 3.2. The single-material results are obtained using only steel.

The ultimate goal of this work is to see whether multi-material TO applied to multi-scale structures is able to improve the global stiffness of the structure compared to single-material TO. The idea is to solve the single-material version of the hierarchical problem formulated in (4.1) and (4.2) with a given mass threshold M^*. The value for M^* must be chosen with care. Small values for M^* tend to create discontinuous designs, while high values for M^* might compromise stiffness gains through multi-material design. A good reference value for M^* requires calculating the total mass of the structure, composed only by the stiffest material, assuming a material volume fraction of 30%. This gives room for multi-material design to improve the stiffness of single-material continuous designs. In fact, with multi-material design is possible to obtain continuous structures that would be impossible to obtain using only one material with lower volume fractions.

The hierarchical TO problem is computational expensive by nature since several microstructural optimizations are performed in a single iteration of the macrostructural optimization. Therefore, both macro and micro models must have a modest mesh discretization, otherwise high computational times would prevent obtaining results in a timely manner. The macro model is the classical example of a cantilever beam with dimensions 1×0.2, discretized in a 50×20 mesh. The micro model (homogenization) considers a unitary square mesh using a discretization of 40×40.

This section is structured as follows. Firstly, one addresses single-material hierarchical TO in Section 4.5.1 performing a Layer-by-Layer parametrization (Section 4.5.1.1) and an Element-by-Element parametrization (Section 4.5.1.2). Then, multi-material hierarchical TO is performed in Section 4.5.2 for both Layer-by-Layer parametrization (Section 4.5.2.1) and Element-by-Element parametrization (Section 4.5.2.2).

4.5.1 Single-material hierarchical TO

As mentioned before, this section presents results obtained solving the hierarchical TO problem in its single-material version using two different design parametrizations (Layer-by-Layer and Element-by-Element). Next, one benefits from the reduced computational time of the Layer-by-Layer parameterization to compare different algorithmic strategies.

4.5.1.1 Layer-by-Layer

Here one solves the single-material hierarchical problem using three different approaches: (1) Type I Strategy using OC, (2) Type I Strategy using GMMA and (3) Type II Strategy using GMMA. Solving the hierarchical problem with these approaches one aims to compare them and validate the algorithm developed. All approaches are solved using the sensitivity filter, while the third approach also uses the density filter for comparison purposes.

The results for the three different approaches are shown in Fig. 4.5, Fig. 4.7 and Fig. 4.9. The optimization histories are shown right below the results in Fig. 4.6, Fig. 4.8 and Fig. 4.10. Fig. 4.11 and Fig. 4.12 shown the results obtained using density filter and the optimization history, respectively. The results are organized in the following way. Since the macro design is symmetric, the mass density distribution ($\boldsymbol{\rho}^*$) is shown on the upper half of the beam, while the corresponding stress distribution is shown on the lower half. Each layer of the macrostructure is characterized by having a microstructure, which is also shown for the different layers. A stress analysis is also performed on the microscale. One chooses the most stressed macro elements in different layers to see the corresponding stress distribution in the microstructure.

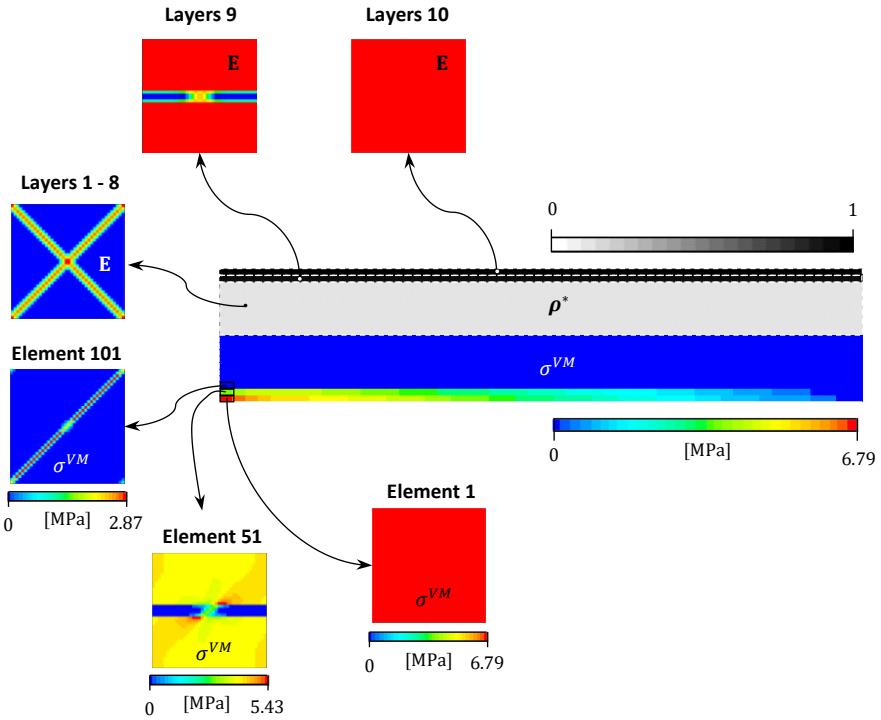

Fig. 4.5: Results obtained solving the single-material hierarchical problem using the Type I Strategy with OC.

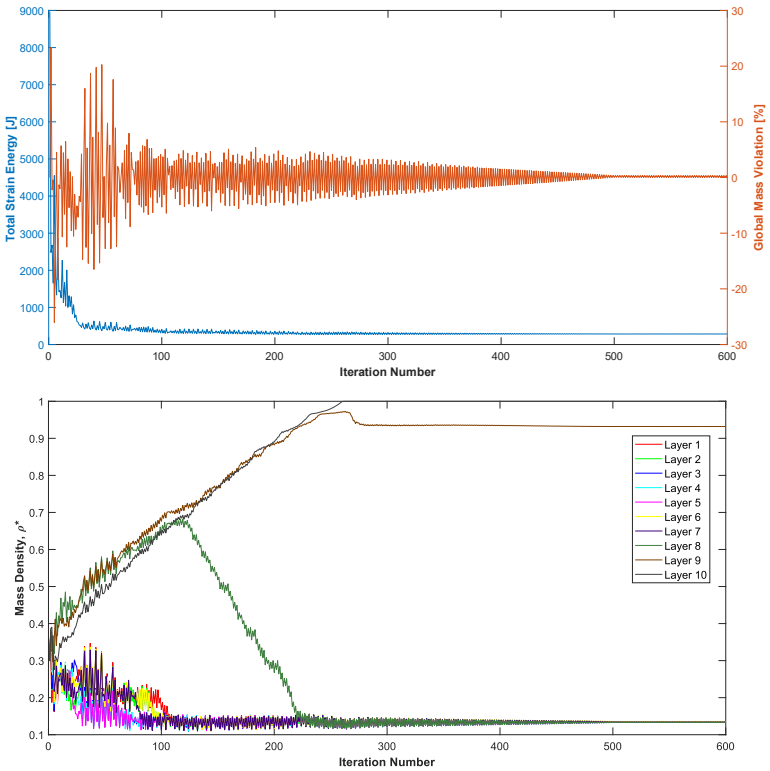

Fig. 4.6: Optimization history of the Type I Strategy with OC. Total strain energy and global mass constraint violation are shown upside. Mass density values for the different layers throughout the optimization are shown downside.

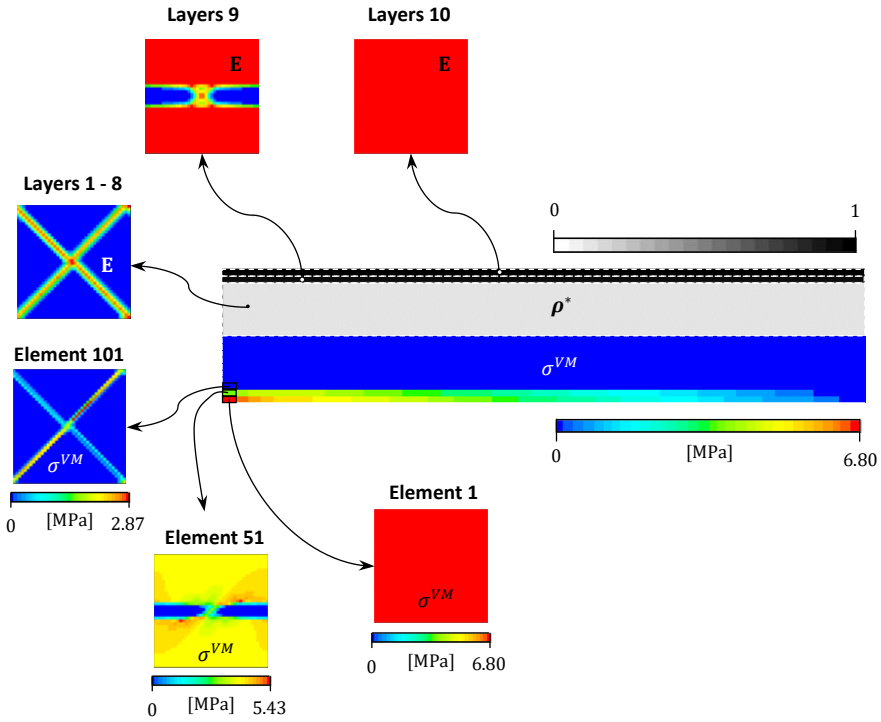

Fig. 4.7: Results obtained solving the single-material hierarchical problem using the Type I Strategy with GMMA.

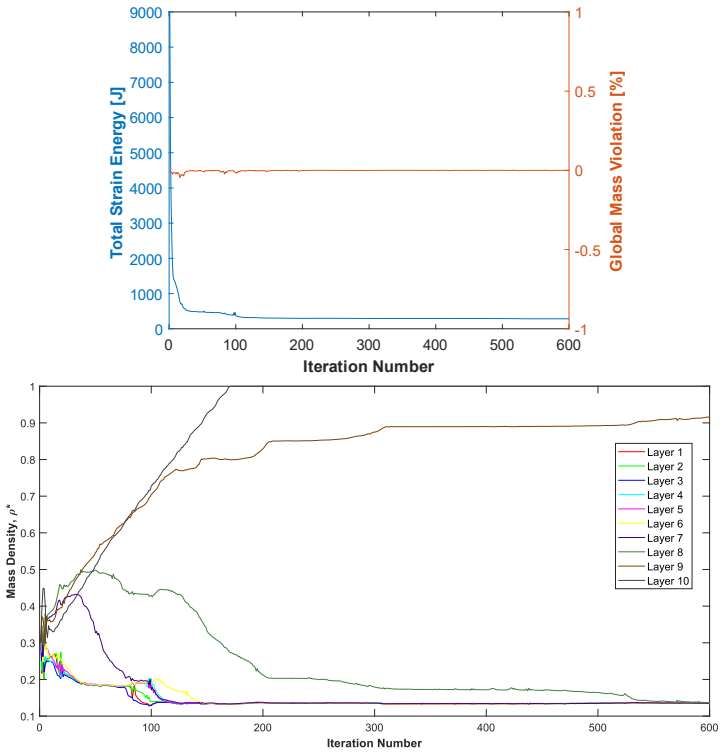

Fig. 4.8: Optimization history of the Type I Strategy with GMMA. Total strain energy and global mass constraint violation are shown upside. Mass density values for the different layers throughout the optimization are shown downside.

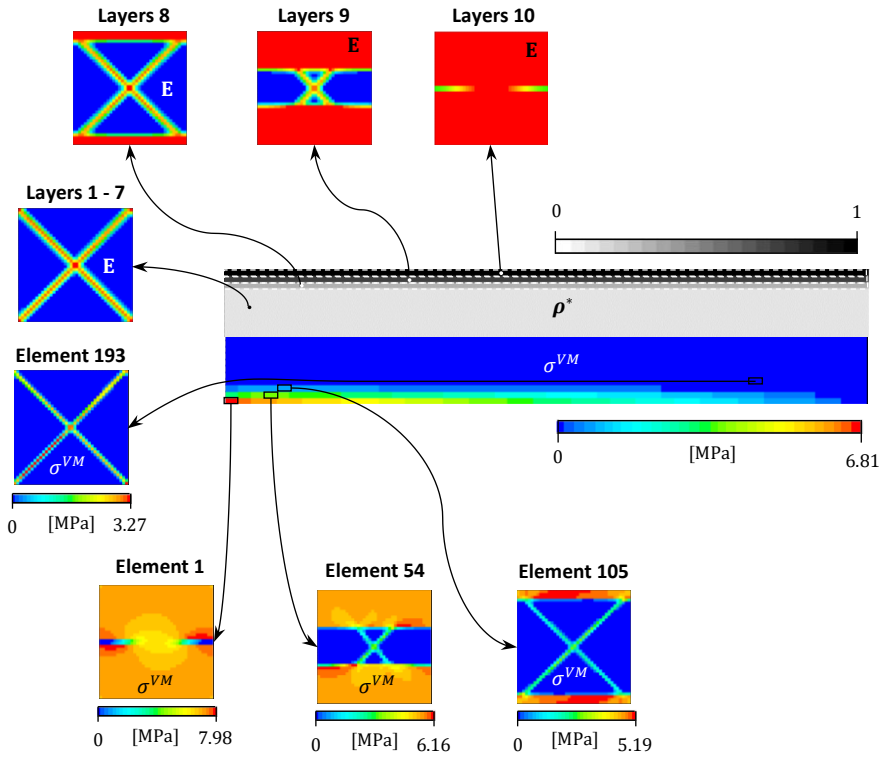

Fig. 4.9: Results obtained solving the single-material hierarchical problem using the Type II Strategy with GMMA. Sensitivity filtering technique is used here.

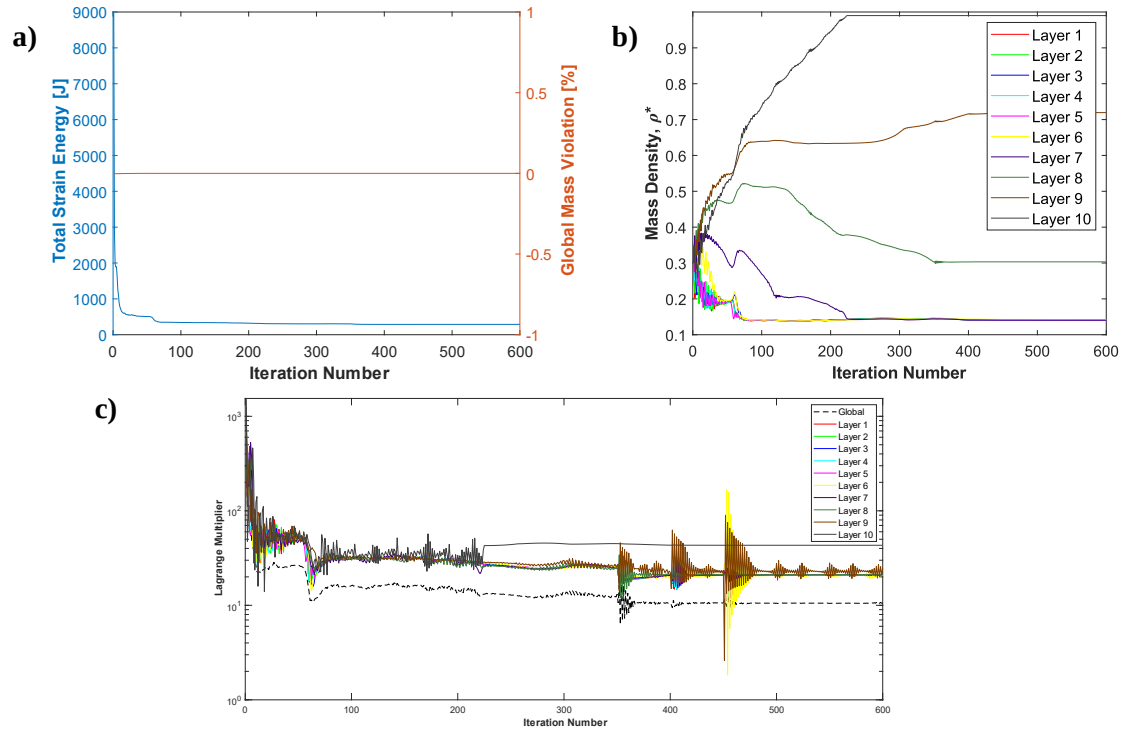

Fig. 4.10: Optimization history of the Type II Strategy with GMMA using sensitivity filter: (a) Total strain energy and global mass constraint violation; (b) Mass density values; and (c) Lagrange multiplier values.

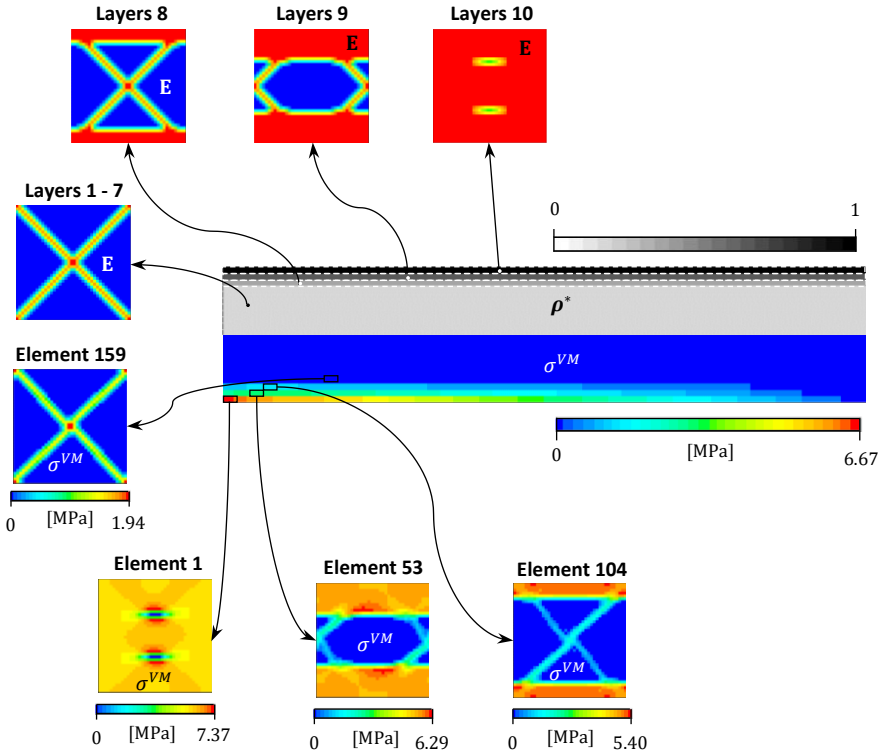

Fig. 4.11: Results obtained solving the single-material hierarchical problem using the Type II Strategy with GMMA. Density filtering technique is used here.

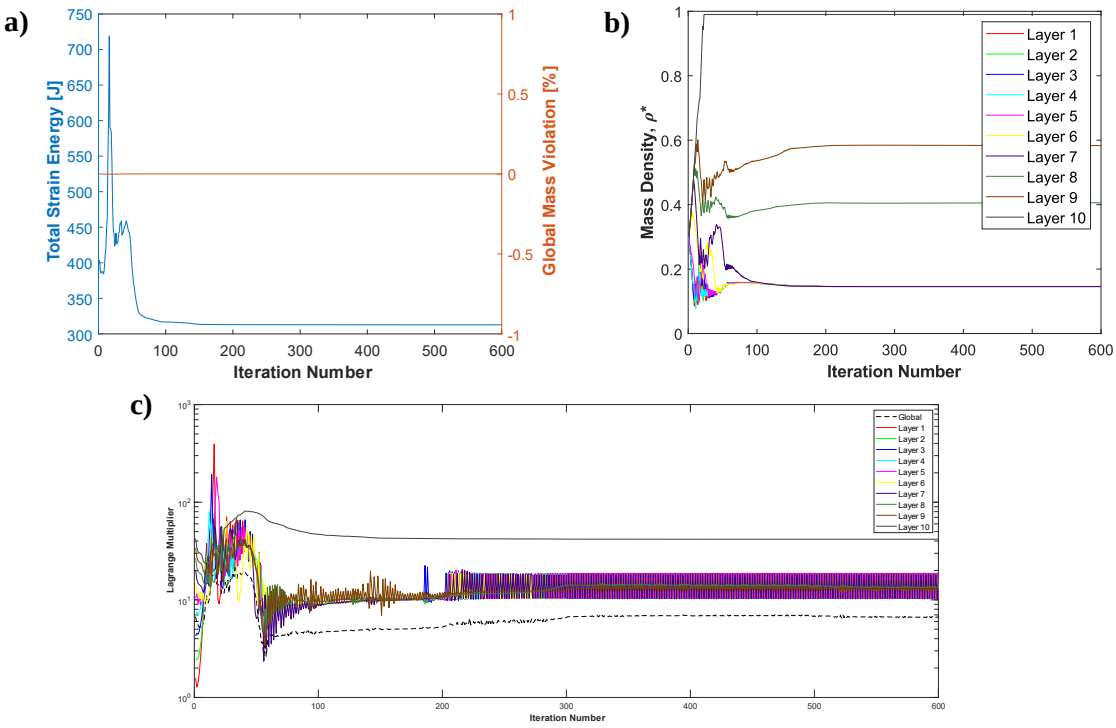

Fig. 4.12: Optimization history of the Type II Strategy with GMMA using density filter: (a) Total strain energy and global mass constraint violation; (b) Mass density values; and (c) Lagrange multiplier values.

The single-material hierarchical problem was solved using different algorithmic strategies and filtering techniques, where optimal solutions with similar total strain energy values were found (see Table 4.2). Thus, it can be stated that all different approaches manage to solve the problem. Nevertheless, it is appropriate to perform a comparative analysis among the different approaches used. The Type I Strategy using OC is the simplest approach to solve the single-material hierarchical problem, as previously mentioned. The OC method is straightforward to implement, but the most challenging part is tuning its parameters. This can be a time-consuming task, discouraging the use of this method. Besides, this method is characterized by an unstable convergence (see Fig. 4.6) and its efficiency can be questioned when dealing with several constraints. Alternatively, GMMA can be used to solve the hierarchical problem using a Type I Strategy. This robust optimizer is suitable to solve optimization problems with high number of design variables and low/moderate number of constraints. The convergence is now much smoother compared to OC (see Fig. 4.8). Since GMMA optimizes all micro design variables at the same time, the various local design problems cannot be tackled on different processors (coarse-grain parallelism). Only fine-grain parallelism can be applied in this case (e.g., to GMMA). However, this is not ideal

from a computational efficiency point of view. A coarse-grain parallelism is preferable over a fine-grain parallelism whenever it is possible. With this in mind, the Type II Strategy is the most promising approach to solve the hierarchical problem. When using this strategy, the optimality condition (4.4) must be verified in the optimum (see Figs. 4.10c and 4.12c). Both the sensitivity filter and density filter were tested out using this strategy. The density filter tends to optimal designs with increased strain energy (see Table 4.2). In Fig. 4.12a, the total strain energy does not monotonously decrease due to the *continuation approach* applied to the penalization exponent p in the SIMP law during the first 50 iterations. In fact, such continuation approach proved to be beneficial whenever the density filter is used. Using the density filter, one can explore different objective functions beyond compliance (out of the scope of this work).

Table 4.2: Total strain energy values obtained using different algorithmic strategies and filtering techniques. SF means Sensitivity Filter and DF means Density Filter.

	Type I Strategy (OC)	Type I Strategy (GMMA)	Type II Strategy (GMMA - SF)	Type II Strategy (GMMA - DF)
Total Strain Energy [J]	285.93	283.50	288.60	312.73

4.5.1.2 Element-by-Element

This section presents the obtained results solving the single-material hierarchical problem using the Type II Strategy, the sensitivity filter and an Element-by-Element parametrization. In Fig. 4.13 one shows the mass density distribution ($\boldsymbol{\rho}^*$), where now each macro element can have a different mass density and consequently a different microstructure. Representing all microstructures would be cumbersome, so only a few are shown here. Stress plots are provided as well for both macro and micro scales. Symmetry is not enforced when solving the optimization problem. Fig. 4.14 shows the optimization history.

An Element-by-Element parametrization naturally has greater design freedom, achieving designs with better performance (greater stiffness) compared to the Layer-by-Layer parametrization. The strain energy value obtained here is 223.32 J, which represents a decrease of 22.6% compared to the optimal solution obtained using a Layer-by-Layer parametrization. However, some microstructures lost the material connectivity. This is the major drawback of this parametrization and must be conveniently addressed in the future.

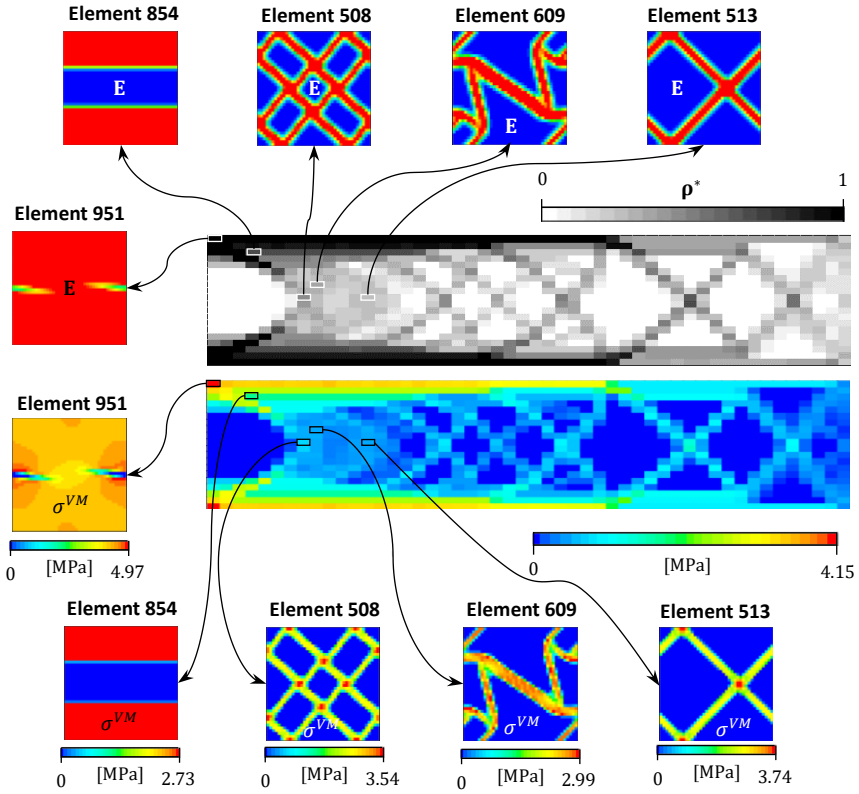

Fig. 4.13: Results obtained solving the single-material hierarchical problem using an Element-by-Element parametrization.

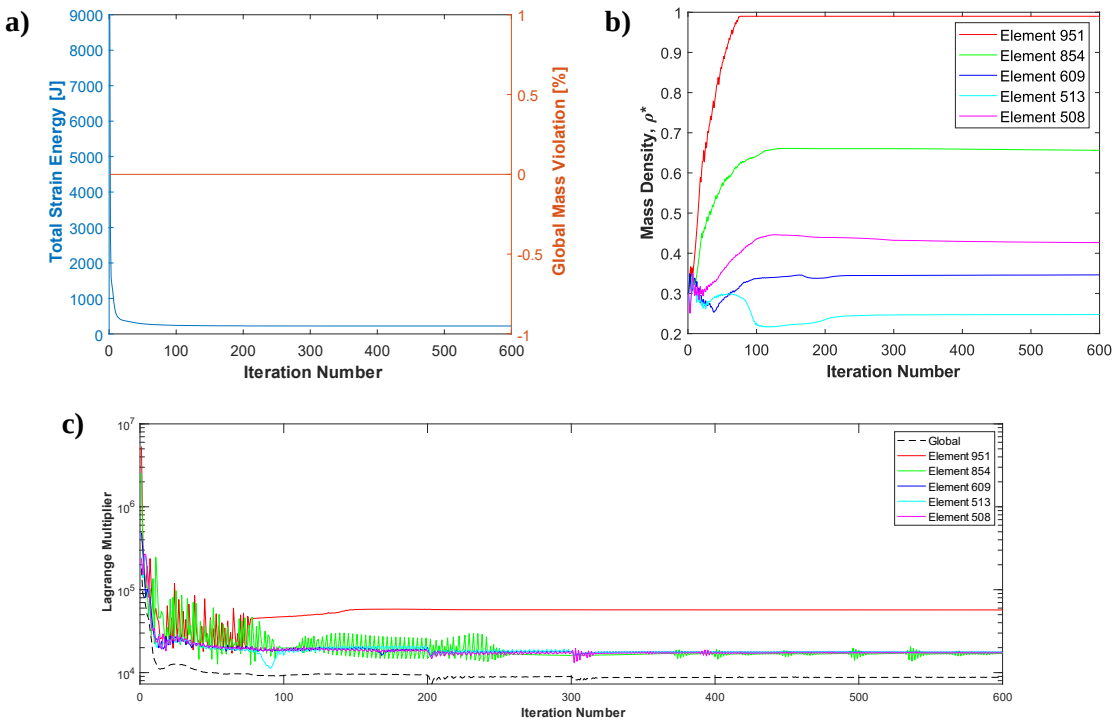

Fig. 4.14: Optimization history of the single-material hierarchical problem using an Element-by-Element parametrization: (a) Total strain energy and global mass constraint violation; (b) Mass density values; and (c) Lagrange multiplier values.

4.5.2 Multi-Material Hierarchical TO

The objective of this section is to support the premise that structures composed of more than one solid material perform better than single-material structures. In this case, one aims to improve the global stiffness of a structure with a given mass threshold by designing its microstructure using two different solid materials (Steel and Aluminum, see material properties in Table 3.2). The color scheme used to plot the material properties distribution **E**, follows the one used in Chapter 3, i.e., the red corresponds to steel, the green to aluminum and the blue to void.

4.5.2.1 Layer-by-Layer

Here one solves the multi-material hierarchical TO problem formulated in (4.1) and (4.2). Once again, both types of algorithmic strategies can be used to solve this problem. For brevity, only results obtained using a Type II Strategy and two filtering techniques are presented. The results obtained here are to be compared with the single-material ones to see if improvements are achieved. Fig. 4.15 and Fig. 4.17 show the optimal multi-material solutions using the sensitivity filter and density filter, respectively. The corresponding optimization histories are right bellow in Fig. 4.16 and Fig. 4.18. Table 4.3 shows the total strain energy values for the multi-material solutions and the decrease δ in these values compared to the single-material solutions with the corresponding filtering technique.

Table 4.3: A comparison between the total strain energy values obtained for multi-material and single-material using different filtering techniques.

	Multi-Material (SF)	Multi-Material (DF)
Total Strain Energy [J]	234.43	255.10
δ [%]	-19	-19

Performing hierarchical multi-material TO one discovers designs with increased performance compared to the single-material ones. An increase on material's stiffness of approximately 20% is achieved by considering multi-material design. Even further gains could be achieved for lower mass thresholds. Besides the increased stiffness of multi-material designs, they are less stressed than their single-material counterparts, meaning stronger designs as well.

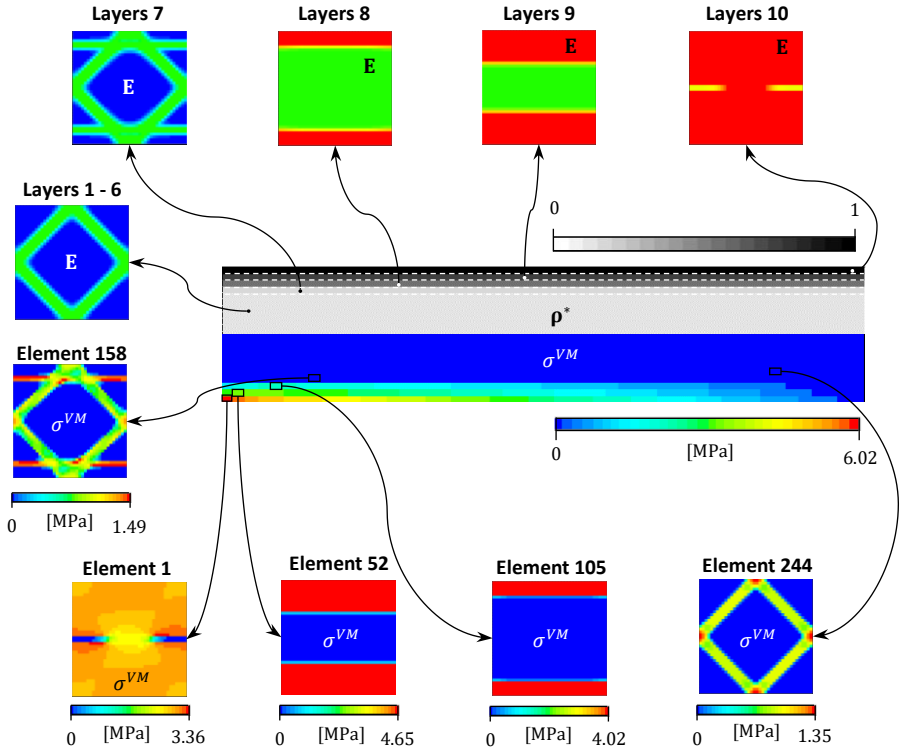

Fig. 4.15: Results obtained solving the multi-material hierarchical problem using the Type II Strategy with GMMA. Sensitivity filtering technique is used here.

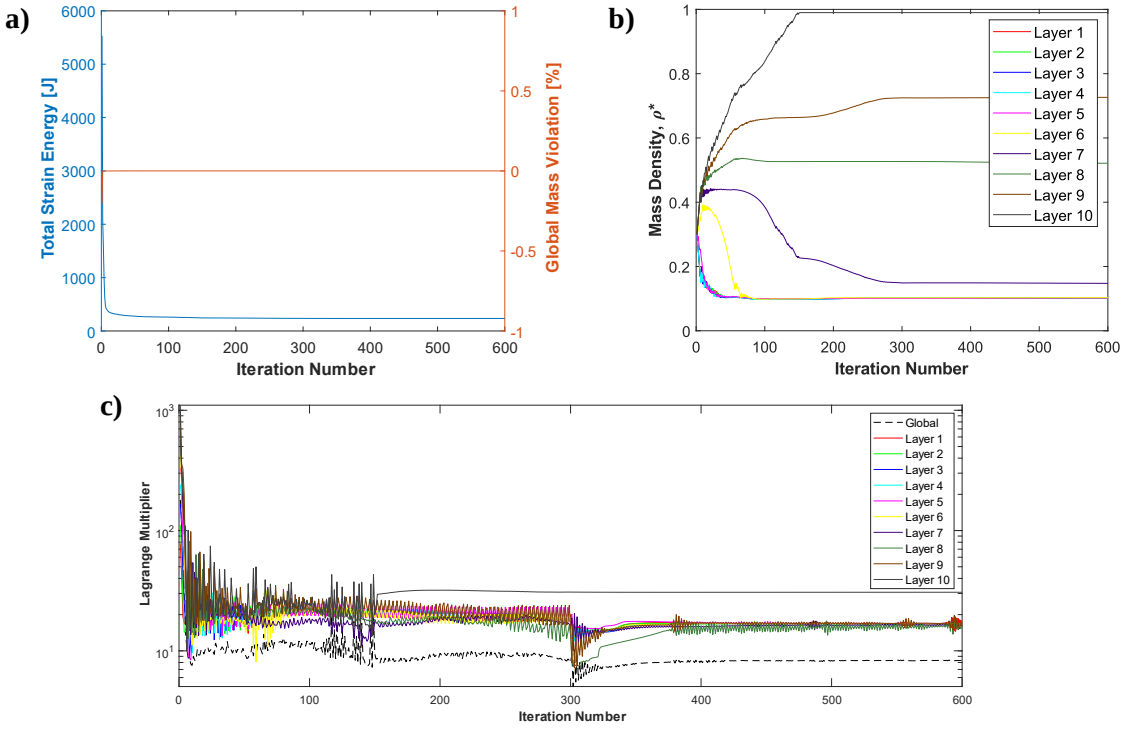

Fig. 4.16: Optimization history of the Type II Strategy with GMMA using sensitivity filter: (a) Total strain energy and global mass constraint violation; (b) Mass density values; and (c) Lagrange multiplier values.

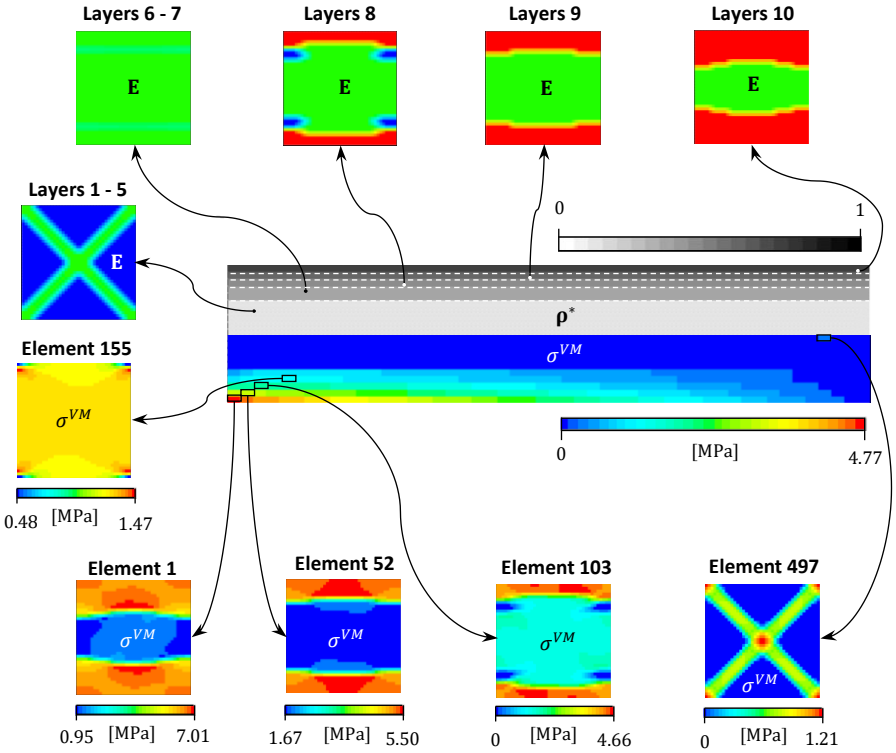

Fig. 4.17: Results obtained solving the multi-material hierarchical problem using the Type II Strategy with GMMA. Density filtering technique is used here.

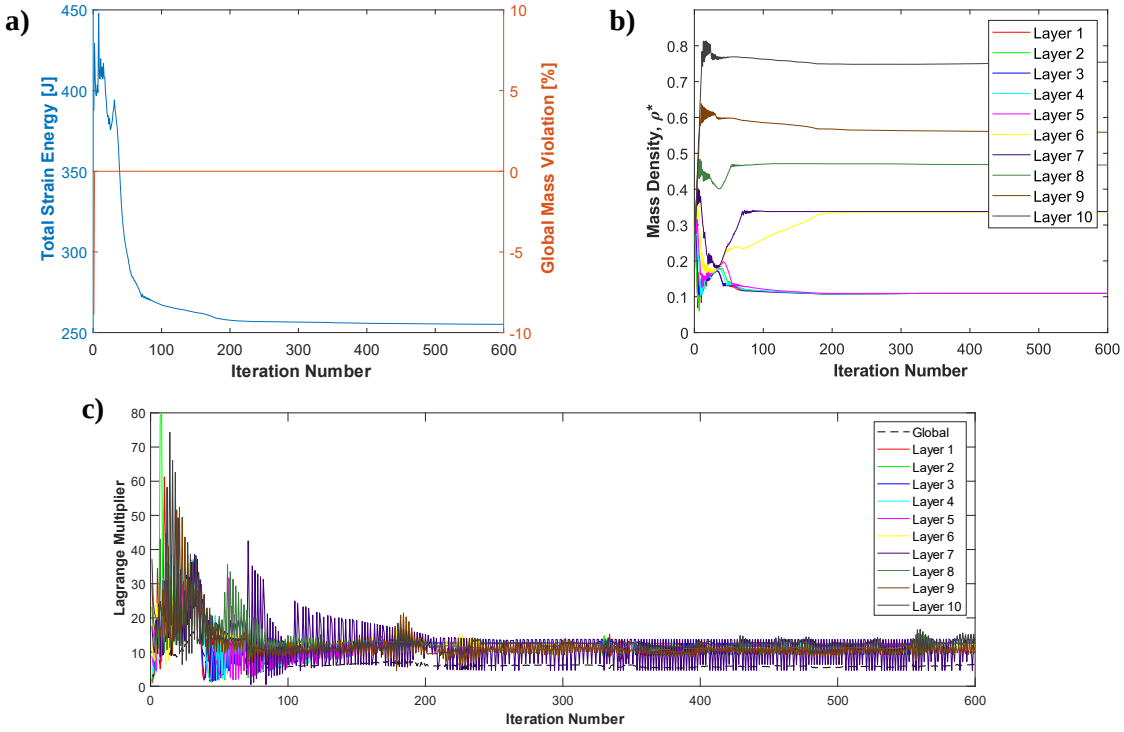

Fig. 4.18: Optimization history of the Type II Strategy with GMMA using density filter: (a) Total strain energy and global mass constraint violation; (b) Mass density values; and (c) Lagrange multiplier values.

4.5.2.2 Element-by-Element

Here one solves the multi-material hierarchical problem using an Element-by-Element parametrization. The optimal designs are shown in Fig. 4.19, where the total strain energy value is 193.78 J. Comparing this value with the one obtained solving the single-material version of the problem, an increase of 13% in the overall structure's stiffness is achieved by considering multi-material-design. Less stressed microstructures are typically obtained by performing multi-material design, despite here the maximum macro stress value is actually greater.

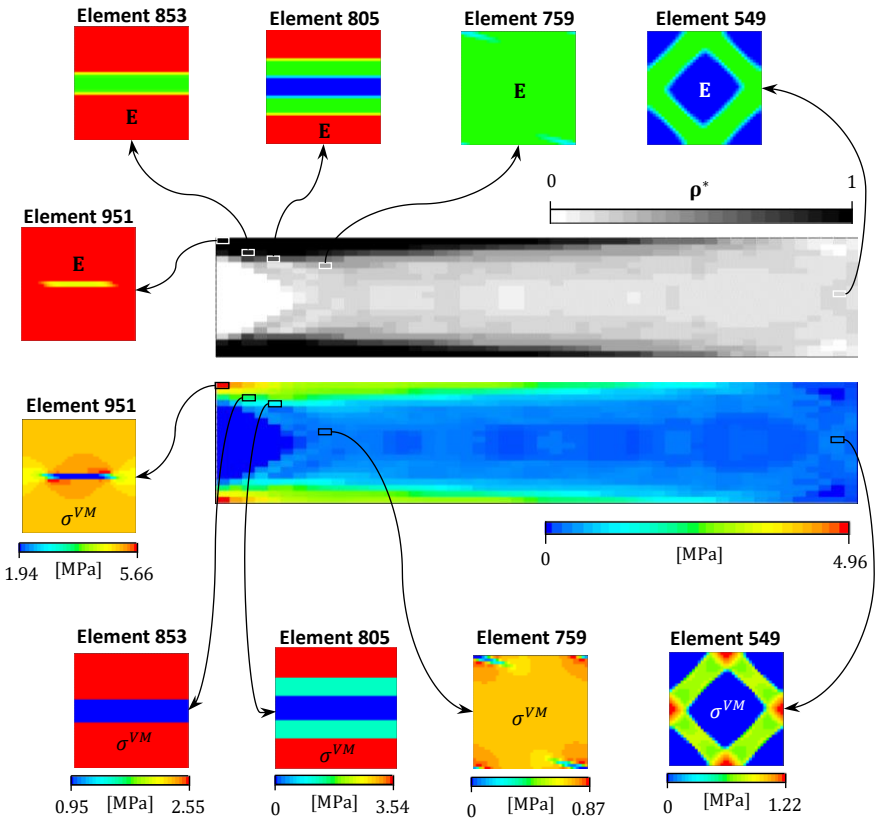

Fig. 4.19: Results obtained solving the single-material hierarchical problem using an Element-by-Element parametrization.

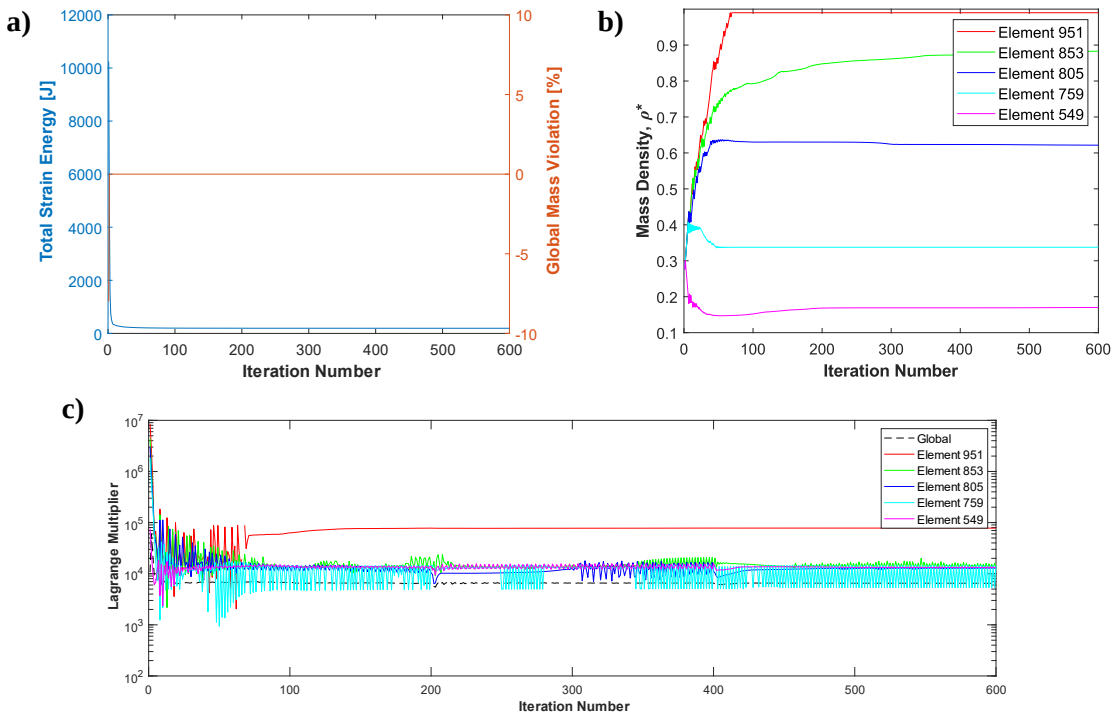

Fig. 4.20: Optimization history of the multi-material hierarchical problem using an Element-by-Element parametrization: (a) Total strain energy and global mass constraint violation; (b) Mass density values; and (c) Lagrange multiplier values.

4.6 Conclusions: Multi-Scale Topology Optimization

Multiscale topology optimization is an interesting, challenging, and quite active research thematic. This part of the work contributes to the state-of-art of this thematic by successfully performing multi-scale TO considering multi-material design in the microscale aiming for improved overall structure's stiffness. The hierarchical optimization problem solved here considers the compliance minimization subject to mass constraint.

Two different macro design parametrizations are used and compared within the scope of this part of the work. On one hand, an Element-by-Element parametrization of the macro domain is considered. In this case, to each macro FE is associated a periodic material/microstructure that needs to be locally optimized. Therefore, there are as many local problems to solve as macro elements. This parametrization offers the possibility of optimizing the material domain of a structure in a pointwise manner, at the expense of poor manufacturability and high computational cost. On the other hand, one also considers a Layer-by-Layer parametrization that divides the macro domain into several subdomains, each one composed of a pair of symmetric layers. This parametrization delivers optimal designs with decent manufacturability at reduced computational cost

but with worst performance when compared to the ones obtained using an Element-by-Element parametrization.

The hierarchical problem can be solved using two different algorithmic strategies, the so-called Type I and II Strategies. Both strategies managed to solve the problem, where different solutions but with similar performance were obtained. The Type II Strategy is the most promising technique to solve the problem when more elements and constraints are considered.

Multi-material design undoubtedly offers the possibility to improve structural performance. This was proved back in Chapter 3 for single scale (microscale) problems for stiffness and stress. In this chapter, the overall stiffness of a multi-scale structure composed of two different solid materials is improved compared to the single-material structure for the same mass. The minimum compliance problem solved in its multi-material version tends to less stressed designs, which is in agreement with what was said back in Chapter 3. Exception made for the results obtained using an Element-by-Element parametrization. In fact, solving the multi-material hierarchical problem for compliance minimization does not guarantee a lower stress peak on the structure. The only way to assure this is to control the stresses through design constraints, which is an interesting path for future works. However, performing a stress-based multiscale optimization is not straightforward. Besides, the issue related with non-defined Lagrange multipliers using a Type II strategy when the micro design variables touch their bounds must be correctly handled to avoid irregularities in the stress field that might compromise the optimization procedure.

PART TWO

Microstructural Optimization in Non-Linear Plastic Regime

5

STATE OF THE ART: LONGITUDINAL FRACTURE OF HYBRID COMPOSITES

So far, the focus of this work was on modelling and optimizing composite materials aiming for stress and compliance reduction. In Chapter 3, a microstructural stress-based topology optimization was carried out, achieving optimal microstructures with minimal stress values. In that study, exceeding the yield strength (failure) of the material was disregarded. Undoubtedly, this is a rather important aspect when designing a composite structure. Now, such consideration is studied within the frame of unidirectional (UD) fibre-reinforced composites. This second part of the dissertation consists in modelling the fracture of UD composites, which are characterized by having a brittle failure, and optimize its non-linear behaviour in order to have a more safe and controlled failure by means of introducing a so-called pseudo-ductile behaviour.

This chapter begins with a brief introduction to the mechanisms of longitudinal fracture of UD composites. Multi-material design of UD composites, by means of fibre hybridization, aiming for a pseudo-ductile behaviour is then discussed.

5.1 Mechanisms of longitudinal fracture

Modelling composite materials is a challenging task due to the complexity of its internal structure and interactions between constituents (interface fibre/matrix). The mechanisms of longitudinal failure of UD composites under longitudinal loadings are based on two essential aspects: (1) fibres do not have a deterministic value for tensile strength [156] and (2), after a fibre fractures,

the stress is redistributed among the intact fibres in a complex way [157]. The failure of UD composites occurs in the following way: as one increases the applied strain, the weakest fibres fail, meaning that, locally, they are no longer able to carry stress. At low applied strains the fibres fail in random locations and there is nearly no interaction between breaks. Once a fibre fractures, the matrix is loaded and it transfers the load back to the broken fibre, making it able to carry stress away from the point of fracture. The stress is redistributed to the remaining intact fibres by the matrix, which leads to stress concentrations in the intact fibres, increasing their probability of failure. The stress concentration in the intact fibres will cause their failure leading to the creation of clusters of broken fibres. These clusters will grow, when other fibres fail and, when a cluster reaches a certain critical size, it will propagate unstably leading to the failure of the composite. Therefore, the tensile strength of a UD composite is of statistical nature and function of the mechanics of load redistribution around broken fibres [158]. In Fig. 5.1 is shown this process, helping to understand the failure of UD composites.

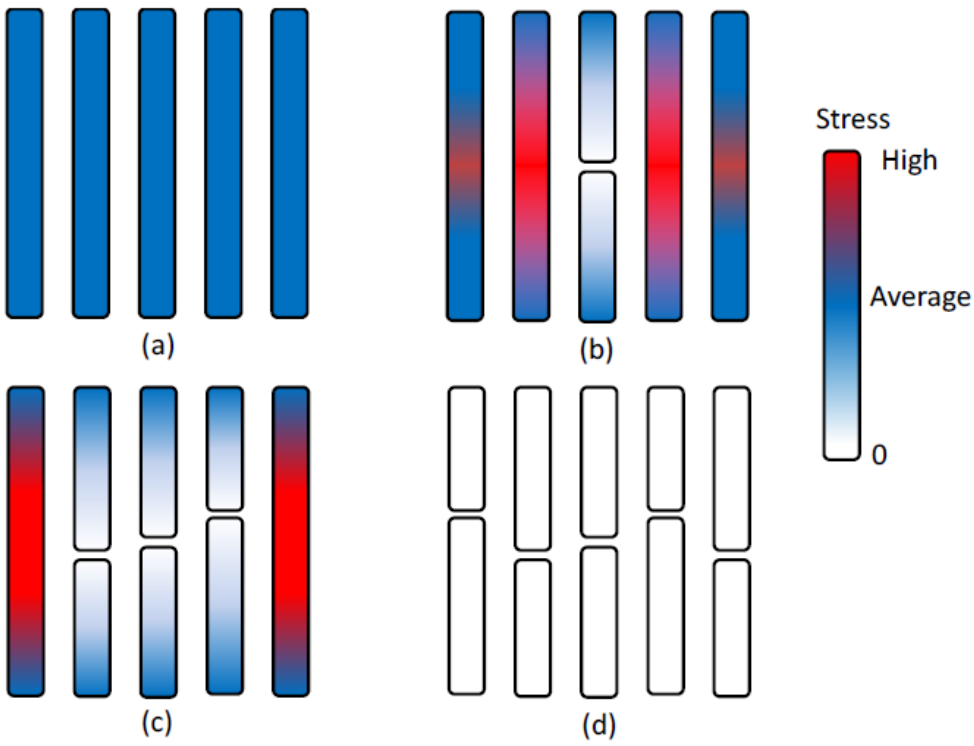

Fig. 5.1: Schematic representation of the failure development in unidirectional non-hybrid composites: (a) all fibres intact, (b) one broken fibre, with the surrounding fibres subjected to stress concentrations, (c) development of a broken fibre cluster, and (d) crack propagation and final failure. Retrieved from [159].

As previously mentioned, fibres do not have a single and deterministic value for tensile strength. Due to their brittle behaviour the fibre tensile strength is governed by surface or volume flaws [156] and exhibits weak-link characteristics. There are several statistical distributions that

can be used to characterize the strength of fibres, being the most used the Weibull distribution, proposed by Weibull in 1951 [160].

5.1.1 Weibull distribution

The standard Weibull probability distribution is given by:

$$P(\sigma) = 1 - \exp\left(-\left(\frac{L}{L_0}\right)\left(\frac{\sigma}{\sigma_0}\right)^m\right) \tag{5.1}$$

where P is the failure probability at the applied stress σ, L is the characteristic gauge length, L_0 is the reference gauge length, σ_0 is the scale parameter and m is the shape parameter or Weibull modulus [160].

This distribution usually leads to the overestimation of the fibre strength at short gauge lengths [161] and it is very sensitive to the statistical parameters [162]. The discrepancy between the Weibull distribution and the experimental results for short gauge lengths can be attributed to variations in fibre diameter, variations of the Weibull distribution from fibre to fibre and presence of different flaw populations [161]. According to Curtin [163] this distribution is not the most accurate to describe the strength of fibres, however it is still the most used to characterize the tensile strength of technical fibres.

Determining the values for the parameters of this distribution is not straightforward, i.e., many fibre samples need to be tested in order to find representative values. Problems associated with obtaining statistical parameters make it difficult to obtain a simple distribution to characterize a property and, therefore, many statistical parameters can be found in the literature for the same fibre.

5.1.2 Stress redistribution after fibre failure

Remember that a broken fibre does not fully lose its load carrying capability because the surrounding matrix is loaded in shear and transfers stress back onto the unbroken fibre part. There are two types of approaches to simulate this effect: the Global Load Sharing (GLS) and the Local Load Sharing (LLS).

In a GLS model, the stress released from a broken fibre is equally distributed among the remaining unbroken fibres because the interaction between fibres is not taken into account and so no local fields due to fibre fracture are considered [164].

On the contrary, a LLS model takes into account the interaction between fibres in the longitudinal failure of UD composites [165]. The interaction between the fibres and between the fibres and the matrix results in a non-uniform stress redistribution to the intact fibres, which is highly dependent on the composite geometry [166]. For composite systems the redistribution of stresses is a complex process that depends on several parameters, including the strength and sliding resistance of the fibre/matrix interface, the fibre to matrix moduli ratio, the matrix cracking or yield stress, the regularity of the fibre spacing and debonding of the fibre-matrix interface [167].

This complex stress redistribution is often characterised by the Stress Concentration Factor (SCF) and the ineffective length [161]. The SCF is defined as the ratio between the longitudinal stress in an intact fibre after the failure of a neighbour fibre and the longitudinal stress in the absence of breaks. The ineffective length is a measure of the stress recovery length of the fibre and can be defined, for instance, as twice the length at which the broken fibre can carry 90% of the applied stress [168]. These parameters are crucial to model composite materials as they affect the stress redistribution and, therefore, the damage accumulation and the formation of clusters of broken fibres. The redistribution of stresses closely depends on the fibre packing of the UD composite [158], see Fig. 5.2.

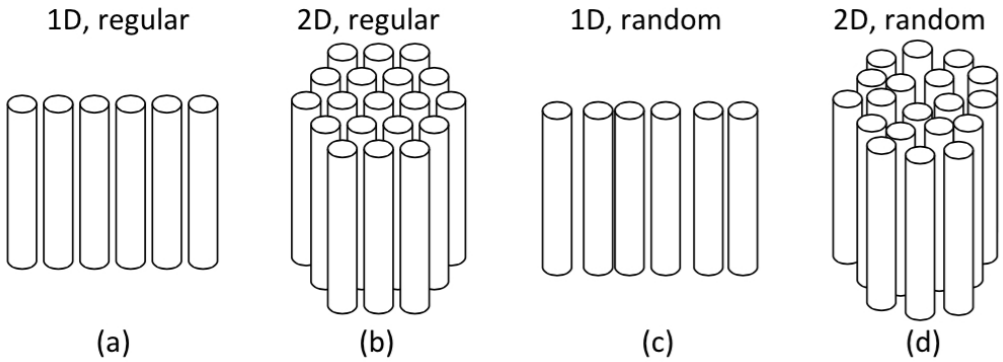

Fig. 5.2: Schematic illustration of fibre packings: (a) 1D regular packing; (b) 2D regular packing; (c) 1D random packing and (d) 2D random packing. Retrieved from [161].

5.1.3 Effects of the matrix and fibre-matrix interface

Despite the tensile failure of composite materials is a fibre dominated phenomenon, the matrix also plays an important role, according to Fig. 5.3. Composite materials made with a more ductile matrix are stronger than composites made with a stiffer matrix. It can be also seen that the matrix strength directly impacts on the composite's strength. The matrix allows the stress recovery of a broken fibre due to shear stress transfer [161] and its properties affect the SCF and failure mechanisms.

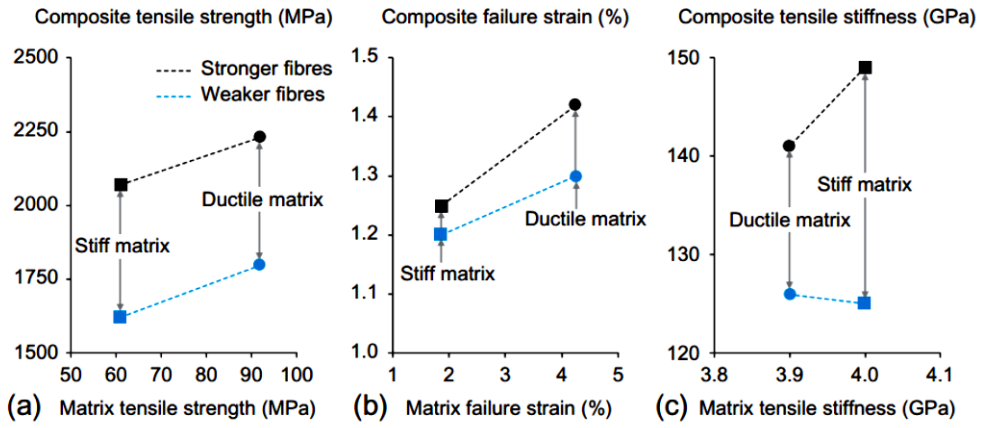

Fig. 5.3: Influence of different matrix properties on tensile properties of UD composites: (a) tensile strength, (b) failure strain and (c) tensile stiffness [169].

Several models consider the fibres and matrix to be perfectly bonded, which leads to an infinite SCF in the matrix around a fibre break. Since the matrix and the interface fibre/matrix are unable to support such a high stress, one or a combination of three scenarios can occur: (1) the matrix yields, (2) the interface debonds and (3) the matrix cracks in the break plane [161].

Zeng et al. [170] studied the influence of interfacial damage in the stress redistribution in UD composites and concluded that the stress concentrations increased with increasing the strength of the interface. He also concluded that matrix shear yielding resulted in lower stress concentration factors in intact fibres. The matrix yield strength also affects the ineffective length significantly, the lower the shear yield stress, the larger the ineffective length [171]. Interfacial debonding tends to occur in composites with weak interfacial bonds and has a similar effect as matrix yielding. [158]

Recently, Swolfs et al. [172] studied the influence of matrix cracks in both the SCF and the ineffective length in a composite with a random distribution of fibres. It was concluded that the matrix cracking increases the ineffective length, drastically changing the stress recovery profile. As one can see in Fig. 5.4, the stress in the broken fibre rapidly increases to 35% when there isn't a crack in the matrix, however, in the model with a crack, the stress slowly increases from zero, due to the presence of a crack in the matrix. It was also shown that matrix cracks not only increase the ineffective length but also the stress concentration factor, leading to an overall higher failure probability of the intact fibres. [158]

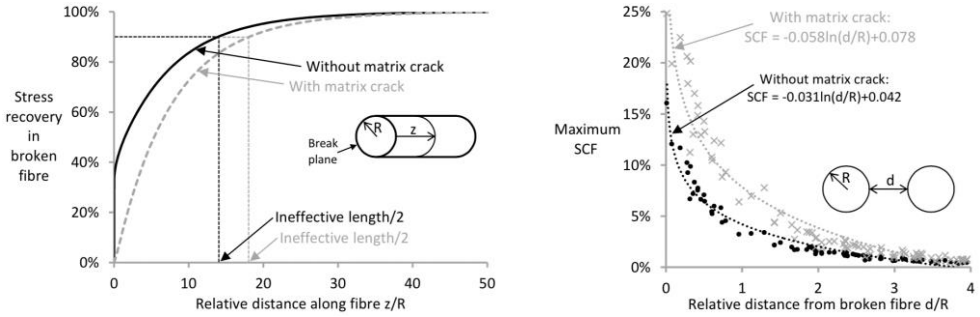

Fig. 5.4: Effect of matrix cracks in the ineffective length (left) and the stress concentration factors (right) [161].

5.1.4 Critical cluster size

The failure of a UD composite under tensile loads is due to the unstable propagation of a cluster of broken fibres. The clusters are formed due to stress concentrations in the intact fibres that neighbour a broken one. This increase in SCF causes the stress in the intact fibres to increase, thus increasing their probability of failure, increasing the probability of fibres to break in clusters. When a cluster of broken fibres is large enough, it propagates in an unstable manner leading to the composite failure. Critical cluster size is, therefore, an important topic in understanding the failure of UD composites. [158]

Ibnabdeljalil and Curtin [173] studied this problem and derived an equation for the critical cluster size (n^{crit}):

$$n^{crit} = 403m^{-1.28} \tag{5.2}$$

where m is the Weibull modulus. This equation was derived from numerical simulations using Green's function for stress redistribution, whose parameter Ω characterises the level of localization of the stress redistribution. The result presented in Eq. (5.2) is for $\Omega = 0.001$, that represents a very local load sharing model ($\Omega \to \infty$ corresponds to global load sharing). As the Weibull modulus presents some degree of dispersion, even for the same type of fibre, one can expect that, in a composite material, there are stronger and weaker regions, which will translate in variations of the critical cluster size and composite strength. [158]

5.1.5 Modelling the tensile failure of unidirectional composites

There are several models to predict the tensile failure strength of UD composites in the literature. In this Section, one will briefly describe three different types of models: (1) analytical fibre bundle models, (2) continuum damage mechanic-based models, and (3) micromechanical models based on Monte-Carlo simulations.

5.1.5.1 Analytical fibre bundle models

Fibre Bundle Models (FBMs) consider a bundle of parallel fibres with stochastic tensile strength, but with the same elastic properties and loaded under uniaxial tension [174], see Fig. 5.5. When the remote stress is high enough that causes a fibre to fail, the stress is redistributed towards the remaining intact fibres. If the stress concentration, due to this stress redistribution, is enough to cause another fibre to fail, the stress is redistributed again, and so on. Otherwise, the remote stress is increased. This process is repeated until all fibres fail or until the material cannot withstand further load increments.

FBMs have been developed for dry bundles (with no matrix) and for composite materials, considering the influence of the matrix. The matrix acts as a connector between fibres and alters the stress redistribution, affecting the ineffective length (δ) and the stress concentrations in the neighbouring fibres of a broken one.

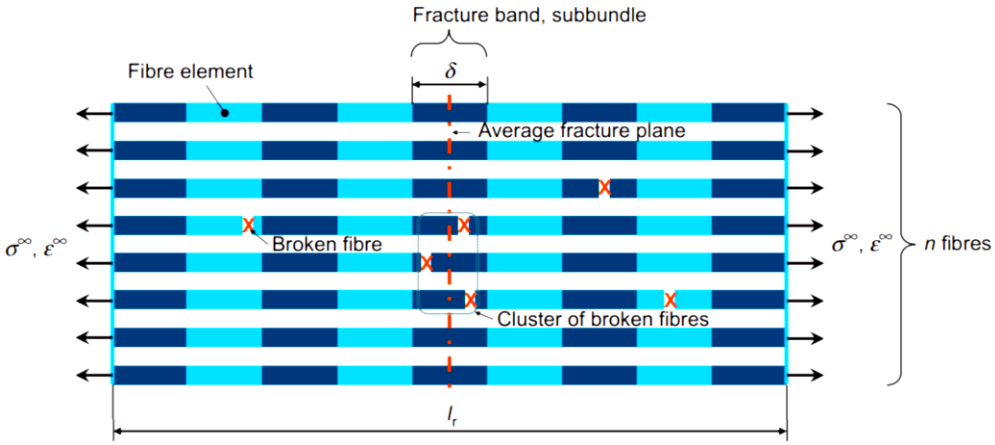

Fig. 5.5: Diagram of a fibre bundle model with length l_r, subject to an applied stress σ^{∞} or strain ε^{∞}. Retrieved from [169].

According to the stress distribution rule these models can be divided into GLS and LLS models. The GLS models are able to predict the failure of a dry bundle where the interaction between the fibres is low [175]. The LLS models consider that there isn't a uniform stress redistribution due to the presence of the matrix.

5.1.5.2 Continuum damage mechanic-based models

The failure mechanisms of UD composites can be described in the framework of continuum damage mechanics. This type of modelling uses simple definitions of internal damage variables, formulated in the framework of the thermodynamics of irreversible processes [174]. These damage variables are then used to alter the mechanical properties of the constituents, namely the reduction of stiffness.

This type of modelling has been tackled by several authors and can be divided into three stages: (1) definition of a suitable norm for the damage variable, (2) definition of a damage criterion and (3) definition of the evolution law for the damage variable [176].

More recently, Turon et al. [176] developed a progressive damage model, implemented in a FE model, based on fibre fragmentation for UD composites to study the effect of several parameters on the stress-strain curve and were able to accurately capture the stiffness loss in UD composites. This model proposes a degradation of composite effective stiffness based on fibre fragmentation. The fibre fragmentation model considers that the fibre strength follows a Weibull distribution, and when the applied stress reaches the fibres tensile strength it will break. A broken fibre is still capable of carrying stress (shear lag theory), and therefore it can fracture again at a certain distance from the original fracture. A fibre will fracture into shorter fragments until the shear stress transfer across the interface is no longer able to cause another fracture, see Fig. 5.6.

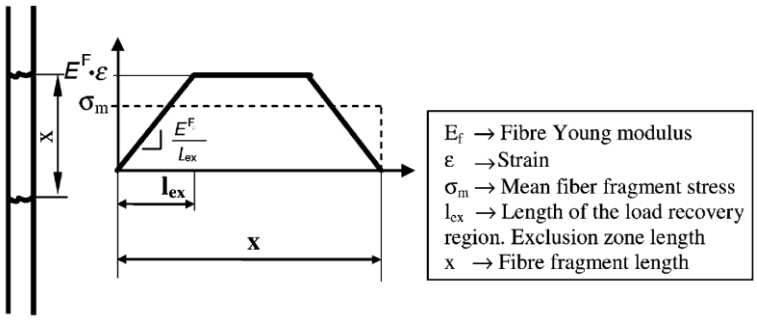

Fig. 5.6: Stress profile at a fragment of broken fibre. At a break the axial stress is zero and it increases until it reaches the far-field stress (also known as ineffective length). Retrieved from [176].

5.1.5.3 Micromechanical models based on Monte-Carlo simulations

Recently, several micromechanical models based on Monte-Carlo simulations have been developed in order to model the behaviour of UD composites. These models simulate the accumulation of fractures in a large number of fibres and the corresponding redistribution of stresses for an increasing applied load. This analysis is repeated many times with different fibre strengths, which are usually derived from the Weibull distribution, until a sufficient number of results are obtained to characterize the material's behaviour.

The main challenges when developing a Monte-Carlo simulations-based model are: (1) calculate the stress fields around broken fibres and (2) perform a progressive failure analysis of cluster growth. According to [169], these models are usually grouped into three different categories: (1) Single-step Spring-based models, (2) Combined field-superposition and fibre bundle simulations and (3) Finite Element (FE) models.

Single-step spring-based models consider a lattice of nodes that are longitudinally connected by fibre springs and transversely by matrix springs. The fibre springs can only support longitudinal load and their strength is stochastic. The matrix springs are considered to only being able to support shear stress. The movement of the nodes is limited to longitudinal displacement, which means that there is only one degree of freedom per node. One of the most acknowledged single-step spring-based models is the one developed by Okabe et al. [177,178] and is named Spring Element Model (SEM).

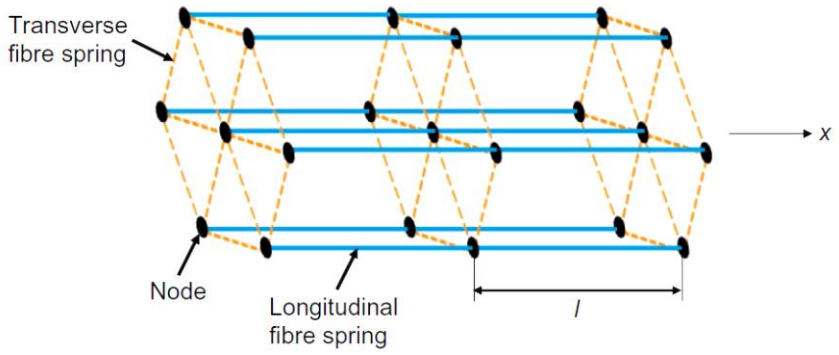

Fig. 5.7: Schematic representation of a Spring Element Model. Retrieved from [169].

The combined field-superposition and fibre bundle models consider the superposition of stress fields around a broken fibre. The stress fields are obtained for a single broken fibre, and a superposition of the fields is imposed as more fibres break. These stress fields are included in the Monte-Carlo simulations of fibre bundles. Briefly, combined field super-position and fibre bundle

simulations models derive from the basic fibre bundle models (Section 5.1.5.1), but consider more accurate stress redistribution rules. One of the most recent models was developed by Swolfs [161].

FE are extensively used in modelling composite materials. However, the prediction of micro-mechanical behaviour requires extremely refined meshes, making the models computationally costly. This fine mesh is required in order to accurately capture the stress redistribution. In order to avoid the use of such refined meshes in full scale models, coupled two-scale FE models have been developed [179,180]. This separation of micro-macro scales allows the simulation of composites specimens with millions of fibres. [158]

5.2 Fibre hybridization

Hybrid composites behave differently than non-hybrid composites. In this Section, the focus is on understanding how these hybrid composites work in order to introduce a pseudo-ductile behaviour on them. Firstly, one will briefly describe hybrid composites and the so-called hybrid effect. Afterwards, a study on the failure and stress redistribution in UD hybrid composites is performed. Ultimately, fundamental concepts to model the failure stress of these composites will be addressed.

5.2.1 Hybrid composites

Hybrid composites can be defined as a composite material that contains more than one of type of fibre and/or matrix system [181]. In this work, hybrid composites with more than one type of fibres, more precisely two, are consider. These are known as fibre hybrid composites and is the most common set up of hybrid composites.

Fibre hybridization allows to maintain the advantages of both fibres while mitigating some disadvantages. For instance, replacing some carbon fibres in the laminate with glass fibres can significantly reduce its cost, while the flexural properties of the composite remain practically unchanged. If a set of hybrid fibres is subjected to a uniaxial load, the more fragile fibres are, the sooner they will break. This behaviour at the failure of the composite can be used for purposes of failure monitoring [182] or as a warning signal before the material fails [183].

In hybrid composite materials it is usual to refer the two types of fibres as: Low Elongation (LE) and High Elongation (HE) fibres. The LE fibres are the ones that have the lowest failure strain, being the first ones to fail. On the contrary, the HE fibres have the highest failure strain,

being the last ones to fail. Note that high and low are relative terms, i.e., a given fibre can be LE if it is paired with a fibre that has a higher failure strain, however, if the same fibre is now paired with another fibre that has a lowest failure strain, the fibre initially designated as LE becomes HE.

The LE and HE fibres can be combined in different ways, where the most important ones are shown in Fig. 4.1.

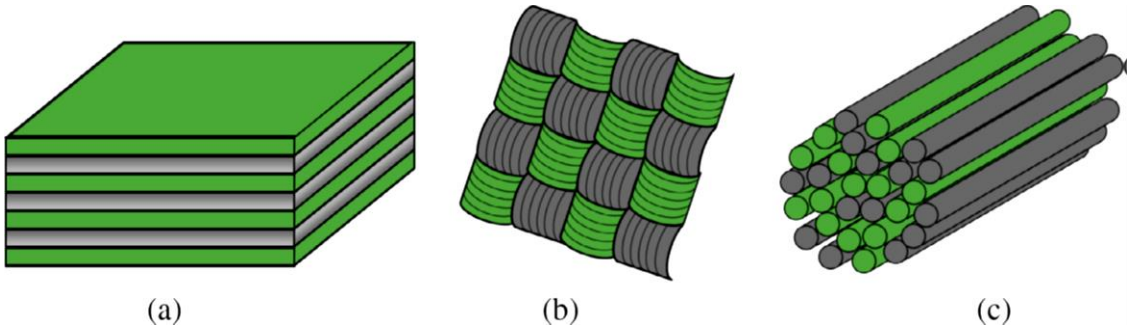

Fig. 5.8: Hybrid configurations: (a) interlayer, (b) intralayer and (c) intratow configurations. Retrieved from [159].

As illustrated in Fig. 4.1, there are mainly three types of fibre-hybrid composites, defined according to the configurations of both fibre types:

- **Interlayer** or layer-by-layer hybrids have different types of fibres in different layers, being that each layer only has a single fibre type (Fig. 5.8a);
- **Intralayer** or yarn-by-yarn hybrids have both types of fibres in a single layer (Fig. 5.8b);
- **Intratow** or fibre-by-fibre hybrids have both fibre types in a single tow (Fig. 5.8c). This type of configuration is the one that leads to a better dispersion of both fibre types.

An important factor in the behaviour of hybrid composites is the dispersion of the two types of fibres. Fibre dispersion is a measure of how well mixed the fibres are in a hybrid composite, and it is defined has the reciprocal of the length of the smallest repeat unit of the composite [184,185]. In Fig. 4.2 different degrees of fibre dispersion are illustrated.

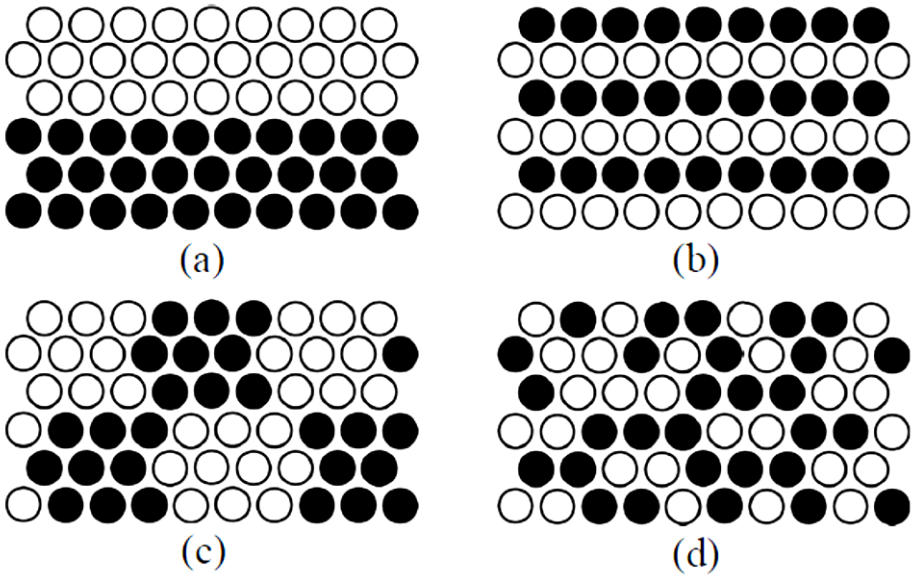

Fig. 5.9: Dispersion in hybrid composites: the degree of dispersion increases from (a) to (d). Retrieved from [159].

In Fig. 4.2a, a hybrid composite with low dispersion is illustrated, since the two types of fibre are arranged in two distinct layers. The dispersion can be increased by increasing the number of layers or decreasing the thickness of the layers, as illustrated in Fig. 4.2b. Another way to increase the degree of dispersion is to hybridize fibre bundles, as seen in Fig. 4.2c. The best degree of dispersion is achieved when the fibres are randomly arranged, as in Fig. 4.2d.

In the thematic of hybrid composites, the hybrid effect is often mentioned, whose definition and characteristics will be presented below.

5.2.2 Hybrid effect

In 1972, Hayashi [186] defined the hybrid effect when he noticed that the apparent failure strain of the carbon fibres in a carbon/glass hybrid was enhanced in relation to that of the non-hybrid carbon composite. This experimental observation led to the creation of the first definition of hybrid effect, defined as the apparent failure strain enhancement of the LE fibres in a hybrid composite compared to the failure strain of the LE fibres in the non-hybrid reference composite (Fig. 5.10).

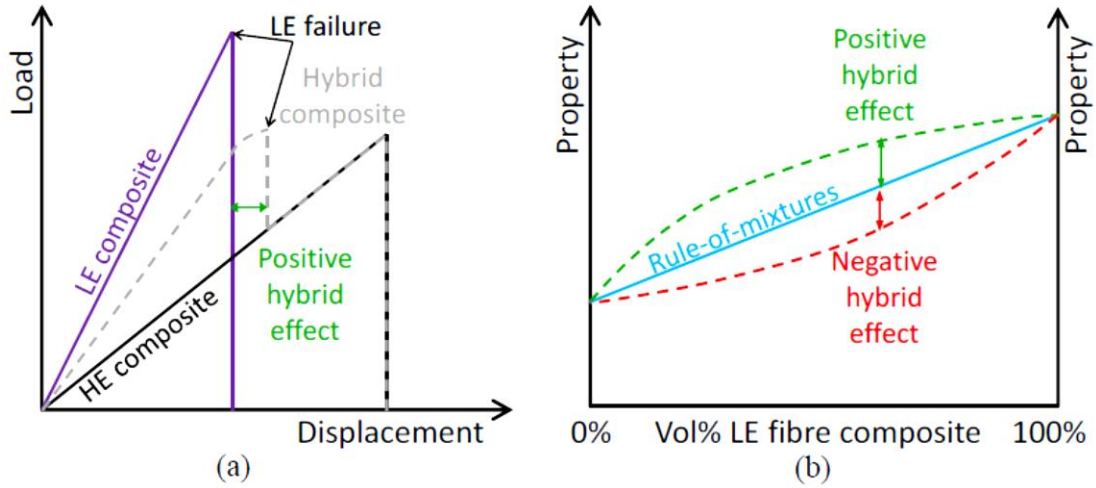

Fig. 5.10: Diagrams for the definition of the hybrid effect: (a) first definition proposed by Hayashi and (b) general definition based on the rule-of-mixtures. Retrieved from [159].

The definition proposed by Hayashi [186] for the hybrid effect refers only to the enhancement of apparent failure strain, however, hybridization introduces changes in other mechanical properties [184]. This led to the necessity of a new, more general definition for the hybrid effect. Hybrid effect was then defined as a deviation from the rule of mixtures [187]. This definition is more general and allows it to be applied to several mechanical properties, also allowing the existence of positive or negative hybrid effect (Fig. 2.10b) if there is, respectively, an improvement or a deterioration of the property in question. [158]

Three different hypotheses for the hybrid effect have been coined by now: (1) residual stresses, (2) changes in the damage development leading to final failure of the hybrid composite, and (3) dynamic stress concentrations [159]. These hypotheses will be discussed next.

5.2.2.1 Residual stresses

In the first hypothesis, the hybrid effect is attributed to residual shrinkage stresses due to differences in the thermal contraction of the two fibre types. Consider the classic combination of carbon and glass fibres in an epoxy matrix. After impregnation of the fibres, the temperature is raised to cure the epoxy. Both fibres will have the tendency to change their length due to their Coefficient of Thermal Expansion (CTE). The CTE of carbon fibre is typically between -1 and +1 10^{-6} K^{-1} [185,188,189], while the CTE of glass fibre is 5 and 10 10^{-6} K^{-1} [185, 190]. This causes the glass fibres to increase their length upon heating, while carbon fibres will practically maintain their length. This does not yet result in stress build up, as the resin is still liquid [159].

After the resin is cured and the composite is cooled down, the glass fibres will shrink, while the carbon fibres will more or less maintain their length. This can only occur in a situation without constraints. In reality, the cured resin connects the layers reinforced with different fibre types and prevents them from having a different length. A force equilibrium is established, putting compressive stresses on the carbon fibres and tensile stresses on the glass fibres. These compressive stresses counteract the applied stress and increase the apparent failure strain of the carbon fibres. In contrast, the apparent failure strain of the glass fibres is reduced [159].

While the thermal effect can contribute to the hybrid effect, it is insufficient to explain the full hybrid effect [185,191]. Thus, other effects affect the hybrid effect as previously mentioned.

5.2.2.2 Failure development

The second hypothesis for the hybrid effect is related to changes in the way failure develops. As explained in the Section 5.1, the failure of unidirectional composites is determined by the stochastic strength of fibres and the stress redistribution after fibre failure. Hybridizing a composite material significantly changes both these parameters. As the composite is constituted by more than one type of fibres, their strengths will be represented by different distributions, meaning that the fibres may not fail at the same range of applied stress/strain which, by itself, strongly changes the behaviour of the composites [158].

In a fibre hybrid composite, there are two different types of fibres (LE and HE), leading to a more complex failure development than in the case of non-hybrid composites. Since LE fibres have a lower failure strain, they will probably break first, arising stress concentrations in the remaining intact fibres. As the fibres have different elastic properties the stress distribution does not depend only on the distance to the fibre break, as in non-hybrid UD composites [157, 192]. Hybridization not only changes the SCFs but also changes the ineffective lengths [193].

The HE fibres in a hybrid composite serve as bridging points, that hinder crack propagation and cluster development, delaying the failure of the composite. The intact HE fibres among the broken LE fibres increase the fragmentation process in the LE fibres, such that theses fibres will fragment multiple times [194]. Another aspect that can have effect in the damage development in hybrid materials are the size effects [195,196].

According to Swolfs et al. [192], the factor that most contributes to the hybrid effect is the fact that HE fibres support the failure of the LE fibres, delaying the failure of the composite.

5.2.2.3 Dynamic stress concentrations

The dynamic stress concentrations play an important role in the failure of UD composite materials. When a fibre breaks, the load on that fibre is locally relaxed and the fibre springs back. This creates a stress wave travelling along each fibre, causing a temporary increase in the stress concentration. This was first pointed out by Hedgepeth in 1961 [197].

Later, Xing et al [198] extended the dynamic model developed by Hedgepeth to hybrid composites. These authors considered hybrid composites composed of one row of LE and one row of HE fibres. Their theoretical model demonstrated that two independent stress waves develop and propagate through the hybrid composite when an LE fibre breaks in a hybrid composite. The first wave propagated in the LE layer, while the second one propagated in the HE layer. Both waves were always out-of-phase, which led to lower stress concentrations in LE/HE fibre-reinforced hybrid composites compared to those in LE fibre-reinforced composites. From this point of view, a positive hybrid effect for failure strain can always be expected. [159]

5.2.3 Mechanical properties of hybrid composites subjected to tensile loads

In this subsection, one briefly reviews the effects of hybridization on the mechanical properties of composites subjected to tensile loads, namely the tensile modulus, the failure strain and the tensile strength.

5.2.3.1 Tensile modulus

The longitudinal tensile modulus can be accurately predicted by a linear rule-of-mixtures:

$$E^* = E_{f1}V_{f1} + E_{f2}V_{f2} + E_mV_m \tag{5.3}$$

where E_{f1} and E_{f2} are the longitudinal tensile modulus of both fibres, E_m is the matrix elastic modulus, and V are the volume fractions of the respective component.

Since the longitudinal tensile modulus can be predicted by a linear rule-of-mixtures, hybrid effects are not expected for this property. However, hybrid effect may occur in the transverse direction [199].

5.2.3.2 Failure strain

The first definition of the hybrid effect, given in Section 5.2.2, was based on the apparent failure strain enhancement of the LE fibres in a hybrid composite compared to the failure strain of a LE fibre-reinforced non-hybrid composite. Therefore, it is expected that hybrid effect can occur in this property.

In Fig. 4.4, results obtained from several authors for the hybrid effect on this property are presented, by varying the volume fraction of LE fibres in the composite. Results inside the red line should be treated with care because of improper testing, definition of the reference failure strain or definition of the hybrid effect.

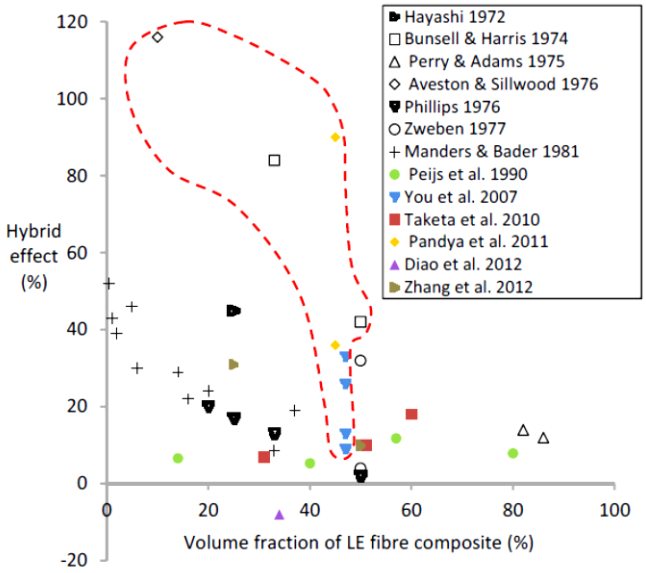

Fig. 5.11: The hybrid effect for tensile failure strain as a function of the volume percentage of the LE fibre composite. The information inside the red line should be interpreted with care, due to errors. Retrieved from [159].

5.2.3.3 Tensile strength

The hybrid effect for tensile strength should be determined based on a bilinear rule-of-mixtures, as shown in Fig. 5.12a.

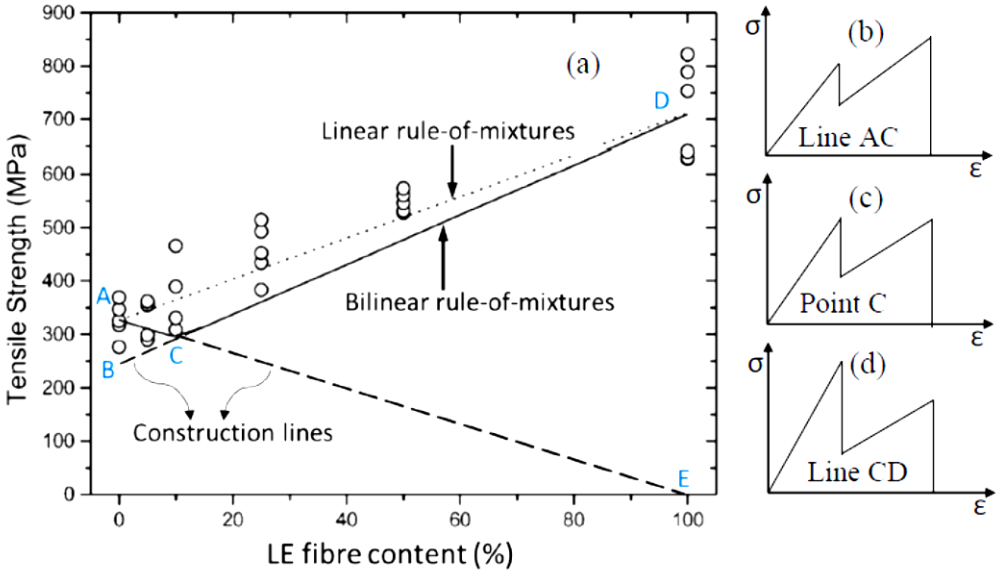

Fig. 5.12: (a) Illustration of the bilinear rule of mixtures for the tensile strength of carbon/glass hybrid composites, and corresponding tensile diagrams of hybrid composites for (b) line AC, (c) point C, and (d) line CD. Retrieved from [159].

Considering the failure strains, LE fibres fail first followed by the HE fibres. Depending on whether the volume fraction of HE fibres is high or low, two possibilities arise after the LE fibre failure: (1) if the HE volume fraction is high, the tensile strength is dominated by the HE fibres, and the stress is able to reach higher levels than the stress at the failure strain of the LE fibres, as illustrated in Fig. 5.12b; and (2) if the HE volume fraction is low, then the tensile strength is dominated by the LE fibres and the stress at HE fibres failure does not exceed the stress at the failure strain of the LE fibres, see Fig. 5.12d.

5.2.4 Modelling the tensile failure of UD hybrid composites

In 1961, Hedgepeth [197] was the first to develop a shear lag model for non-hybrid fibre-reinforced composites, by assuming that the fibres carry all the axial load, and that the matrix carries only the shear load. Hedgepeth calculated the stress concentration factor when one or more fibres are broken in a 1D fibre packing, which is an infinite row of fibres, see Fig. 5a.

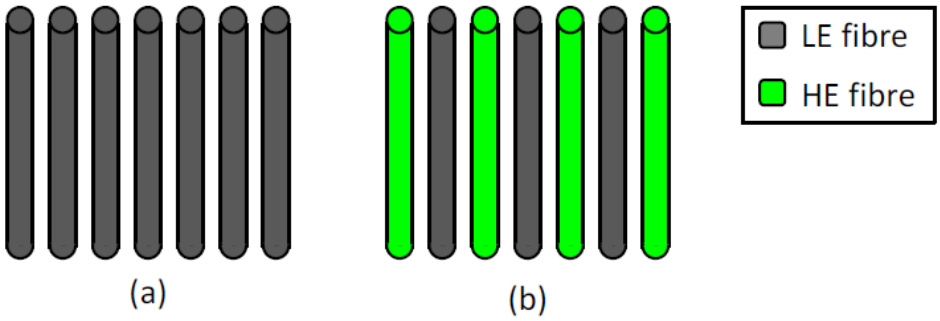

Fig. 5.13: Schematical representation of 1D fibre packings: (a) only LE fibres and (b) alternating LE and HE fibres. Retrieved from [159].

Modelling strength of hybrid composites is more complex than of non-hybrid composites. When a single fibre breaks in a unidirectional composite, the broken fibre locally loses its load transfer capacity over a certain length, already mentioned by ineffective length. Simultaneously, the nearby fibres take over the load of the broken fibre and are hence subject to stress concentrations. Both the stress concentrations and ineffective length depend on the type of the nearby fibres. This additional geometrical complexity makes modelling hybrid composites a challenging task. [159]

In 1977, Zweben [193] was the first author to extend shear lag models for unidirectional composites to hybrid composites and model the hybrid effect for failure strain. This author modelled one dimensional fibre packing, arranged as shown in Fig. 5.13b.

Zweben's model is powerful, as it is simple and allows for an easy interpretation. The simplified fibre packing leads to three limitations: (1) overestimations of the stress concentrations compared to the more realistic 2D packings; (2) the LE and HE fibres are arranged in an alternating manner, leading to the highest possible dispersion for the fixed 50/50 ratio of LE/HE fibres. A broken LE fibre is always shielded from the next LE fibre by the HE fibre in between. It does not allow to investigate the influence of dispersion; and (3) the packing leads to a fixed ratio of LE over HE fibres, which means it cannot investigate the influence of the LE fibre volume fraction. [159]

Recently, Pimenta and Robinson [200] developed a more sophisticated model, capable of overcoming the limitations presented above for the Zweben's model.

5.2.5 Influencing parameters in the strength of hybrid composites

There are several parameters that can influence the behaviour of hybrid composites, however, only those considered to be the most relevant are presented next: (1) fibre volume fraction, (2) elastic properties of the fibres, (3) failure strain ratio, (4) fibre strength distribution, (5) degree of fibre dispersion, and (6) matrix properties.

Next, the parameters mentioned above will be presented regarding their influence on the hybrid effect.

5.2.5.1 Fibre volume fraction

The fibre volume fraction represents the relative amount of both fibre types in the material and has been shown to have a large effect in the hybrid composite behaviour. According to Kretsis [184], increasing the volume content of HE fibres increases the hybrid effect. The earlier models for hybrid composites were not able to study this effect due to the limitations mentioned above. However, recent models have been able to do so, proving the results obtained by Kretsis.

5.2.5.2 Elastic properties of the fibres

The elastic properties of the fibres are an important parameter as it affects: (1) the static stress concentrations; (2) the dynamic stress concentrations; and (3) the ineffective lengths.

According to Swolfs [161], increasing the stiffness of the HE fibres (maintaining same properties for the LE fibres) leads to a small increase of the hybrid effect, which is attributed to a decrease in the SCFs in the LE fibres with the increase of the HE fibres' stiffness.

5.2.5.3 Failure strain ratio

Zweben's model [193] considers the ratio of the failure strains of both fibres to be the most influential parameters in the hybrid effect. However, Fukuda [201] contradicted the results of Zweben's model and considered that the failure strain ratio has no influence on the hybrid effect. This difference is due to different failure definitions considered for the hybrid composite. Zweben defines the hybrid effect is based on the fracture of a HE fibre near a broken LE fibre, while Fukuda defines the hybrid effect is based on the fracture of a LE fibre near a broken LE fibre.

More recently, Swolfs [161] addressed this issue and concluded that the failure strain ratio significantly affects the hybrid effect for failure strain ratios above two, see Fig. 5.14. However, for bellow two this influence is reduced. If the HE fibre failure strain is close to the LE fibre failure strain, then some HE fibres will break prior to full failure of the LE fibres. This should reduce the hybrid effect. By contrast, if the HE fibre failure strain is much larger than LE fibre failure strain, then the two fibres act independently and a larger hybrid effect can be expected.

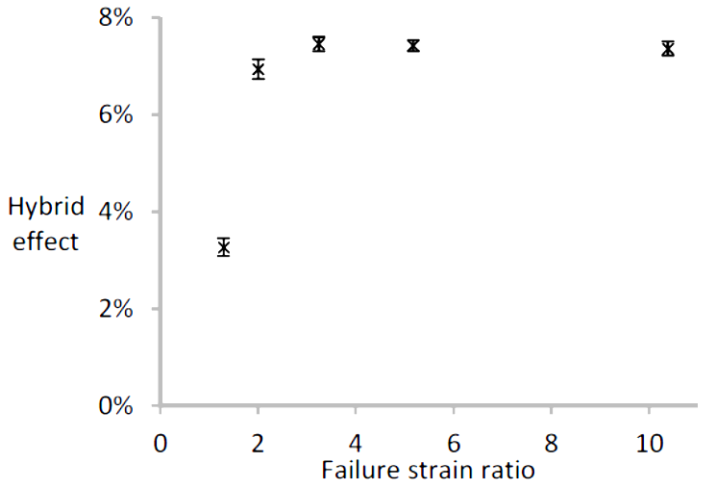

Fig. 5.14: Influence of failure strain ratio in the hybrid effect, for a hybrid composite with 50% of each fibre type. Retrieved from [161].

5.2.5.4 Fibre strength distribution

Both Zweben's [193] and Fukuda's [201] models consider the fibre strength distribution to have a large influence on the hybrid effect and concluded that, increasing the dispersion of the strength of the fibres, by decreasing the Weibull modulus, increases the hybrid effect. Swolfs [161] addressed this issue and reached the same conclusions as the previous authors, stating that reducing the Weibull modulus from 4.8 to 3 doubled the hybrid effect, as illustrated in Fig. 5.15.

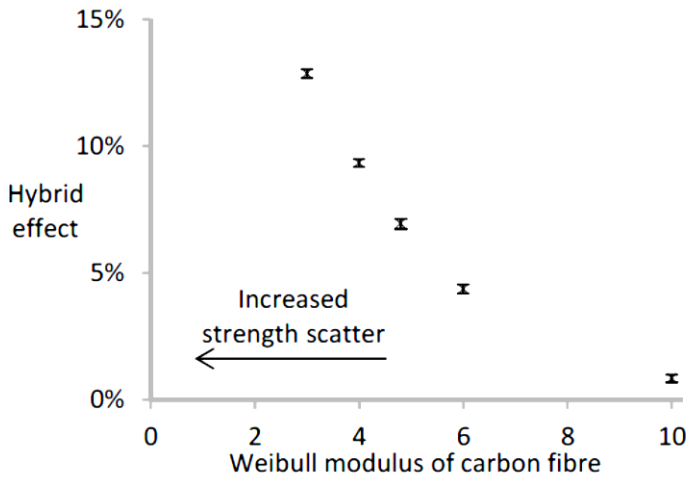

Fig. 5.15: Influence of the Weibull modulus on the hybrid effect, for a hybrid composite with 50% of each fibre type. Retrieved from [161].

5.2.5.5 Degree of fibre dispersion

Fibre dispersion, as mentioned above, is a measure of how well the fibres are mixed, which is a very important factor for the behaviour of hybrid composites.

Swolfs et al. [202] extensively studied this topic. The authors considered a RVE with three different types of fibre combinations: in bundles (Fig. 5.15a), in layer (Fig. 5.15b) and random dispersion. In this study, the authors concluded that increasing dispersion, by either reducing bundle size or reducing layer thickness, increased the hybrid effect, as shown in Figs. 5.15b and 5.15c.

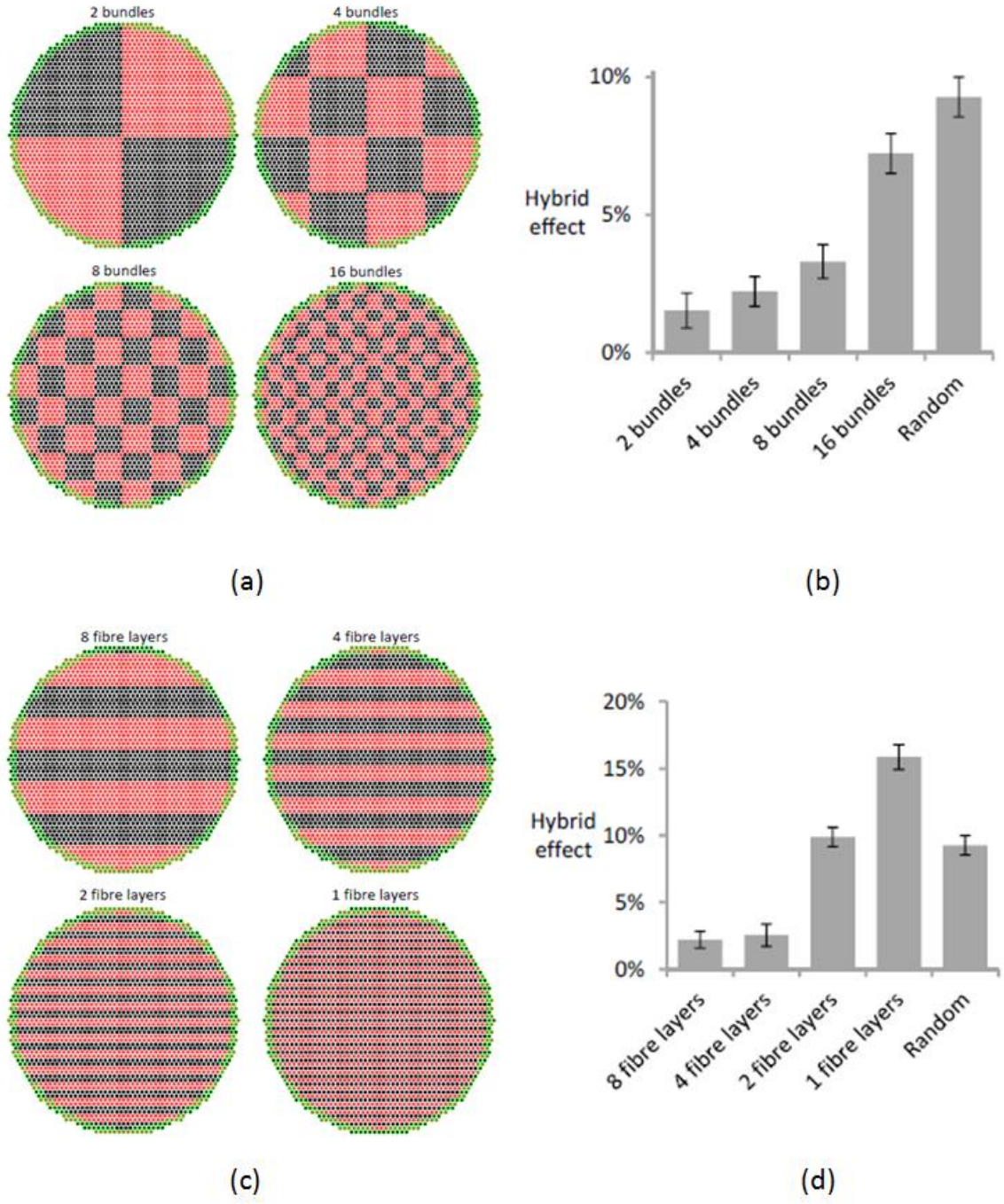

Fig. 5.16: Influence of fibre dispersion on the hybrid effect considering different fibre arrangements: (a) bundle-by-bundle; (b) hybrid effect for bundle-by-bundle fibre arrangement; (c) layer-by-layer; and (d) hybrid effect for layer-by-layer fibre arrangement. Retrieved from [161].

5.2.5.6 Matrix properties

The matrix properties are expected to have only a secondary effect in the composite properties, by influencing the SCFs and the ineffective lengths. The matrix shear modulus has an influence on the ineffective length, however its effect on the SCFs is usually not represented in the models due to shear-lag assumptions [158].

5.2.6 Pseudo-ductility

Fibre-reinforced non-hybrid composites are characterized by having excellent mechanical properties and low density, however, their failure is abrupt and catastrophic, coming without any warning, as illustrated in Fig. 5.17a. Another problem lies in the fact that the material can be damaged in its interior (delamination or cracking of the matrix) without being noticeable, leading to mechanical properties lower than expected. This behaviour of composite materials leads to high safety factors, preventing their optimal design.

Fibre hybridization can tackle some of the challenges mentioned above by developing a more gradual failure of the material. The typical response of hybrid composites is as illustrated in Fig. 5.17b, characterized by having a load drop when the brittle fibres break. However, if the material is designed correctly, it is possible to obtain a more gradual failure as shown in Fig. 5.17c. This type of response is characterized by presenting a yielding plateau before the material failure happens. This is the so-called pseudo-ductile behaviour, that allows the identification of the material failure before it completely loses its structural integrity.

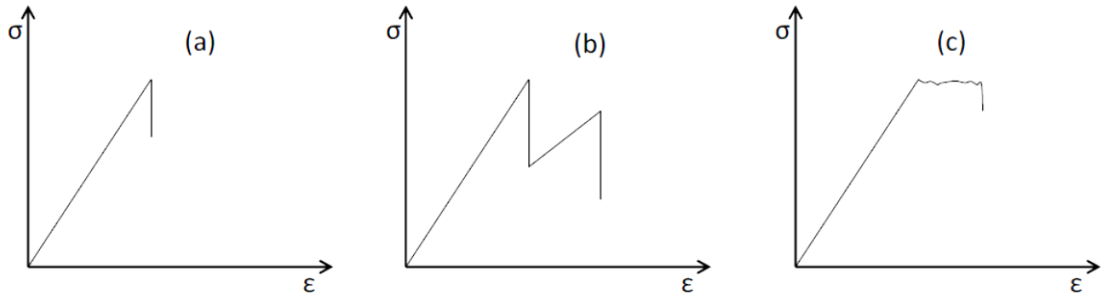

Fig. 5.17: Schematic stress–strain diagrams for (a) non-hybrid composites, (b) typical hybrid composites, and (c) pseudo-ductile hybrid composites. Retrived from [159].

Nowadays, there is a great interest in composite materials that present a pseudo-ductile behaviour, mainly in the aeronautical industry. This behaviour allows the reduction of enforced safety factors in the composites design and increases the material's toughness. Pseudo-ductility can be

obtained by controlling the damage mechanisms in non-hybrid composites [203,204], however in this work the objective will be to achieve a pseudo-ductile behaviour through fibre hybridization.

Czél et al. [183] managed to obtain a pseudo-ductile behaviour for hybrids composites with a thin layer of carbon fibres between two thicker layers of glass fibres. By making the carbon fibre layer thin enough, a change in the material behaviour was observed. The carbon fibre layer was able to break several times along the length of the sample, before the glass fibre layers break. Further understanding of this phenomenon was performed by Jalalvand et al. [205], who developed a finite element model for these thin ply hybrid composites. This led to the development of damage mode maps with relative thickness and absolute thickness on x and y-axis (see Fig. 5.18), showing four quadrants, each of which represent a different failure behaviour of the hybrid composite.

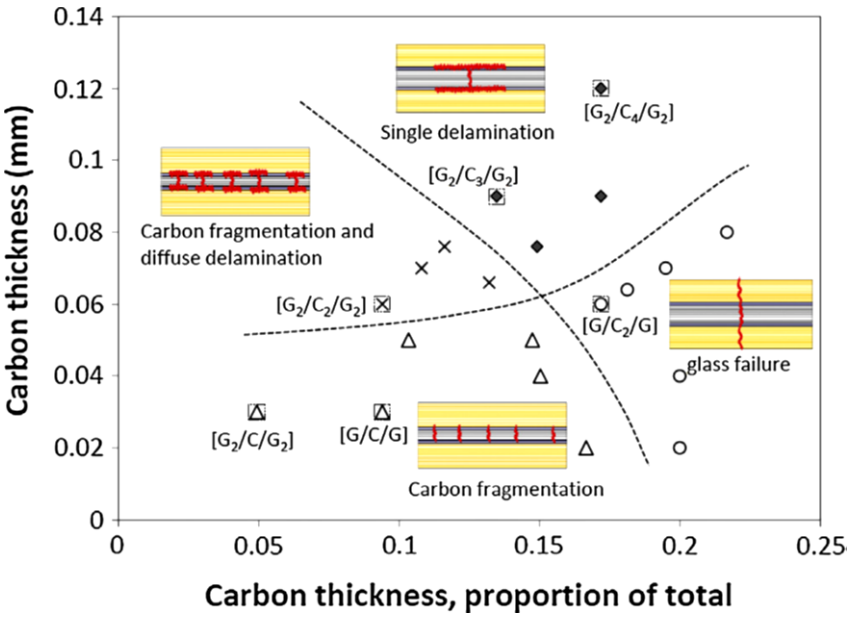

Fig. 5.18: Damage mode map for carbon/glass hybrid composites. The experimental data points are marked with an additional square marker. Retrieved from [159].

It was observed that when there was a multiple fragmentation of the carbon fibre layer, the material exhibited a pseudo-ductile behaviour. This multiple fragmentation can be achieved when the carbon layer thickness is reduced.

In order to optimize the pseudo-ductility of the composite, it is necessary to quantify it. The pseudo-ductility can be characterized by the pseudo-ductile strain. The definition proposed by Yu et al. [206] for the pseudo-ductile strain (ε_d) is used here, and consists in the difference between the strain at which the specimen loses is integrity (ε_{max}) and the elastic strain (ε_{E_0}), at the same stress level as ε_{max} but based on the initial Young's modulus (E_0), as illustrated in Fig. 5.19. In

this assumption, ε_d could be interpreted as the length of a yielding plateau, where the material would deform at nearly constant stress after leaving the elastic domain, typical of a ductile behaviour.

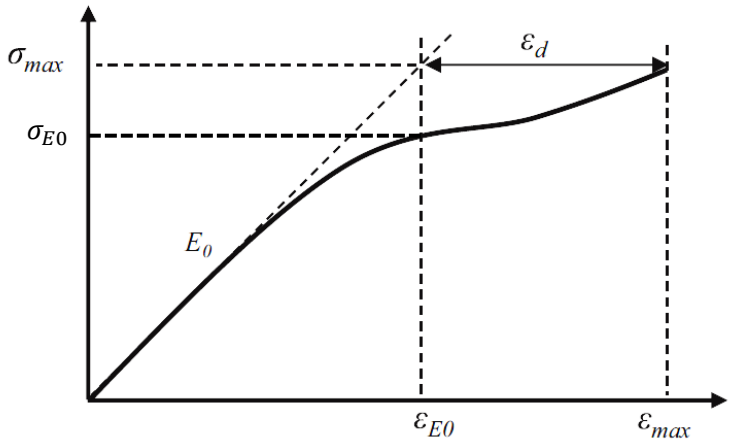

Fig. 5.19: Diagram of the pseudo-ductile strain. Retrieved and adapted from [158].

The initial Young's modulus for a hybrid fibre bundle can be estimated using the rule-of-mixtures, through the following equation:

$$E_0 = E_{f1}V_{f1} + E_{f2}V_{f2} \tag{5.4}$$

and so, ε_{E_0} can be easily computed using the Hook's law $\varepsilon_{E_0} = \sigma_{max}/E_0$.

Although many authors have already studied fibre hybridization aiming a pseudo-ductile behaviour in composite materials, in practice this behaviour was only achieved for small volume fractions of LE fibres, such as carbon fibres, and therefore the mechanical properties of the composite are generally limited. New strategies need to be developed to achieve this behaviour in higher LE fibre fractions.

Recently, Conde et al. [207-209] optimized the hybrid composites behaviour such that the pseudo-ductile behaviour is maximized. In the next chapter, the latest developments regarding this topic are presented.

6

MICROSTRUCTURAL OPTIMIZATION OF UNIDIRECTIONAL HYBRID COMPOSITES UNDER UNIAXIAL TENSILE LOADS

This chapter focus on achieving a pseudo-ductile behaviour in the response of unidirectional hybrid composites when subjected to uniaxial traction. To understand under what circumstances such behaviour is obtained, optimization problems are formulated and solved here.

In [208] a multi-objective optimization problem was formulated with the goal of finding a fibre hybridization that had an optimal trade-off between pseudo-ductility and failure strength. The search for the optimal fibre hybridization was carried out in a discrete design space, where pre-defined fibres were used as design variables, as well as in a continuous design space, where the fibre properties could vary continuously within certain bounds. This previous work left room for further improvements and extensions. Therefore, an alternative formulation for the optimization problem is proposed in the present work. Borrowing from design of structures subjected to plastic deformations, this formulation uses a "pseudo-plastic deformation energy" per unit volume as objective function. This is a single-objective optimization problem which is simpler and problem independent when compared to the weighted sum method previously proposed. Besides this, [208] used analytical models that do not account important mechanisms which play a role in the longitudinal failure of unidirectional composites. The present work enriches the composite modelling using a numerical model of the microstructure taking into account more realistic failure

mechanisms. Furthermore, a relationship between two design variables, the elastic modulus and the failure strength of a fibre, is used here as a problem constraint in the frame of the continuous optimization in order to achieve optimal properties for fibres that can be considered more realistic.

To predict the response curve of a hybrid fibre reinforced composite a LLS Spring Element Model (SEM) developed by [210] is used in this work. This model is an extension of the SEM approach initially proposed by [178] to both random distribution of fibres and hybrid composites, where the fibres can have different geometrical and mechanical properties. The model assumes local stress redistribution and can be seen as a low computational cost alternative to 3D Finite Element Models. The computational cost is an important issue since optimization requires several analyses of the composite response.

The SEM is based on the definition of a Representative Volume Element (RVE) where two types of fibres embedded in a polymer matrix can be randomly or periodically distributed in space. It is worth studying how clusters of fibres of one type or another impact the overall composite response. This motivates pursuing here a lay-out optimization problem. Predefined fibre locations are considered and then the optimizer decides which fibre type is used at each location (fibre "0" or "1") to target a certain level of fibre dispersion, therefore a measure of the degree of fibre dispersion in space is proposed. This metric is then used to study how the fibre dispersion (or clustering) influences the composite pseudo-ductile behaviour.

This chapter of the thesis is currently published in a peer-reviewed journal, see [209]. For this reason, most of the content presented here was transcribed directly from the journal. The overall objective of this part of the work is to find optimal fibres to hybridize, as well as an optimal fibre spatial arrangement for such hybridization that produces a relevant pseudo-ductile behaviour in the composite under uniaxial traction. This chapter is structured in the following way. Firstly, Section 6.1 presents a brief description of the SEM used in this work to obtain the response curve of the hybrid composite material. Optimization problems are formulated in Section 6.2. These optimization problems involve coupling the SEM with an optimization algorithm, which is detailed in Section 6.3. Optimal fibre hybridizations and fibre arrangements obtained by solving the proposed optimization problems are shown in Section 6.4. The main conclusions of the work are presented in Section 6.5.

6.1 Spring Element Model (SEM)

The SEM proposed by [210] is summarized in this section. This is a numerical model consisting of longitudinal spring elements, representing the fibres, connected by transverse spring elements, representing the matrix. The matrix carrying capacity of axial load is disregarded, which is a typical assumption for UD polymer composites. Fig. 6.1 shows a flowchart of the numerical implementation of the model in Matlab®, which is also further detailed below.

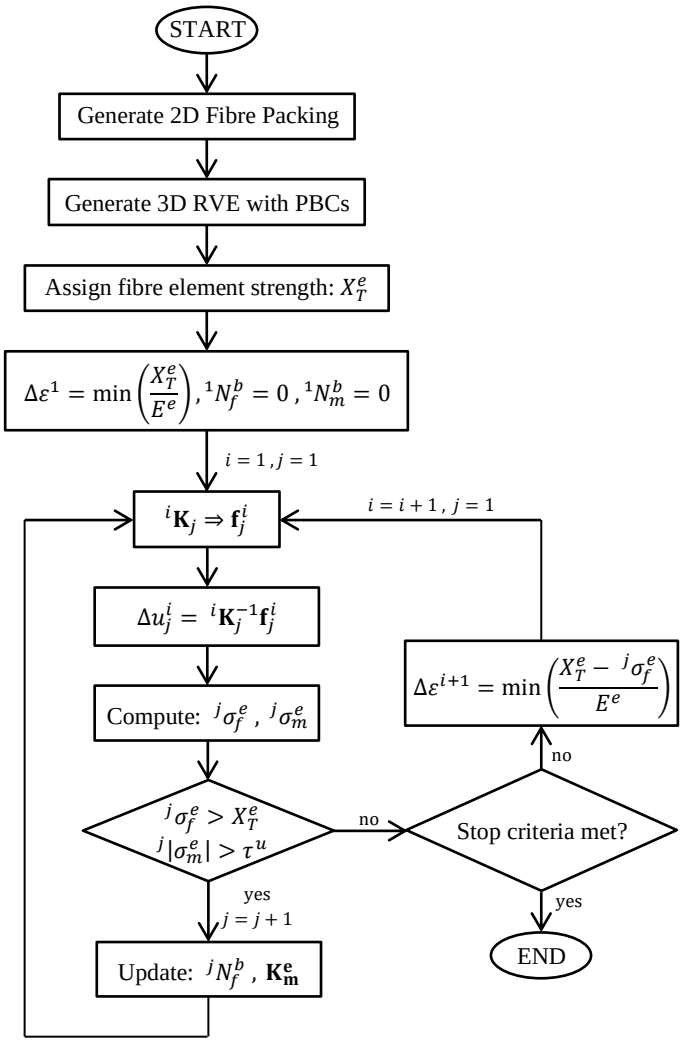

Fig. 6.1: Flowchart of the numerical implementation of SEM [210].

Firstly, the model places fibres in a 2D arrangement, which is then extruded to generate the 3D periodic RVE with dimensions $a \times b \times c$, with $a = \delta_x R_{max}$, $b = \delta_y R_{max}$ and $c = \delta_z R_{max}$, where δ_x, δ_y and δ_z are user-specified parameters responsible for scaling the RVE in the various

spatial directions based on the maximum fibre radius R_{max}. The implementation of the Periodic Boundary Conditions (PBCs) is done through the elimination of the redundant degrees of freedom on the RVE boundary, as it is also done in [211]. The spatial arrangement of fibres in the RVE can be random [212] or periodic with a square or hexagonal mesh, as shown in Fig. 6.2. Actually, it was seen in [210] that although the local stress fields are affected by the spatial arrangement of fibres chosen, the stress-strain behaviour is not affected. Thus, a periodic fibre arrangement in the RVE with a square mesh (Fig. 6.2b) is used in this work. For all the fibre elements and according to the Weibull distribution (see Eq. 5.1), a random strength is assigned to each of the fibre element e, X_T^e. This explains variability in the results obtained rerunning the SEM for the same hybridization.

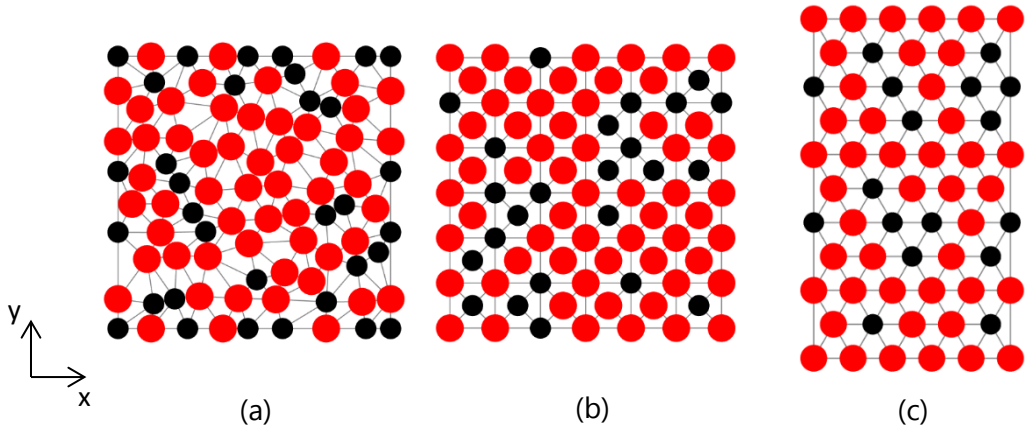

Fig. 6.2: Possible meshes to be used in SEM: (a) Random spatial arrangement of fibres; (b) Square mesh with periodic arrangement of fibres; (c) Hexagonal mesh with periodic arrangement of fibres. Retrieved from [209].

An evolutive strain incrementation procedure is considered, to ensure that a strain increment only forces one fibre to fail, given by:

$$\Delta\varepsilon = min\left(\frac{X_T^e - \sigma_f^e}{E^e}\right) \tag{6.1}$$

where σ_f^e is the stress in the fibre element from the previous strain increment and E^e is the elastic modulus of the element. The global stiffness matrix of the model with the updated number N_f^b of broken fibre elements and updated shear stress stiffness is:

$$\mathbf{K} = \sum_{e=1}^{N_f - N_f^b} \mathbf{K}_f^e + \sum_{e=1}^{N_m} \mathbf{K}_m^e \tag{6.2}$$

where $\mathbf{K}_f^e$ is the stiffness matrix of each fibre element and $\mathbf{K}_m^e$ is the stiffness matrix of each matrix element determined respectively by the following equations:

$$\mathbf{K}_f^e = \frac{A_f^e E^e}{l^z}\begin{bmatrix} 1 & -1 \\ -1 & 1 \end{bmatrix} \tag{6.3}$$

$$\mathbf{K}_m^e = \frac{G\left(A_m^{(2)} - A_m^{(1)}\right)}{d \ln\left(A_m^{(2)}/A_m^{(1)}\right)}\begin{bmatrix} 1 & -1 \\ -1 & 1 \end{bmatrix} \tag{6.4}$$

where A_f^e is the fibre element cross section area, l^z is the predefined length for fibre spring elements, G is the shear modulus of the matrix, $A_m^{(1)}$ and $A_m^{(2)}$ are the areas on each fibre of the transverse spring element representing the matrix that connects both fibres (see Fig. 6.3) given by:

$$A_m^{(1)} = \frac{2\pi R_1}{n_1} l^z \quad \text{and} \quad A_m^{(2)} = \frac{2\pi R_2}{n_2} l^z \tag{6.5}$$

where R_1 and R_2 are the fibres radii that are connected to the matrix element and n_1 and n_2 are the number of fibres that each fibre is connected to, respectively.

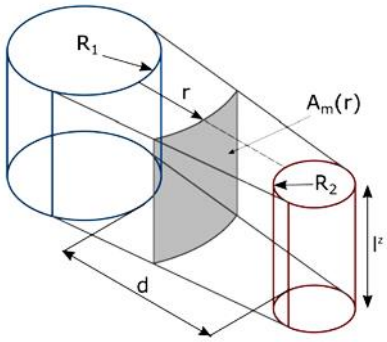

Fig. 6.3: Matrix shear element connecting two fibres. Retrieved from [210].

The external force vector $\mathbf{f}_j^i$ is obtained based on the current stiffness matrix and the applied displacement. Solving the system of equations, $\mathbf{Ku} = \mathbf{f}$, the unknown displacement vector is calculated. If any fibre element fails ($\sigma_f^e > X_T^e$) or if the shear stress in a matrix element exceeds τ^u (yield stress of the matrix), the number of broken fibre elements or the stiffness of the matrix elements are respectively updated. Then, a new global stiffness matrix is computed, and the system of equations is solved once more, until no fibre or matrix element fails. If the stop criteria are not met, a new strain increment is determined and the iterative process continues, otherwise the

model stops. In this work $\|\mathbf{f}_j^i\| < c \max\|\mathbf{f}_j^i\|_{\forall i,j}$ with $c = 0.6$ and $i_{max} = 1000$ are used as stop criteria.

6.2 Optimization problems formulation

The failure of a hybrid composite can happen in different ways, depending on the fibre properties and on their spatial arrangement in the RVE. When the hybridization is characterized by having two types of fibres with similar failure strains, this leads to a catastrophic failure, as in the case of non-hybrid composites (see Fig. 5.17a). On the contrary, when the failure strains of the two fibre types are quite different this can lead to a response with a load drop (see Fig. 5.17b). The desired pseudo-ductile behaviour (see Fig. 5.17c) is attained only when the two types of fibres have different failure strains such that there is continuity between the failure of the LE and the HE fibres forming a pseudo-yielding plateau in the response curve.

To find out the optimal fibre properties to hybridize, such that an outstanding pseudo-ductile behaviour is attained, an optimization problem is proposed in Section 6.2.1. To end this section, another optimization problem is proposed aiming to investigate the sensitivity of the pseudo-ductile behaviour to fibre dispersion or clustering, Section 6.2.2.

6.2.1 Fibre properties optimization problem

To formulate the fibre properties optimization problem, it is needed control over the shape of the material response curve. Therefore, a parametrization of that curve is required using parameters as the pseudo-ductile strain, tensile strength and stress amplitude. In [208] such curve parametrization is suggested, and it is revisited here, see Fig. 6.4. Four parameters (σ_{max}, ε_d, δ and λ) are used for quality evaluation of the response curve. Remember that the pseudo-ductile strain (ε_d) is defined as in [203], see Section 5.2.6. The amplitude (δ) is defined as the difference between the maximum and minimum stresses in the interval between the elastic and maximum strains. This characterizes how horizontal the pseudo-yielding plateau is. Finally, the amplitude (λ) is defined as the difference between two stress levels, one associated to the value of the elastic strain and another associated to the minimum value of the stress found in the range $[\varepsilon_{E_0}, \varepsilon_{max}]$. This characterizes a possible load drop in the response curve.

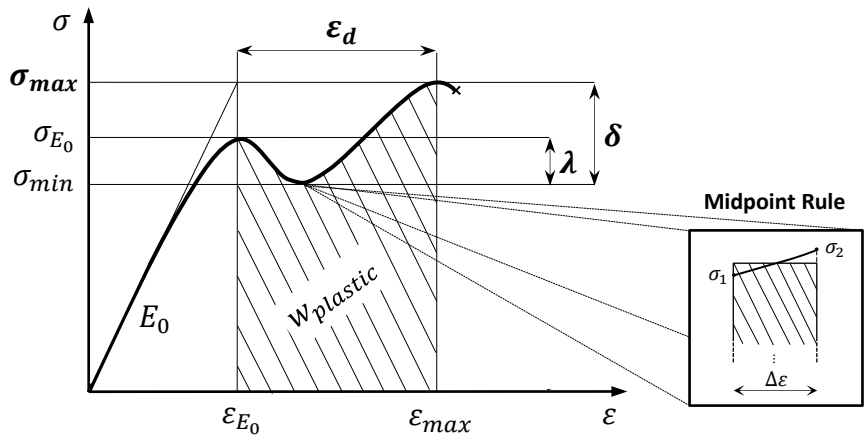

Fig. 6.4: Parametrization of a hypothetical response curve of a hybrid composite. Retrieved from [209].

This optimization problem can be formulated either using a weighted sum function including several objectives (Section 6.2.1.1 – Multi-objective approach) or a single-objective function (Section 6.1.1.2 – Single-objective approach). Regardless the objective function used, two different types of optimization problems are proposed: a mixed-integer and a continuous optimization problem. On the one hand, in the mixed-integer optimization problem, the goal is to find, among twenty pre-defined fibres available in the market (see Table 6.1), the optimal pair of fibres to be hybridized such that a good pseudo-ductile behaviour is attained. On the other hand, in the continuous problem, one aims to find out properties of the fibres that could be considered ideal to achieve the best possible pseudo-ductile behaviour.

To find an optimal combination of fibres or fibre properties to hybridize that produces a considerable pseudo-ductile behaviour, the following optimization problem is solved:

$$\begin{aligned} &\min_{\mathbf{x}=\{\mathbf{s},V_{F_{LE}}\}} \quad f(\mathbf{x}) \\ &\text{s.t.} \\ &\lambda - \alpha\sigma_{E_0} \leq 0 \\ &\sigma_0 - mE - b \leq 0 \\ &\delta - \delta^* \leq 0 \end{aligned} \tag{6.6}$$

where **s** and $V_{F_{LE}}$ are the design variables. In the mixed-integer optimization problem, the **s** integer type design variable corresponds to a vector containing two integer numbers representing the position or row number in a table (see Table 6.1) containing the properties of the pre-defined fibres to be hybridized, $\mathbf{s} = (s_1, s_2)$ with $s_i \in \{1, \dots, 20\}$. In the continuous optimization problem, the **s** design variable is a vector containing eight real numbers that correspond directly to the fibre

properties, $\mathbf{s} = (s_1, \dots, s_8) \mid \underline{s_i} \leq s_i \leq \overline{s}_i$ where $\underline{s_i}$ and $\overline{s}_i$ are the lower and upper bounds of fibre properties, respectively. The design variable representing the LE fibres volume fraction can be any real number between 0 and 1 in both optimization types, $V_{F_{LE}} \in [0; 1]$. The HE fibres volume fraction is $1 - V_{F_{LE}}$. Regarding the constraints, the first one guarantees that an admissible solution has no load drop in the response, where α could be seen as a percentage of the stress level σ_{E_0}, meaning that values of λ greater than $\alpha\sigma_{E_0}$ are unfeasible. The second constraint is only used in the continuous optimization problem. At equality, this constraint is the equation of a straight line (m and b are the slope and intercept constants) that relates the elastic modulus E and the Weibull scale parameter σ_0 (directly related to the fibres strength) of both fibres to be hybridized. This limits more the design space, but it accounts for more realistic optimal solutions as explained afterwards. The last constraint is only needed when using a single-objective function in order to control the stress amplitude δ such that does not exceed the maximum admissible value (δ^*) for this parameter. Using the weighted sum function such constraint is not needed because the stress amplitude δ is an objective to be minimized.

6.2.1.1 Multi-objective approach

To solve the optimization problem formulated in Eq. (6.6) as multi-objective, a weighted sum function is considered, where some of the parameters described in Fig. 6.4 are used. The pseudo-ductile strain ε_d and the failure stress σ_{max} are to be maximized while the parameter δ is minimized in order to obtain deformation at a constant stress in the pseudo-plastic region. Therefore, the following weighted objective function is proposed:

$$f(\boldsymbol{x}) = \left(\frac{1}{\varepsilon_d}c_1\right)w_1 + (\delta c_2)w_2 + \left(\frac{1}{\sigma_{max}}c_3\right)w_3 \tag{6.7}$$

where w_i are weighting constants and c_i are normalization constants to obtain objective functions with same order of magnitude and preventing thus scale problems. The tuning of weighting constants is mandatory, and it can be a time-consuming task as it demands multiple runs for each different optimization problem. Regarding the normalization constants, their values can be approximately equal to the inverse of the optimal value of the respective objective function. A multi-objective function could be used to construct a Pareto front. However, it is shown in [208] that the optimizer is inefficient to find solutions as good as those found by the weighted sum function. Therefore, only the weighted sum function is revisited here in the multi-objective setting. In the next section, a single-objective function is proposed which avoids the aforementioned required adjustments of the weighting and normalization constants.

Table 6.1: Mechanical properties for 20 pre-defined fibres [213].

Fibre	Reference	Material	R [μm]	E [GPa]	σ_0 [MPa]	L_0 [mm]	m [-]	$\langle\varepsilon\rangle$ [%]
HTS	[214]	Carbon	3.5	230	4493	19	4.8	1.34
X5	[215]	Carbon	5.05	520	2500	25	6.1	0.37
AS4	[216]	Carbon	3.5	234	4275	12.7	10.7	1.48
T300	[216]	Carbon	3.5	232	3170	25	5.1	1.01
T300	[217]	Carbon	3.5	232	3200	30	5.5	1.08
T300-B4C	[217]	Carbon	3.5	232	3150	30	5.4	1.06
700˚C	[218]	Carbon	3.3	55	1400	10	11	2.02
1000˚C	[218]	Carbon	2.9	240	4500	10	4.5	1.09
T800G	[218]	Carbon	2.75	295	6800	10	4.8	1.39
M30S	[218]	Carbon	2.8	295	6400	10	4.6	1.28
M40S	[218]	Carbon	2.7	380	4900	10	5.2	0.81
M50S	[218]	Carbon	2.65	480	4600	10	9	0.73
E-Glass	[177]	Glass	6.5	76	1550	24	6.34	1.59
E-Glass	[219]	Glass	7.8	66.9	1649	20	3.09	1.44
AR-HP	[220]	Glass	7	70	1363	60	9.6	1.81
AR-HD	[220]	Glass	7	70	876	60	4.8	1.09
Kevlar 29	[221]	Kevlar	6.895	85.3	3445.8	25	11.8	3.52
Kevlar 49	[221]	Kevlar	5.135	149.1	4083.3	25	8.2	2.26
Kevlar 119	[221]	Kevlar	5.46	61.4	3101.2	25	11.8	4.41
Kevlar 129	[221]	Kevlar	5.79	99	3433	25	10.3	2.97

6.2.1.2 Single-objective approach

The proposed single-objective function is the pseudo-plastic deformation energy per unit volume. The maximization of this energy improves the composite's toughness. However, since the optimizer minimizes a function, one consistently defines the objective as:

$$f(\mathbf{x}) = -w_{plastic} \tag{6.8}$$

where $w_{plastic}$ is the pseudo-plastic deformation energy per unit volume which corresponds to the area defined below the response curve in the pseudo-plastic deformation region, i.e.,

$$w_{plastic} = \int_{\varepsilon_{E_0}}^{\varepsilon_{max}} \sigma \, d\varepsilon \tag{6.9}$$

where this integral is computed using the midpoint rule or middle Riemann sum [222], see Fig. 6.4.

An optimization problem with objective function (6.8) alone is not capable of evaluating the stress amplitude of a response. However, controlling such amplitude is necessary in order to achieve a pseudo-yielding plateau as desired, therefore the parameters λ and δ are included in the problem formulation, see Eq. (6.6).

It's worth mentioning that the single-objective function in (6.6) cannot actually distinguish the three response curves in Fig. 6.5. All curves have the same pseudo-plastic deformation energy per unit of volume. A clearer distinction between these three curves in Fig. 6 would only be possible returning to the multi-objective formulation where weights are used. Therefore, the main interest of the energy-based formulation is the maximization of the overall composite's toughness, regardless on account of increasing the failure stress or increasing pseudo-ductility. This formulation can then be seen as more parameter independent.

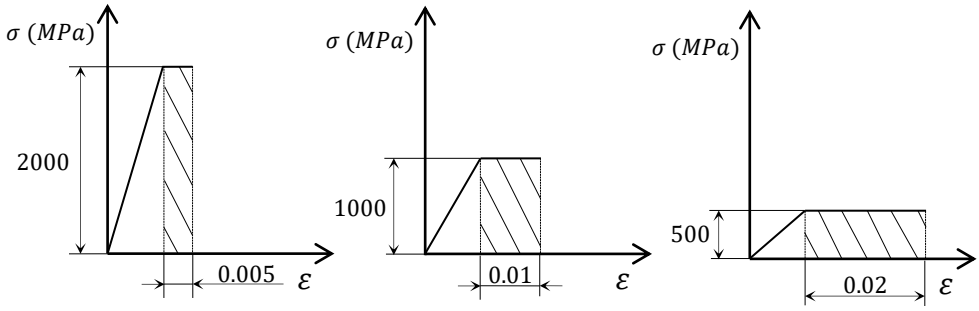

Fig. 6.5: Three hypothetical response curves with the same plastic deformation energy per unit of volume. Retrieved from [209].

6.2.2 Fibre layout optimization problem

The fibre layout optimization problem aims to understand the influence of the fibre dispersion on the composite response. Firstly, a parameter *DD* that measures the dispersion degree of fibres in the RVE is proposed here. This parameter works well with SEM definition, where the fibres are connected with other fibres through a transverse spring that corresponds to a matrix element. It is defined as follows:

$$DD = \frac{Total\ number\ of\ conections\ between\ fibres\ of\ diferent\ types}{Total\ number\ of\ conections\ in\ the\ RVE} \cdot 100\ (\%) \tag{6.10}$$

where a connection corresponds to a matrix element, see Fig. 6.6.

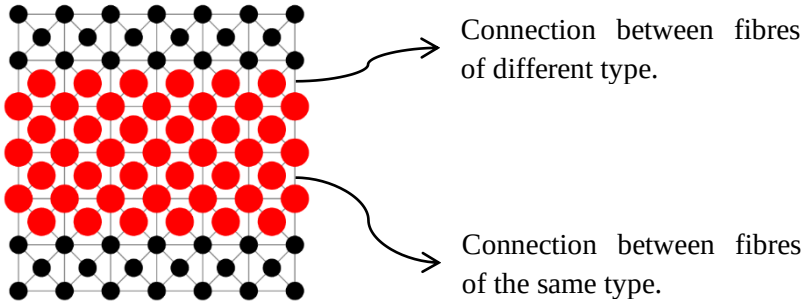

Fig. 6.6: Connections between fibres in a Layer-by-Layer layout. Retrieved from [209].

The range of this parameter *DD* varies depending on the fibres to hybridize and their respective volume fractions. Therefore, it is important to know a priori the range of values for this parameter depending on the chosen hybridization. Actually, it is known that the minimal dispersion degree value is obtained using the Layer-by-Layer (LbL) fibre layout seen in Fig. 6.6. To find out a fibre arrangement with the maximum dispersion degree, the following fibre layout optimization problem is solved with $f(\mathbf{x}) = -DD$:

$$\begin{aligned} &\min_{\mathbf{s}} && f(\mathbf{x}) \\ &\text{s.t.} && \\ &V_{LE} = V_{LE_{req.}} && \end{aligned} \tag{6.11}$$

where **s** is the design variable, which is a vector with length equal to the total number *n* of fibres in the RVE and each entry can take the value 0 or 1 depending on the fibre type (0 corresponds to a LE fibre while 1 corresponds to a HE fibre), i.e. $\boldsymbol{s} = (s_1, s_2, \dots, s_n)\ \forall\ s_i \in \{0,1\}, i = 1, \dots, n$. The optimization problem chooses from all solutions that have the same LE fibres volume fraction. This admissibility condition is introduced by the equality constraint imposing a required volume fraction ($V_{LE_{req.}}$).

To study the sensitivity of the pseudo-ductile behaviour to fibre dispersion or clustering, it is necessary the segmentation of the entire range of dispersion degree *DD* into sub-intervals. Then it is possible to investigate how the pseudo-ductile behaviour is affected by different values of fibre dispersion along the entire range. Therefore, fibre arrangements related to specific dispersion degrees within the full range are determined. This can be done using $f(\mathbf{x}) = \left|DD_{Target} - DD\right|$ in (6.11), where DD_{Target} is the desired dispersion degree to be targeted. Further details about the fibre layout optimization procedure are explained in the next section.

6.3 Methodology

The methodology used to solve the optimization problems (6.6) and (6.11) is presented in this section. The Genetic Algorithm (GA) available in Matlab® is chosen as the optimizer.

Regarding the **fibre properties optimization**, there are two versions of this problem to be considered: mixed-integer and continuous. In both the SEM is coupled with the GA using Matlab® (see Fig. 6.7).

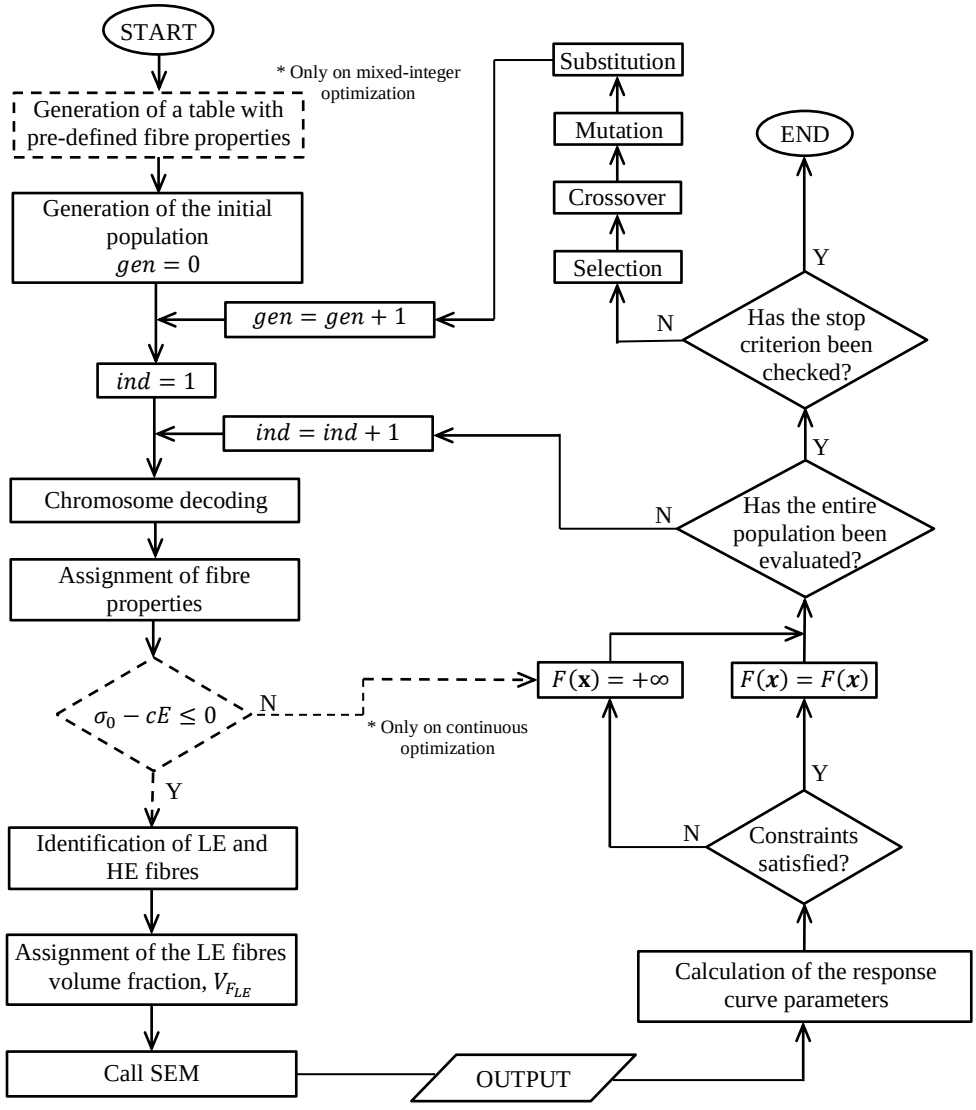

Fig. 6.7: Flowchart of the developed algorithm to solve the fibre properties optimization problem. Retrieved from [209].

The mixed-integer optimization problem starts with the reading of Table 6.1, which contains the properties of 20 pre-defined fibres, where E and R are the elastic modulus and the radius of

the fibres, σ_0 and m are the Weibull scale and shape parameters at the characteristic length L_0, respectively. In the continuous optimization such table is not used because the objective is to determine the optimal values of the fibre properties within a specified and realistic range.

Based on Table 6.1, the GA generates an initial population, *gen*=0, with a certain number of individuals, *ind*. In the mixed-integer optimization, each individual corresponds to a chromosome encoding the entries of the table, which identify the properties of the fibres to be hybridized. In the continuous optimization, real numbers are assigned to the genes of the chromosome such that they are within a specified range for each fibre property treated as a design variable. Table 6.2 shows the lower $\underline{s}_i$ and upper $\overline{s}_i$ bounds of the properties of the fibres. In both types of optimizations, the last entry of the chromosome is used to encode the LE fibres volume fraction.

Table 6.2: Lower and upper bounds of fibres properties used in continuous optimization.

Properties	$\underline{s}_i$	$\overline{s}_i$
R [μm]	2.65	7.8
E [GPa]	55	520
σ_0 [MPa]	876	6800
m	3.09	11.8

In the continuous optimization, limiting only the range of the fibre properties does not guarantee that the obtained hybridization is made of fibres available in market. Despite the optimal fibre properties values being within certain bounds, the relationship between those properties may not be entirely realistic. In [208] is concluded that fibres with optimal properties combine a relatively low stiffness with high strength. To highlight this peculiar characteristic, look at the remote small cluster of points shown in Fig. 6.8. However, it is observed in Table 6.1 that stiffness and strength are properties that seem to go hand in hand, i.e., the higher the strength the higher the stiffness. Therefore, a relationship between these two properties is mandatory for the sake of attaining optimal properties that are more realistic. To the author's knowledge, such relationship is not really disclosed in fibre manufacturer's brochures available in the market. Therefore, the fibre properties available in Table 6.1 are used here to propose a relationship. Fig. 6.8 shows a plot relating the elastic modulus E and the scale parameter σ_0 of all fibres in Table 6.1. It is possible to draw a straight line as defining an envelope enclosing a so-called feasible region where the two properties could relate to each other. Problem (6.6) is then properly constrained to include this depicted feasible region. The failure model is not called if combinations of E and σ_0 are out of such region. Fig. 6.8 can also be used to identify to which class of materials belongs an optimal solution found in the continuous optimization problem.

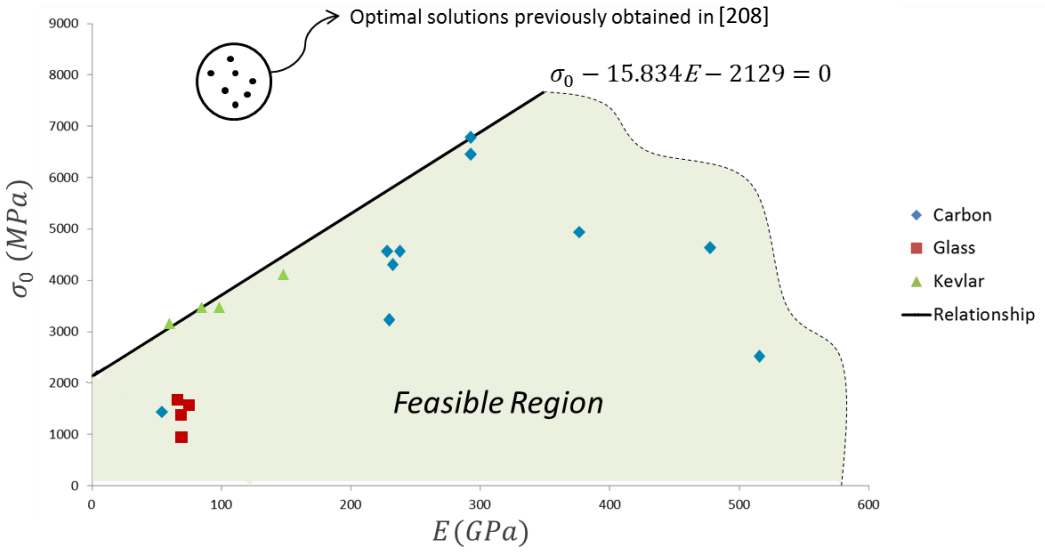

Fig. 6.8: Plot relating the elastic modulus (E) and the Weibull scale parameter (σ_0) of the fibres in Table 6.1. It shows a feasible region for these two properties when the fibre properties optimization problem is solved in a continuous setting. Retrieved from [209].

Once the properties of the fibres to be hybridized are defined, it is necessary to find out which are the LE (or HE) fibres, i.e., which fibres have a lower (or higher) failure strain. To this purpose, the average failure strain $\langle\varepsilon\rangle$ is used in such way that LE fibres have the lowest average failure strain while HE fibres have the highest average failure strain. The average failure strain $\langle\varepsilon\rangle$ is the strain to which one type of fibres presents a 50% failure probability and can be computed by the following equation:

$$\langle\varepsilon\rangle = \frac{\langle\sigma\rangle}{E} \tag{6.12}$$

where $\langle\sigma\rangle$ is the average failure stress of the fibre and E its respective elastic modulus. The Weibull distribution for fibre strength leads to an average fibre strength given by:

$$\langle\sigma\rangle = \sigma_L \Gamma\left(1 + \frac{1}{m}\right) \tag{6.13}$$

where $\Gamma()$ is the gamma function, defined as:

$$\Gamma(x) = (x-1)! \tag{6.14}$$

if x is a positive integer, or

$$\Gamma(x) = \int_0^\infty t^{x-1} e^{-t}\, dt \tag{6.15}$$

if *x* is a complex number with positive real part. The reference stress σ_L at gauge length L (considered 75mm in Table 6.1) is related to σ_0 and L_0 by:

$$\sigma_L = \sigma_0 \left(\frac{L_0}{L}\right)^{1/m} \tag{6.16}$$

Once the LE fibres are identified, it is necessary to know the number of LE and HE fibres present in the RVE which can be determined from the LE fibres volume fraction $V_{F_{LE}}$ after rounding. In the SEM pre-processing, these fibres are randomly distributed in a square periodic mesh (see Fig. 6.2b). The SEM provides as an output the response curve of the actual hybridization and then the corresponding response curve parameters values can be calculated. These parameters are the ones necessary for the objective function evaluation either in the form of a weighted sum or a single objective function. The constraints of problem (6.6) are implemented using an extreme barrier function, i.e., the value of the objective function is set to infinite in case any constraint is violated.

Regarding the GA, all individuals of the actual population are evaluated, then the three genetic operators are applied: selection, crossover and mutation (see [223]). A new population of individuals is generated, and it replaces the previous one (substitution) which completes an iteration of the optimization process. This process is repeated until a stop criterion is satisfied. A limit on the total number of generations is used here.

Regarding the **fibre layout optimization**, the goal is to understand the influence of the fibre dispersion on the composite response. For this purpose, the fibre layout optimization problem (6.11) is also solved using the GA and the flowchart describing this procedure is shown in Fig. 6.9.

Looking at Fig. 6.9, some data has to be initially loaded, such as: the fibres radii, LE fibres volume fraction and elements (fibres and matrix) strength. The optimal fibre hybridization that is solution of the mixed-integer optimization problem provides the needed data. Index *i* is the counter used to specify in which step the fibre layout optimization is. Firstly, the range of the *DD* parameter for the specific hybridization considered here needs to be found. The lower bound of this range (DD_{min}) is simply obtained through a LbL fibre arrangement, corresponding this to $i = 1$. The upper bound of this range (DD_{max}) is obtained by solving the fibre layout optimization problem (6.11). The result is a fibre arrangement that has the maximum dispersion degree, corresponding this to $i = 2$. Once these bounds are found, one considers three different intermediate target values DD_{target} for the dispersion degree, i.e. ${}^{i-2}DD_{target} \in [DD_{min}; DD_{max}] \; \forall \; i = \{3; 4; 5\}$, where $i = 3$ corresponds to the first *DD* target and so forth. A fibre layout optimization

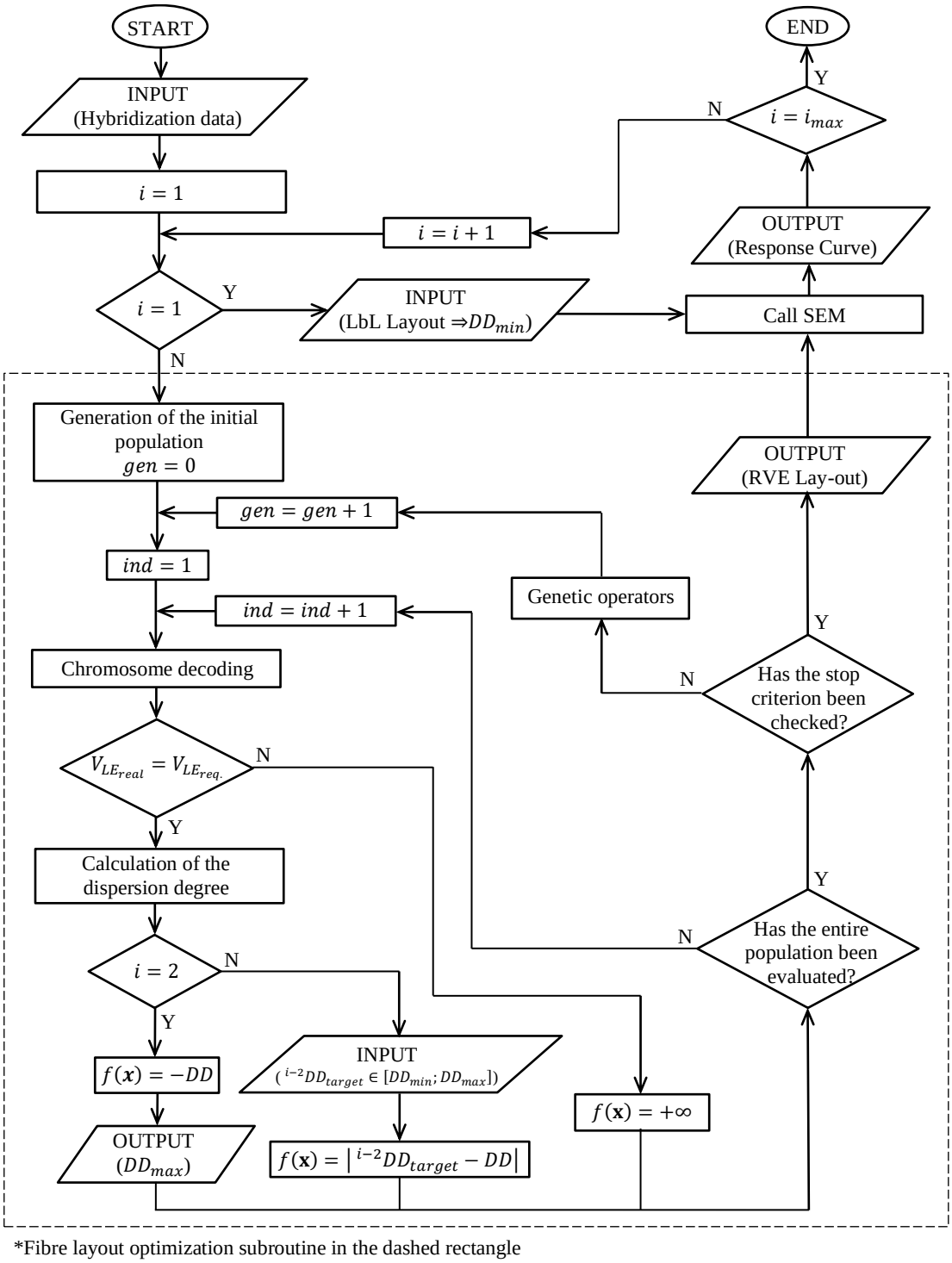

Fig. 6.9: Flowchart of the developed algorithm to solve the fibre layout optimization. Retrieved from [209].

problem (6.11) is solved using $f(\boldsymbol{x}) = \left|{}^{i-2}DD_{target} - DD\right|$ as the objective function in order to find out a fibre arrangement for each $DD = {}^{i-2}DD_{target}$. For each DD value between DD_{min} and DD_{max} (inclusive), a response curve is obtained. This procedure stops when $i = i_{max}$, where

$i_{max} = 5$ corresponds to the total number of dispersion degrees studied. In fact, this means that the full range of *DD* has been divided into 4 intervals. The response curves obtained for each *DD* can be compared in order to understand the fibre dispersion influence in the pseudo-ductile behaviour. Realize that the fibre layout optimization problem is purely geometric in nature, i.e., it does not depend on running the SEM. The SEM is only called later to obtain the response curve corresponding to a fibre arrangement with prescribed *DD*.

Since the fibre layout optimization problem is solved by the GA, an initial population that satisfies the imposed constraint in (6.11) must be generated. Otherwise, the GA convergence can be jeopardized due to the algorithm difficulty in satisfying the volume constraint when an initial population is unfeasible. This initial population is mostly comprised by individuals corresponding to solutions of random fibres arrangements. If a low dispersion degree is aimed, the initial population should be a LbL fibre arrangement to ease the GA convergence. If the actual LE fibres volume fraction is not equal to the required LE fibres volume fraction, the value of the objective function is set to infinite, i.e., the constraint is handled here using again the so-called extreme barrier function.

6.4 Results: Microstructural Optimization of UD Hybrid Composites

To perform a simulation using the SEM, a RVE must be properly sized. This is a sensitive issue because it is important to reduce the computational time cost of a SEM simulation but at the same time the quality of the results obtained should not be compromised. Notice that the SEM runs several times as demanded by the GA. Smaller RVE's are cheaper in terms of computational cost, but they may not be representative enough, leading to higher variability of results obtained for different simulations with the same hybridization. After conducting some numerical simulations, it is concluded that the smallest RVE that guarantees sufficiently representative results have $\delta_x = \delta_y = 50$ and $\delta_z = 4\delta_x = 200$. Note that the RVE size depends on the maximum radius of the fibres in the hybridization (see Section 6.1).

As mentioned in Section 6.1, a random strength is assigned to each of the fibre elements according to the Weibull distribution. This explains variability among results obtained for different runs of the SEM with the same hybridization. This variability could be handled running the SEM several times and then taking the average response curve for the hybridization at stake. This would

undoubtedly lead to a considerable extra computational cost. Fortunately, the author notices that the variability of results, only due to the assignment of random strength values to fibres according to the Weibull distribution, has a small impact on the pseudo-ductile behaviour. Therefore, the SEM is only called once per each evaluation of an individual in the GA. This saves in the computational time without undue loss of reliability on the results obtained.

The results for the fibre properties and fibre layout optimization problems formulated in Sections 6.2.1 and 6.2.2 are shown in Sections 6.4.1 and 6.4.2, respectively. Section 6.4.1 is divided into two Sections 6.4.1.1 and 6.4.1.2 corresponding to the results of the mixed-integer and continuous optimization of the fibre properties, respectively.

6.4.1 Fibre properties optimization

A square mesh with periodic arrangement of fibres (see Fig. 6.2b), where the position of the LE and HE fibres are randomly assigned, is used. The optimization problem of fibre properties formulated in (6.6) can be solved using either a weighted sum function (6.7) or a single-objective function (6.8). The optimal solutions obtained in the frame of this work, using these two objective functions, lead to the same optimal solution or to similar solutions of good quality. Actually, the weighting and normalization constants in (6.7) chosen below lead to an optimal solution with considerable pseudo-ductile behaviour and relatively high failure stress. Interestingly, this solution also increases the pseudo-plastic deformation energy per unit of volume. Therefore, the direct maximization of this energy may attain the simultaneous maximization of both pseudo-ductile strain and the failure stress.

On the one hand, the advantage of the single objective function (6.8) is to avoid any weighting, assuming that the amplitude of the pseudo-yielding plateau δ is not over a certain threshold δ^* and there is no load drop. On the other hand, the weighting strategy (6.7) could be more advantageous in case a hybridization with more pseudo-ductile strain and less maximum stress (or vice-versa) is sought over another hybridization that has a greater pseudo-plastic deformation energy per unit of volume. Thus, the objective function to be used, (6.7) or (6.8), must be chosen depending on whether one wants only the maximization of the pseudo-plastic deformation energy per unit volume or to have more control over the relative importance of each parameter that characterize the response curve.

The random (probabilistic) nature of the SEM and the GA motivates here running several times the same optimization problem. The parameters $\alpha = 0.05$ and $\delta^* = 250$ are used in (6.6) to solve both the mixed-integer and continuous optimization problems.

6.4.1.1 Mixed-integer optimization

The mixed-integer optimization problem of the fibre properties can be solved using either a weighted sum function (6.7) or a single function (6.8) as objective function. If a weighted sum function is used, a tuning of both the weighting and normalization constants is mandatory. In order to obtain a response curve with a well-defined pseudo-yielding plateau at a relatively high tensile stress, after some simulations, the following weighted sum function is introduced:

$$f(\mathbf{x}) = \left(\frac{1}{\varepsilon_d}2\right)0.35 + \left(\delta\frac{1}{100}\right)0.4 + \left(\frac{1}{\sigma_{max}}2500\right)0.25 \tag{6.17}$$

Table 6.3 shows the GA input parameters used to solve the mixed-integer optimization problem. Running the optimizer several times shows that it is possible to find solutions with a substantial pseudo-ductile behaviour in a relatively high stress level. The solution that stood out the most as optimal is the Carbon T300 (LE) and the Kevlar 119 (HE) hybridization, with 19% of LE fibre volume fraction. Fig. 6.10 shows the response curve of the optimal hybridization, as well as the response curves of the non-hybrid composite materials. The response curve parameters of the hybridization are shown in Table 6.4. Notice that the pseudo-ductile behaviour in the hybrid composite response is obtained at the expense of reducing σ_{max} seen in the non-hybrid composites using the previous fibres.

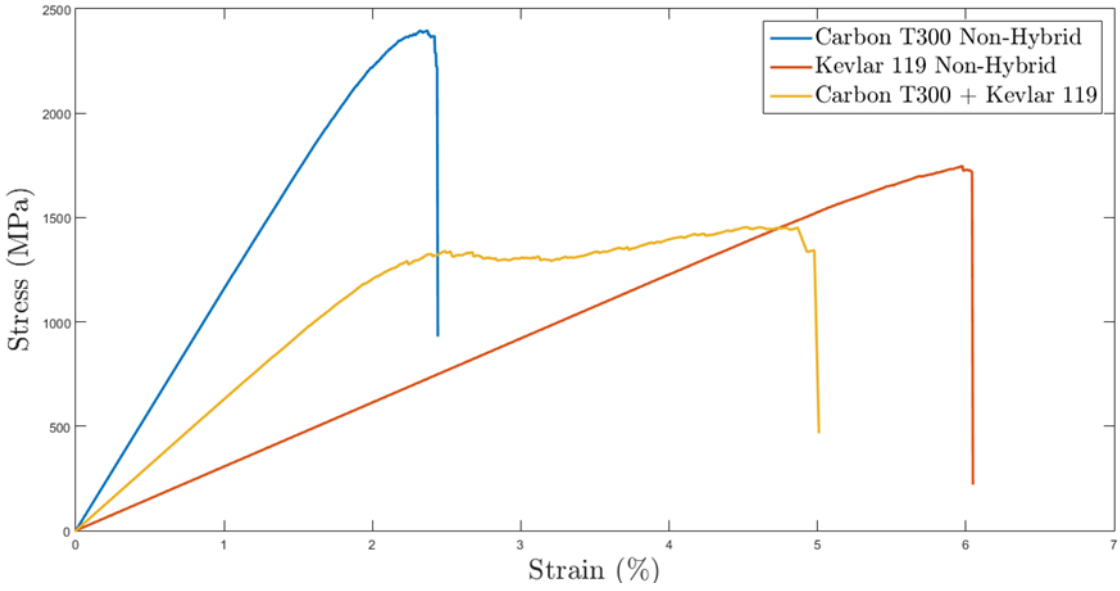

Fig. 6.10: Stress-strain diagrams of the optimal hybridization and non-hybrid fibres obtained in the mixed-integer optimization. Retrieved from [209].

Table 6.3: GA input parameters for the mixed-integer optimization of the fibre properties.

Population (Type/Size)	**Fitness scaling** (Scaling function)	**Selection** (Type)	**Crosso-ver** (Type)	**Mutation** (Type)	**Reproduc-tion** (Elitism)	**Genera-tions** (Size)
Double Vector 24	Rank	Stochastic Uniform	Special procedure (See [Deep *et al.*])		2	20

Table 6.4: Response curve parameters of the Carbon T300 (19%) + Kevlar 119 (81%) hybridization.

Hybridization	$\boldsymbol{\varepsilon_d}$ [%]	$\boldsymbol{\delta}$ [MPa]	$\boldsymbol{\sigma_{max}}$ [MPa]	$\boldsymbol{\lambda}$ [MPa]	$\boldsymbol{w_{plastic}}$ [MJ/m^3]
Carbon T300 + Kevlar 119	2.34	157	1434	5	31.4

6.4.1.2 Continuous optimization

A different optimization problem requires a new adjustment of the normalization and weighting constants in the weighted sum objective function. See in Eq. (6.18) the values used in this section. To solve the continuous optimization problem, the GA input parameters shown in Table 6.5 are used. Recall that the design variables of the continuous optimization problem are the fibres radii (R_{LE} and R_{HE}), the elastic modulus (E_{LE} and E_{HE}) and the Weibull scale ($\sigma_{0_{LE}}$ and $\sigma_{0_{HE}}$) and shape parameters (m_{LE} and m_{HE}) of both fibres to hybridize. Notice that the characteristic length (L_0) is not a design variable, its value is $L_0 = 25\text{mm}$. As in the case of the mixed-integer optimization, one runs here the GA several times. The design space is now very large, and the algorithm may find different optima. Among those optima found one reports the ideal hybridization shown in Table 6.6 due to its great pseudo-ductile behaviour and high failure stress. Fig. 6.11 shows the response curve of this ideal hybridization and its response curve parameters are in Table 6.7.

$$f(\boldsymbol{x}) = \left(\frac{1}{\varepsilon_d}2.5\right)0.4 + \left(\delta\frac{1}{150}\right)0.25 + \left(\frac{1}{\sigma_{max}}2500\right)0.35 \tag{6.18}$$

Table 6.5: GA input parameters for the continuous optimization of the fibre properties.

Population (Type/Size)	**Fitness scaling** (Scaling function)	**Selection** (Type)	**Crosso-ver** (Type)	**Mutation** (Type)	**Reproduc-tion** (Elitism)	**Genera-tions** (Size)
Double Vec-tor 56	Rank	Stochastic Uniform	Scattered	Adaptive feasible	2	20

Table 6.6: Optimal fibre properties of the hybrid composite obtained in the continuous optimization.

	E [GPa]	R [µm]	σ_0 [MPa]	m	$\langle\varepsilon\rangle$ [%]	V_f
LE Fibre	55	2.65	876	5.62	1.21	0.662
HE Fibre	177.282	3.53	3998.2	3.09	1.41	0.338

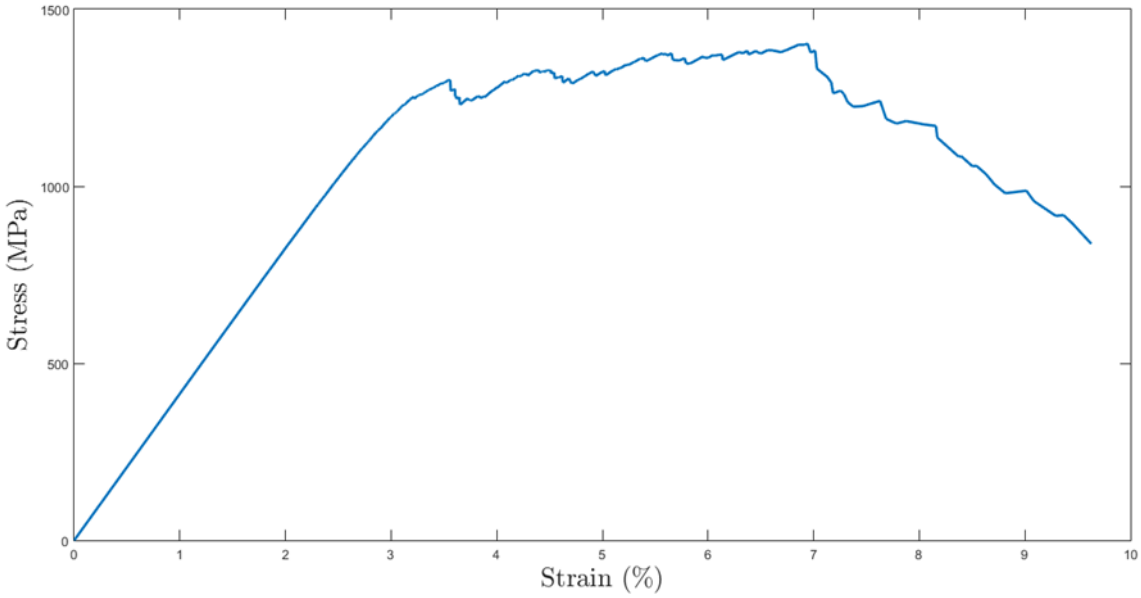

Fig. 6.11: Stress-strain diagram of the ideal hybridization obtained in the continuous optimization. Retrieved from [209].

Table 6.7: Response curve parameters of the ideal hybridization obtained in the continuous optimization.

Hybridization	ε_d [%]	δ [MPa]	σ_{max} [MPa]	λ [MPa]	$w_{plastic}$ [MJ/m^3]
Ideal Hybridization	3.55	172.8	1403.2	46.8	47.32

Comparing the optimal solution obtained in the mixed-integer optimization with the one obtained in the continuous optimization, it is possible to see a significant improvement in terms of pseudo-ductility, approximately more 50% of pseudo-ductile strain in the continuous optimization solution. In [208], the continuous optimization of the fibre properties is carried out without any relationship between the elastic modulus and strength. Although these properties are related here, one may not yet find in the market exactly the predicted optimal values. Nevertheless, it becomes apparent the type of material from which the ideal fibres should be made of. Looking at Fig. 6.8, the LE and HE fibres could possibly be Glass and Kevlar fibres, respectively.

6.4.2 Fibre layout optimization

In this section, the optimal hybridization of Carbon T300 (LE) and the Kevlar 119 (HE), with volume fraction of 19% of LE fibres, is used to study the fibre dispersion influence on the composite response. Firstly, as explained in Section 4, one needs to find out the minimum and maximum values of the dispersion degree *DD* that applies to the actual hybridization. The minimum dispersion degree is equal to 7% and corresponds to a LbL layout. The maximum dispersion degree is 67% and corresponds to the optimal solution obtained when solving the fibre layout optimization problem (6.11) with the objective function $f(\boldsymbol{x}) = -DD$. Then one solves (6.11) again for the following intermediate dispersion degree targets, $DD_{Target}(\%) = \{15; 30; 45\}$. After this, the composite response curves can be obtained as a result of running the SEM for each fiber arrangement and corresponding dispersion degree, see Fig. 6.12.

A pseudo-ductile behaviour is obtained for high fibre dispersion degrees but severely compromised for lower dispersion degrees as seen in Fig. 6.12. This can be explained through the Stress Concentration Factor (SCF) definition. After a fibre breaks, the stress previously carried by such fibre is redistributed among the surrounding intact fibres. In turn, the stress carried by these fibres in the vicinity increases as well as their failure probability. The pseudo-ductile behaviour is seen when the LE and HE fibres break in a continuous fashion. Clusters of fibres of the same type disrupt this process. Imagine that in the neighbourhood of a broken fibre only fibres of similar failure strain exist, which is easily found in the LbL layout shown in Fig. 6.12. In this case, th failure progress of LE and HE fibres is obviously not continuous. When a LE fibre breaks it triggers the failure of all fibres in the vicinity because no HE fibres exist there to bear the SCF caused by the LE fibre failure (exception made for those fibres in the interface between layers). Therefore, in order to have a pseudo-ductile behaviour, the LE and HE fibres must be well mixed (see case $\mathrm{DD} = 67\%$ in Fig. 6.12). In this case when a LE fibre breaks there is always a HE fibre in the neighbourhood to carry an increased stress caused by the reduced bearing load capacity of a LE fibre that just broke.

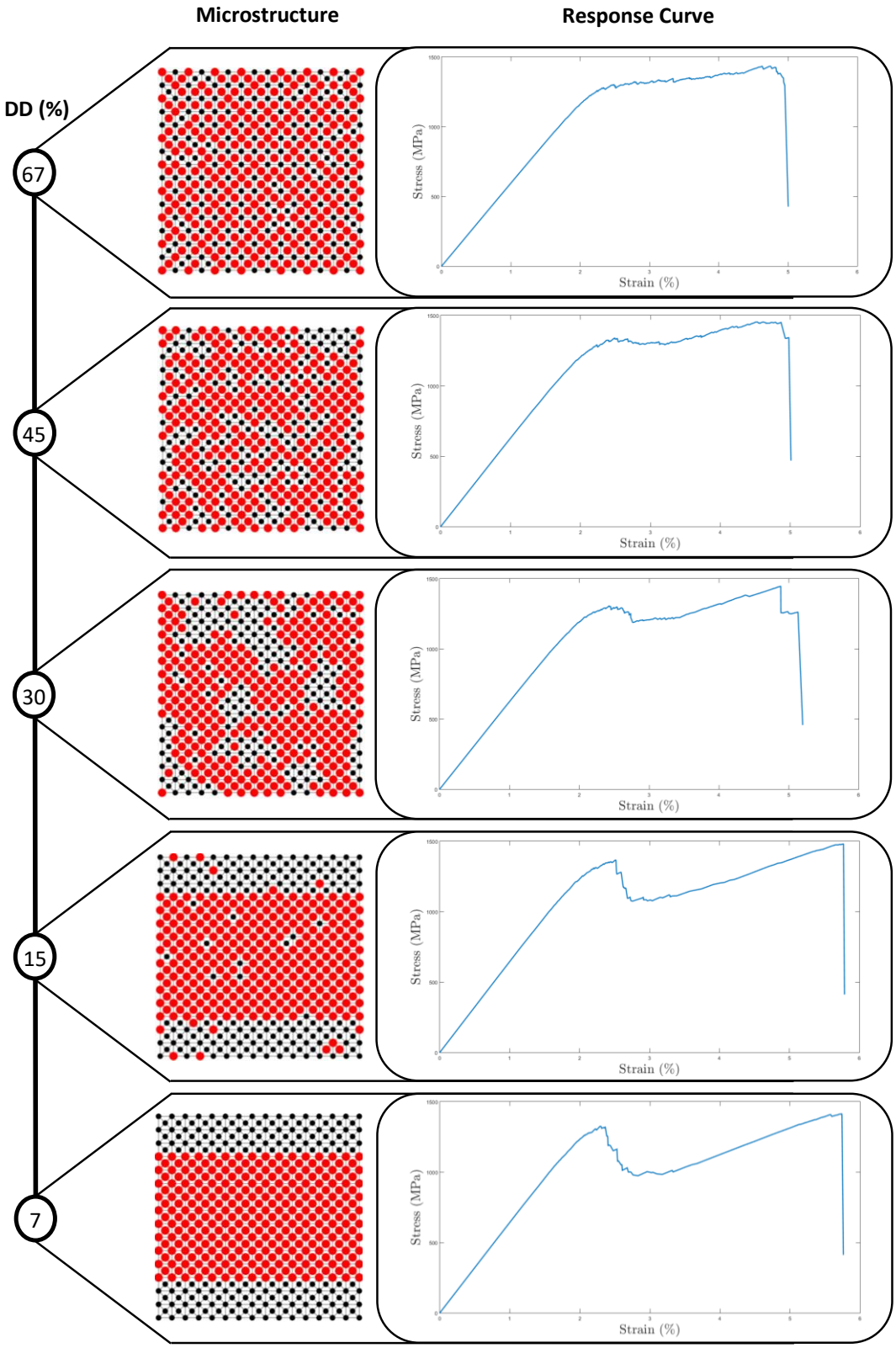

Fig. 6.12: Microstructures obtained from the fibre layout optimization and respective stress-strain diagrams for the different dispersion degrees investigated. Retrieved from [209].

Analysing the formation of clusters of broken fibres helps to understand what was just aforementioned. A cluster of broken fibres is defined following [224]: two fibres are considered to be part of the same cluster if (i) the distance between the centres of the two fibres is lower than four times the fibre radius and (ii) the axial distance between break planes was less than ten times the fibre radius. [224] defines two types of clusters: *disperse* clusters if the axial distance between the break planes is higher than a fibre radius and *co-planar* clusters if this distance is lower. In this work a cluster is considered co-planar if the break planes in the axial direction distance themselves by no more than one axial element length. Fig. 6.13 shows the fibre break density or the number of breaks per mm^3 as increases the strain applied to the composite. The trend seen on the number of breaks per unit volume always increases as expected and it is quite smooth for high dispersion degrees. For low dispersion degrees a large increment on the applied strain is not accompanied by any breaks till eventually all the remaining unbroken fibres break at once. In the case of high dispersion degrees, more fibres are able to break before the ultimate failure of the composite because the failure mechanism is more localized rather than being cluster dominated. An interesting result that supports this is now shown in Fig. 6.14. The maximum cluster size (or the maximum number of broken fibres in a single cluster) for high dispersion degrees is around 6/7 broken fibres, while for low dispersion degrees it is around 11/14 broken fibres. An analysis of the evolution of clusters of different sizes (*i*-plets, where *i* denotes the number of broken fibres present in the same cluster) is also done in Fig. 6.15 for the Layer-by-Layer layout as well as for the RVE with the maximum dispersion degree. The main conclusion that can be drawn from this figure is that with high dispersion degree there are a lot more singular fibre breaks (1-plet) than with low dispersion degree as well as a delay in the formation of larger clusters. Therefore, it can be concluded that the failure of a composite with high dispersion degree is not governed by the formation of large clusters (>6-plet), but by the failure of many singular fibres. To help understanding this, the percentage of broken fibres in each section of the RVE for all the sections along the fibre direction (Z coordinate in abscissa) for six different applied strains, which are marked in the stress-strain curve, can be seen in Fig. 6.16 and Fig. 6.17 for the Layer-by-Layer and the maximum dispersion degree layouts, respectively. In each figure, the microstructures shown represent the broken fibres within 10 fibre radius (maximum radius in the hybridization) in each direction of the critical section, for the applied strains.

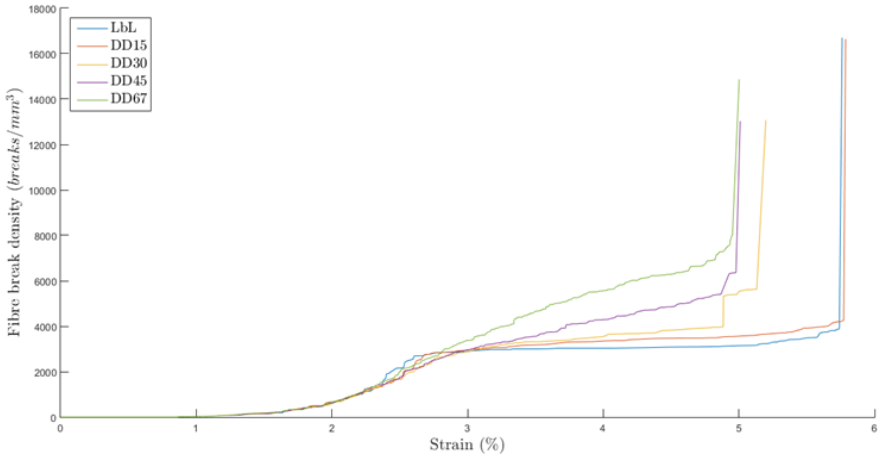

Fig. 6.13: Fibre break density in the fracture process for the different dispersion degrees simulated. Retrieved from [209].

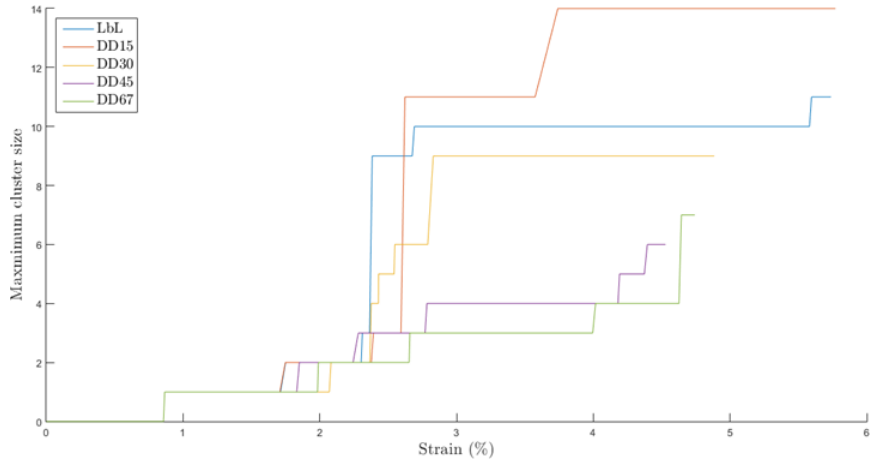

Fig. 6.14: Maximum cluster size in the fracture process for the different dispersion degrees simulated. Retrieved from [209].

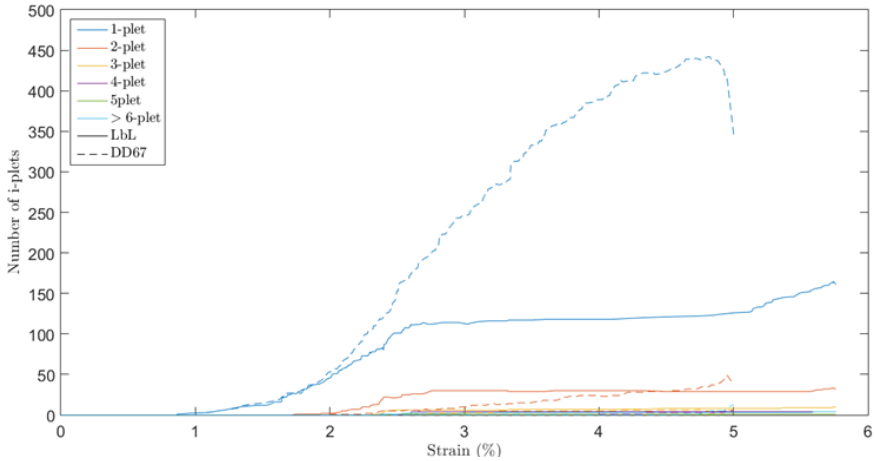

Fig. 6.15: *i*-plet growth during the fracture process for the LbL and maximum dispersion degree layouts. Retrieved from [209].

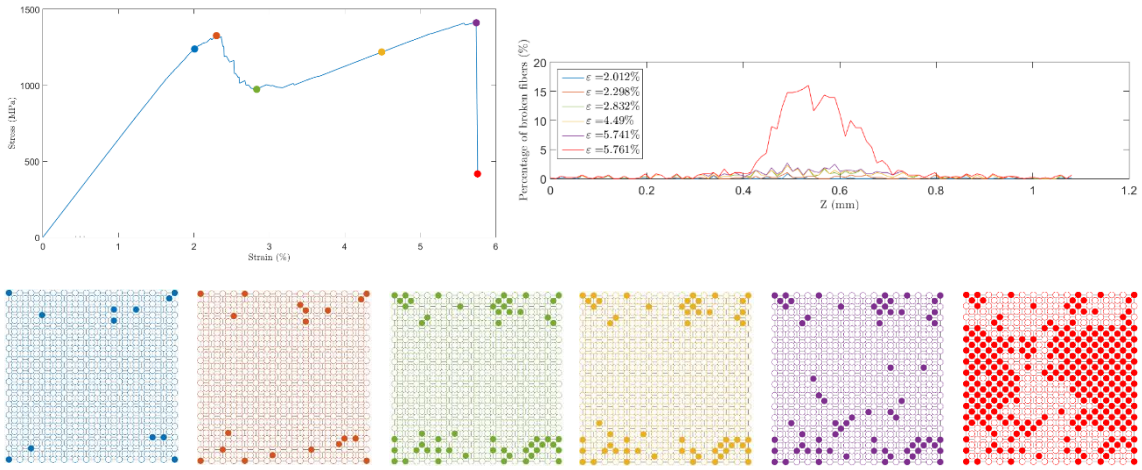

Fig. 6.16: Stress-strain diagram for the LbL layout, accompanied by the percentage of broken fibres in each section of the composite and the microstructures at the critical section at different stages. Retrieved from [209].

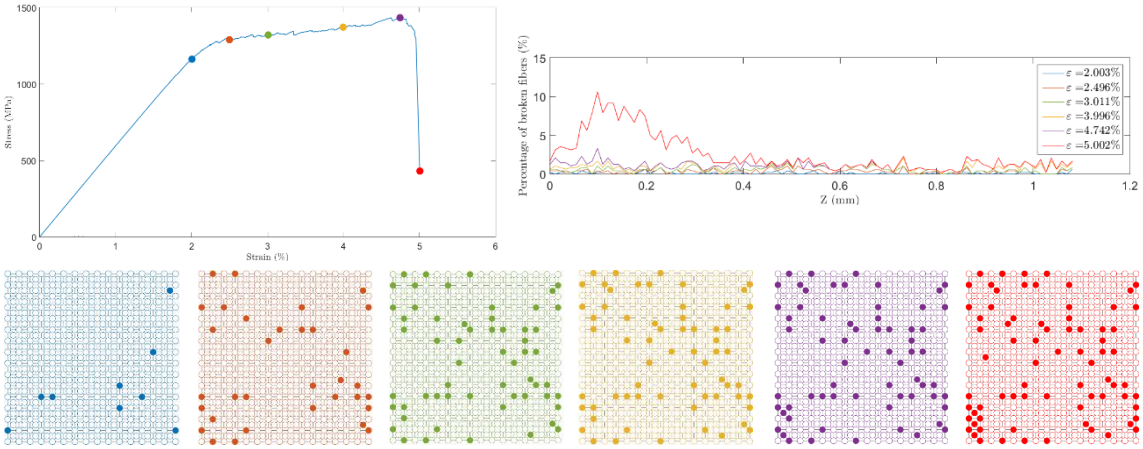

Fig. 6.17: Stress-strain diagram for the maximum dispersion degree layout, accompanied by the percentage of broken fibres in each section of the composite and the microstructures at the critical section at different stages. Retrieved from [209].

Comparing Fig. 6.16 with Fig. 6.17, there are remarkable differences in the fibre fracture process. In Fig. 6.16, the LE fibres break first and in a catastrophic way, forming large clusters of broken fibres at the bottom and top of the RVE, i.e., where the LE fibres are, leading to a load drop in the response curve, see the green marker in Fig. 6.16. Only after this, the HE fibres start to fail leading eventually to the catastrophic failure. In this case, there is no pseudo-ductile behaviour because the LE and HE fibres do not break gradually. That is not the case in Fig. 6.17 where the two types of fibres are well dispersed. Here, the HE fibres can carry the increase on stress due to the failure of LE fibres which prevents the formation of clusters of broken fibres. As a result, the composite failure is more gradual. Note also that the percentage of broken fibres in the longitudinal direction Z in Fig. 6.16 is higher than the result in Fig. 6.17. Furthermore, unlike Fig. 6.17, this percentage in Fig. 6.16 is approximately zero for Z values away from the critical

section. This means that for a higher dispersion degree, the fibres can break throughout their length and not just near the critical section.

Now an issue may arise regarding the representativeness of the response curves obtained in Fig. 6.12. In fact, the same dispersion degree may be attained by different fibre spatial arrangements, which means that the composite response curve may not be unique. Fig. 6.18 shows the response curves obtained considering four different RVEs with the same dispersion degree (*DD* = 30%) and fibres strength, i.e., RVEs only differ in terms of fibres positioning. Table 6.8 shows the response curve parameters values to evaluate the differences. From Fig. 6.18 and Table 6.8 is possible to conclude that the different RVEs, have small differences among response curves.

Another issue may be raised related to the change in the fibres strength distribution, in particular if that compromises the pseudo-ductile behaviour in a composite that has a high dispersion degree. Fig. 6.19 along with Table 6.9 help solving this issue. The same RVE with 67% of dispersion degree is tested considering four different fibres strength distributions. Basically, it can be concluded that a composite with high dispersion exhibits a pseudo-ductile behaviour regardless the different fibres strength distributions but the pseudo-ductile strain may slightly increase or decrease, see Table 6.9. This change is mainly due to the differences in the failure strain of the material, which is more affected by the strength distribution of the HE fibres.

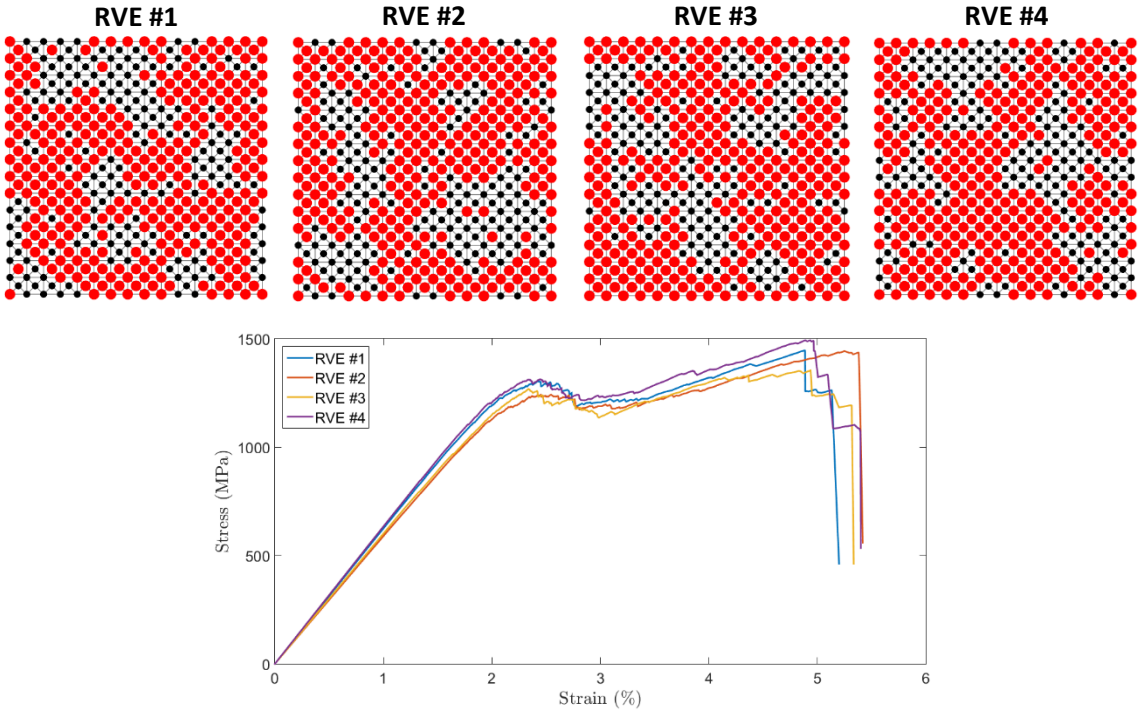

Fig. 6.18: Stress-strain diagrams obtained for four different microstructures with the same dispersion degree of 30% and fibres strength. Retrieved from [209].

Table 6.8: Response curve parameters of the four stress-strain diagrams obtained with the different microstructures shown in Fig. 6.18.

	RVE			
	#1	**#2**	**#3**	**#4**
ε_d (%)	2.57	2.8	2.69	2.58
σ_{max} [MPa]	1447	1443	1354	1493
δ [MPa]	259	270	218	276
λ [MPa]	85	64	106	93
$w_{plastic}$ [MPa(%)]	3327	3584	3363	3431

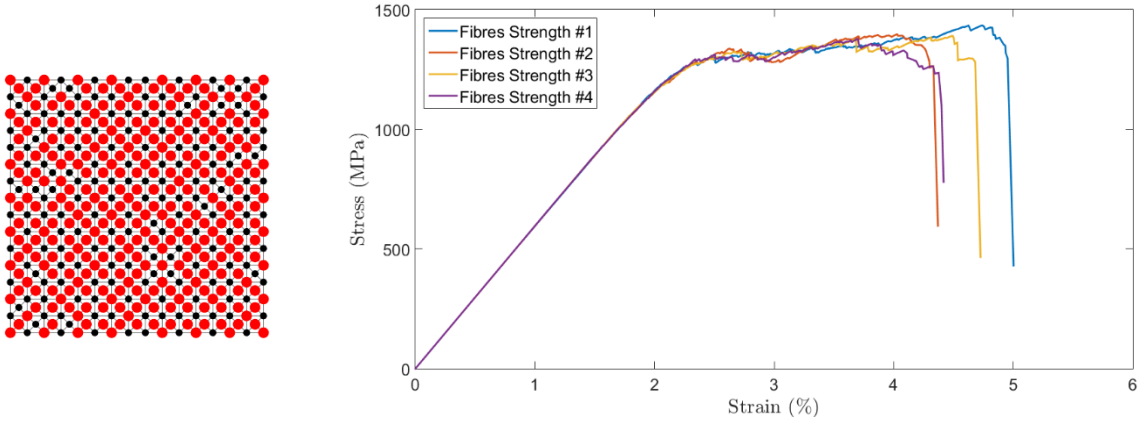

Fig. 6.19: Stress-strain diagrams obtained for the same microstructure with 67% of dispersion degree for four different fibres strength distributions. Retrieved from [209].

Table 6.9: Response curve parameters of the four stress-strain diagrams obtained for same micro-structure with 67% of dispersion degree for four different fibres strength distributions shown in Fig. 6.19.

	Fibres Strength			
	#1	**#2**	**#3**	**#4**
ε_d (%)	2.34	1.7	2.16	1.39
σ_{max} [MPa]	1434	1397	1391	1378
δ [MPa]	157	125	125	103
λ [MPa]	5	8	0	0
$w_{plastic}$ [MPa(%)]	3140	2247	2881	1833

6.5 Conclusions: Microstructural Optimization of UD Hybrid Composites

The optimization of the fibre properties using a composite material model with fibre hybridization to attain pseudo-ductile behaviour had been preliminary studied in [207,208]. In that work, analytical models were used to simulate the composite response and optimization problems were formulated and solved. The analytical models have a very low computational cost becoming thus very attractive in the frame of optimization studies which often require many analyses. However, some important failure mechanisms of the composites are not taken into account in such simplified models and that may jeopardize the quality of the predictions obtained. An analysis on the formation of clusters of broken fibres cannot be done analytically without using simplifying assumptions. As an alternative, the SEM is a numerical model with a RVE that predicts more accurately the composite response, and it has relatively low computational cost to be linked with an optimization algorithm.

Two different types of optimization problems are formulated and solved. Firstly, a fibre properties optimization problem is formulated. The objective is to find fibre properties that give a pseudo-ductile behaviour in the composite response. The fibre properties can be selected from a list of pre-defined values or ideal values may be found by letting those properties vary continuously within certain bounds and complying with some restrictions to ensure realistic results. A weighted sum function considering some specific objectives and a function considering the pseudo-plastic deformation energy per unit of volume are used here as objective functions. Actually, the optimal solutions obtained using these two different objective functions are quite similar. This means that the optimal solutions obtained by the weighted sum function have also the greatest pseudo-plastic deformation energy per unit of volume in the feasible design space. Using predefined fibres available in the market one finds an optimal hybridization of Carbon and Kevlar fibres which exhibits large pseudo-ductility. An even better pseudo-ductility is obtained in the continuum problem and from here one gains insight about what might be an ideal hybridization, i.e., possibly a hybridization of Glass and Kevlar like fibres, although fibres with the exact optimal properties are not readily seen among the existing market options.

Finally, a fibre layout optimization problem is solved to study how the fibre dispersion degree in the RVE influences the composite response. Several RVEs with different dispersion degrees are simulated. It is concluded that the dispersion degree has a great influence on the composite response. Higher dispersion degrees favour more the pseudo-ductile behaviour. To better

comprehend how the dispersion degree affects the composite response, an analysis of the formation of clusters of broken fibres is presented. In the case of the composite having low fibre dispersion degree, clusters of LE fibres and clusters of HE fibres exist apart from each other. Thus, when a LE fibre breaks, the surrounding fibres are of the same type, i.e., having the same failure strain. Therefore, a large cluster comprised of LE fibres fail at once accounting for a load drop in the response curve of the composite. This disrupts pseudo-ductile behaviour. Therefore, co-existing LE and HE fibres should break in a gradual (continuous) fashion by means of multiple fragmentations. To attain this, it is important that in the vicinity of a LE fibre exists a HE fibre in order to carry the increase on stress due to the LE fibre failure. This explains why a higher fibre dispersion degree is so important to attain the pseudo-ductile behaviour.

Fibre hybridization is a promising technique to obtain the pseudo-ductile behaviour on a composite. It is important to hybridize fibres with average failure strains that are compatible, i.e., that prevents them from breaking all at once or that one type breaks long before the other. It is important that the fibres embedded in the polymer matrix are well mixed as regards their spatial location to ensure that in the neighbourhood of a LE fibre there is always a HE fibre nearby. This prevents premature load drop in the composite response. In reality, the state-of-art regarding manufacturability of fibre reinforced composites to include fibre hybridization shows technological limitations preventing fine control over dispersion of fibres of each type as they are embedded in the matrix. This compromises the goal of reaching higher fibre dispersion degrees in the resulting hybrid composite. Therefore, on the one hand, some results and concluding remarks presented in this work may be seen beyond what nowadays is possible from a technological point of view. On the other hand, the present study may inspire the development of innovative hybridization technology that may allow for better control on fibre dispersion.

PART THREE

Conclusions

7 FINAL REMARKS AND FUTURE WORKS

This dissertation successfully applied multi-material design to improve the performance of non-conventional composites. Firstly, one performed a microstructural TO with the goal of discovering stiffer and, especially, stronger multi-material microstructures than its single-material counterparts. In that study, different problem formulations, multi-material settings, and loadings were investigated, paving the way for multi-scale TO. The results show that multi-material designs can be stiffer and stronger for the same mass requirement, and stress reductions can be achieved for the same material volume fraction requirement if an increased compliance is allowed. For instance, solving the compliance-based problem, one discovered multi-material designs up to 35% more stiff and 56% less stressed compared to their single material counterparts with the same mass. This was achieved on account of neglecting any material volume fraction (or porosity) requirement. If a porous material is required, then solving the stress-based problem one discovered quite stronger multi-material designs, up to 37% less stressed designs, compared to their single material counterparts with the same material volume fraction requirement. This was achieved on account of allowing a compliant design.

Afterwards, the multi-material design of the microstructure was extended to multi-scale TO. Different hierarchical strategies, with different macro design parametrizations, were used to solve a compliance-based multi-scale problem. The optimal multi-scale structures composed of more than one material proved to be stiffer, up to 19%, than its single-material counterparts for the same global mass requirement. However, with the present methodology to solve the hierarchical problem, there is no guarantee that the optimal solutions will (1) be stronger and (2) have

material's connectivity. These two points represent possible future work. In order to have a strong structure, it must be designed in such way that stress concentrations are as low as possible. To accomplish that, a stress-based problem must be solved. Bear in mind that, multi-scale TO with stress control (e.g., using stress constraints) is not straightforward, and highly increases the complexity of the hierarchical problem. To improve the material's connectivity, the approaches present in [134,135] could be applied. However, the ideal solution to this problem is yet to be discovered, which encourages the development of new methodologies to solve this problem.

Ultimately, the multi-material design was applied on fibre reinforced composites, where fibres of different types were combined on the microscale level to promote a well-behaved response of the material after the yielding point. Hybrid composites presenting the so-called pseudo-ductile behaviour were obtained. More specifically, a pseudo-ductile strain of 2.3% was achieved for predefined fibres available in the market, and for an ideal hybridization a remarkable pseudo-ductile strain of 3.5% was obtained. It was also concluded that the fibre dispersion in the RVE has a great impact on the composite's behaviour. In fact, lower fibre dispersions tend to disrupt pseudo-ductile behaviour with a load drop on the material's response, while higher fibre dispersions promote a regular pseudo-ductile behaviour. For future work, it would be interesting to explore the hybridization of UD composites using more than two fibres, as done in [225] for analytical models. This study performed here using a SEM could be naturally extended to more complex models (e.g., multi-scale models) to predict the composite's response more accurately. This would obviously increase the computational cost of the optimization process, which represents a great challenge to surpass. Also, the experimental validation of the results obtained here would be an interestingly path to be explored in the future.

Undoubtedly, a multi-material design can achieve superior performance when compared to a single-material one. In this dissertation, one explored the benefits of multi-material design for improving the structural stiffness and strength, and also the material's behaviour after the yielding point. The benefits of multi-material design can be further explored in other subjects, e.g., anepectic materials (materials with both negative Poisson's ratio and thermal expansion coefficient) [226] or thermo-elasticity problems [227].

BIBLIOGRAPHY

[1] Coelho, P. (2009). Modelos hierárquicos para a análise e síntese de estruturas e materiais com aplicações à remodelação óssea. Doctoral Thesis, Faculty of Sciences and Technology, NOVA University of Lisbon (FCT/UNL).

[2] Przemieniecki, J.S. (1968). *Theory of matrix structural analysis* (Vol. 1). New York: McGraw-Hill.

[3] Hrennikoff, A. (1941). Solution of Problems in Elasticity by the Frame work Method. *Journal of Applied Mechanics*, Vol. 8, No. 4, pp. 169–175.

[4] McHenry, D. (1943). A Lattice Analogy for the Solution of Plane Stress Problems. *Journal of Institution of Civil Engineers*, Vol. 21, pp. 59–82.

[5] Turner, M.J., Clough, R.W., Martin, H.C., and Topp, L.J. (1956). Stiffness and Deflection Analysis of Complex Structures. *Journal of Aeronautical Sciences*, Vol. 23, No. 9, pp. 805–824.

[6] Martin, H.C. (1961). Plane Elasticity Problems and the Direct Stiffness Method. *The Trend in Engineering*, Vol. 13, pp. 5–19.

[7] Levy, S. (1947). Computation of Influence Coefficients for Aircraft Structures with Discontinuities and Sweepback. *Journal of Aeronautical Sciences*, Vol. 14, No. 10, pp. 547–560.

[8] Levy, S. (1953). Structural Analysis and Influence Coefficients for Delta Wings. *Journal of Aeronautical Sciences*, Vol. 20, No. 7, pp. 449–454.

[9] Kardestuncer, H. (1974). *Elementary Matrix Analysis of Structures*. McGraw-Hill, New York.

[10] Logan, D.L. (2011). *A first course in the finite element method*. Cengage Learning.

[11] Schmit, L.A. (1960). Structural design by systematic synthesis. In Proceedings of the Second National Conference on Electronic Computation, ASCE, Pittsburgh, pp.105-132.

[12] Zienkiewicz, O.C. and Campbell, J.S. (1973). Shape optimisation and sequential linear programming. *Optimal Structural Design*, Wiley, New York, pp. 109-126.

[13] Haftka, R.T. and Grandhi, R.V. (1986). Structural shape optimization – A survey. *Computer methods in applied mechanics and engineering*, Vol. 57, No. 1, pp. 91-106.

[14] Maxwell, C. (1890). On reciprocal figures, frames and diagrams of forces. *Scientific Papers*, vol 2, pp.175-177.

[15] Michell, A.G.M. (1904). The limits of economy of material in frame structures. *Phil. Mag.*, Vol. 8, pp. 589–597.

[16] Bendsøe, M.P. and Kikuchi, N. (1988). Generating optimal topologies in structural design using a homogenization method. *Computer methods in applied mechanics and engineering*, Vol. 71, pp. 197-224.

[17] Bendsøe, M.P., and Sigmund, O. (2003). *Topology optimization: theory, methods, and applications*. Springer Science & Business Media.

[18] Wang, M.Y., Wang, X., and Guo, D. (2003). A level set method for structural topology optimization. *Computer methods in applied mechanics and engineering*, Vol. 192 (1-2), pp. 227-246.

[19] J. Sokolowski and A. Zochowski. (1999). On the Topological Derivative in Shape Optimization. *SIAM Journal on Control and Optimization*, Vol. 37, No. 4, pp. 1251–1272.

[20] B. Bourdin and A. Chambolle. (2003). Design-dependent loads in topology optimization. *ESAIM Control, Optimisation and Calculus of Variations*, Vol. 9, pp. 19–48.

[21] Eschenauer, H.A., Kobelev, V. and Schumacher, A. (1994). Bubble method for topology and shape optimization of structures. *Structural Optimization*, Vol. 8, pp. 42-51.

[22] Sui, Y., & Peng, X. (2017). *Modeling, Solving and Application for Topology Optimization of Continuum Structures: ICM Method Based on Step Function.* Butterworth-Heinemann.

[23] Christensen, P.W. and Klarbring, A. (2008). *An introduction to structural optimization* (Vol. 153). Springer Science & Business Media.

[24] Zeman, J. (2003). *Analysis of composite materials with random microstructure.* Czech Technical University, Faculty of Civil Engineering.

[25] Y.W. Knon, D.H. Allen, and R.Taleja. (2008). *Multiscale Modeling and Simulation of Composite Materials and Structures*, Springer.

[26] Z. Xia and W. A. Curtin. (2008). Multiscale Modeling of Tensile Failure in Fiber-Reinforced Composites. *Multiscale Modeling and Simulation of Composite Materials and Structures*, pp. 37-82.

[27] Hill, R. (1963). Elastic properties of reinforced solids: some theoretical principles. *Journal of the Mechanics and Physics of Solids*, Vol. 11, No. 5, pp. 357-372.

[28] Sánchez-Palencia, E. (1980). Non-homogeneous media and vibration theory. *Lecture notes in physics*, 127.

[29] Papanicolau, G., Bensoussan, A., and Lions, J.L. (1978). *Asymptotic analysis for periodic structures*. Elsevier.

[30] Cioranescu, D. and Paulin, J.S.J. (1979). Homogenization in open sets with holes. *Journal of mathematical analysis and applications*, Vol. 71, No. 2, pp. 590-607.

[31] Oleinik, O.A. (1984). On homogenization problems. In *Trends and applications of pure mathematics to mechanics* (pp. 248-272). Springer, Berlin, Heidelberg.

[32] Hassani, B. and Hinton, E. (2012). *Homogenization and structural topology optimization: theory, practice and software*. Springer Science & Business Media.

[33] Fish, J., Nayak, P. and Holmes, M.H. (1994). Microscale reduction error indicators and estimators for a periodic heterogeneous medium. *Computational Mechanics*, Vol. 14, No. 4, pp. 323-338.

[34] Ghosh, S. and Mukhopadhyay, S.N. (1993). A material based finite element analysis of heterogeneous media involving Dirichlet tessellations. *Computer Methods in Applied Mechanics and Engineering*, Vol .104, No. 2, pp. 211-247.

[35] Lissenden, C.J. and Herakovich, C.T. (1995). Numerical modelling of damage development and viscoplasticity in metal matrix composites. *Computer Methods in Applied Mechanics and Engineering*, Vol. 126, No. 3-4, pp. 289-303.

[36] Hollister, S.J. and Kikuchi, N. (1992). A comparison of homogenization and standard mechanics analyses for periodic porous composites. *Computational Mechanics*, Vol. 10, No. 2, pp. 73-95.

[37] Guedes, J. and Kikuchi, N. (1990). Pre-processing and postprocessing for materials based on the homogenization method with adaptive finite element methods. *Computer methods in applied mechanics and engineering*, Vol. 83, No. 2, pp. 143-198.

[38] Fish, J. and Shek, K. (2000). Multiscale analysis of composite materials and structures. *Composites Science and Technology*, Vol. 60, No. 12-13, pp. 2547-2556.

[39] Belytschko, T., Fish, J. and Bayliss, A. (1990). The spectral overlay on finite elements for problems with high gradients. *Computer Methods in Applied Mechanics and Engineering*, Vol. 81, No. 1, pp. 71-89.

[40] Fish, J. (1992). Hierarchical modelling of discontinuous fields. *Communications in Applied Numerical Methods*, Vol. 8, No. 7, pp. 443-453.

[41] Rank E. and Krause R. (1995) A multiscale finite element method. *Numerische Methoden und Informationsverarbeitung report*, University of Dortmund, Germany.

[42] Robbins, D.H. and Reddy, J.N. (1996). Variable kinematic modelling of laminated composite plates. *International Journal for Numerical Methods in Engineering*, Vol. 39, No. 13, pp. 2283-2317.

[43] Noor, A.K., Burton, W.S. and Peters, J.M. (1994). Hierarchical adaptive modeling of structural sandwiches and multilayered composite panels. *Applied Numerical Mathematics*, Vol. 14, No. 1-3, pp. 69-90.

[44] Dym, C.L. and Shames, I.H. (2013). *Solid Mechanics: A Variational Approach, Augmented Edition.* New York, McGraw-Hill.

[45] Bauchau, O.A. and Craig, J.I. (2009). *Structural analysis: with applications to aerospace structures* (Vol. 163). Springer Science & Business Media.

[46] Gould, P.L. (2013). *Introduction to linear elasticity*. 3rd Edition. New York: Springer Science & Business Media.

[47] Timoshenko S.P. and Goodier J.N. (1951). *Theory of Elasticity*. McGraw Hill

[48] Lions, J.L. (1981). *Some methods in mathematical analysis of systems and their control*. Kexue Chubanshe Science Press, Beijing, and Gordon and Breach, London.

[49] Deaton JD, Grandhi RV (2014). A survey of structural and multidisciplinary continuum topology optimization: post 2000. *Struct Multidisc Optim*, 49: 1-38.

[50] M. P. Bendsøe (1989). Optimal shape design as a material distribution problem. *Struct. Optim.*, vol. 1, n. 4, pp. 193–202.

[51] Bazaraa, M. S., Sherali, H. D. and Shetty, C. M. (2013). *Nonlinear programming: theory and algorithms*. John Wiley & Sons.

[52] Svanberg, K. (1987). The method of moving asymptotes - a new method for structural optimization. *International journal for numerical methods in engineering*, 24(2), 359-373.

[53] Svanberg, K. (1995). A globally convergent version of MMA without linesearch. In G. Rozvany and N. Olhoff, editors, *First World Congress of Structural and Multidisciplinary Optimization*, pages 9–16.

[54] Svanberg, K. (2002), A class of globally convergent optimization methods based on conservative convex separable approximations. *SIAM journal on optimization*, *12*(2), 555-573.

[55] Zhang, W. H., Fleury, C., Duysinx, P., Nguyen, V. H. and Laschet, I. (1996). A generalized method of moving asymptotes (GMMA) including equality constraints. *Structural optimization*, *12*(2), 143-146.

[56] C. Fleury (1979). Structural weight optimization by dual methods of convex programming. *International Journal of Numerical Methods in Engineering*, 14:1761–1783.

[57] Luenberger D, Ye Y (1984). Linear and nonlinear programming (Vol. 2). Reading, MA: Addison-wesley. https://doi.org/10.1007%2F978-3-319-18842-3

[58] Haftka, R. T. and Gürdal, Z. (2012). *Elements of structural optimization* (Vol. 11). Springer Science & Business Media.

[59] Sigmund, O. (2007). Morphology-based black and white filters for topology optimization. *Struct Multidisc Optim* **33,** 401–424. https://doi.org/10.1007/s00158-006-0087-x

[60] Bruns TE and Tortorelli DA (2001). Topology optimization of nonlinear elastic structures and compliant mechanisms. *Comput Methods Appl Mech Eng* 190(26-27):3443–3459.

[61] Bourdin B (2001). Filters in topology optimization. *Int J Numer Methods Eng* 50(9):2143–2158.

[62] Sigmund O (1997) On the design of compliant mechanisms using topology optimization. *Mechan Struct Mach* 25(4):493–524.

[63] Coelho, P. G., Guedes, J. M., and Cardoso, J. B. (2019). Topology optimization of cellular materials with periodic microstructure under stress constraints. *Structural and Multidisciplinary Optimization*, *59*(2), 633-645.

[64] Collet, M., Bruggi, M., and Duysinx, P. (2017). Topology optimization for minimum weight with compliance and simplified nominal stress constraints for fatigue resistance. *Structural and Multidisciplinary Optimization*, *55*(3), 839-855.

[65] Taylor J, Bendsoe M (1984) An interpretation of min-max structural design problems including a method for relaxing constraints. *Int J Solids Struct* 20:301‑314.

[66] Le C, Norato J, Bruns T, Ha C and Tortorelli D (2010). Stress-based topology optimization for continua. *Structural and Multidisciplinary Optimization*, 41:605‑620.

[67] Deaton JD and Grandhi RV (2014) A survey of structural and multidisciplinary continuum topology optimization: post 2000. *Structural and Multidisciplinary Optimization*, 49:1‑38.

[68] Coelho, P. G., Barroca, B. C., Conde, F. M., & Guedes, J. M. (2021). Minimization of maximal von Mises stress in porous composite microstructures using shape and topology optimization. *Structural and Multidisciplinary Optimization*, *64*(4), 1781-1799.

[69] Zhao, R., Zhao, J., & Wang, C. (2021). Stress-constrained concurrent topology optimization of two-scale hierarchical structures. *International Journal for Numerical Methods in Engineering*, *122*(21), 6126-6154.

[70] Yang, R. J. and Chen, C. J. (1996). Stress-based topology optimization. *Structural optimization*, *12*(2), 98-105.

[71] Duysinx, P. and Sigmund, O. (1998). New developments in handling stress constraints in optimal material distribution. In *7th AIAA/USAF/NASA/ISSMO symposium on multidisciplinary analysis and optimization* (p. 4906).

[72] Luo, Y. and Kang, Z. (2012). Topology optimization of continuum structures with Drucker–Prager yield stress constraints. *Computers & Structures*, *90*, 65-75.

[73] Holmberg, E., Torstenfelt, B., and Klarbring, A. (2013). Global and clustered approaches for stress constrained topology optimization and deactivation of design variables. In *10th World Congress on Structural and Multidisciplinary Optimization, May 19-24, 2013, Orlando, Florida, USA* (pp. 1-10).

[74] G. Sved and Z. Ginos (1968). Structural optimization under multiple loading, *Int. J. Mech. Sci.*, vol. 10, n. 10, pp. 803–805.

[75] U. Kirsch (1990), On singular topologies in optimum structural design, *Struct. Optim.*, vol. 2, n. 3, pp. 133–142.

[76] Cheng GD and Guo X (1997). ε-Relaxed approach in structural topology optimization. *Struct Optim* 13(4):258‑266.

[77] Duysinx P and Bendsøe MP (1998). Topology optimization of continuum structures with local stress constraints. *Int J Numer Methods Eng*, 43(8):1453‑1478.

[78] Bruggi M (2008) On an alternative approach to stress constraints relaxation in topology optimization. *Struct Multidiscip Optim*, 36:125‑141.

[79] Sanders, E. D., Aguiló, M. A. and Paulino, G. H. (2018). Multi-material continuum topology optimization with arbitrary volume and mass constraints. *Computer Methods in Applied Mechanics and Engineering*, *340*, 798-823.

[80] Woischwill C and Kim IY (2018). Multimaterial multijoint topology optimization. *Int J Numer Methods Eng*, 115(13):1552‑1579.

[81] Bendsøe MP and Sigmund O (1999). Material interpolation schemes in topology optimization. *Arch Appl Mech*, 69:635–654.

[82] Conde, F. M., Coelho, P. G., and Guedes, J. M. (2022). Multi-material and strength-oriented microstructural topology optimization applied to discrete phase and functionally graded materials. *Structural and Multidisciplinary Optimization*, *65*(4), 1-22.

[83] Ramani A (2011). Multi-material topology optimization with strength constraints. *Structural and Multidisciplinary Optimization*, 43:597‑615.

[84] Kennedy GJ (2016). A full-space barrier method for stress-constrained discrete material design optimization. *Structural and Multidisciplinary Optimization*, 54(3):619‑639.

[85] Zegard, T. and Paulino, G. H. (2016). Bridging topology optimization and additive manufacturing. *Structural and Multidisciplinary Optimization*, *53*(1), 175-192.

[86] Robbins, J., Owen, S. J., Clark, B. W. and Voth, T. E. (2016). An efficient and scalable approach for generating topologically optimized cellular structures for additive manufacturing. *Additive Manufacturing*, *12*, 296-304.

[87] M. Y. Wang and X. Wang (2004). “Color” level sets: a multi-phase method for structural topology optimization with multiple materials. *Comput. Methods Appl. Mech. Eng.*, vol. 193, n. 6–8, pp. 469–496.

[88] R. Tavakoli and S. M. Mohseni (2014). Alternating active-phase algorithm for multimaterial topology optimization problems: a 115-line MATLAB implementation. *Struct. Multidiscip. Optim.*, vol. 49, n. 4, pp. 621–642.

[89] S. Zhou and M. Y. Wang (2006). Multimaterial structural topology optimization with a generalized Cahn–Hilliard model of multiphase transition. *Struct. Multidiscip. Optim.*, vol. 33, n. 2, pp. 89–111.

[90] Sigmund, O. and Torquato, S. (1997). Design of materials with extreme thermal expansion using a three-phase topology optimization method. *Journal of the Mechanics and Physics of Solids*, *45*(6), 1037-1067.

[91] Bruyneel, M. (2011). SFP—a new parameterization based on shape functions for optimal material selection: application to conventional composite plies. *Structural and Multidisciplinary Optimization*, *43*(1), 17-27.

[92] Stegmann, J. and Lund, E. (2005). Discrete material optimization of general composite shell structures. *International Journal for Numerical Methods in Engineering*, *62*(14), 2009-2027.

[93] Gao, T., Zhang, W. and Duysinx, P. (2012). A bi-value coding parameterization scheme for the discrete optimal orientation design of the composite laminate. *International Journal for Numerical Methods in Engineering*, *91*(1), 98-114.

[94] Zuo, W. and Saitou, K. (2017). Multi-material topology optimization using ordered SIMP interpolation. *Structural and Multidisciplinary Optimization*, *55*(2), 477-491.

[95] Lund, E. and Stegmann, J. (2005). On structural optimization of composite shell structures using a discrete constitutive parametrization. *Wind Energy: An International Journal for Progress and Applications in Wind Power Conversion Technology*, *8*(1), 109-124.

[96] Hvejsel, C. F. and Lund, E. (2011). Material interpolation schemes for unified topology and multi-material optimization. *Structural and Multidisciplinary Optimization*, *43*(6), 811-825.

[97] Hvejsel, C. F., Lund, E. and Stolpe, M. (2011). Optimization strategies for discrete multi-material stiffness optimization. *Structural and Multidisciplinary Optimization*, *44*(2), 149-163.

[98] Nikbakht S, Kamarian S and Shakeri M (2019). A review on optimization of composite structures part II: functionally graded materials. *Composite Structures*, *214*, 83-102.

[99] Xia, Q. and Wang, M. Y. (2008). Simultaneous optimization of the material properties and the topology of functionally graded structures. *Computer-Aided Design*, *40*(6), 660-675.

[100] Hashin Z and Shtrikman S (1963) A variational approach to the theory of the elastic behaviour of multiphase materials. *J Mech Phys Solids*, 11(2):127‑140.

[101] Dunning PD, Brampton CJ and Kim HA (2015). Simultaneous optimisation of structural topology and arterial grading using level set method. *Materials Science and Technology*, 31(8): 884-894.

[102] Taheri AH and Suresh K (2017). An isogeometric approach to topology of multi-material and functionally graded structures. *Int J Num Meth Eng*, 109:668-696.

[103] Conlan-Smith C and Bhattacharyya A (2018). Optimal design of compliant mechanisms using functionally graded materials. *Structural and Multidisciplinary Optimization*, 57: 197-21.

[104] Radman, A., Huang, X. and Xie, Y. M. (2013). Topology optimization of functionally graded cellular materials. *Journal of Materials Science*, *48*(4), 1503-1510.

[105] Vermaak, N., Michailidis, G., Parry, G., Estevez, R., Allaire, G. and Bréchet, Y. (2014). Material interface effects on the topology optimizationof multi-phase structures using a level set method. *Structural and Multidisciplinary Optimization*, *50*(4), 623-644.

[106] Kang, Z., Wu, C., Luo, Y. and Li, M. (2019). Robust topology optimization of multi-material structures considering uncertain graded interface. *Composite Structures*, *208*, 395-406.

[107] Lipton, R. (2002). Design of functionally graded composite structures in the presence of stress constraints. *International journal of solids and structures*, *39*(9), 2575-2586.

[108] Stump, F. V., Silva, E. C. and Paulino, G. H. (2007). Optimization of material distribution in functionally graded structures with stress constraints. *Communications in numerical methods in engineering*, *23*(6), 535-551.

[109] Conlan-Smith, C. and James, K. A. (2019). A stress-based topology optimization method for heterogeneous structures. *Structural and Multidisciplinary Optimization*, *60*(1), 167-183.

[110] Allaire, G. and Aubry, S. (1999). On optimal microstructures for a plane shape optimization problem. *Struct Optim*, 17(2), 86-94.

[111] Lurie K.A., Cherkaev A.V. (1984). G-closure of a set of anisotropically conducting media in the two-dimensional case. *J Optim Theory Appl*, 42(2), 283-304.

[112] Norris A. (1985). A differential scheme for the effective moduli of composites. *Mech Mater*, 4(1), 1-16.

[113] Francfort, G. A. and Murat, F. (1986). Homogenization and optimal bounds in linear elasticity. *Archive for Rational mechanics and Anal*ysis, 94(4), 307-334.

[114] Milton G.W. (1986). Modelling the properties of composites by laminates. In: Ericksen JL, Kinderlehrer D, Kohn R, Lions JL (eds) *Homogenization and effective moduli of materials and media*. Springer, New York, pp 150-174.

[115] Wu, J., Sigmund, O. and Groen, J. P. (2021). Topology optimization of multi-scale structures: a review. *Structural and Multidisciplinary Optimization*, 63(3), 1455-1480.

[116] Zhang W. and Sun S. (2006). Scale-related topology optimization of cellular materials and structures. *Int J Numer Methods Eng*, 68(9), 993-1011.

[117] Wu J., Aage N., Westermann R. and Sigmund O. (2018) Infill optimization for additive manufacturing – approaching bone-like porous structures. *IEEE Trans Vis Comput Graph*, 24(2), 1127-1140.

[118] Rodrigues H, Guedes JM, Bendsøe MP (2002) Hierarchical optimization of material and structure. Struct Multidisc Optim, 24(1), 1-10.

[119] Allaire G (2002) Shape optimization by the homogenization method, vol 146. Springer Science & Business Media.

[120] Sigmund O (1994) Materials with prescribed constitutive parameters: an inverse homogenization problem. *Int J Solids Struct*, 31(17), 2313-2329.

[121] Pantz O. and Trabelsi K. (2008). A post-treatment of the homogenization method for shape optimization. *SIAM J Control Optim*, 47(3), 1380-1398.

[122] Guest J.K., Prévost J.H. and Belytschko T. (2004). Achieving minimum length scale in topology optimization using nodal design variables and projection functions. *Int J Numer Methods Eng*, 61(2), 238-254.

[123] Liu L., Yan J. and Cheng G. (2008). Optimum structure with homogeneous optimum truss-like material. *Comput Struct*, 86(13), 1417-1425.

[124] Clausen A., Aage N. and Sigmund O. (2015). Topology optimization of coated structures and material interface problems. *Comput Methods Appl Mech Eng*, 290, 524-541.

[125] Groen J.P., Wu J. and Sigmund O. (2019) Homogenization-based stiffness optimization and projection of 2d coated structures with orthotropic infill. *Comput Methods Appl Mech Eng*, 349, 722-742.

[126] Luo Y, Li Q, Liu S (2019) A projection-based method for topology optimization of structures with graded surfaces. *Int J Numer Methods Eng*, 118(11), 654–677.

[127] Barbarosie C. and Toader A.M. (2014). Optimization of bodies with locally periodic microstructure by varying the periodicity pattern. *Netw Heterog Media*, 9(3), 433-451.

[128] Soto C.A. and Díaz A.R. (1993). On the modelling of ribbed plates for shape optimization. *Struct Optim*, 6(3), 175-188.

[129] Cherkaev A, Krog L, Kucuk I (1998) Stable optimal design of two-dimensional elastic structures. *Control Cybern*, 27(2), 265-282.

[130] Fujii D., Chen B.C., Kikuchi N. (2001). Composite material design of two-dimensional structures using the homogenization design method. *Int J Numer Methods Eng*, 50(9), 2031-2051.

[131] Wu J., Wang W. and Gao X. (2021). Design and optimization of conforming lattice structures. *IEEE Trans Vis Comput Graph*, 27(1), 43-56.

[132] Coelho P.G., Fernandes P.R., Guedes J.M. and Rodrigues H.C. (2008). A hierarchical model for concurrent material and topology optimization of three-dimensional structures. Struct Multidisc Optim, 35(2): 107-115.

[133] Coelho P, Cardoso J, Fernandes P, Rodrigues H (2011) Parallel computing techniques applied to the simultaneous design of structure and material. *Adv Eng Softw*, 42(5), 219-227.

[134] Zhou XY, Du Z, Kim HA (2019) A level set shape metamorphosis with mechanical constraints for geometrically graded microstructures. *Struct Multidiscip Optim*, 60(1), 1–16.

[135] Liu P, Kang Z, Luo Y (2020) Two-scale concurrent topology optimization of lattice structures with connectable microstructures. *Addit Manuf*, 36,101427.

[136] Garner E., Kolken H.M., Wang C.C., Zadpoor A.A., Wu J. (2019). Compatibility in microstructural optimization for additive manufacturing. *Addit Manuf*, 26, 65-75.

[137] Fletcher, R. (1987). *Practical methods of optimization*. John Wiley & Sons.

[138] Vigdergauz, S. (2001). The effective properties of a perforated elastic plate numerical optimization by genetic algorithm. Int J Solids Struct 38: 8593–8616.

[139] Vigdergauz, S. (2002). Genetic algorithm of the effective Young moduli in a perforated plate. Struct Multidisc Optim 24(2): 106–117.

[140] Cherepanov GP (1974) Inverse problems of the plane theory of elasticity. J Appl Math Mech 38: 915-931.

[141] Vigdergauz S (1993) Optimal stiffening of holes under equibiaxial tension. Int J Solids Struct 30(4): 569–577.

[142] Ituarte IF, Boddeti N, Hassani V, Dunn ML and Rosen DW (2019). Design and additive manufacture of functionally graded structures based on digital materials. Addit Manuf 30: 100839.

[143] Sigmund O and Maute K (2013) Topology optimization approaches. Struct Multidisc Optim 48, 1031–1055.

[144] Bruggi M and Duysinx P (2012) Topology optimization for minimum weight with compliance and stress constraints. Struct Multidisc Optim 46: 369–384.

[145] Gill, S. (1958). Parallel programming. *The computer journal*, *1*(1), 2-10.

[146] Hermanns, M. (2002). Parallel programming in Fortran 95 using OpenMP. *Technique Report, Universidad Politecnica De Madrid*.

[147] Gropp W, Lusk E, Skjellum A (1999) Using MPI: portable parallel programming with the message passing interface. Second Edition. MIT Press

[148] Aage N, Lazarov B (2013) Parallel framework for topology optimization using the method of moving asymptotes. Struct Multidisc Optim 47(4): 493-505.

[149] Dagum L, Menon R (1998) OpenMP: an industry standard API for shared-memory programming. IEEE computational science and engineering, 5(1), 46-55.

[150] Ashby M (1999) Materials selection in mechanical design (2nd Edition). Butterworth Heinemann.

[151] Collet M, Noël L, Bruggi M, Duysinx P (2018) Topology optimization for microstructural design under stress constraints. Struct Multidisc Optim 58(6): 2677-2695.

[152] Zhao L, Xu B, Han Y, Rong J (2021a) Concurrent design of composite macrostructure and cellular microstructure with respect to dynamic stress response under random excitations. Compos Struct 257: 113123.

[153] Du Z, Zhou XY, Picelli R, Kim HA (2018) Connecting microstructures for multiscale topology optimization with connectivity index constraints. J Mech Des 10(1115/1):4041176.

[154] Kikuchi, N. (1986). *Finite element methods in mechanics*. CUP Archive.

[155] Coelho, P. G., & Rodrigues, H. C. (2015). Hierarchical topology optimization addressing material design constraints and application to sandwich-type structures. Structural and Multidisciplinary Optimization, 52(1), 91-104.

[156] A. S. Argon (1974). Statistical Aspects of Fracture. In L J Broutman, editor, *Composite Materials: Fatigue and Fracture*, vol 5, chapter 4, pages 153–190. Academic Press, New York.

[157] Y. Swolfs, L. Gorbatikh, V. Romanov, S. Orlova, S. V. Lomov, and I. Verpoest (2013). Stress concentrations in an impregnated fibre bundle with random fibre packing. *Composites Science and Technology*, 74(0):113–120.

[158] Tavares, R. P. (2020). Mechanics of deformation and failure of fibre hybrid composites. Doctoral Thesis in University of Porto and University of Girona.

[159] Y. Swolfs, L. Gorbatikh and I. Verpoest (2014). Fibre hybridization in polymer composites: A review. *Composites part A: Applied Science and Manufacturing*, vol. 67, no.0, pp. 181-200.

[160] W. Weibull (1951). A Statistical Distribution Function of Wide Applicability. *Journal of Applied Mechanics - Transactions of the ASME.*, 58(7): 1001–1010.

[161] Y. Swolfs. *Hybridisation of Self-reinforced Composites: Modelling and Verifying a Novel Hybrid Concept*. PhD thesis, KU Leuven 2015.

[162] M. R'Mili, N Godin, and J. Lamon (2012). Flaw strength distributions and statistical parameters for ceramic fibers: The normal distribution. *Phys. Rev. E*, 85(5):51106.

[163] W. A. Curtin (2000). Tensile Strength of Fiber-Reinforced Composites: III. Beyond the Traditional Weibull Model for Fiber Strengths. *Journal of Composite Materials*, 34(15):1301–1332.

[164] W. A. Curtin (1991). Theory of Mechanical Properties of Ceramic-Matrix Composites. *Journal of the American Ceramic Society*, 74(11):2837–2845.

[165] C. Zweben (1968). Tensile failure of fiber composites. *AIAA Journal*, 6(12):2325–2331.

[166] W. A. Curtin (2000). Dimensionality and size effects on the strength of fibre reinforced composites. *Composites Science and Technology*, 60(4):543–551.

[167] C. Landis and R. M. McMeeking (1999). Stress concentrations in composites with interface sliding, matrix stiffness and uneven fiber spacing using shear lag theory. *International Journal of Solids and Structures*, 36(28):4333–4361.

[168] B. W. Rosen (1964). Tensile failure of fibrous composites. *AIAA Journal*, 2(11):1985–1991.

[169] S. Pimenta (2015). "Fibre failure modelling", in *Numerical Modelling of Failure in Advanced Composite Materials* (P. P. Camanho and S. R. Hallet, eds.), ch.25, Woodhead Publishing.

[170] Q. Zeng, Z. Wang, and L. Ling (1997). A study of the influence of interfacial damage on stress concentrations in unidirectional composites. *Composites Science and Technology*, 57(1):129–135.

[171] P. W. J. van den Heuvel, T. Peijs, and R. J. Young (2000). Failure phenomena in two-dimensional multi-fibre microcomposites. Part 4: a Raman spectroscopic study on the influence of the matrix yield stress on stress concentrations. *Composites Part A: Applied Science and Manufacturing*, 31(2):165–171.

[172] Y. Swolfs, R. M. McMeeking, I. Verpoest, and L. Gorbatikh (2015). Matrix cracks around fibre breaks and their effect on stress redistribution and failure development in unidirectional composites. *Composites Science and Technology*, 108(0):16–22.

[173] M. Ibnabdeljalil and W. A. Curtin (1997). Strength and reliability of fiber-reinforced composites: Localized load-sharing and associated size effects. *International Journal of Solids and Structures*, 34(21):2649–2668.

[174] L. Mishnaevsky Jr. and P. Brøndsted (2009). Micromechanical modeling of damage and fracture of unidirectional fiber reinforced composites: A review. *Computational Materials Science*, 44(4):1351–1359.

[175] V. Calard and J. Lamon (2004). Failure of fiber bundles. *Composites Science and Technology*, 64(5):701–710.

[176] A. Turon, J. Costa, P. Maimí, D. Trias, and J. A. Mayugo (2005). A progressive damage model for unidirectional fibre-reinforced composites based on fibre fragmentation. Part I: Formulation. *Composites Science and Technology*, 65(13):2039–2048.

[177] T. Okabe, N. Takeda, Y. Kamoshida, M. Shimizu, and W. A. Curtin (2001). A 3D shear-lag model considering micro-damage and statistical strength prediction of unidirectional fiber-reinforced composites. *Composites Science and Technology*, 61(12):1773–1787.

[178] T. Okabe, H. Sekine, K. Ishii, M. Nishikawa, and N. Takeda (2005). Numerical method for failure simulation of unidirectional fiber-reinforced composites with spring element model. *Composites Science and Technology*, 65(6):921–933.

[179] S. Blassiau, A. Thionnet, and A. R. Bunsell (2009). Three-dimensional analysis of load transfer micro-mechanisms in fibre/matrix composites. *Composites Science and Technology*, 69(1):33–39.

[180] A. Thionnet, H. Y. Chou, and A. R. Bunsell (2014). Fibre break processes in unidirectional composites. *Composites Part A: Applied Science and Manufacturing*, 65(0):148–160.

[181] A. K. Kaw. *Mechanics of Composite Materials*. Tayler and Francis, 2nd edition, 2006.

[182] Z. S. Wu, C. Q. Yang, Y. H. Tobe, L. P. Ye, and T. Harada (2006). Electrical and Mechanical Characterization of Hybrid CFRP Sheets. *J. Compos. Mater.*, vol. 40, no. 3, pp. 227–244.

[183] G. Czél and M. R. Wisnom (2013). Demonstration of pseudo-ductility in high performance glass/epoxy composites by hybridisation with thin-ply carbon prepreg. *Compos. Part A Appl. Sci. Manuf.*, vol. 52, pp. 23–30.

[184] G. Kretsis (1987). A review of the tensile, compressive, flexural and shear properties of hybrid fibre-reinforced plastics. *Composites*, vol. 18, no. 1. pp. 13–23.

[185] P. W. Manders and M. G. Bader (1981). The strength of hybrid glass/carbon fibre composites. *J. Mater. Sci.*, vol. 16, no. 8, pp. 2233–2245.

[186] T. Hayashi (1972). On the improvement of mechanical properties of composites by hybrid compositon. *Proc 8th int reinforced plastics conference*, pages 149–152.

[187] G. Marom, S. Fischer, F. R. Tuler, and H. D. Wagner (1978). Hybrid effects in composites: conditions for positive or negative effects versus rule-of-mixtures behaviour. *Journal of Materials Science*, 13(7):1419–1426.

[188] R. Kulkarni and O. Ochoa (2005). Transverse and Longitudinal CTE Measurements of Carbon Fibers and their Impact on Interfacial Residual Stresses in Composites. *J. Compos. Mater.*, vol. 40, no. 8, pp. 733–754.

[189] C. Dong (2008). Development of a model for predicting the transverse coefficients of thermal expansion of unidirectional carbon fibre reinforced composites. *Appl. Compos. Mater.*, vol. 15, no. 3, pp. 171–182.

[190] D. Motoc, J. Ivens and N. Dadirlat (2013). Coefficient of thermal expansion evolution for cryogenic preconditioned hybrid carbon fiber/glass fiber. *Journal of Thermal Analysis and Calorimetry*.

[191] M. Phillips (1981). Composition parameters for hybrid composite materials. *Composites*, vol. 12, no. 2, pp. 113-116.

[192] Y. Swolfs, L. Gorbatikh and I. Verpoest (2013). Stress concentrations in hybrid unidirectional fibre-reinforced composites with random fibre packings. *Composites Science and Technology*, vol. 85, no. 0, pp. 10-16.

[193] C. Zweben (1977). Tensile strength of hybrid composites. *Journal of Materials Science*, vol. 12, no. 7, pp. 1325-1337.

[194] R. P. Tavares, A. R. Melro, M. A. Bessa, A. Turon, W. K. Liu, and P. P. Camanho (2016). Mechanics of hybrid polymer composites : analytical and computational study. *Computational Mechanics*, 57(3):405–421.

[195] M. R. Wisnom (1999). Size effects in the testing of fibre-composite materials. *Composites Science and Technology*, 59(13):1937–1957.

[196] M. R. Wisnom, B. Khan, and S. R. Hallett (2008). Size effects in unnotched tensile strength of unidirectional and quasi-isotropic carbon/epoxy composites. *Composite Structures*, 84(1):21–28.

[197] J. M. Hedgepeth (1961). Stress concentrations in filamentary structures. tech. rep. in *NASA Langley Research Center*, Hampton, VA United States.

[198] J. I. Xing, G. C. Hsiao, and T. Chou (1981). A Dynamic Explanation of The Hybrid Effect. *Journal of Composite Materials*, 15(5):443–461.

[199] I. Taketa. *Analysis of Failure Mechanisms and Hybrid Effects in Carbon Fibre Reinforced Thermoplastic Composites*. PhD thesis, KU Leuven, Leuven, 2011.

[200] S. Pimenta e P. Robinson (2014). Modelling the tensile response of unidirectional hybrid composites. *European Conference on Composite Materials*, ECCM.

[201] H. Fukuda (1984). An advanced theory of the strength of hybrid composites. *Journal of Materials Science*, 19(3):974–982.

[202] Y. Swolfs, R. M. McMeeking, I. Verpoest, and L. Gorbatikh (2015). The effect of fibre dispersion on initial failure strain and cluster development in unidirectional carbon/glass hybrid composites. *Composites Part A: Applied Science and Manufacturing*, 69(0):279–287.

[203] H. Yu, K. D. Potter, and M. R. Wisnom (2014). A novel manufacturing method for aligned discontinuous fibre composites (High Performance-Discontinuous Fibre method). *Compos. Part A Appl. Sci. Manuf.*, vol. 65, pp. 175–185.

[204] G. Czél, S. Pimenta, M. R. Wisnom, and P. Robinson (2015). Demonstration of pseudo-ductility in unidirectional discontinuous carbon fibre/epoxy prepreg composites. *Compos. Sci. Technol.*, vol. 106, pp. 110–119.

[205] M. Jalalvand, G. Czél and M. R. Wisnom (2014). Numerical modelling of the damage modes in UD thin carbon/glass hybrid laminates. *Composites Science and Technology*, vol. 94, no. 0, pp. 39-47.

[206] H. Yu, M. L. Longana, M. Jalalvand, M. R. Wisnom and K. D. Potter (2015). Pseudo-ductility in intermingled carbon/glass hybrid composites with highly aligned discontinuous fibres. *Composites Part A: Applied Science and Manufacturing*, vol. 73, no. 0, pp. 35-44.

[207] Conde, F. (2017). Análise e otimização de materiais compósitos de matriz polimérica não convencional em tração uniaxial. Master Thesis, Faculty of Sciences and Technology, NOVA University of Lisbon (FCT/UNL).

[208] Conde, F. M., Coelho, P. G., Tavares, R. P., Camanho, P. C., Guedes, J. M. and Rodrigues, H. C. (2018). Optimization of hybrid polymer composites under uniaxial traction. *Engineering Computations*, *35*(2), 904-931.

[209] Conde, F. M., Coelho, P. G., Tavares, R. P., Rodrigues, H. C., Guedes, J. M. and Camanho, P. P. (2020). Optimization of the microstructure of unidirectional hybrid composites under uniaxial tensile loads. *Composite Structures*, *235*, 111795.

[210] Tavares, R. P., Otero, F., Turon, A. and Camanho, P. P. (2017). Effective simulation of the mechanics of longitudinal tensile failure of unidirectional polymer composites. *International Journal of Fracture*, *208*(1), 269-285.

[211] Otero, F., Oller, S., Martinez, X. and Salomón, O. (2015), "Numerical homogenization for composite materials analysis. Comparison with other micro mechanical formulations", *Composite Structures*, Vol. 122, pp. 405-416.

[212] Melro, A.R., Camanho, P.P. and Pinho, S.T. (2008), "Generation of random distribution of fibres in long-fibre reinforced composites", *Composites Science and Technology*, Vol. 68, No. 9, pp. 2092-2102.

[213] R. P. Tavares (2015). Mechanics of hybrid polymer composites. Master's Thesis, University of Porto, 2015.

[214] Beyerlein, I.J. and Phoenix, S. (1996). Statistics for the strength and size effects of microcomposites with four carbon fibres in epoxy resin. *Composites Science and Technology*, vol. 56, no. 1, pp. 75-92.

[215] Nakatani, M., Shioya, M. and J., Yamashita (1999). Axial compressive fracture of carbon fibers. *Carbon*, vol. 37, no. 4, pp. 601-608.

[216] Curtin, W.A. and Takeda, N. (1998). Tensile strength of fibre-reinforced composites: Ii. Application to polymer matrix composites. *Journal of Composites Materials*, vol. 32, no. 22, pp. 2060-2081.

[217] Mili, M.R., Bouchaour T. and Merle P. (1996). Estimation of weibull parameters from loose-bundle tests. *Composites Science and Technology*, vol. 56, no. 7, pp. 831-834.

[218] Tanaka, F., Obake, T., Okuda, H., Kinloch, I.A. and Young, R.J. (2014). Factors controlling the strength of carbon fibres in tension. *Composites Part A: Applied Science and Manufacturing*, vol. 57, no. 0, pp. 88-94.

[219] Feih, S., Thraner, A. and Lilholt, H. (2005). Tensile strength and fracture surface characterisation of sized and unsized glass fibres. *Journal of Materials Science*, vol. 40, no. 7, pp. 1615-1623.

[220] Foray, G., Descamps-Mandine A., Mili, M.R. and Lamon J. (2012). Statistical flaw strength distributions for glass fibres: Correlation between bundle test and afm-derived flaw size density functions. *Acta Materialia*, vol. 60, no. 9, pp. 3711 – 3718.

[221] Naito, K. (2013). Tensile properties and Weibull modulus of some high-performance polymeric fibers. *Journal of Applied Polymer Science*, vol. 128, no. 2, pp. 1185-1192.

[222] Ostebee, A. and Zorn, P. (2001). *Calculus from graphical, numerical, and symbolic points of view*. Houghton Mifflin School, 2nd edition.

[223] Arora, J.S (2016), *Introduction to optimum design - 4th ed.*, Academic Press.

[224] Swolfs, Y., Morton, H., Scott, A., Gorbatikh, L., Reed, P., Sinclair, I., Spearing, S. and Verpoest, I. (2015). Synchrotron radiation computed tomography for experimental validation of a tensile strength model for unidirectional fibre-reinforced composites. *Composites Part A: Applied Science and Manufacturing*, Vol. 77, pp. 106-113.

[225] Correia, A., Leal, F., Tavares, R. and Conde, F. (2018). Optimizing hybrid fiber-reinforced composites with more than two fibers for pseudo-ductile behavior. Conference abstract in *EngOpt2018 - 6th International Conference on Engineering Optimization*.

[226] Han, Z. and Wei, K. (2022). Multi-material topology optimization and additive manufacturing for metamaterials incorporating double negative indexes of Poisson's ratio and thermal expansion. *Additive Manufacturing*, 54, 102742.

[227] Gao, T. and Zhang, W. (2010). Topology optimization involving thermo-elastic stress loads. *Structural and multidisciplinary optimization*, 42(5), 725-738.

⟨2022⟩

Fábio Rúben Monteiro Conde

Multiscale optimization of non-conventional composite structures for improved mechani-cal response